Behaviour of accelerating entropy spots

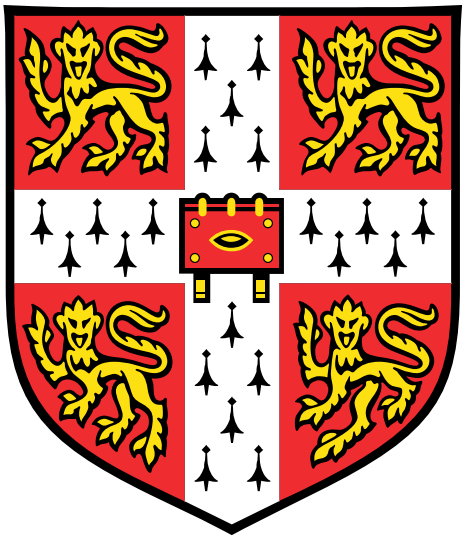

Francesca De Domenico

Department of Engineering
University of Cambridge

This dissertation is submitted for the degree of
Doctor of Philosophy

Jesus College July 2019

Declaration

I hereby declare that except where specific reference is made to the work of others, the contents of this dissertation are original and have not been submitted in whole or in part for consideration for any other degree or qualification in this, or any other university. This dissertation is my own work and contains nothing which is the outcome of work done in collaboration with others, except as specified in the text and Acknowledgements. This dissertation contains fewer than 65,000 words including appendices, bibliography, footnotes, tables and equations and has fewer than 150 figures.

The chapters are written in the active voice. The subject "*we*" refers only to me, my supervisor and the people who contributed to the work, as specified in the relevant bibliography.

Francesca De Domenico
July 2019

Abstract

Behaviour of accelerating entropy spots

Francesca De Domenico

Combustion noise has become a major research interest within the aerospace community. Stricter pollutant emission regulations have forced the introduction of lean premixed pre-vaporised combustors, which produce less NOx but burn more unsteadily, generating more noise and creating the potential for combustion instabilities. Pressure fluctuations in combustion chambers are traditionally classified as direct and indirect noise. The former arises directly from the heat release rate perturbations in the flame. The latter is generated indirectly from the acceleration of regions of non-uniform temperature, density and composition (entropy and composition spots) through narrow passages such as nozzles or turbine guide vanes. Entropy-generated sound waves are both transmitted downstream of the acceleration point, contributing to the overall noise emission, and reflected upstream, where they may couple with the acoustics of the system, potentially triggering instabilities.

Presently, the processes causing the generation of indirect noise and the triggering mechanisms for secondary instabilities are still not completely understood and need further investigation. The aim of this thesis is to shed light on the behaviour of accelerating entropy spots, providing analytical and experimental tools to identify and isolate travelling entropy spots and the sound generated from their acceleration. The physical mechanisms of entropy-to-sound conversion are investigated using a model non-reacting flow system (the Entropy Generator Rig, EGR), designed to mimic the behaviour of a combustor in a controlled environment. The contribution of indirect noise can be easily identified and isolated in the acquired pressure traces, allowing the first direct comparison between experimental data and a newly developed analytical model for the entropy-to-sound conversion in non-isentropic systems.

An important challenge that has limited the understanding of indirect noise is the lack of experimental techniques capable to detect and characterise the production and decay of entropic perturbations in combustion chambers. Laser-Induced Grating Spectroscopy (LIGS) is a promising optical technique for the diagnostics in the gas phase, which measures the

local speed of sound, temperature and composition. LIGS has been previously applied as a low frequency (10 Hz) diagnostic technique in flows containing a seeded or natural absorbing molecule. In the present work, two advances are demonstrated. Firstly, LIGS is applied in a pressurised reacting flow environment using the fundamental Nd:YAG laser wavelength, taking advantage of the absorption line of the water in the flame products. Secondly, high repetition rate lasers (1-100 kHz) are used to obtain signals at high frequency in non-reacting and reacting flows, enabling time resolved measurements. This work opens up a new avenue to capture the evolution of unsteady scalars involved in the convection of entropy spots and turbulence.

Happiness is a way of travel, not a destination.
To all the people that made me smile during the PhD journey.

Acknowledgements

This thesis would not have been possible without the support, advice and inspiration of the wonderful people that I met in these years, to whom I am forever grateful.

First and foremost, I would like to thank my supervisor, Prof. Simone Hochgreb, for her exceptional help, guidance and support. This PhD has been the greatest learning experience that I have ever had, and I could have not asked for a better supervisor. Professionally, her wise advice, explosive creativity and great expertise have guided me through the fun and challenges of doing research. Personally, she has been great role model and a fantastic source of advice and encouragement during these years.

I would like to extend my gratitude to Prof. William L. Roberts and Prof. Gaetano Magnotti for giving me the opportunity to perform experiments at KAUST. I extremely enjoyed the five months that I spent in the spotless CCRC, and I learned a lot. Then, I would like to thank my advisor, Prof. Matthew Juniper, who has been an exceptional source of wise advice and encouragement over these years. Finally, I gratefully acknowledge the help of some great LIGS people from the other place: Dr. Ben Williams for his help in setting up the joint Oxbridge LITGS experiment and for fruitful inputs and discussions and Prof. Paul Ewart for hosting me in his lab and for being always available to answer my questions.

A special mention goes to Dr Luca Magri, who has been my greatest ally since the very first day. I cannot find enough words to thank him for his help, support, patience and friendship over these years. Without him, I would not be writing these acknowledgements, but I would be stuck in the middle of the Black Forest. His advice, comments and constructive critics have been crucial for improving the quality of my research. I am very grateful for all the time that he spent sorting out my research drama and listening to my problems, and for all his support beyond the PhD.

Now I have to admit it: I had never been in a lab before starting my PhD. All the experimental results of this thesis could have not been possible without the help and guidance of several outstanding researchers, technicians and engineers. The biggest thank you goes to Dr Thibault Guiberti, the best and most patient lab teacher that I have ever had. He taught me how not to risk my life every time I enter into a lab, how to be (a bit) less clumsy and

more meticulous during experimental campaigns. Doing experiments together was extremely enjoyable and made the long hours spent in the lab pass quicker. I am very grateful to Dr Lee Weller for his constant availability in helping me in the lab, discussing problems and ideas and checking my writings. I also acknowledge several great people who showed me the ropes in the lab and shared their knowledge with me: Dr Steven Lowe, Dr Georgios Rigas, Dr Patton Allison, Dr Yi Gao, Dr Luming Fan, Dr Yedhu Krishna, Dr Davor Dukic and Priyav Shah. The help of the technicians of the Hopkison lab, Roy, Mark, Rob, Ken, John, has also been crucial for the success of the experiments. Finally, a big thank you goes to Peter Benie, for his much needed help with the computers and his massive kindness and patience in sorting out my IT problems.

In these years, I have probably spent more time in the Hopkinson lab than in my room, and many people there are now much more than just colleagues. The biggest thank you goes to Erwan, who shared part of the entropy journey with me, and has always been a great source of inspiration and motivation. Working with him highly improved my understanding of the physics of indirect noise. Thank you to Steve, whose LITGS lessons have been the funniest time that I have ever had in the lab. He warmly welcomed me in the group from the very beginning, and has been a great friend since then. Thank you to Anh Khoa for his unconditional patience and friendship. I strongly value the constant support and encouragement that he gave me in these years. Thank you to Nick, my best conference buddy. Without him and Becky, Cambridge would have not been the same: much more computer, way less wine, way less social (# I'll bloody miss you Mr & Mrs Jamo). Thank you to Alessandro, who helped me going through a very difficult time. Thank you to Giacomo, who actually does not live in Cambridge, but has been a great source of encouragement, support and inspiration from the continent. Finally, thank you to all the other lab buddies, for all the fun times we spent together in and out of the lab: (in a random order) Joc, Rob, Max, James, Girish, my deskmates Francisco and Richard, Hans, Jose, Jack, Francesco (the boxer), Phil, Petr, Filip, Brian, Pedro, Christian, Jean, Fiona, Andrej, Pau, Cen, Bo, Dante, Hassan, Andrea, Aaron, Jenna.

In these years in Cambridge, I have been so lucky to meet fantastic people with whom I shared amazing times and great memories, and I cannot thank them enough. I want to send the warmest thank you to Anna, for her exceptional patience, friendship and understanding. Thank you for being my solid rock since the very first day in Jesus. Also, the support that she and May gave to me while writing this thesis was truly exceptional and they never made me feel alone. Thus, a big thank you goes to May too, who always lifts me up and has always been so sweet and kind with me. Warmest thanks Alessandra, for all the fun we had together, for her contagious energy, for the amazing bike trips, for her patience in listening and for

her wise advices. Many thanks to Ingrid, who is a breath of fresh air after stressful days in the lab, and is such a generous and caring young lady. I am also extremely grateful to the Neapolitans & Co, who are the best Cambridge family I could ask for: (in the order in which I met them) Anjali, Leonardo, Francesco C., Matteo, Karla, Iacopo, Julie, Dodo, Gianni, Veronica, Francesco A., Garazi, Rapha, Shivani, Ascanio, Miriam. Several big hugs and a massive thank you to my dear CCRC friends: Erica, Paolo and Abdul, who helped me survive the heat of the Red Sea. Finally, thank you to my friends from home, who are always so close no matter how far we live: Betta, Gemma, Camilla, Alessandra, Spe.

Last but not least, I would like to thank my parents Antonella and Umberto and my sisters Claudia and Federica, for their massive, endless and unconditional love, understanding and support. We might not see each other that often, but we are always there one for each other. I am especially grateful to my mother, who spent so much time listening to my endless calls, trying to calm me down and sort out my silly troubles.

To conclude, I want to thank some necessary ingredients that kept me alive, almost safe and sound, in these years: several pairs of running shoes, a lot of music and the Pal who brought music into my life.

This research would have not been possible without the financial support of Qualcomm, EPSRC, Zonta International and of the KAUST visiting programme.

Associated publications

Journal publications

- **De Domenico, F.**, Guiberti, T. F., Hochgreb, S., Roberts, W. L. (2019). Tracer-free laser-induced grating spectroscopy using a pulse burst laser at 100 kHz. *Optics Express* (accepted for publication);

- **De Domenico, F.**, Guiberti, T. F., Hochgreb, S., Roberts, W. L. (2019). Temperature and water measurements in flames using 1064 nm Laser-Induced Grating Spectroscopy (LIGS). *Combustion and Flame*, 205, 336–344;

- **De Domenico, F.**, Rolland, E., Hochgreb, S. (2019). A generalised model for acoustic and entropic transfer function of nozzles with losses. *Journal of Sound and Vibration*, 440, 212–230;

- **De Domenico, F.**, Shah, P., Lowe, S. M., Fan, L., Ewart, P., Williams, B. A. O., Hochgreb, S. (2019). High frequency measurement of temperature and composition spots with LITGS. *Journal of Engineering for Gas Turbines and Power*, 141(031003), 1–11;

- Rolland, E. O., **De Domenico, F.**, Hochgreb, S. (2018). Direct and indirect noise generated by entropic and compositional inhomogeneities. *Journal of Engineering for Gas Turbines and Power*, 140(8)1-9;

- Rolland, E. O., **De Domenico, F.**, Hochgreb, S. (2017). Theory and application of reverberated direct and indirect noise. *Journal of Fluid Mechanics*, 819, 435–464;

- **De Domenico, F.**, Rolland, E. O. , Hochgreb, S. (2017). Detection of direct and indirect noise generated by synthetic hot spots in a duct. *Journal of Sound and Vibration*, 394, 220–236.

Articles in preparation

- Rolland, E., **De Domenico, F.**, Magri, L., Hochgreb, S. (2019). Compositional and entropic noise generated in anisentropic nozzles.

Conference proceedings

- Rolland, E. O., **De Domenico, F.**, Magri, L., Hochgreb, S. (2019). Direct, indirect and compositional noise generated in a nozzle with losses. In *Proceedings of the 11th Mediterrenean Symposium of Combustion*, Tenerife, Spain, 16-20 June 2019 (pp. 1–20);

- **De Domenico, F.**, Fan, L., Lowe, S. M., Weller, L., Hochgreb, S. (2018). Trade off between thermalisation and spatial resolution for LITGS. In *19th International Symposium on the Application of Laser and Imaging Techniques to Fluid Mechanics*, Lisbon, Portugal, 16-20 July 2018 (pp. 1–24);

- **De Domenico, F.**, Rolland, E. O., Hochgreb, S. (2017). Acoustic and entropic transfer functions of a generalised subsonic nozzle. In *24th International Congress on Sound and Vibration*, London, UK, 23-27 July 2017 (pp. 1–8);

- **De Domenico, F.**, Rolland, E. O., Hochgreb, S. (2017). Measurements of the effect of boundary conditions on upstream and downstream noise arising from entropy spots. In *Proceedings of ASME Turbo Expo 2017: Turbomachinery Technical Conference and Exposition*, Charlotte, NC, USA, 26-30 June 2017 (pp. 1–13).

Table of contents

List of figures

List of tables

Chapter 1

Introduction

Over the last few decades, noise emission has become a topic of increasing concern to society. As a result, stricter regulations have been introduced for air, road and rail transport technology. Within the various transportation noises, aircraft noise is considered the most detrimental due to its intermittent nature. Aircraft noise has damaging effects not only on the environment but also on human health. Beyond immediate consequences, such as annoyance, interruption of conversations and disturbed sleep, it can also cause long term effects such as increase in the risk of strokes, heart attack and dementia [4]. Increasingly restrictive rules to limit and counteract the growth of noise pollution have been introduced, led also by the fact that air traffic is expected to grow by 42% in the next 20 years, according to the International Civil Aviation Organisation (ICAO) [6]. The Advisory Council for Aviation Research and Innovation in Europe (ACARE) is committed to reduce the perceived noise by 65% by 2050 (compared to 2000 levels) [3, 45].

In an aircraft, the major sources of noise are the airframe (fuselage, nacelle, landing gear, wings) and the engine (fan, compressor, combustor, turbine and jet exhaust) [58, 114] (Fig. 1.1). Turbojet, fan and external aerodynamical noise have been significantly reduced in the last years, so that the reduction of combustion noise has now become a major priority for aircraft manufactures. The problem of combustion-generated noise and instabilities has been heightened by the introduction of Lean Premixed (LPM), Lean Premixed Prevaporised (LLP) and Rich-Quench-Lean (RQL) combustors, which became necessary given the new regulations on lowering NOx emissions from gas turbine. In these combustors, the temperature of the burnt gases is reduced by increasing the bypass ratio of air through the combustion chamber. This makes the combustion more unsteady, which considerably increases the emitted sound and the potential for catastrophic damage [30, 61, 133, 31, 166]. For these reasons, in the last decade, a significant effort has been undertaken to understand and reduce noise and instabilities in combustion chambers whilst maintaining emission

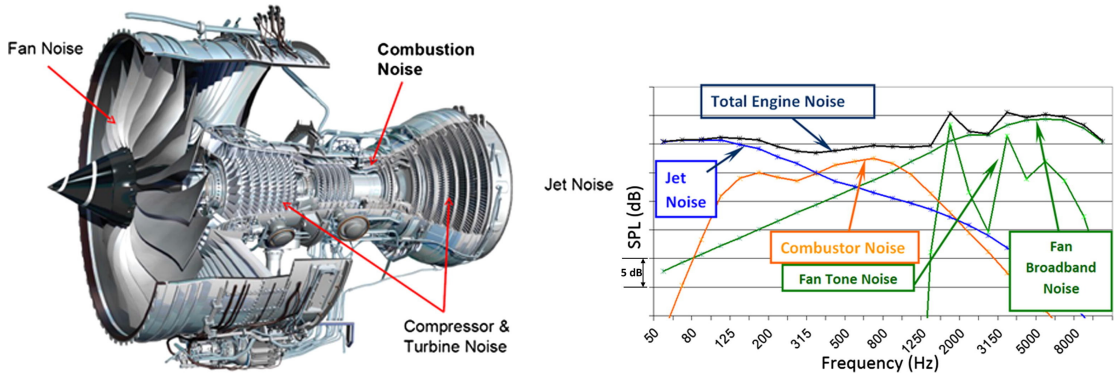

Fig. 1.1 Summary of the noise sources in an aeroegine (Rolls-Royce Trent 1000) (left); Typical contribution of the noise sources in a turbojet engine at approach, from SAFRAN Snecma [108] (right).

benefits. Therefore, it is crucial to investigate combustion noise, in order to develop a new generation of cleaner, quieter, more stable and more efficient aero-engines and gas turbines.

1.1 Combustion noise

Unsteady combustion is one of the main issues in the current design and development of combustion systems. Combustion processes can be transient, time harmonic, statistically stationary and stochastic and they usually involve the coupling between chemical kinetics, mass and energy transport, flame propagation, hydrodynamics and flame-structure interaction [132]. Unfortunately, there is still a lack of analytical and numerical models to explain unsteady reacting flows. Combustion chambers are extremely complicated and expensive to model, due to the multitude of phenomena occurring at different time and space scales. Experimental studies are challenging and expensive too: only simplified configurations can be tested in laboratories, but these might not develop some of the mechanisms occurring in full scale engines. Moreover, diagnostics in reacting flows are complex and there is a lack of experimental techniques able to acquire the quantities of interest with the needed accuracy and precision [58, 166].

From the standpoint of noise generation, the (unsteady) combustion in a confined environment produces essentially two effects, usually called direct and indirect noise [196, 147, 58]. The unsteady expansion of burning gases generates isentropic pressure waves (acoustic waves), propagating upstream and downstream of the flame in the combustion chamber, which are generally called *direct noise*. When these waves reach the upstream or downstream boundaries, they are partially reflected, transmitted and dissipated. Waves that reflect back into the combustion chamber may further couple with the acoustics of the system,

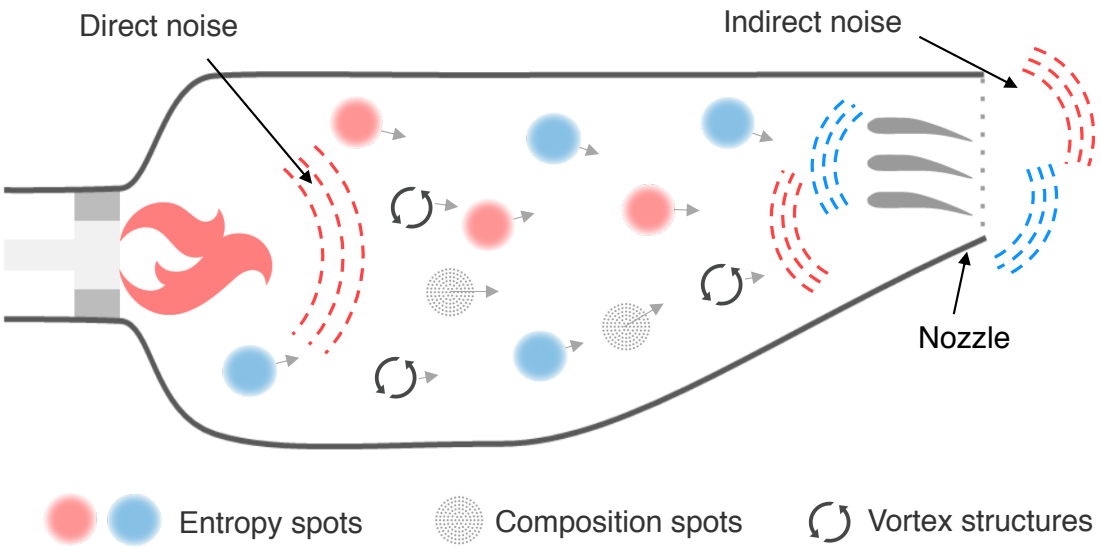

Fig. 1.2 Sources of noise in a combustion chamber, adapted from Dowling et al. [58].

stabilising or destabilising the original flame oscillation. Waves that propagate through the turbomachinery stages contribute to the sound emitted by the engine.

The unsteady heat release of the flame also causes the production of pockets of different temperature and density (called *entropy spots*) or composition (*composition spots*) or vortical disturbances (*vorticity waves*) that are advected towards the turbine with the mean flow. The generation and advection of these convective perturbations do not create any pressure fluctuations in the linear approximation. However, when they reach regions with gradients in the mean flow properties (such as turbine blades or exhaust nozzles) a compensating pressure gradient is needed to accelerate them. These acoustic waves (entropic, compositional or vortical noise, called in general *indirect noise*) are both reflected back into the combustor and transmitted downstream into the gas turbines. The upstream propagating waves may interfere with the acoustics of the system, giving rise to combustion instabilities (secondary instabilities) while the downstream propagating waves may contribute to the overall core noise generated by the engine.

In this thesis, we use the term direct and indirect noise to refer both to the sound waves reflected into the combustion chamber and to the sound waves transmitted through the gas turbine.

1.1.1 Direct noise: coupling mechanisms between flame and acoustics

From the sixties, the generation of direct noise has been extensively studied in unbounded turbulent flames under premixed and non-premixed conditions [24]. Sound waves result from the unsteady volumetric expansion of the gas in the reactive regions. Fluctuations in the heat release rate associated with the chemical reactions generate expansion and compression waves with a broadband nature and frequencies lower than 2000 Hz that propagate in all directions. Strahle [195], and later on Crighton [36] and Candel [31] described the mechanisms linking the far field pressure perturbations and the density changes in a turbulent flame zone by using the Lighthill analogy and the balance equations of fluid dynamics.

Most of the theoretical, numerical and experimental investigations on direct noise have been performed in open flames, which are much simpler to analyse. In fact, the pressure fluctuations do not depend on the geometry of the system, as the sound generation is not modified by the acoustic waves reflected at the boundaries. Also, the modelling of the systems is simplified as the flow can be described as isobaric and low Mach number. Finally, experiments in unconfined flames offer a wider optical access to the flow and do not require the pressurisation of the rigs. Research efforts have helped to develop a stronger understanding of the mechanisms driving the generation of sound from the unsteady heat release, so that several solutions to reduce the occurrence and effects of direct noise in combustion chambers have been designed. Control of noise has been achieved both with passive devices (such as liners, dampers, resonators [222, 124]) or with active control systems (active decoupling of the pressure and heat-release cycles [163, 186]).

However, in practical applications, flames are commonly enclosed in confined environments, such as combustion chambers, where the sound waves generated by the flame are reflected on the walls and nozzles. This might establish a feedback loop between unsteady heat release and pressure perturbations, so that the noise becomes coherent as it is tuned on one of the resonance frequencies of the system [37, 133]. The interaction between heat release rate and acoustics was noticed for the first time by Higgins in 1802 in the so called *singing flame*, which refers to a flame producing sound when placed inside a tube of proper length [102]. Lord Rayleigh [137] was the first to explain how acoustic waves can be excited and maintained by heat additions, introducing the so-called *Rayleigh criterion*. The interaction between the sound produced by a flame and the hydrodynamic flow through the scattering and reflection of the sound waves at the boundaries can lead to strong discrete-frequency oscillations, and can eventually trigger thermoacoustic instabilities.

Thermoacoustic instabilities

Thermoacoustic instabilities are one of the most serious concerns in the development of combustion systems. The term "*thermoacoustic instabilities*" refers to organised oscillatory motions having well-defined frequencies, typically linked to the resonant frequencies predicted for the combustion chamber [30, 133, 58, 166]. They arise primarily from a resonant coupling of the acoustics of the chamber with the heat release rate of the flame (primary instabilities), but they can also be triggered by the entropic and compositional generated sound (secondary instabilities), oscillations of fuel in the feed lines, atomisation lines and vortex shedding. Combustion instabilities are characterised by large-amplitude oscillations of one or more natural acoustic modes of the combustors, which might result in thrust oscillations, severe vibrations, enhancement of heat transfer and thermal stresses, oscillatory load and fatigue on the structural components and flame blow-off or flashback. Such instabilities have been encountered during the development and operation of propulsion systems (e.g. rockets, ramjets, and afterburners), power generation units (e.g. land-base gas turbines), boiler and heating systems and industrial furnaces [133].

For example, combustion instabilities have significantly hindered the development of solid and liquid rocket engines by NASA in the sixties [35, 37] (Fig. 1.3). The most intensive (and expensive) program devoted to solve a problem of combustion instabilities was performed during the development of the F-1 engine that powered the Saturn rockets to the Moon. The F-1 encountered instabilities with peak amplitudes greater than or comparable to

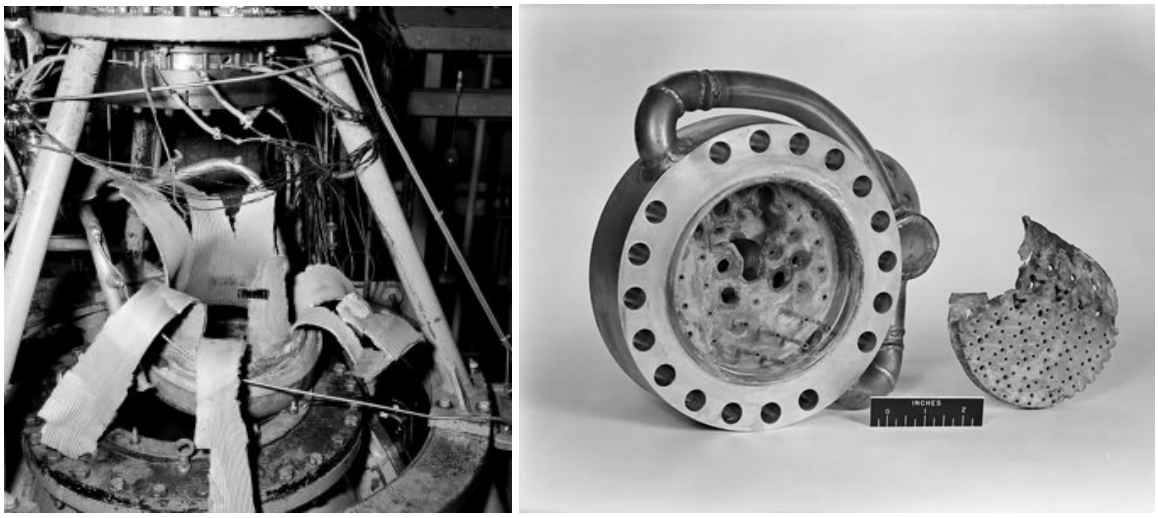

Fig. 1.3 Engine failure in the Rocket Engine Test Facility (RETF) test stand (9/16/1958 (left) and damage in a rocket injector 50-4-HF-7-600 (Hydrogen Fluorine, 5000 pound thrust) (right) [1].

the average pressure in the chamber (i.e. more than 140 bar) with frequencies in the 200 to 500 Hz range. These instabilities, produced by a coupling between the injection plate and the chamber, caused explosions in the combustor, and their elimination required a costly trial and error development programme that included 2000 full scale tests (of a total of 3200).

Trial and error methods are neither economical nor practical. Ideally, one would like to predict the onset of a thermoacoustic instability during the early phases of design. Unfortunately, prediction models are often characterised by a high sensitivity to small variations in the design parameters, thus, small initial errors can lead to wrong predictions of the overall stability of the system. Moreover, as these instabilities are often related to the actual dimensions and geometry of the combustion chamber and its components, they might manifest themselves only in the latest phases of the development, as had happened in the case of the Saturn V rockets.

1.1.2 Indirect noise: current challenges

The processes causing the generation of indirect noise and the triggering mechanisms for secondary instabilities are still not completely understood and need further investigation [58, 154, 114, 166]. Indirect noise is widely believed to be one of the main contributors to combustion noise, however, there are still several issues that limit its understanding and modelling. The effect of entropy modes in the stability of a combustor depends on the specific configuration under investigation, the indirect noise generation being sensitive to the geometry, operating conditions and flow properties. The mechanisms in which these parameters affect the overall combustor noise and stability are still not totally clear, so it is difficult to predict and/or identify the relative contribution of indirect noise in the overall pressure traces. Simplified analytical and numerical models/laboratory scale experiments enable physical insight into the phenomena, but it is not completely clear whether these results are relevant to full scale aero-engines.

The major difficulties in the identification and analysis of indirect noise are [58, 154, 114]:

- identification and separation of the contributions of the pressure waves directly generated from the heat release rate fluctuations and indirectly generated from the acceleration of convecting entropic and compositional spots and vortex structures;
- lack of experimental techniques capable of identifying and isolating entropic and compositional spots and their pressure traces while accelerated;
- difficulties in the characterisation of the mean flow properties and acoustic boundary conditions of combustion chambers;

- lack of models relating the relative amplitudes and phases of the convective perturbations to the properties of the mean flow, frequency, geometry and operating conditions;
- difficulties in the characterisation of the decay and dispersion of entropic and vortical perturbations in a combustion chamber;
- poor understanding of the behaviour of nozzles and turbine guide vanes as converters of entropic and vortical disturbances into acoustic waves.

1.2 Thesis motivation and outline

The objective of this thesis is to shed some light on the behaviour of accelerating entropy spots and to develop diagnostics for measuring entropy waves in combustion chambers. Two main parts can be identified, with the common leitmotiv of providing analytical and experimental tools to directly detect and quantify the origin and propagation of entropy and composition spots and the generation of indirect noise. In the first part of the thesis (Chapters 2-5), the physical mechanisms of the entropy-to-sound conversion are investigated experimentally and analytically using a model non-reacting flow system for validation (the Entropy Generator Rig, EGR). Within the various results, these experiments highlight the difficulties in obtaining accurate measures of travelling entropy spots in turbulent flow environments. The second part of the thesis (Chapters 6-9) deals with this challenge: Laser-Induced Grating Spectroscopy (LIGS) is demonstrated as a good candidate to detect and time resolve the unsteady passage of temperature and composition variations in reacting flows.

Chapter 2 gives a brief summary of the previous research on indirect noise, reviewing the analytical, numerical and experimental efforts to gain insight into it. In particular, the theoretical and experimental challenges limiting the understanding of the phenomenon are highlighted. In Chapter 3, the governing equations for reacting and non-reacting flows are introduced, focusing on the physical mechanisms driving the generation of direct and indirect noise in enclosed environments, such as combustion chambers and entropy generator rigs. The general low order models describing the generation of waves at unsteady sources, the reverberation of the sound waves in enclosed environments and the acoustic and entropic nozzle transfer functions are derived. A non-reacting flow system, the Entropy Generator Rig, is built to experimentally validate these low order models. Its design and operation are described in Chapter 4, showing that it allows a clear time separation between direct and indirect noise. From the acquired experimental data, it is demonstrated that the observed nozzle behaviour is not captured by traditional analytical models describing the flow as isentropic (Chapter 5). The isentropic nozzle assumption is therefore relaxed, introducing an

analytical model describing the nozzle transfer functions in situations with pressure losses and flow recirculations which often happen in real systems.

The second part of the thesis explores laser diagnostic measurements for detecting entropy and composition spots. Chapter 6 gives an overview of the available techniques for high speed temperature and composition measurements in reacting flows. Then, LIGS is introduced as a tool to measure the local speed of sound, temperature and composition in the gas phase. Resonant (thermal) or non-resonant (electrostrictive) signals are obtained if the flow absorbs or does not absorb the laser wavelength respectively. Relevant previous applications are reviewed, prior describing the signal formation and the experimental procedures used in this thesis. Thermal LIGS at high repetition rate is initially applied to detect and time resolve unsteady temperature and composition variations in the EGR using a high repetition rate PIV laser (Chapter 7). LIGS is then applied to more complex scenarios with flames, using a burner installed in a pressurised, optically accessible vessel. Low repetition rate (Chapter 8) and high repetition rate (Chapter 9) LIGS measurements are performed in premixed methane-air flames. A particular novelty of the development is to demonstrate the technique using the popular Nd:YAG laser at 1064 nm, without adding seedings to the flow to generate LIGS signals, but taking advantage of water molecules which are common products of the flames and absorb the 1064 nm wavelength light. Finally, Electrostrictive LIGS (LIEGS) with a pulse burst laser is used to probe unsteady density variations in a helium-air jet (Chapter 9). Advantages and disadvantages of the use of a pulse burst laser for LIGS diagnostics are discussed. The main findings and conclusions of this thesis are presented in Chapter 10, along with possible avenues for future work.

Chapter 2

State of the art: entropy waves and indirect noise

A number of investigations have contributed to analyse the interaction between flow inhomogeneities produced from turbulent combustion and accelerating elements such as nozzles and turbine blades. However, there are still many open questions on the physical mechanisms behind the entropy- and composition-to-sound conversion and on the importance of indirect noise in the overall combustion noise. This chapter gives a brief summary of the previous research on the topic, to highlight the current theoretical and experimental challenges that are limiting its understanding.

2.1 Theoretical modelling of indirect noise

2.1.1 Sound generated by the acceleration of temperature and density inhomogeneties

The first distinction between acoustic, entropic and vorticity modes for a compressible, viscous and heat-conductive gas was made in 1953 by Kovasznay [122]. He showed that the three disturbance fields obey three independent differential equations: a hyperbolic differential equation for acoustic waves and parabolic differential equations for entropy and vorticity waves. The acoustic waves propagate with the speed of sound relative to the mean flow, while the entropy and vorticity waves are advected with the mean flow. In the absence of spatial gradients in the mean flow properties, the three modes are independent for small fluctuations: their interaction is a second order effect that can be neglected in the linear analysis. Thus, the advection of small entropy or vorticity disturbances does not generate sound waves, unless their intensities become larger and these modes couple together due to

second order non-linear phenomena [34]. However, when there is a spatial gradient in the steady flow properties (such as an acceleration/deceleration point), the interaction of these modes becomes a first order effect: the acceleration of entropic or vorticity perturbations generates sound waves which propagate both upstream and downstream of the acceleration point. The first analytical investigation of the sound radiated by the acceleration of these inhomogeneties was done by Morfey [153] in the seventies. His work extended the Lightill theory on jet noise [134, 135] by adding the so called "excess jet noise" to incorporate indirect noise. Since then, several theoretical investigations have been performed to understand and explain the indirect noise generated by the acceleration of fluid inhomogeneties and vortical structures [29, 71, 19, 197, 42]. These studies suggested that indirect noise is a non-negligible component of the overall combustion noise, but they could not be validated due to the lack of experimental data [195].

Marble and Candel summarised these analytical results [147], deriving a linear model to describe the transfer functions of a compact convergent/divergent nozzle with impinging acoustic and entropic disturbances, in subsonic and supersonic conditions. The compactness hypothesis implies that the length of the nozzle is small in comparison to the acoustic/entropic wavelengths of the incoming disturbances. This limits the validity of the analysis to low frequency acoustic and entropic waves, which are assumed to propagate quasi-steadily through the nozzle, without being distorted or phase shifted between the inlet and the outlet. This quasi-steady theory was then extended to systems where the flow is accelerated through a series of compact turbine blade rows [41, 43].

To obtain a more realistic description of the problem, further investigations relaxed both the quasi-steady assumption and the one dimensional assumption and analysed how the geometry of a system and the frequency dependence of the perturbations affect the entropy-to-sound conversion [131, 152, 107, 80, 81]. The quasi-steady 1-D case remains a valid asymptotic limit but, for a non-compact nozzle, the geometry can have a non-negligible effect on its response to high frequency perturbations [17, 21]. Goh et al. [85] extended the compact solution from low to mid frequencies through an asymptotic expansion of the linearised Euler equations. They showed that the reflection and transmission across a nozzle can be extended to non-zero frequencies using an effective nozzle length that depends on the mean flow through the shape of the nozzle. Duran and Moreau [62] analysed the acoustic and entropic transfer functions of a non-compact nozzle and diffuser in subsonic and supersonic conditions, solving the Euler equations using the Magnus expansion. They determined both the amplitude and the phase of the reflected and transmitted waves as a function of the frequency of the impinging disturbance and the geometry of the nozzle, concluding that the non-compact effects should be taken into account when studying the noise

propagating through accelerating and decelerating flows, especially for choked conditions. Stow et al. [194] expanded the theory to annular nozzles, where vorticity waves (three dimensional effects) can not be neglected. They used at first an asymptotic analysis and then an effective length to include the flow behaviour into the model. Later, Duran et al. [64] applied the Magnus expansion to predict the response of circumferential nozzles to high frequency acoustic, entropical and vortical circumferential waves. Most of these findings on the acoustic and entropic transfer functions of nozzles were summarised in a review paper by Dowling and Mahmoudi [58], where a linear model to describe direct, indirect and vortical noise generated in combustion chambers was also developed and validated.

All of these developments were carried out in the linear regime, e.g. assuming small amplitude perturbations. After revisiting the previous work on the acoustics of gas turbines and LPP combustors, Dowling and Stow [59] concluded that although the linear analysis is simplified, it remains a good tool for preliminary design, as it is able to predict resonances, limit cycles and the development of combustion instabilities. Non-linear effects should only be considered in the case of large amplitude fluctuations. The non-linear forced response of subsonic and choked nozzles (with shocks) was analysed by Moase et al. [152], Huet and Giaucque [111] and Huet [110].

Compositional noise

Magri et al. [145, 144] recently theorised the existence of an additional source of indirect noise, called *compositional noise*. Compositional noise is generated by the acceleration of regions with a different mixture fraction and composition (and therefore different chemical potential) relatively to the mean flow (*compositional inhomogeneties*). Theoretical predictions show that compositional noise can even exceed direct and entropic noise under certain conditions. Rolland et al. [173] experimentally validated these findings in a model experiment where synthetic composition spots were generated via unsteady mass injection, showing that the contribution of compositional noise is comparable to direct and entropic noise. In a real combustion chamber, compositional inhomogeneities are produced at the flame location due to incomplete mixing of fuel and air, or oscillations in the flame structure. The overall amount of compositional noise produced depends on the strength of the entropy and composition spots that, after being advected through the chamber, are accelerated in the nozzle or in the turbine. With a LES simulation in a realistic system, Giusti et al. [83] demonstrated that non-negligible compositional spots reach the inlet of the turbine in a RQL Rolls Royce combustor, producing a clear pressure signature when accelerated. This study suggests that neither entropic nor compositional noise can be neglected while analysing the pressure output of a combustion chamber.

2.1.2 Role of indirect noise in combustion systems

In the last 20 years, the research effort to understand the role of indirect noise in the overall combustion noise has increased substantially. There are still many open questions on the physical mechanisms behind indirect noise, but there is general agreement that it must be included in the modelling of combustion noise, since it can couple with the acoustics of a system, enhancing as well as reducing the overall stability of the system [56, 86, 168]. A common approach to describe and analyse combustion chambers is the use of low order models [59]. Using this approach, Leyko et al. [131] quantified both direct and indirect noise in a simple quasi 1-D combustor model of an aero-engines terminated with a choked nozzle, assuming an isentropic mean flow and performing the analysis in a cold flame. The theory of Marble and Candel [147] agreed well with their numerical solution of the Euler equations at low frequencies. Moreover, they showed that the ratio of indirect-to-direct noise depends on the Mach number in the flame zone and on the Mach number at the nozzle outlet. This ratio can be small for laboratory experiments but large in most real aero-engines, so they concluded that indirect noise can be the dominant source of combustion noise in real situations, even exceeding direct noise by one order of magnitude.

However, as already pointed out, the amount of indirect noise generated in a system is highly affected by the strength of the entropy and composition fluctuations that survive till the acceleration region, which is often unknown. There are no simple methods to measure unsteady temperature and composition oscillations along a combustion chamber with sufficient accuracy and frequency resolution. This translates to difficulties in the validation of models for the dispersion of entropy and vorticity waves and lack of information on the amplitude of the disturbances impinging in the nozzle. Also, it is hard to draw any universal conclusions on the survival of the entropy waves, as their dissipation and dispersion in a combustor strongly depend on the geometric, thermal and hydrodynamic characteristics of the chamber. Sattelmayer [185] suggested an analytical model for the dispersion of scalar perturbations such as equivalence ratio and entropy fluctuations. From his results, he concluded that most entropy fluctuations deteriorate before reaching the nozzle, and therefore they do not have a major effect on the overall stability of a combustor. However, LES simulations of combustion chambers showed that significant entropy waves survive until the combustor exit [75], even for fairly long chambers [220], and generate acoustic waves when accelerated [157]. Using a Gaussian model for the dissipation and shear dispersion of entropy waves and a turbulent velocity profile, Morgans et al. [155] obtained that significant entropy waves survive at the combustor exit in the frequency range relevant for the thermoacoustics of a combustor. They showed that entropy waves are only attenuated by shear dispersion arising from the mean velocity profile, while their dissipation is negligible. Also, a theoretical

and experimental study from Wassmer et al. [212] demonstrated that convective processes dominates over diffusive processes. In a lab-scale combustor, entropy spots were generated with low frequency pulsed fuel injection (5-50 Hz), and survived till the combustor exit.

However, further investigations suggested that the survival of inhomogeneties through the chamber till the nozzle is highly linked to their frequencies. For low values of the Helmholtz number, Giusti et al. [84] and Mahmoudi et al. [146] highlighted that the shear dispersion arising from spatial variations of the mean velocity profile is responsible for attenuation of entropy fluctuations. For high values of the Helmholtz number, turbulent mixing and diffusion might instead enhance the decay of the entropy fluctuations, as demonstrated by an experimental study by Hajialigo et al. [90]. However, all these studies emphasise how the geometric, thermal and hydrodynamic properties of combustion chambers highly affect the dissipation and dispersion of entropy spots, so that it is not possible to draw any general conclusions.

2.2 Experimental studies on indirect noise

2.2.1 Experiments in combustion chambers

Combustion experiments in open flames at atmospheric pressure give important insights on direct combustion noise and thermoacoustic oscillations [30, 132]. Indirect noise and resulting secondary instabilities can only be generated when the combustion chambers and/or the experimental rigs are terminated by a restricted flow boundary (such as a nozzle) to accelerate the flow. This corresponds to a pressurisation of the rigs, which substantially complicates their design and operation. For this reason, there have been only few attempts to design and manufacture experiments aimed to identify and isolate indirect noise in a reacting flow environment.

The first experimental analysis indicating indirect noise as the major source of combustion noise was performed on a combustor taken from a Boeing 502-7D unit [159]. Indirect noise was identified via a coherence analysis between the pressure and temperature spectrum. Experimentally and analytically, it was shown that with a sufficient acceleration of the flow (when the combustor was choked at the outlet), the emitted sound could be mainly attributed to indirect noise. As gas turbines operate in choked conditions, this experiment suggested that entropy noise could represent the major contributor to the core noise in aero-engines. However, Eckstein et al. [67] reached opposite conclusions while studying the role of entropy waves in a low-frequency RQL combustor. They observed that the entropy waves were highly dissipated before reaching the outlet, concluding that the entropy-to-sound conversion did

not play a significant role for the occurrence of low frequency combustion instabilities. It was later suggested that the high dissipation encountered by the entropy waves was due to the relatively large transversal length of the combustor, which facilitated the dispersion of the entropy spots and also did not allow a 1-D analysis.

Further experimental studies performed in lab-scale combustors suggested the existence of non-negligible entropy-generated sound. In the combustor analysed by Bake et al. [10], the entropy noise was found to be the dominant source of the pressure fluctuations acquired in the exhaust duct. Measurements of the density oscillations in the throat section via Rayleigh scattering confirmed that significant entropy spots had survived until the nozzle [170], as the spectral density of the Rayleigh and pressure signal were highly correlated. Hield and Brear [101] investigated the behaviour of a premixed laboratory combustor with an open and a choked downstream end. When the exit was choked, the pressure trace displayed a broadband low frequency spectrum which agreed with the frequency determined from the convective time scale of the chamber. Hochgreb et al. [103] also obtained a strong evidence of entropy spots in a learn burn combustor with a choked exit. The clear self-excited peak in the pressure trace was attributed to an entropy mode, and CFD simulations validated this hypothesis. A low frequency instability observed in the pressure traces of a SAFRAN combustor was also attributed to a mixed entropy/acoustic mode. The corresponding frequency was indeed lower than the first pure acoustic mode of the combustor, and large entropy spots were found to have survived through the chamber [156]. Recently, Bonciolini et al. [22] identified a peak in the pressure trace of the ETH sequential combustor which was attributed to a convective-driven mechanism. However, in an experiment performed with the CESAM-HP burner, Mazur et al. [149] did not obtain any significant influence of indirect noise in the acoustics of the system, as all the acoustic modes observed in the combustor could be linked to geometrical parameters of the rig, including the injection tube, the combustion chamber and the feeding lines.

These contrasting conclusions on the role of indirect noise in the overall combustion noise emphasise the lack of a full physical understanding of the mechanisms behind its generation and propagation. Although many of these experiments qualitatively testified the existence of indirect noise, a proper quantitative comparison between data and theoretical models was not possible, due to the difficulties in measuring the strength of the accelerated entropy spots and in isolating the indirect contribution in the pressure traces.

2.2.2 Model experiments in controlled environments

Given the difficulties in the identification and separation of direct and indirect noise in real or lab-scale combustors, several simplified experiments with synthetic entropy spots have been

performed instead. To eliminate some of the complications of the experiments in combusting flows, synthetic entropy spots are mainly obtained by generating or injecting packets of hotter/colder air or of different composition in a non-reacting mean flow.

The first rig generating synthetic hot spots was built in Caltech in the seventies [20, 19]. Entropy waves were produced via the Joule effect, by pulsating current into an electric grid of wires at 100 Hz, to replicate realistic frequencies. However, due to the thermal inertia of the wires, a temperature increase of only 1 K could be achieved, which was too small to allow a quantitative analysis of the pressure signal in the time domain. Moreover, there was little scope for parametric variations, and the data acquisition and processing systems did not have sufficiently high time resolution to separate the direct and indirect noise components.

The problem was studied again in 2007 when a small scale generic test rig Entropy Wave Generator (EWG) was built in DLR Berlin to generate synthetic hot spots [11]. Entropy spots were produced with a heating grid of thin wires and then accelerated through a convergent/divergent nozzle, which was operated both in subsonic and sonic conditions. The acoustic oscillations were acquired downstream of the nozzle with microphones. The DLR experiment generated interest in the community and initiated multiple theoretical and numerical investigations to explain the experimental results [58] but different modelling strategies led to opposite conclusions in the interpretation of the pressure signals. Initially, it was believed that the acoustic oscillations were a manifestation of pure indirect noise [11, 158]. However, following studies [63, 130] realised that also the contribution of direct noise had to be evaluated to explain the acquired pressure traces. For the subsonic case, it was found out that the signal was mainly due to direct rather than indirect noise [63]. For the supersonic case, instead, the signal was explained as a mixture of indirect noise and multiple reflections at the boundaries, which were not perfectly anechoic [130]. The debate went on: all the following attempts to model the experimental results emphasised the importance of the accurate determination of the reflection coefficients of the boundaries and of the transfer function of the unsteady heating source to correctly determine the origin of the pressure signal. Up until now, the community has not agreed yet on whether the acquired signal could be attributed to direct or indirect noise [13, 110, 138].

Later on, a similar experiment was performed in DLR for analysing the sound generated from the acceleration of vorticity waves [117]. Vorticity fluctuations were created artificially by the injection of a swirling flow. It was claimed that the strong pressure trace obtained in the experiment was caused by the acceleration of vorticity waves, demonstrating the vorticity-to-acoustics conversion mechanism.

Since then, further model experiments have been developed to investigate the indirect noise mechanisms more in depth. A new Hot Acoustic Test rig (HAT) was set-up in the

DLR Berlin to look at various thermoacoustic phenomena [118, 120]. Entropy waves were created by injecting cold spots into a heated mean flow. From the pressure traces acquired downstream of the nozzle, it was shown that indirect noise was generated from the acceleration of these cold spots, and that its amplitude increased with steeper temperature gradients. At Politecnico of Milan (Italy) a new concept of entropy wave generator was also developed. It was based on the alternate injection of hot/cold air upstream of a turbine, by using a two way rotatory valve, in a rig designed and manufactured by SMCPFA (Romania). Tests were performed using different insulation systems, investigating the propagation of entropy waves both in free and immersed jet configuration [79]. The results seemed to indicate that in the upstream section of the turbine, the pressure signal was dominated by vorticity and direct noise from the injection system, while in the downstream side the pressure signal was mainly due to indirect noise. The test-rig was also used to study the attenuation of entropy waves through the turbine stage. The entropy waves were observed to undergo a significant attenuation throughout the stator blade row, while they were less altered through the rotor blades [78]. Finally, Tao et al. [201] built a Temperature and Acoustic Fluctuation Generator (TAFG), consisting of a tube fitted with a converging nozzle. Entropic waves were generated by injecting hot air into the tube and then accelerated through the nozzle. The injection process was driven by a loudspeaker, so that acoustic and entropic waves were created simultaneously and at the same frequency (from 20 to 100 Hz). The acoustic reflection coefficients recovered from the pressure measurements were found to be in good agreement with the model of Marble and Candel [147], but the entropic transfer functions of the nozzle could not be extracted from the data due to the poor signal-to-noise ratio and the to low amount of entropic noise produced in the experiment.

2.3 Conclusions

Sound waves (indirect noise) are generated when regions of different temperature or composition are accelerated through nozzles or turbine guide vanes in combustion chambers. Theoretical models have been developed to explain and model this entropy- and composition-to-sound conversion. However, experimental validation in combustion chambers is difficult due to the lack of clear experimental data: direct and indirect noise are merged into the acquired pressure traces. In addition, the intensity of the sound waves generated depends on the strength of the entropy and composition spots surviving until the acceleration region, but it is challenging to extract this information directly in reacting flows. Several experiments were designed to analyse the generation and propagation of indirect noise, but they led to opposite conclusions on its importance in the overall pressure output.

To overcome these problems, simplified non-reacting rigs simulating the behaviour of a combustor in a controlled environment have been built. In these experiments, entropy and composition spots are synthetically generated by pulsed sources and then accelerated through nozzles. These experiments have more clearly demonstrated the existence of non-negligible entropic and compositional noise. However, no experimental study has yet provided a quantitative measurement of indirect noise for comparison with theoretical models, so that the analytical models for indirect noise generation have not yet been validated. Thus, unambiguous experimental measurements are needed to confirm or refute theoretical predictions and evaluate the actual contribution of indirect noise to the overall combustion noise. Not only clear pressure data isolating indirect noise is needed, but also simultaneous reliable measurements of the amplitude of the entropy spots surviving through the chamber and entering into the acceleration region.
The validation of entropy-to-sound conversion models and the development of techniques for time-resolving the passage of entropy and composition spots are the main objectives of this thesis.

Chapter 3

Theoretical framework

In this chapter we introduce the governing equations for reacting and non-reacting flows highlighting the physical mechanisms driving the generation of direct and indirect noise in enclosed environments, such as combustion chambers and entropy generator rigs.

3.1 Governing equations

The theoretical framework of the governing equations for a chemically reacting, multi-component, perfect gas is described here. Under the continuum hypothesis, the governing equations for a viscous compressible flow in differential form are [167, 132]:

- Conservation of mass:

$$\frac{D\rho}{Dt} + \rho \bigtriangledown \cdot \mathbf{u} = 0 \tag{3.1}$$

- Conservation of momentum:

$$\rho \frac{D\mathbf{u}}{Dt} = -\nabla p + \nabla \cdot \boldsymbol{\tau} + \rho \sum_{i=1}^{N} Y_i \mathbf{F}_i \tag{3.2}$$

- Equation of state:

$$p = \frac{\rho RT}{W} \tag{3.3}$$

- Conservation of energy:

$$\rho \frac{Dh}{Dt} = \frac{Dp}{Dt} + \dot{q} + \nabla \cdot (k \nabla T) + \boldsymbol{\tau} : \nabla \mathbf{u} + \rho \sum_{i=1}^{N} Y_i \mathbf{u}_{D,i} \mathbf{F}_i \tag{3.4}$$

- Conservation of chemical species:

$$\rho \frac{DY_i}{Dt} = \dot{\omega}_i - \nabla \cdot (\rho Y_i \mathbf{u}_{D,i}) \tag{3.5}$$

- Gibbs equation:

$$dh = T ds + \frac{1}{\rho} dp + \sum_{i=1}^{N} \frac{\mu_i}{W_i} dY_i \tag{3.6}$$

In these equations, the flow is characterised by the scalar variables density ρ, pressure p, temperature T, and entropy s, the vectorial velocity $\mathbf{u}$, and the related enthalpy h, and molecular mass W, which in turn depend on the species properties as a function of temperature and pressure. The gas is composed of N components, each of molar fraction Y_i, characterised by a chemical potential μ_i and a molecular mass W_i. The rate of mass consumption of species i is $\dot{\omega}_i$, while $\boldsymbol{u}_{D,i}$ is the diffusive velocity. $\boldsymbol{\tau}$ is the viscous stress tensor, $\dot{q}$ is the external rate of heat transfer to the flow and F_i are the external body forces per unit of mass acting on the i-th component of the mixture.

In the absence of body forces, the entropy generation can be expressed as [59]:

$$\rho T \frac{Ds}{Dt} = \dot{q} + \nabla \cdot (k \nabla T) + \boldsymbol{\tau} : \nabla u - \rho \sum_{i=1}^{N} \frac{\mu_i}{W_i} \frac{DY_i}{Dt} \tag{3.7}$$

showing that entropy can be produced or removed by heat release, thermal gradients, viscous dissipation and variations in the local composition.

3.1.1 Small perturbations approach

The thermoacoustic behaviour of a combustion chamber is usually analysed by assuming that the perturbations of the mean flow quantities are small. Under this assumption, each flow variable $\alpha(x,t)$ is assumed to be represented by a spatially uniform base quantity $\bar{\alpha}$ and an small first order perturbation $\alpha'(x,t)$, such as:

$$\alpha(x,t) = \bar{\alpha} + \alpha'(x,t) \tag{3.8}$$

If we assume that the gas is non-reacting and calorically perfect, and with no gradients in the mean flow properties, no viscous dissipation and no heat release perturbations, we can derive the linearised governing equations that describe the perturbed behaviour of the flow.

The continuity equation becomes:

$$\frac{D\rho'}{Dt} = -\bar{\rho}\nabla\mathbf{u}' \tag{3.9}$$

As we neglect molecular transport terms and chemical reactions ($Ds/Dt = 0$), Eq. 3.9 can be transformed into:

$$-\frac{1}{\gamma\bar{p}}\frac{Dp'}{Dt} = \nabla\mathbf{u}' \tag{3.10}$$

In the case of small perturbations, it is often assumed that viscous effects are negligible, so that the momentum equation becomes:

$$\bar{\rho}\frac{D\mathbf{u}'}{Dt} = -\nabla p' \tag{3.11}$$

For small acoustic perturbations, it is usually assumed that entropy is unaffected by heat transfer or viscous effects, so that the linearised energy equation, written in terms of entropy, becomes:

$$\frac{Ds'}{Dt} = 0 \tag{3.12}$$

As the flow is irrotational:

$$\frac{D(\nabla\times\mathbf{u}')}{Dt} = 0 \tag{3.13}$$

In the case of non-reacting systems, with no mass addition or subtraction, the composition does not change, therefore:

$$\frac{DY_i'}{Dt} = 0 \tag{3.14}$$

After defining the local speed of sound as:

$$\bar{c}^2 = \left(\frac{\partial p}{\partial\rho}\right)_s \tag{3.15}$$

from Eq. 3.10 and 3.11, assuming a one dimensional flow, we obtain the wave equation for the pressure in a duct with uniform mean flow [172]:

$$\left(\frac{\partial}{\partial t} + \bar{u}\cdot\nabla\right)^2 p' - \bar{c}\nabla^2 p' = 0 \tag{3.16}$$

which has solutions in the form of rightward and leftward propagating waves π^+ and π^- travelling at the sound speed relative to the medium $\bar{u}+\bar{c}$ and $\bar{u}-\bar{c}$ respectively, such as:

$$\frac{p'}{\gamma p}(x,t) = \pi^+\left(t - \frac{x}{\bar{c}+\bar{u}}\right) + \pi^-\left(t - \frac{x}{\bar{c}-\bar{u}}\right) \tag{3.17}$$

Equation 3.16, 3.12 and 3.13 show that, in the absence of mean flow gradients and heat, mass or momentum injection; acoustic, entropic and vortical perturbations are independent in a first approximation, which means that the modes are decoupled. While acoustic perturbations p' are isentropic and irrotational and travel at the relative speed of sound $\bar{u}\pm\bar{c}$, entropic disturbances are incompressible and irrotational and are advected with the flow at the mean velocity $\bar{u}$, while vorticity waves are incompressible and isentropic. However, acoustic, entropic and vortical perturbations might couple one with each other at boundaries, in regions of flow inhomogeneties and through non-linearities. In this work, we consider the coupling effect that occurs through boundary conditions, which is typically called "mode conversion". In particular, we are interested in the entropy- and composition-to-sound conversion that occurs through nozzles and turbine guide vanes. When a region of different temperature, density or composition is accelerated by the mean flow in a nozzle, a differential force is needed to compensate for the gradient in density of the flow. Disturbances couple as the condition imposed by the boundary applies to the total value of the fluctuation itself, and not to its components. For this reason, when entropy, composition or vortical spots are accelerated, a gradient in the pressure is generated, which results in sound waves propagating both upstream and downstream of the acceleration region [132]. Tam [200] suggested that pressure waves are created to maintain a pressure balance between the front and the rear of the accelerating spot, as a differential acceleration (and consequently a differential rarefaction) occurs through the spot while it is accelerated or decelerated, leading to the generation of compression and expansion waves to maintain the pressure balance.

3.2 Analytical 1D model of an entropy-generator rig

The theoretical underpinnings of the generation of acoustic waves via entropy spots in a flow have been discussed in a number of papers [34, 147], and further developed more recently [86, 63, 198]. Most theoretical studies consider the 1D case of entropy and composition spots generated from a source at rest and then convected through a compact nozzle. The flow is described as a non-reacting perfect gas. Waves are decomposed as a combination of acoustic, entropic and compositional waves. The forward (π^+) and backward (π^-) acoustic waves propagate at the relative speed of sound $\bar{u}+\bar{c}$ and $\bar{u}-\bar{c}$ respectively, while the entropic (σ)

and compositional (ξ) inhomogeneties are convected at the flow speed $\bar{u}$. The specific heat capacity is assumed be constant with temperature and changes only due to the composition. These four waves are defined as follows:

$$\pi^+ = \frac{1}{2}\left(\frac{p'}{\gamma p} + \frac{u'}{c}\right); \qquad \pi^- = \frac{1}{2}\left(\frac{p'}{\gamma p} - \frac{u'}{c}\right); \qquad \sigma = \frac{s'}{c_p}; \qquad \xi = Z' \tag{3.18}$$

where Z is a mixture fraction, which is here defined as the normalised mass fraction of the perturbing species.

Using the Gibbs relation (Eq. 3.6) the entropy waves can be expressed as

$$\sigma = \frac{T'}{\bar{T}} + \frac{c_p'}{\bar{c}_p} - (\gamma - 1)\frac{p'}{\bar{\gamma} p} - \frac{1}{\bar{c}_p \bar{T}} \sum_{i=1}^{N} \frac{\mu_i}{W_i} \frac{dY_i}{dZ} Z' \tag{3.19}$$

Thus, entropic and compositional perturbations are related, as the specific entropy is related to the local gas composition. Following a derivation similar to Magri [144], we define two terms Ψ and $\aleph$ as

$$\Psi = \frac{1}{\bar{c_p}\bar{T}} \sum_{i=1}^{N} \left(\frac{\mu_i}{W_i}\right) \frac{dY_i}{dZ} \tag{3.20}$$

$$\aleph = \sum_{i=1}^{N} \left(-\frac{1}{\bar{c}_p}\frac{dc_p}{dY_i} + \frac{1}{R}\frac{dR}{dY_i}\right) \frac{dY_i}{dZ} \tag{3.21}$$

which take into account the variation in chemical potential (Ψ) and in the specific heat capacity ratio and molecular mass ($\aleph$) due to the presence of a secondary gas of a different composition. From Eq. 3.20 and 3.21, the entropy wave σ from Eq. 3.19 can be briefly expressed as:

$$\sigma = \frac{p'}{\bar{\gamma}\bar{p}} - \frac{\rho'}{\rho} - (\aleph + \psi)\xi \tag{3.22}$$

3.2.1 Jump conditions across a compact wave source

Here we briefly describe the generation of acoustic, entropic and compositional perturbations from a compact source in a 1D system with no area change. The compactness hypothesis means that the axial length of the source is much smaller than the characteristic wavelengths of the system and can therefore be neglected. This is often the case for synthetic entropy and composition spots generators such as heating grids or a mass injection ports. At the source location, fluxes of mass ϕ_m, momentum ϕ_M, energy ϕ_e and composition ϕ_Z are injected into the system. Under these hypothesis, the mass, momentum, energy and composition

conservation across the source can be expressed as:

$$[\rho u]_0^1 = \phi_m; \tag{3.23}$$

$$\left[p + \rho u^2\right]_0^1 = \phi_M;$$

$$[\rho u h_{\text{tot}}]_0^1 = \phi_e;$$

$$[Z]_0^1 = \phi_Z$$

where $[-]_0$ and $[-]_1$ denote the upstream and downstream sections across the jump respectively (See Fig. 3.1). In entropy generator rigs, the injected fluxes ϕ are usually small, so it can be assumed that they do not modify the mean flow properties across the jump, but that they only generate small perturbations ($\bar{\phi} = 0$; $\phi' \neq 0$). Once the small perturbation approach defined in Eq. 3.18 is applied to Eq. 3.23, the normalised transfer functions across a compact source read[1]:

$$\left[\left(1 + \frac{1}{\bar{M}}\right)\pi^+ + \left(1 - \frac{1}{\bar{M}}\right)\pi^- - \sigma - (\Psi + \aleph)Z'\right]_0^1 = \varphi'_m; \tag{3.24}$$

$$\left[\left(1 + \frac{1}{\bar{M}}\right)^2\pi^+ + \left(1 - \frac{1}{\bar{M}}\right)^2\pi^- - \sigma - (\Psi + \aleph)Z'\right]_0^1 = \varphi'_M;$$

$$\left[\left(\frac{3}{2}(\bar{\gamma}-1)\bar{M} + \bar{\gamma} + \frac{1}{\bar{M}}\right)\pi^+ + \left(-\frac{3}{2}(\bar{\gamma}-1)\bar{M} + \bar{\gamma} - \frac{1}{\bar{M}}\right)\pi^- - \aleph Z'\right]_0^1 = \varphi'_e;$$

$$\left[Z'\right]_0^1 = \varphi'_Z$$

where the normalised fluxes are defined as:

$$\varphi'_m = \frac{\phi'_m}{\bar{\rho}\bar{u}}; \qquad \varphi'_M = \frac{\phi'_M}{\bar{\rho}\bar{u}^2}; \qquad \varphi'_e = \frac{\phi'_e}{\bar{\rho}\bar{u}\bar{c}_p\bar{T}}; \qquad \varphi'_Z = \phi'_Z. \tag{3.25}$$

[1]These equations were derived by E.O. Rolland [174] to include the effects of mass, momentum and composition addition in the heating grid model described by Duran et al. [63]

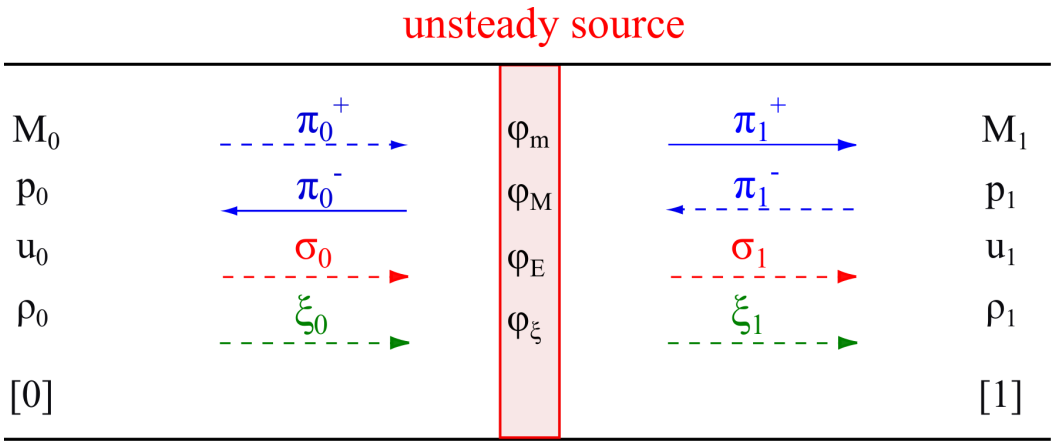

Fig. 3.1 Forward and backward acoustic (π^+ and π^-), entropic (σ) and compositional (ξ) waves generated by a wave source. φ: injected fluxes of mass (φ_m), momentum (φ_M), energy (φ_e) and composition (φ_Z). Solid arrows: waves generated by the source; dashed arrows: waves impinging on the source.

Waves generated at a compact heating grid

The experiments described in Chapters 4 and 5 refer to a set-up where entropy spots are generated via the unsteady heating of a grid of thin wires. This heater generates only small changes in the temperature of the flow ($T'/T < 10\%$) so it can be modelled as an unsteady compact source which does not modify the mean flow properties.

From Eq. 3.25, the normalised heat flux $q' = \varphi'_e$ at the heater location can be expressed as:

$$q' = \varphi'_e = \frac{Q'}{\bar{\rho}\bar{u}\bar{c}_p\bar{T}} \tag{3.26}$$

defining Q' as the heat release rate per unit volume.

Since the activation of the heating grid does not generate either changes in the composition or net forces on the flow ($\varphi_M = \varphi_E = \varphi_Z = 0$), the waves generated by the heating grid are [63]:

$$\pi^+ = \frac{1}{2}\frac{\bar{M}}{\bar{M}+1}\varphi'_e; \qquad \pi^- = \frac{1}{2}\frac{\bar{M}}{1-\bar{M}}\varphi'_e; \qquad \sigma = \varphi'_e = q' \tag{3.27}$$

Eq. 3.27 shows that the unsteady heat addition generates two sound waves which propagate at the relative speed of sound upstream and downstream the grid, and an entropy spot which is convected downstream with the mean flow.

3.2.2 Reverberation of waves in an enclosed chamber

In this section we briefly describe how the multiple reflections of sound waves at the boundaries of an enclosed chamber affect the shape and amplitude of the acquired pressure traces. After being generated, for example at the heating grid location, the acoustic waves propagate both upstream and downstream of the source, travelling at the local speed of sound. When they reach the boundaries of the system, such as the nozzle or the turbine guide vanes (downstream) or the injection plate (upstream), these sound waves are partially reflected, partially transmitted and partially dissipated. The reflected waves propagate back into the chamber, where they travel in the opposite direction at the relative speed of sound until they reach the opposite boundary, where again they are partially reflected, transmitted or dissipated. The multiple reflections of sound waves inside a chamber, called *reverberation*, continue up until the waves extinguish due to losses and viscous and thermal dissipations. Reverberation can substantially affect the shape and amplitude of the acquired pressure traces, both in the time and in the frequency domain, so it must be taken into account to accurately predict and/or understand the acquired pressure signals and the acoustics of the chamber [175]. Fig. 3.2 shows a schematic of the multiple reflections encountered by a downstream-travelling sound wave π^+ generated at the entropy source location.

Combustion noise is usually characterised of a large spectrum of frequencies (50-2000 Hz), whose corresponding wavelengths scale with the longitudinal extension of the chamber. Analysing the acoustic response of combustion systems in the frequency domain is more effective for dealing with a broad range of frequencies. The frequency-dependent acoustic reflection and transmission coefficients can be experimentally measured with well established techniques, such as the multi-microphone method [44], which allows one to extract the acoustic transfer functions of the boundaries over a large frequency range. However, there are no experimental techniques to easily measure the entropy- and composition-to-sound conversion coefficients of acceleration/deceleration regions over the whole frequency range. Thus, there has been no direct way to experimentally validate the models describing the high frequency indirect noise in a system and to experimentally verify its relevance.

The design and development of suitable experiments to generate entropy or compositional spots offers a number of challenges, primarily associated with the generation and measurement of the respective perturbations. For example, one can think of two ways to generate entropic and compositional perturbations: by using heated wires or actuated valves in non-reacting flows, one has control of the source; or by using fuel or spark fluctuations in a combustor, one has control of the timing. Generating temperature and composition fluctuations using heated wires or actuation valves is limited to low frequencies and low intensities, owing to the inertia of the wires, time delay of the valves, or limited dimensions of

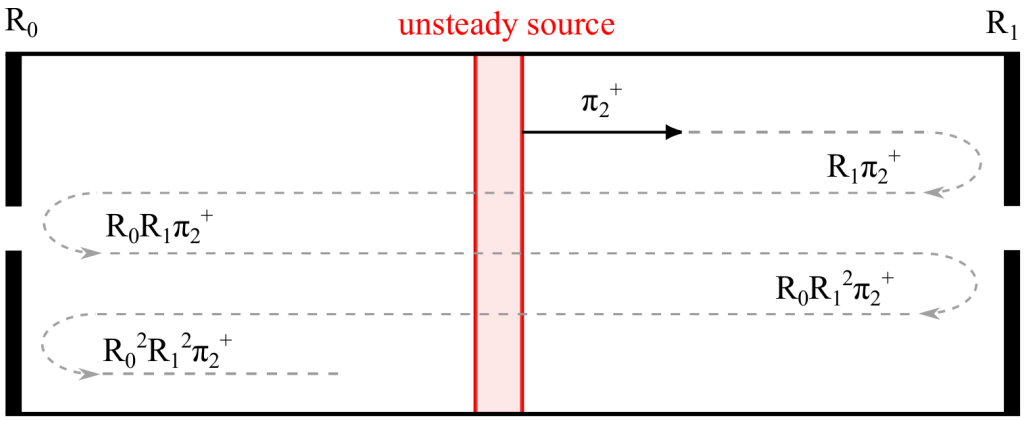

Fig. 3.2 Reverberation of acoustic waves in an enclosed chamber, where π_2^+ is the original wave and R_0 and R_1 are the inlet and outlet reflection coefficients.

the systems [11]. Conversely, methods generating higher frequency sparks or fuel modulation in a mixture create uncertainties in the propagation of the hot spots. The entropy generation device described in this thesis uses the former method, and is limited to frequencies much lower than the characteristic frequencies of a combustion chamber (less than 50 Hz in the case of the Entropy Generator Rig). The measurement of such low frequency pressure perturbations creates its own problems. Multi-microphone methods require the probes to be spaced at least $\lambda/4$ one from each other, which is not feasible in this experiment, as the longitudinal extension of the rig is typically much smaller than the acoustic wavelengths (the rig is acoustically compact). A frequency-based analysis of the pressure is meaningless, as the phase shift in the traces acquired by two different transducers is negligible. In order to remedy this problem, the transfer function of the boundaries of the system can be extracted from the pressure traces in the time domain by using models that take the multiple reflections of the waves in the system into account. For this purpose, Rolland [175] developed a time-based reverberation model which describes the build up of sound waves in an enclosed system resulting from their multiple reflections. When the model is inverted (*"de-reverberated"*), the reflection coefficients of the boundaries can be extracted, as well as the original source waves. This model is used in this thesis to interpret the pressure traces acquired in the Entropy Generator and to extract the transfer functions at the boundaries. The full derivation of the reverberation expressions developed by Rolland [175] is not reported here, but selected equations are introduced in Chapter 5, where they are used to extract the reflection coefficients of the nozzle in the EGR for model validation.

3.2.3 Jump conditions across a nozzle

The response of a nozzle to acoustic, entropic, vortical and compositional disturbances is typically computed using nozzle transfer functions [147, 144]. Acoustic waves that impinge into a nozzle are partially reflected, transmitted and dissipated, while the acceleration of entropic, compositional or vortical disturbances generates sound waves. The nozzle transfer functions relate the impinging disturbances to the outgoing ones and are derived from the jump conditions across a nozzle (Fig. 3.3):

$$R_+ = \frac{\pi_1^-}{\pi_1^+}; \quad R_- = \frac{\pi_2^+}{\pi_2^-}; \quad T_+ = \frac{\pi_2^+}{\pi_1^+}\frac{\gamma p_2}{\gamma p_1}; \quad T_- = \frac{\pi_1^-}{\pi_2^-}\frac{\gamma p_1}{\gamma p_2}; \quad S_R = \frac{\pi_{1,s}^-}{\sigma_1}; \quad S_T = \frac{\pi_{2,s}^+}{\sigma_1} \tag{3.28}$$

where the subscript notation $_R$ and $_T$ implicitly defines the reflected and transmitted parts of the acoustic waves.

In this thesis, we consider a quasi 1D formulation, allowing only for a variation of the parameters along the nozzle length. The nozzle is assumed to be compact (quasi-steady assumption), meaning that its length is negligible compared to the disturbance wavelength, so that the frequency dependence of the perturbations can be neglected (the validity of the compactness hypothesis is discussed in the next paragraph). The flow in the nozzle is assumed to be adiabatic, with no external addition of mass, momentum, energy or species. Starting from the quasi-one-dimensional linearised Euler equations, the mass flow rate ($\dot{m}$), total temperature (T_t), and species (Z) are conserved across the nozzle. If no losses occur across the area discontinuity, the entropy s is conserved. Instead, if pressure losses occur, the entropy increases and the conservation of momentum is the final jump condition needed to close the problem. Under these hypotheses, the integral forms of the conservation of mass, energy, momentum, entropy and species equations governing the flow behaviour between two generic cross sections A_1 and A_2 in a nozzle are, respectively [8]:

$$[\dot{m}]_1^2 = [\rho A u]_1^2 = 0; \tag{3.29}$$

$$[T_t]_1^2 = \left[T\left(1+\frac{\gamma-1}{2}M^2\right)\right]_1^2 = 0;$$

$$\left[A(p+\rho u^2)\right]_1^2 = \int_1^2 p\, dA;$$

$$[s]_1^2 = \left[\frac{p}{\rho^\gamma}\right]_1^2 = 0;$$

$$[Z]_1^2 = 0$$

The integral term $\int_1^2 p\, dA$ in the conservation of momentum represents the pressure forces acting on the sides of the control surface between A_1 and A_2. When linearised, these equations become:

$$\left[\frac{\dot{m}'}{\dot{m}'}\right]_1^2 = \left[\left(1+\frac{1}{\bar{M}}\right)\pi^+ + \left(1-\frac{1}{\bar{M}}\right)\pi^- - \sigma - (\Psi+\aleph)Z'\right]_1^2 = 0;$$

$$\left[\frac{\dot{T}_t'}{\dot{T}_t'}\right]_1^2 = \left[\frac{\gamma-1}{1+\frac{\gamma-1}{2}\bar{M}^2}\left((1+\bar{M})\pi^+ + (1-\bar{M})\pi^- + \frac{1}{\gamma-1}\sigma + \frac{\Psi}{\gamma-1}Z' - \frac{1}{\bar{c}_p}\frac{dc_p'}{dY_i}\frac{1+\frac{\gamma-1}{2}\bar{M}^2}{\gamma-1}Z'\right)\right]_0^1 = 0;$$

$$\left[\left(\frac{\bar{c}}{\bar{M}}+\bar{M}\bar{c}+2\bar{c}\right)\pi^+ + \left(\frac{\bar{c}}{\bar{M}}+\bar{M}\bar{c}-2\bar{c}\right)\pi^- - \bar{M}\bar{c}\sigma - \bar{M}\bar{c}(\Psi+\aleph)Z'\right]_1^2 = \frac{\int_1^2 pdA}{\bar{\rho}A\bar{u}};$$

$$\left[\frac{s'}{\bar{c}_p\bar{T}}\right]_1^2 = [\sigma]_1^2 = 0;$$

$$\left[Z'\right]_1^2 = [\xi]_1^2 = 0 \tag{3.30}$$

The transfer functions of Eq. 3.29, and Eq. 3.30 are valid both for subsonic and supersonic diffusers. However, if the nozzle chokes at the throat, the information from downstream of the nozzle can not travel upstream (against the flow direction) in sonic or supersonic regions. This poses an extra physical constraint to the system and an additional condition applies to the flow: as the Mach number at the throat $[-]_T$ is fixed to unity ($M_T = 1$), we must have

$$M_T' = \frac{1}{\bar{M}_T}\frac{u_T'}{\bar{c}_T} - \frac{c_T'}{\bar{c}_T} = 0 \tag{3.31}$$

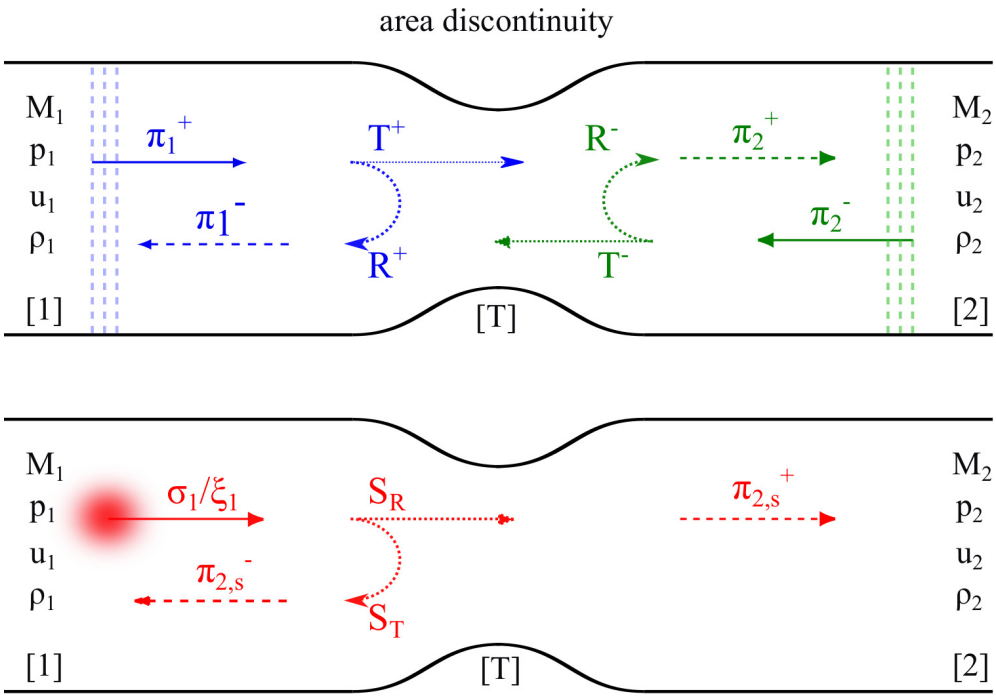

Fig. 3.3 Acoustic and entropic transfer functions in a nozzle: R are the reflection coefficients, while T the transmission coefficients. Impinging perturbations: acoustic (π), entropic (σ) and compositional (ξ).

A detailed description of the acoustic and entropic transfer functions of sonic supersonic nozzles and supersonic nozzles with a shock can be found in previous studies [147, 110] and goes beyond the scope of this thesis, as the nozzles analysed in this work are only in subsonic-to-sonic throat conditions.

The compactness hypothesis

Equations 3.29 describe the nozzle as a compact jump which provides the matching conditions between the flow upstream and downstream of it. In the Entropy Generator Rig (EGR), the nozzle can be assumed to be acoustically compact, as the acoustic wavelength λ_a is much bigger than the nozzle wavelength λ_N, which here is taken as the nozzle length L_N ($L_{N,max} = 0.35$ m in the experiments):

$$\frac{\lambda_a}{\lambda_N} = \frac{c/f}{L_N} > 10^1 \tag{3.32}$$

where f is the frequency of the perturbations, here taken as $f = 10$ Hz. Care must be taken when evaluating the compactness of the nozzle with respect to convective disturbances, as the convective wavelength λ_c is much shorter than the acoustic one. In the experiments on

the EGR, indeed, the flow velocities upstream of the nozzle $\bar{u}$ are designed to be two orders of magnitude smaller than the speed of sound c ($\overline{M} \ll 1$). Physically, this means that the shape of the acceleration profile might affect the shape and amplitude of the indirect noise generated. We have that:

$$\frac{\lambda_c}{\lambda_N} = \frac{u/f}{L_N} \simeq 1 \tag{3.33}$$

However, experimental investigations in the EGR (Chapter 5) demonstrated that the changes in the transfer functions due to the non-compactness of the system are negligible, therefore the compact assumption is considered valid also for entropic disturbances in a first approximation.

Chapter 4

Design and operation of the Entropy Generator Rig (EGR)

This chapter describes the design and operation of the Entropy Generator Rig (EGR). The EGR is an experimental rig that allows the time separation between the direct and indirect noise contributions in a non reacting flow. Synthetic entropy spots are produced in a controlled way via unsteady heating or pulsed injection. Compression waves (direct noise) are generated from the heating and injection processes. The entropy spots are then advected with the mean flow and finally accelerated through orifice plates or nozzles located at the end of the duct, producing a strong acoustic signature which propagates upstream and downstream of the nozzle (indirect noise). The convective time is selected to be longer than the pulse length, in order to obtain a clear time separation between direct and indirect noise in the acquired pressure traces. A long tube (30–60 m) can be added to the rig as an anechoic termination, in order to isolate the original acoustic pulses from their corresponding reflections at the boundaries. The contribution of indirect noise to the overall noise is shown to be non negligible either in subsonic or sonic throat conditions. However, the absolute amplitude of direct noise is larger than the corresponding fraction of indirect noise, explaining the difficulty in clearly identifying the two contributions when they are merged. Further, we show the importance of using appropriate pressure transducer instrumentation and correcting for the respective transfer functions in order to account for low frequency effects in the determination of pressure fluctuations [1].

[1] The results of this chapter are published in *Journal of Sound and Vibration* [50] and in the *Proceedings of the ASME Turbo Expo 2017* [51]

4.1 Introduction

There is a lack of experimental data that clearly shows the role of indirect noise in the overall acoustics of a combustion chamber. Direct and indirect noise are mixed, so it is difficult to identify and separate their relative contributions and importance. For these reasons, simplified experiments where indirect noise is generated in a controlled way by synthetic entropy spots have been built, as described in Chapter 3. Entropy noise can be isolated in the acquired pressure traces, without the complications induced by flames, so that models of entropy-to-sound conversion can be validated. Before the Entropy Generator Rig was designed, there had been no measurements of the upstream propagating entropy noise: entropy noise had only been acquired downstream of the nozzle [11]. Yet the backward propagating waves have a clear impact in the acoustics of a system, as they can adversely affect the flame leading to instabilities [168, 86, 103].

The Entropy Generator Rig aims to investigate the physical mechanisms involved in the generation of direct and indirect noise in a controlled environment. The experiment produces a very simple geometric situation, amenable to one-dimensional modelling. Synthetic entropy spots are generated either via the Joule effect or unsteady injection of gases with a different density and then accelerated via orifice plates or nozzles. Indirect noise can be acquired both upstream and downstream of the acceleration point; therefore, these results are complementary to other experiments using EWGs.

A detailed description of the experimental apparatus and instrumentation is provided in Sections 4.2 and 4.3. This is followed by some experimental results on entropy noise obtained with the Entropy Generator Rig (Sec. 4.4). In these results, the pressure traces are measured only upstream of the acceleration point. These pressure traces are acquired for four different configurations, to obtain a comprehensive understanding of the behaviour of the system and provide limit cases for validation of models: (A) an *open end* configuration, with clear boundary conditions; (B) a *closed tube* configuration with no bulk flow, where only direct noise is produced; (C) a set-up where the flow is accelerated in a *subsonic orifice plate*; (D) a set-up where the flow is accelerated in a *sonic orifice plate*. The transducer data shows that direct noise is generated when the heating device is activated, while indirect noise is generated when the hot spots are accelerated in the orifice plate, both in subsonic and sonic conditions. The modular set-up enables the unambiguous time separation of direct and indirect noise in the overall pressure trace using a sufficient convective distance between the entropy spot source and the acceleration point.

In this chapter, we also discuss an important issue which has not been previously reported, regarding the inadvertent use of condenser microphones in the low frequency range typical

of synthetic entropy spot generators. In the ultra low frequency range, they behave as a high pass filter, leading to potentially erroneous outputs.

4.2 Experimental set-up

4.2.1 Entropy Generator Rig (EGR)

The Entropy Generator Rig is shown in Fig. 4.1. Air flows through a tube at a controlled rate. The air flow leaves through an orifice plate and/or nozzles, which can be operated in subsonic and sonic conditions. Entropy spots can be produced synthetically either by pulsing current through a heating device or by injecting a secondary gas with a different density via a solenoid valve. The heating grid generates a heat release pulse via the Joule effect, creating a spot of hotter air, while the gas injection generates a spot of different density and composition with respect to the mean flow. The entropy spots are convected with the flow, and generate indirect and composition noise as they accelerate. Dynamic temperature and pressure measurements are performed downstream of the entropy generation module, upstream or downstream of the nozzle, via flush-mounted pressure transducers, anemometers and thermocouples on the centre-line, as described later. The rig is modular, so its layout can be modified to take measurements in various configurations. A quartz tube can be added downstream of the entropy module to obtain optical access to the flow and perform laser diagnostics measurements. A 30-60 meter long plastic hose, working as an anechoic termination, can be attached to the rig to isolate single travelling pulses and avoid multiple reflections. The behaviour of the various experimental components is now described.

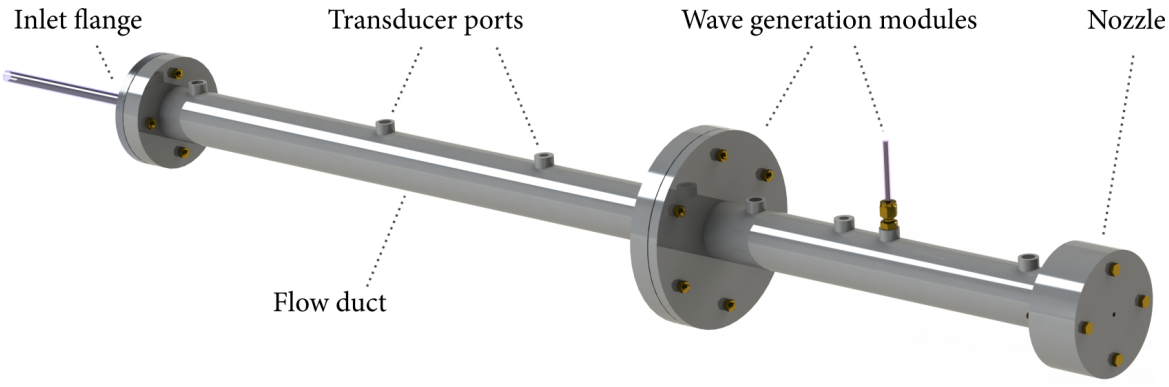

Fig. 4.1 The Entropy Generator Rig (Figure courtesy of E.O. Rolland [174]).

Filtered compressed air from the laboratory air supply system is fed into a 250 L tank to dampen out upstream pressure oscillations. The tank pressure is set to 5 bar using a

pressure gauge. The tank is connected via a 12 mm inner diameter plastic hose to mass flow controllers (MFC, Alicat MCR250, MCR500, accuracy, $\pm$ 1% full scale), or a mass flow meter for high flow rates (MFM, Alicat MCR3000, accuracy $\pm$ 1% full scale). The MFC/MFM are connected to the test section via a 12 mm, 1.2 meter long plastic hose via a flat flange to provide a simple boundary condition.

The rig has an inner diameter of 42.6 mm and is made from sections of PVC and stainless steel 316. The PVC tube inner diameter is slightly larger than the steel tube by 0.2%, so the discrepancy is assumed to be negligible. The different materials are used to address both safety and sealing considerations: the PVC pipe is lighter and easier to handle, but is prone to air leakages if fitted with transducer ports. Thus, it is used only in the sections of the tube where there are no transducers. The heating device (Sec. 4.2.2) and the injection valve (Sec. 4.2.3) are located 700 mm downstream of the tube inlet. The length of the tube downstream of the entropy generator module can be varied to modify the convective distance travelled by the hot spots before being accelerated. Various nozzles and downstream terminations are used in the experiments. Thus, as the experiments described in this thesis are performed in slightly different configurations of the rig, a schematic and a brief description of the experimental arrangement is given in each chapter.

In the work described in this chapter (Sec. 4.4), the EGR is terminated with an orifice plate, and the accelerated flow ejects into the room (Fig. 4.2). The distance between the heating grid and the acceleration point is varied. In the *short* tube configuration, this distance is 400 mm, whereas in the *long* tube case, it is 1400 mm. These two different tube lengths have been chosen to enable a partial or total time separation between the generation of the heating pulse and the acceleration of the hot spots. In this way, direct and indirect noise can be initially separated in time and afterwards partially merged in time. In an alternative configuration, the 60 meter long hose is added to the section downstream of the rig generating effectively an anechoic termination for the time needed for a sound wave to travel through it and be reflected back (Sec. 4.3.4).

The air temperature is determined using thin K-type thermocouples (fine gauge exposed welded tip thermocouples type K, 0.076 mm wire diameter, labelled T_i in Fig. 4.2), whose time constant is found experimentally to be around 300 ms. In order to correct for the long response time relative to the 200 ms heating pulses, a hot film anemometer (Dantec gold plated wire probe type 55R01) with a wire diameter of 5 μm (response time under 10^{-4} ms) is used to obtain the shape of the temperature pulse. The pressure signal is acquired with condenser microphones and piezoresistive pressure transducers at the locations P_i: two G.R.A.S. 40bp (IEC 61094 WS3P 1/4") externally polarised condenser microphones connected to the G.R.A.S. 26AC 1/4" standard preamplifier, four Kulite XTE-190(M) piezoresistive pressure

transducers and a Kulite XT-140M piezoresistive absolute pressure transducer. The transducers are either placed on the same axial plane for calibration cross checking, or along the tube at stations downstream of the heating module. The outputs of the piezoresistive pressure transducers are amplified with a Fylde FE-379-TA modular DC amplifier. Both the Kulite and G.R.A.S. transducers are connected to a NI PCI-5259 board via a NI-2090 DAQ box. The sampling rate used is 8192 samples per second, with a 16-bit resolution.

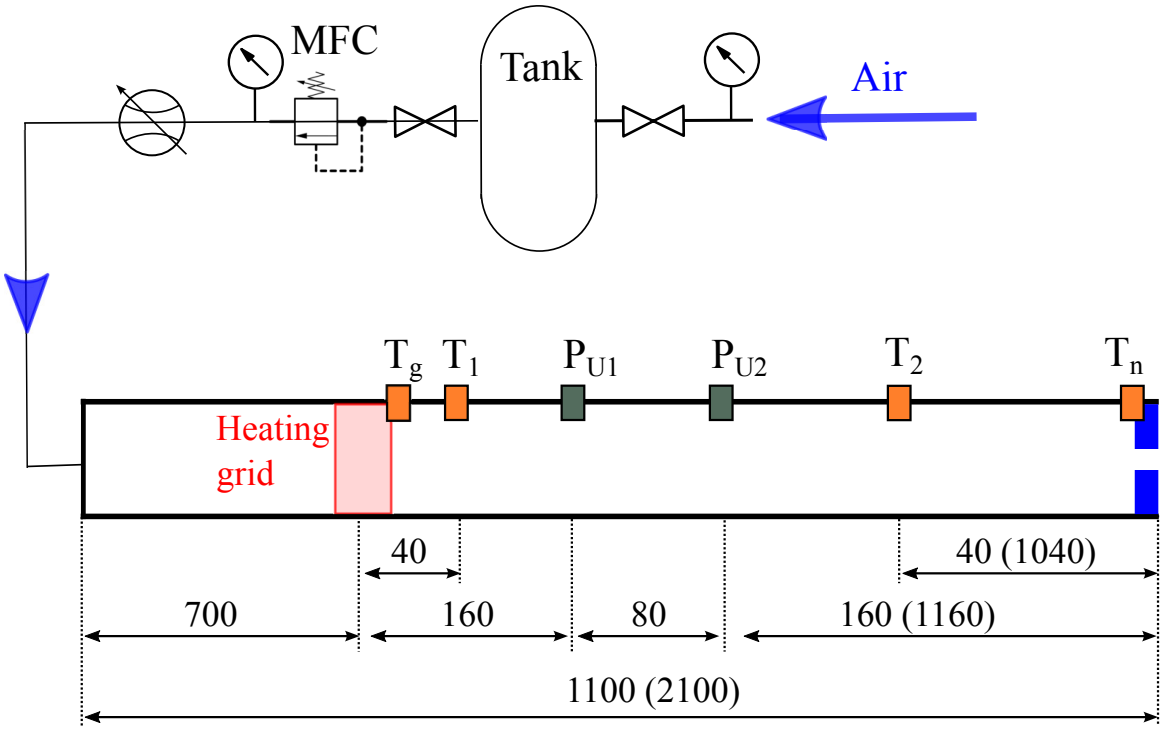

Fig. 4.2 Schematic of the experimental set-up used in the experiments described in this chapter (values in parentheses correspond to the long tube configuration). Dimensions in mm. Dimensions not to scale.

4.2.2 Heating device

Flow perturbations are generated in the primary air flow via the Joule effect by the heating device (Fig. 4.3). The activation of the heating grid generates acoustic waves, as well as an entropy spot which is then advected with the mean flow. The heating device is fitted 700 mm downstream of the tube inlet via a PVC flange for electric isolation. The device itself is composed of three grids of thin tungsten wires (58 μm diameter) connected in series, with an overall resistance of about 1 Ω. Each grid is made of 2.3 m of wire wound around a glass-reinforced epoxy laminate FR4 substrate 1.6 mm thick, which keeps the wires in place using a toothed comb structure. Two copper plates connect the wires on both faces of the module,

so that each heating grid is electrically equivalent to 42 parallel 45-mm-long resistances of tungsten wire. Two consecutive grids are separated by a FR4 insulating plate 1.6 mm thick. The heating device is roughly 10 mm thick, and therefore it can be approximated as a compact element for low frequency disturbances. The heater is fitted with a central hole matching the duct inner diameter. The obstruction due to the heating device is minimal: it occupies less than 0.15% of the duct cross section. As such, we consider that it has a negligible effect on acoustic propagation within the duct. An in-house circuit controlled by a computer drives a power supply (Glassman Lp 60-20), and delivers a current pulse of 21 A to the heating device, with a duration set to 100 or 200 ms. This process heats up the wires of the heating grid via the Joule effect, which in turn heats up the air flowing through the heating device (primarily by conduction and convection).

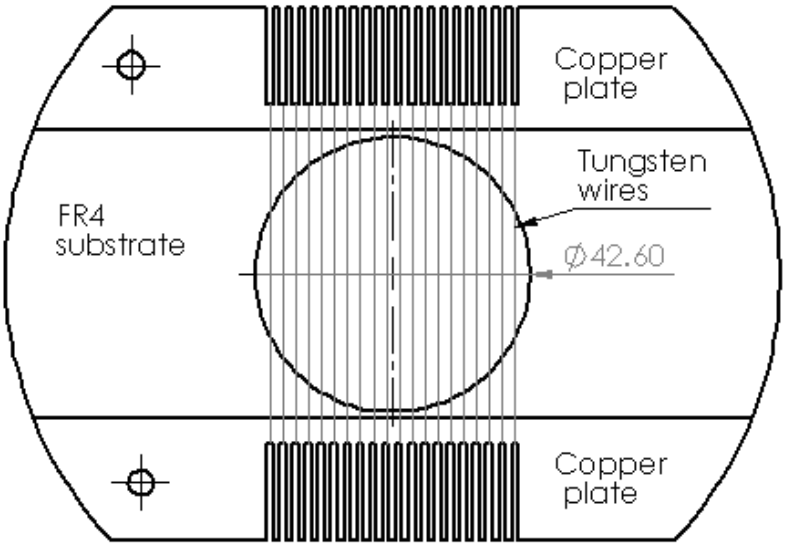

Fig. 4.3 Schematic of the heating grid. Dimensions in mm.

4.2.3 Mass injection set-up

Composition perturbations are generated by pulse injection of a secondary gas (helium, argon or carbon dioxide) via a solenoid valve into the duct (Fig. 4.4). The injection of a secondary gas of a different density and composition into the main gas stream generates acoustic waves as well as compositional and entropic disturbances, as the injected gases have a different entropy than air. The injection system was designed and built by E. O. Rolland [173] and is only briefly described here. The injector port consists of a Swagelok 1/4" fitting, connected to a 0.1 meter long flexible tube (2 mm inner diameter) through which the injected gas is

supplied. The injection is carried out using a fast-response micro-solenoid valve (ASCO Numatics HSM2L7H50V), which is connected to the duct via a 0.1 m length of flexible tubing with a 2 mm inner diameter. The injected gas enters the duct radially. The valve is actuated using a computer-generated pulse signal, which drives the 24 V power supply (Glassman LP 60-20).

The injection is a result of the pressure differential across the fast-response valve: when the valve is open, gas flows at a rate determined by the size of the orifice inside it. The mass flow rate of the injected gases ($\dot{m}_{He}$, $\dot{m}_{Ar}$ or $\dot{m}_{CO_2}$) is adjusted using a pressure regulator upstream of the micro-solenoid valve, and monitored with an Alicat M100 mass flow meter (accuracy: $\pm$ 1%).

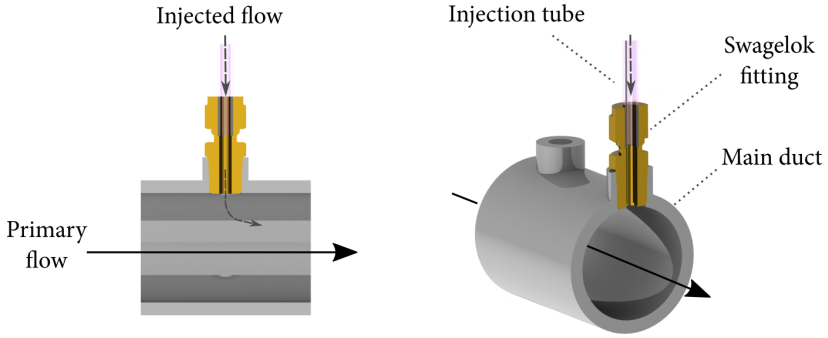

Fig. 4.4 Schematic of the injection system (Figure courtesy of E.O. Rolland [174]).

4.2.4 Anechoic termination

In a reverberating environment, knowledge of the reflection coefficients of the boundaries is needed to compare the acquired pressure traces with theoretical predictions, as multiple reflections change the shape and the amplitude of the original travelling waves. By increasing the distance between the upstream and downstream boundaries, the time separation between the original wave and its reflections at the boundary can become sufficiently large to easily identify and time separate each travelling pulse.

A 60 meter long tube is used to achieve this time separation, in the form of two 45 mm inner diameter - 30 m long PVC tubes connected together (RS lightweight delivery hose reinforced with a rigid internal crush and kink resistant white PVC helix). As a first approximation, it is assumed that the difference in the cross section between the PVC tube (42.6 mm diameter) and the long hose (45 mm diameter) can be neglected (Fig. 4.5). The hose is coiled with a radius of 0.6 m: there is no evidence in the literature suggesting that such a large bend radius might significantly affect the propagation of the sound waves. Over such

a long length, the hot spots are entirely dissipated before the far end of the tube, eliminating the contribution of the indirect noise. Moreover, since the frequency spectrum of the signal is mainly in the 0–50 Hz frequency range, the corresponding wavelengths are at least one order of magnitude longer than this pipe, so the shapes of the reflected waves are not substantially distorted. The working principle of this end termination is similar to the semi-infinite tube of probe microphones [76, 118], but, since the diameter is large and the frequencies of interest are low, the acoustic energy is not sufficiently dissipated, and it is possible to observe the reflections arising at the termination of the tube.

For the 30-meter long tube, the *anechoic time* t_a, defined as the time required for a sound wave to reach the end of the long tube and be reflected back, is approximately:

$$t_a = \frac{L_{tot}}{c} \simeq \frac{2 \times (30 + 1.4)}{343} \simeq 0.18 \text{ s} \tag{4.1}$$

while $t_a \simeq 0.36$ s for the 60-meter long tube. The heating or injection pulse lengths t_p = 0.1-0.2 s are chosen to be shorter than t_a, so the downstream running acoustic waves generated at the heating grid are not superposed with the corresponding reflected ones. This allows further insight on the behaviour of the system: a real anechoic termination is ideal for the characterisation of acoustic sources, but it is not possible to build a totally non-reflective boundary condition for the wavelengths characteristic of this experiment [127]. Using this long tube termination, the downstream end is silent (behaves as anechoic) for $t < t_a$ allowing the isolation of single travelling waves. This "anechoic" behaviour is demonstrated in Sec. 4.3.4

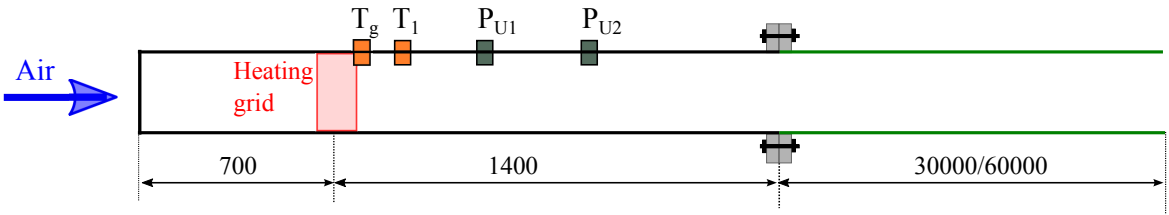

Fig. 4.5 Schematic of the system terminated by the anechoic termination. Dimensions in mm. Dimensions not to scale.

4.2.5 Nozzles and orifice plates

The flow is accelerated using a series of nozzles (convergent only and convergent/divergent) and orifice plates (thin/thick) located at the end of the duct. An orifice plate is easier and cheaper to manufacture than a convergent nozzle, but for low frequency perturbations the two are expected to behave in the same way for the direct and the indirect noise generated

upstream of them. In a first approximation, the flow through a generic area decrease interface can be assumed to be isentropic [59], as the pressure gradient acts in the same direction of the flow, so flow recirculations are negligible. Downstream of a generic area increase, instead, the flow is subjected to non negligible pressure losses after the abrupt area change of an orifice, while the smoother area change of a diffuser improves the pressure recovery [59].

Table 4.1 shows a schematic of the different end terminations used in the experiments. The nozzles and the thick orifice plate are CNC manufactured from a PVC rod. The thin orifice plate, designed following ISO 5167 [171], is made of stainless steel. N4 is the convergent part of a nozzle optimised [81] to generate the highest indirect noise possible [2].

4.2.6 Optical access

Optical access to the flow is needed to perform laser diagnostic measurements. This is obtained using a 42 mm inner diameter, 500 mm long UV grade fused silica tube (wall thickness of 2 mm) (Fig. 4.6). Two metal flanges hold the quartz tube in place, and two 500 mm long rods reinforce the structure. In this optically accessible configuration, the rig is mounted on a three-axes traverse stage. This helps to align the centre-line of the rig with the beams, and then to scan the rig horizontally to access different axial locations during the experiment.

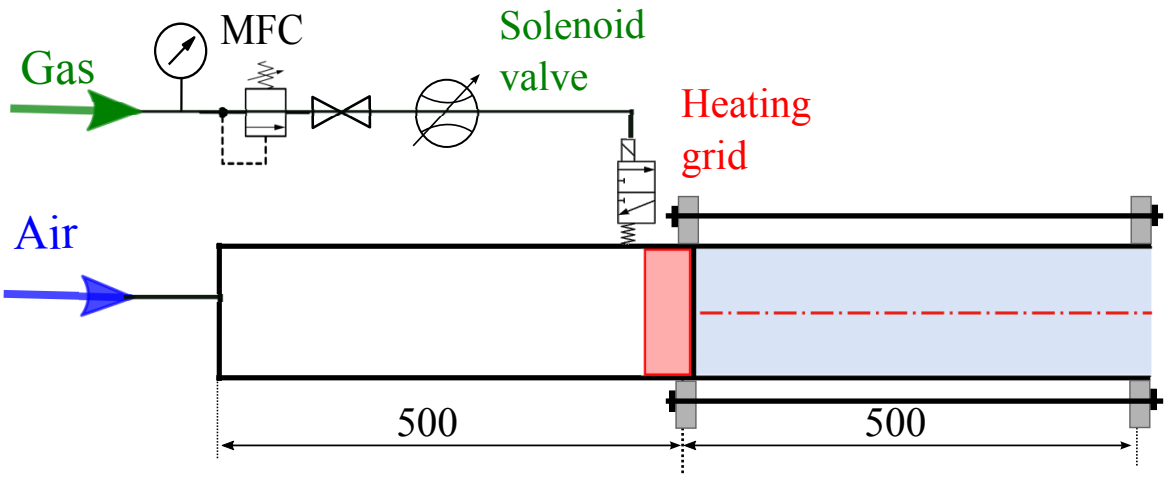

Fig. 4.6 Schematic of the system terminated by the quartz tube. Dimensions in mm. Dimensions not to scale.

[2] Unpublished result, personal communication with Maxime Huet, Onera, and Alexis Giaucque, LMFA EC Lyon.

Table 4.1 Characteristics of nozzles and orifice plates used in the experiments.

Case	Symbols	Schematic	Parameter
C/D nozzle	▶▶	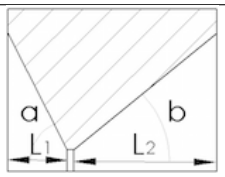	$L_1 = 24$ mm, $L_2 = 230$ mm $a = 40°$, $b = 4.5°$
Orifice plate	●●	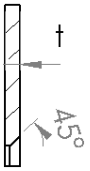	$t = 2.2$ mm
N1	◀	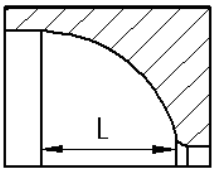	$L = 24$ mm
N2	▲	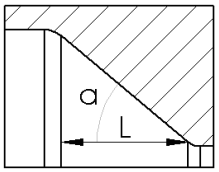	$L = 24$ mm $a = 40°$
N3	▶	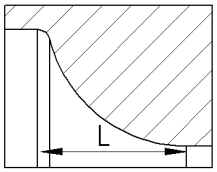	$L = 24$ mm
N4	▼	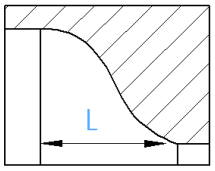	$L = 230$ mm $a = 4.5°$
O1	●	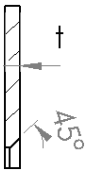	$t = 2.2$ mm
O2	■	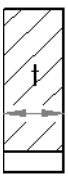	$t = 8$ mm

4.3 Experimental characterisation

The discussion in this chapter refers to the configuration shown in Fig. 4.2, where the rig is terminated by an orifice plate/convergent nozzle and the the flow ejects into the open environment. Synthetic entropy spots are generated via the heating grid.

4.3.1 Flow rate measurements and conditions at the throat

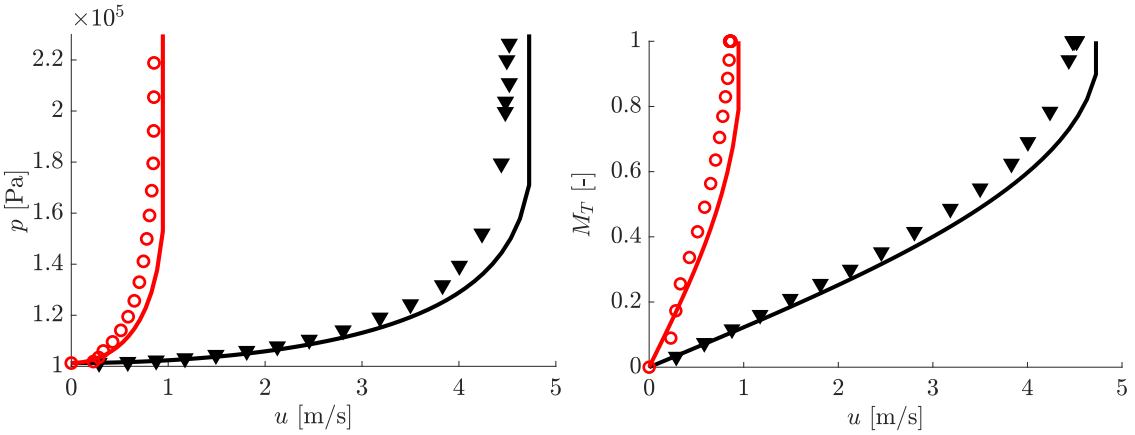

Fig. 4.7 Calculated upstream pressure (left) and nozzle Mach number (right), as a function of bulk flow velocity for the 3.0 mm (red circles) and 6.6 mm (black triangles) diameter orifices. Lines represent the corresponding isentropic values with $\Gamma = 1$.

The flow meter/controller records the volumetric flow rate (Q), mass flow rate ($\dot{m}$), temperature T_f and pressure at the flowmeter p_f at a sampling rate of 20-30 Hz. The bulk flow velocity $\bar{u}$ is calculated as:

$$\bar{u} = \frac{\dot{m}}{A\bar{p}/R\bar{T}} \tag{4.2}$$

where A is the inner cross-sectional area of the tube, $\bar{p}$ and $\bar{T}$ are the measured pressure and temperature in the tube and R is the gas constant for air. In the present analysis, the mean temperature in the tube $\bar{T}$ is assumed to be identical to that acquired at the flow meter T_f since the difference between these two temperatures is expected to be lower than 1%.

The Mach number at the orifice plate throat is necessary to estimate the intensity of the entropy noise, yet it is difficult to measure it directly in subsonic conditions. A calculated value for the Mach number M_T at the throat can be obtained by assuming isentropic expansion from the measured mean pressure in the straight section of the tube, $\bar{p}$, to the pressure at the throat, estimated to be atmospheric pressure ($p_T = p_a$).

$$M_T^2 = \frac{2}{\gamma - 1}\left[\left(\frac{\bar{p}}{p_a}\right)^{\frac{\gamma-1}{\gamma}}\left(1 + \frac{\gamma-1}{2}\bar{M}_u^2\right) - 1\right] \tag{4.3}$$

The upstream pressure $\bar{p}$ is measured using the Kulite absolute pressure transducer, and the upstream Mach number $\bar{M}_u$ is calculated from the bulk velocity and mean temperature ($\bar{M} = \bar{u}/\sqrt{\gamma R\bar{T}}$).

The markers in Fig. 4.7 (left) show the upstream pressure $\bar{p}$ and velocity $\bar{u}$ measured in the tube at several operating points for the 3 mm (red dots) and 6.6 mm (black triangles) orifice. The lines represent the theoretical relation between upstream pressure and velocity assuming an ideal isentropic convergent nozzle with a vena contracta factor $\Gamma = 1$. Fig. 4.7 (right) shows the calculated nozzle Mach number (obtained from Eq. 4.3) versus the upstream bulk flow velocity, comparing the experimental results with the theoretical predictions for an ideal isentropic convergent nozzle. The discrepancy between the ideal and measured cases are due to the vena contracta factor of the orifice which is around 0.87 for all cases.

4.3.2 Characteristics of the heating pulse

Fig. 4.8 shows the normalised current signal pulsed into the heating module and the corresponding induced temperature increase in the flow ΔT, detected with the anemometer 0.5 m downstream of the grid. The current signal is normalised to the maximum nominal current delivered from the power supply, 21 A. In all experiments the current is set to its maximum limit (I_{max}), while the voltage is set to 35 V. The heating module has a resistance $R \sim 1\ \Omega$, requiring a voltage $V = RI_{max} = 21$ V, and the excess energy is dissipated. However, in the first few milliseconds of the pulse, the capacitor in the driving system leads the power supply to release a higher current, before it auto-adjusts the current to its maximum nominal limit. The initial peak in the delivered current makes the wires warm up faster than they would do with a square pulse. It can be observed that there is no relevant time delay associated with the electric circuit: the time constant of the *RC* circuit is much shorter than the characteristic times of the experiment.

4.3.3 Temperature measurements

Accurate information regarding the temperature and shape of the hot spots generated by the heating device is crucial to understand and model the experiment. Three pieces of information are particularly important: the shape of the response of the temperature pulse in the time domain, the maximum temperature change induced in the air flow, and finally the spatial behaviour of the hot spots (how they spread and disperse before reaching the orifice).

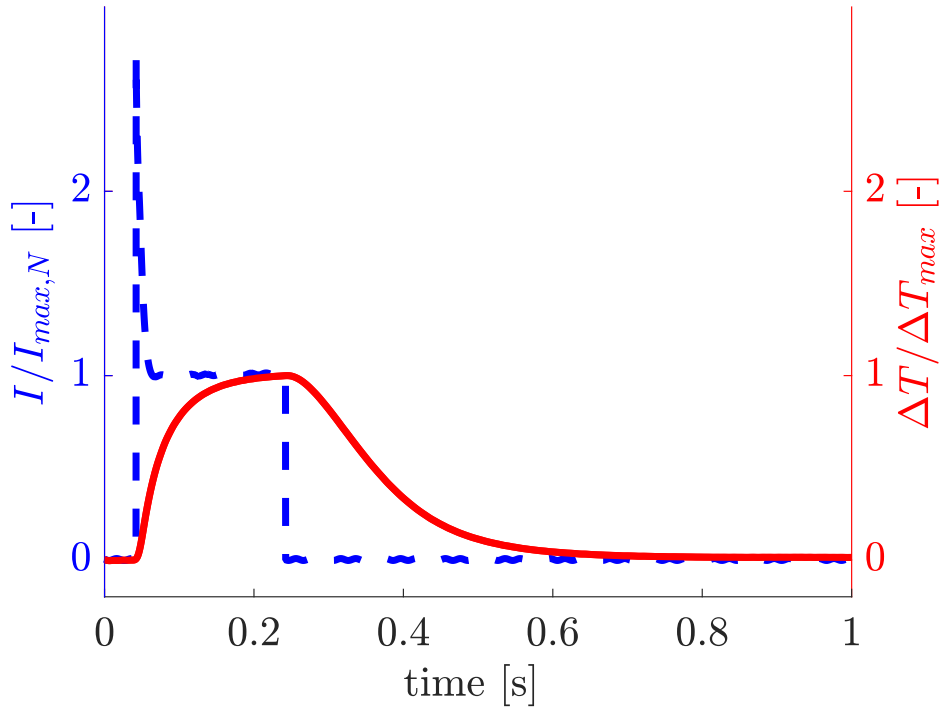

Fig. 4.8 Current pulse delivered by the driving system into the heating module normalised by the maximum nominal current of the power supply $I_{max,N} = 21$ A (blue dashed line); temperature rise profile of the hot spot signal acquired in the centre of the tube by the anemometer normalised by the maximum temperature increase ΔT_{max} (red solid line).

Obtaining accurate measurements is challenging due to the transient nature of the heating process. In order to overcome these difficulties, both thermocouple and hot film anemometry measurements are performed simultaneously. Thermocouples are often used to determine a gas temperature, but, due to the inertia of the thermal junction, their transient output rises more slowly relatively to the actual input signal. For a given temperature input $T_I(s)$, they produce an output $T_O(s)$

$$T_O(s) = \frac{1}{1 + s\tau_{tc}} T_I(s) \tag{4.4}$$

where τ_{tc} is the time constant of the thermocouple.

Fig. 4.9 shows how the actual temperature increase at a given location in the tube (in this case, just downstream of the heating grid) is reconstructed (red dotted line). Commercial beaded wire thermocouples with small diameters (0.076 mm) are used to obtain measurements of the asymptotic temperature rise. For these thermocouples an average time response $\tau_{tc} = 300$ ms was experimentally determined with a step input and an air flow of 20 m/s. For lower flow velocities, the time constant is higher. Therefore, in the 200 ms of the pulse, the

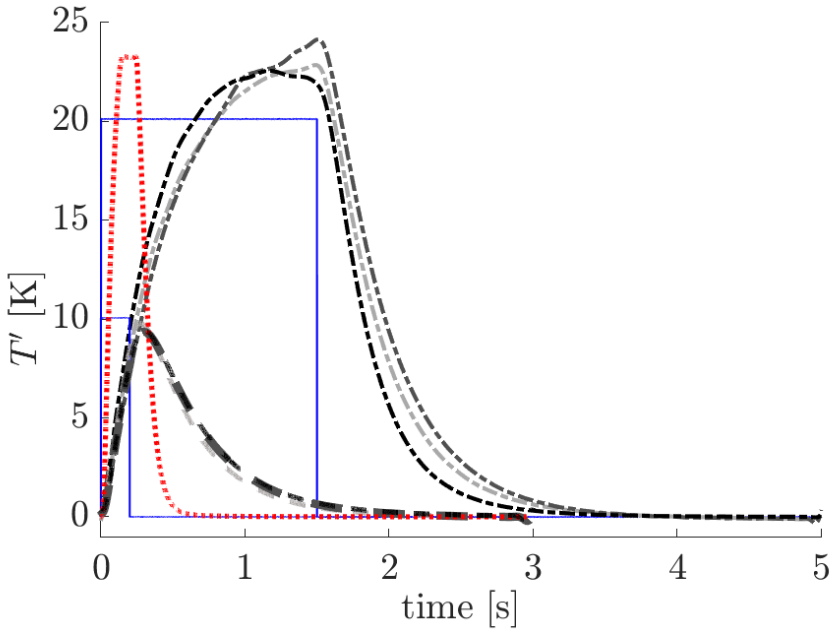

Fig. 4.9 Temperature profiles acquired with three nominally identical thermocouples downstream of the heating grid, for a mean flow velocity of 1 m/s for a 200 ms pulse (dashed lines) and a 1.5 s pulse (dashed-dotted lines). Solid lines: short and long input pulses. Anemometer output (red dotted line) normalised using the measured temperature rise.

thermocouple displays a slower-rising and attenuated output (dashed lines in Fig. 4.9) with respect to the temperature input.

From the temperature signal in Fig. 4.8 it can be noted that in 200 ms the hot spot temperature nearly saturates, which suggests that the wires of the grid have reached their maximum temperature. If the same current and voltage are pulsed into the grid for a sufficiently long time t_p ($t_p > 3\tau_{tc}$) the thermocouples have enough time to asymptote towards the actual value of the temperature. Therefore, the peak temperature value displayed after the 1.5 s long pulses (dashed-dotted lines in Fig. 4.9) is a good representative of the actual peak temperature of the hot spot. The shape of the temperature pulse is reconstructed more precisely using a hot film anemometer (dotted line in Fig. 4.9). The 5 μm Dantec probe has a negligible response time compared to the pulse duration. For moderate variations of the air temperature T_a ($\Delta T_a \sim$ 10-80 K), assuming negligible variations in the bulk flow velocity, the output voltage variation ΔE can be expressed as [27]:

$$\Delta T_a = -2\frac{T_W - T_{a,0}}{E_0}\Delta E \approx -\beta \Delta E \tag{4.5}$$

where T_W is the temperature of the hot wire ($T_W \sim$330°C). For small temperature increases, the change in the output voltage of the anemometer is in a first approximation proportional

to the change in the air temperature. Assuming that the anemometer captures the shape of the temperature pulse without distortion or attenuation, the shape of the output voltage of the anemometer is used to represent of the shape of the hot spot.
The different measurements of the air temperature are kept as consistent as possible, but there is an estimated uncertainty of ± 2 K in the determination of the absolute value of the air temperature rise. This is due to: (i) difficulties in accessing the correct location for some measurements (*i.e.* as close as possible to the heating grid and to the nozzle), (ii) internal differences between the transducers, and (iii) small and uncontrollable variability of the test conditions (*e.g.* replacement of the heating module). The tests for acquiring the air temperature at the grid are performed with an open tube, to enable the thermocouple to be placed as close as possible to the heating grid. It is assumed that the same heating power delivered to the same mass flow rate leads to the same temperature increase in an open and closed tube configurations.

4.3.4 Behaviour of the anechoic termination

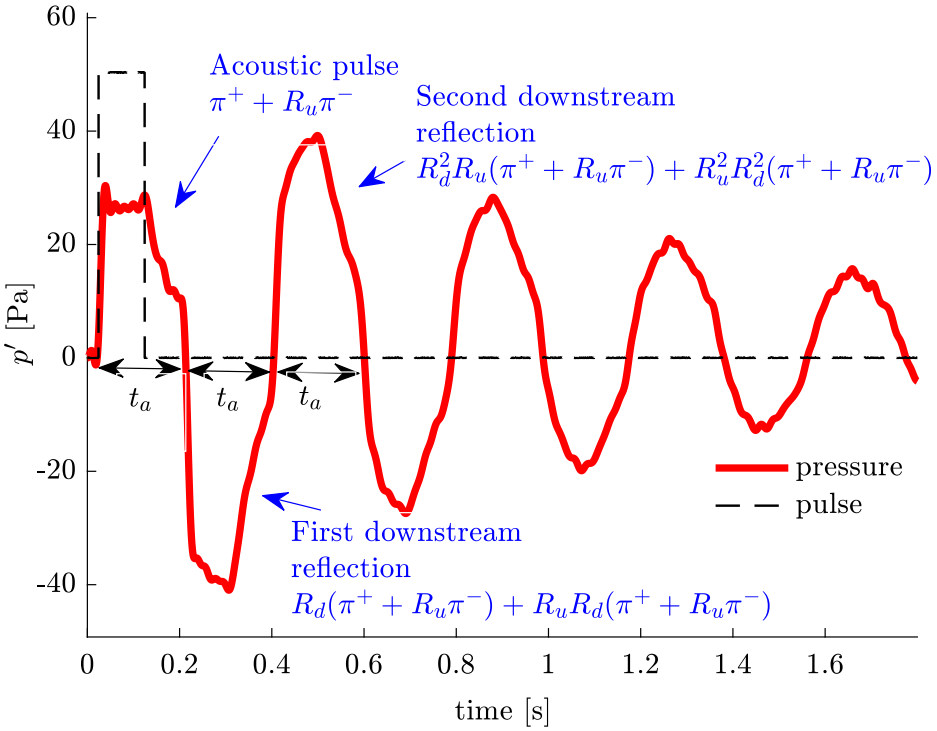

Fig. 4.10 Explanation of the acoustic behaviour of the system with the anechoic termination.

In this section we demonstrate the use of the anechoic termination to isolate the single travelling pulses by delaying the reflection at the boundary. The anechoic termination (here 30 meters long) is attached to the end of the duct, after removing the orifice plate. Fig. 4.10 illustrates the pressure traces acquired in this configuration. The rapid heating of the grid of wires generates upstream and downstream running compression waves (π^- and π^+) which travel with the speed of sound relative to the air flow. π^+ and π^- appear as rectangular waves that recall the heating pulse, but reflections modify the overall shape and amplitude of the pressure trace. In this configuration, the upstream travelling wave π^- reaches the upstream boundary, which has a reflection coefficient close to unity ($R_0 \simeq (1-\bar{M})/(1+\bar{M}) \simeq +1$ [173]), and is positively reflected back within $t_u = 2L_u/c \simeq 0.004\ s$. Since this travel time is much shorter than the heating interval, the two waves $R_0\pi^-$ and π^+ move downstream as one. The passage of the positively added waves is measured by the pressure transducer (acoustic pulse) as they travel to the downstream end (Fig. 4.10). When the 30 meter long tube is left open, these two waves ($R_0\pi^-$ and π^+) are negatively reflected back ($R_dR_0\pi^-$ and $R_d\pi^+$) with nearly the same amplitude ($R_d \simeq -1$), since the open end constitutes a node for the pressure oscillations. $R_dR_0\pi^-$ and $R_d\pi^+$ pass again over the same transducer after $t \simeq t_a$. However, since the travel time between the transducer and the upstream boundary is very short relatively to the travelling pulse length (after t_u), they are again nearly immediately reflected at the upstream boundary and detected at that location. Therefore, the amplitude of the second oscillation is higher than the amplitude of the first oscillation despite the fact that the heating device is now turned off and no further energy is delivered to the system: four waves pass simultaneously over the pressure transducer ($R_dR_0\pi^-$, $R_d\pi^+$, $R_dR_0^2\pi^-$ and $R_dR_0\pi^+$). These waves continue to repeatedly reflect at the boundaries, until viscous and thermal losses dissipate their acoustic energy entirely. This behaviour can be observed in Fig. 4.10, where the system is excited by a square pulse of interval $t_p = 0.1$ s, which is shorter than the anechoic time t_a, so that the heating device is switched off before the reflected negative wave reaches the measurement point. The first positive oscillation has a square shape that resembles the heating pulse, and the pressure rises sharply when the heating device is activated. When the heating grid is switched off, the pressure starts decaying smoothly until, at $t = t_a = 0.183$ s, the pressure decreases sharply upon the arrival of the first upstream propagating wave. The amplitude of this negative peak is higher in its absolute value than the first positive peak, as expected. The pattern repeats itself, with a lower amplitude owing to acoustic losses.

4.3.5 Pressure transducer characteristics

Piezoresistive pressure transducers and microphones convert an acoustic signal into an electrical signal. Piezoresistive transducers rely on the piezoresistive effect that occurs when the electrical resistance of a material changes in response to applied mechanical strain [32]. They offer a flat frequency response and zero phase shift even at very low frequencies. Microphones translate pressure fluctuations into a voltage via a diaphragm or a cantilever beam exposed to the incident sound pressure, using cavities and vents as pressure equalisation channels. Microphones therefore act as differential pressure measurements with capacitance, so that the sensors only respond to dynamic pressure fluctuations, unlike pressure transducers [162, 224]. The added capacitance means that at low frequency they behave as a high pass filter, with lower gain and shift in phase. On the other end, capacitive microphones are capable of higher sensitivity and dynamic range than piezoresistive pressure transducers.

The transfer function $F_p(f)$ of a condenser microphone such as the G.R.A.S. 40bp has been shown to be well represented by that of a high pass filter function [32, 162]:

$$F_p(f) = G\frac{i\frac{f}{f_0}}{1+i\frac{f}{f_0}} \tag{4.6}$$

where f_0 is the cut-on frequency of the microphone and G is the frequency-independent sensitivity of the microphone, called open-circuit voltage [32]. In the present experiment we calibrate the response of the condenser microphone to show that its corrected response can yield the original pressure data.

Predicted and measured transfer function of G.R.A.S. microphones

The high pass filter behaviour of the two G.R.A.S. condenser microphones was measured at frequencies from 1 to 40 Hz, using a calibrated Kulite transducer as a reference, as its output is not distorted at low frequencies. The test tube is attached to a plenum by means of a conical intake, where two opposed loudspeakers are housed. The two loudspeakers excite the tube by generating sinusoidal acoustic waves at a given frequency. All of the transducers are located on the same axial plane along the tube, exposing them to the same pressure signal in the plane wave approximation.

The differences in gain and phase between the signals acquired by the two G.R.A.S. microphones and the Kulite reference transducer are shown in Fig. 4.11. As expected, the signals displayed by the G.R.A.S. transducers are attenuated (Fig. 4.11(left)) and phase shifted (Fig. 4.11(right)). The two G.R.A.S. transducers behave slightly differently at low frequencies. The cut-on frequency was experimentally determined as 1.02 Hz, with a

phase shift of $\pi/4$. This is consistent with the G.R.A.S. 26AC 1/4" standard preamplifier specifications, according to which the cut-on frequency of typical 1/4" microphones is around 1 Hz, as measured [2]. Indeed, from the specifications in the datasheet, the G.R.A.S. 40bp microphones have a frequency range ($\pm$2 dB) of 4 Hz to 70 kHz.

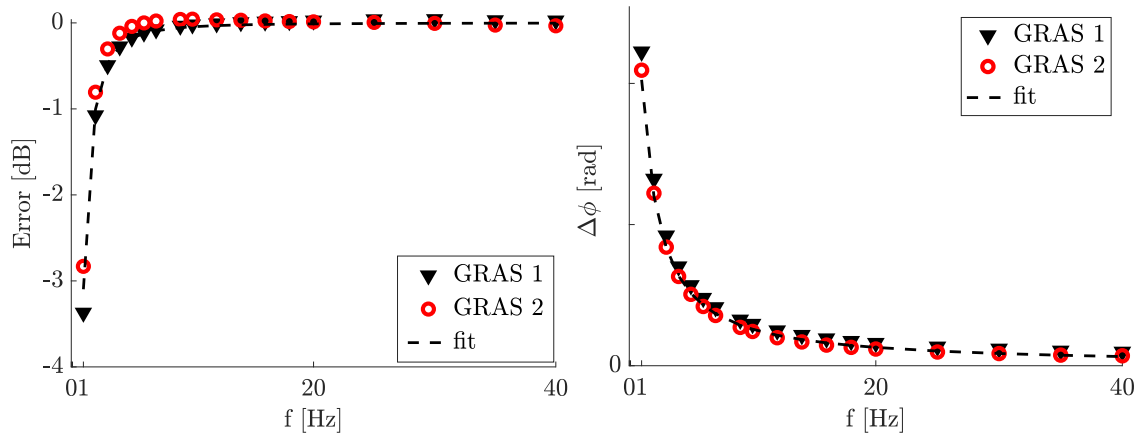

Fig. 4.11 Difference in gain (left) and phase (right) between signals from the reference Kulite and G.R.A.S. transducers (markers), along with the differences for the best fit high pass filter transfer function (dashed line) obtained from the experimental data.

Experimental demonstration of the signal distortion for capacitive microphones

Prior to introducing tests with the heating device, low frequency pulsed excitation using a cold air pulse is used to test the G.R.A.S. sensor response relative to the Kulites, both with and without the microphone transfer function. Pulsating mass flow is injected by driving the mass flow controller with square pulses at 0.22 Hz frequency and a duty cycle of 15%. The rise time of the valve of the mass controller is only 7.4 ms according to the specifications. Measurements are carried out over a period of 32 seconds with a sampling frequency of 2048 Hz. Due to the presence of the orifice plate at the end of the tube, an increase in the flow rate leads to a pressure increase in the tube. Indeed, from Fig. 4.12, it can be seen that the Kulite pressure transducers display the expected shape of the outputs in the form of a pressure rise to a final value (black solid line), whereas the raw signal of the G.R.A.S. transducers (red dashed line) produces a smaller rise and a ringing negative pulse at this low frequency. The red dashed-dotted line shows the output from the G.R.A.S. sensors when corrected by the corresponding transfer function in Eq. 4.6 using the experimental values for f_0. An adequate match in shapes and amplitudes with the Kulite transducers is obtained.

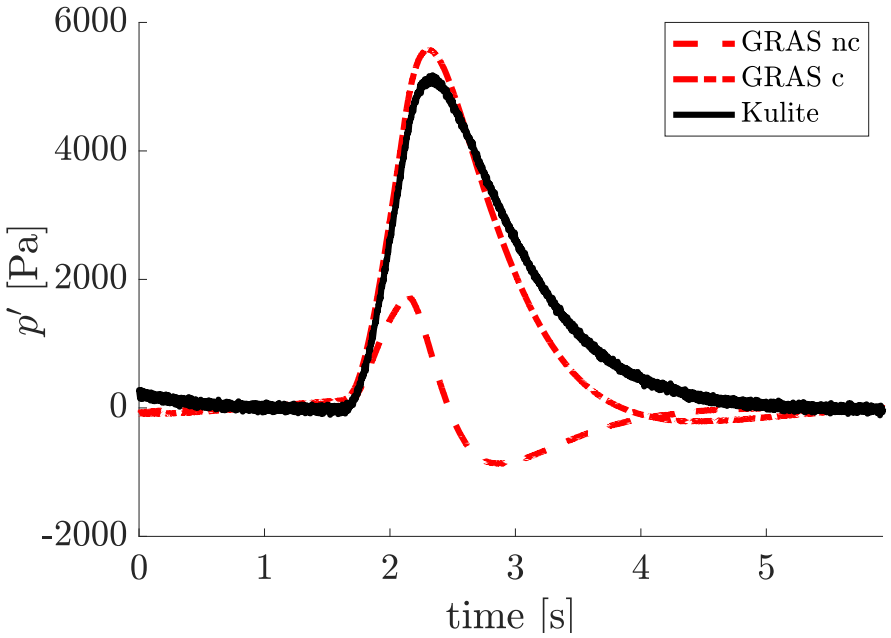

Fig. 4.12 Pressure profile acquired after pulsating mass injection in the tube from Kulite (black solid line) and G.R.A.S. (red lines) transducers. G.R.A.S. microphone raw signal (dashed line) and corrected by the transfer function (dashed-dotted line).

4.4 Results

The response of the system to the generation and convection of synthetic hot spots was measured for four cases: (A) *open tube with flow*, the tube is terminated with an open end; (B) *closed tube with no flow*, the tube is terminated with a rigid cap; (C) *accelerated flow (subsonic)*, the tube is terminated with the 6.6 mm hole orifice plate; (D) *accelerated flow (sonic)*, the tube is terminated with the 3.0 mm hole orifice plate, which is choked. Fig. 4.2 shows a schematic of the system used in this configuration, terminated with the orifice plate. These cases are summarised in Table 4.2. The four cases are used to obtain a clearer understanding of the behaviour of the system and provide a comprehensive frame for further modelling. Indirect noise is generated only in cases (C) and (D), where the hot spots are accelerated in the orifice. The open and closed cases (A and B) add limit situations for comparison and provide information useful to identify the acoustic properties of the system, such as dissipative effects and reflection coefficients at the boundaries. In the ultra-low frequency range of the experiment, traditional techniques for impedance measurements, such as multi microphone methods, cannot be easily used [18]; the present experiments allow the reflection coefficients and the system physics to be extracted from the resulting signal in the open and closed cases as references.

The pressure signals shown in this section are acquired 160 mm downstream of the heating module. All the experiments are carried out in the long tube configuration (1400 mm convective length downstream of the heating module) and the short tube configuration (400 mm convective length). A current of 21 A is pulsed for 200 ms with a voltage of 35 V; both the power and the energy are kept constant for all tests. The pulse period is set to 3 s to obtain a clear time separation between the acoustic oscillations caused by successive pulses. The air flow in the tube is varied between 78 and 250 slpm. The acquisition time is set to 512 seconds, so that the signals are averaged over 170 pulses. Within one test, the normalised RMS deviation on the acquired temperature measurements (calculated on the peak temperature values) is around 2%.

The mean air flow temperature measured at the flowmeter varies between 19 and 21 °C depending on the environmental conditions, and it is taken as 20 °C on average. The data is filtered with a 0–100 Hz rectangular window digital filter.

Case	Description	Tube termination
A	Open tube with flow	Open tube
B	Closed tube without flow	Rigid wall
C	Accelerated flow (subsonic)	Orifice (6.6 mm)
D	Accelerated flow (sonic)	Orifice (3.0 mm)

Table 4.2 Overview of the four experimental cases

4.4.1 Case A: Open tube

Figs. 4.13 show pressure signal results for Case A (open-ended tube) with a mean flow velocity $\bar{u}$= 2.27 m/s (upstream Mach number = 0.0066), in the long (left) and short (right) tube configurations. The acoustic pressure signal measured in the tube is very low, with a few peaks due to the initial gas expansion during heating. The theoretical reflection coefficient of an open end R_d is close to -1 in the low frequency range, meaning that the forward propagating acoustic waves generated by the heating device (direct noise) are approximately instantaneously reflected with an opposite sign at the outlet and propagate back into the tube. The forward and backward waves in the tube nearly cancel out, explaining why the pressure in the tube oscillates around zero. In the long tube data (Fig. 4.13 (left)), the oscillation frequency $f \simeq 38$ Hz corresponds to a quarter wave mode ($\lambda/4 \simeq L$), which is consistent with the fact that the inlet of the tube behaves as a closed wall ($R_0 \simeq +1$).

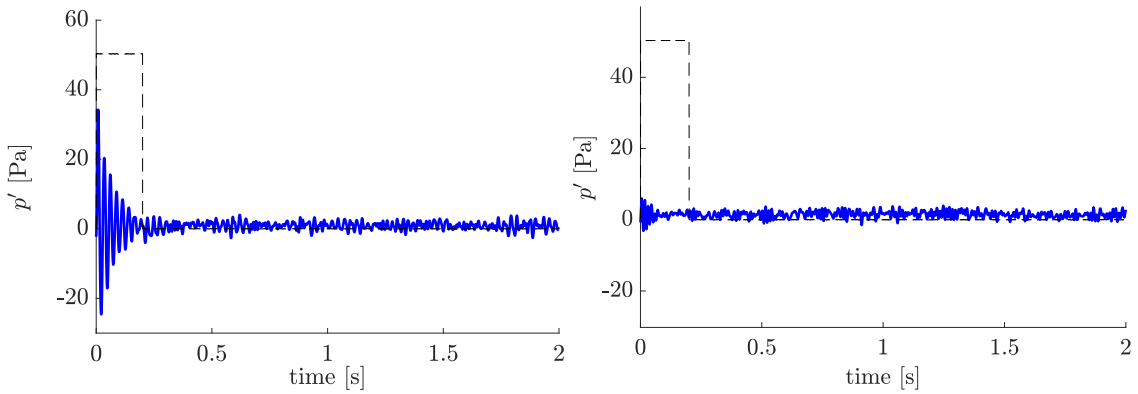

Fig. 4.13 Ensemble-averaged pressure signals as a function of time obtained with an upstream Mach number M=0.0066 and open downstream end in the long (left) and short (right) tube configuration.

4.4.2 Case B: Closed tube

Fig. 4.14 shows the results for Case B (closed tube) with no mean flow. When the heating device is active, the adjacent fluid is heated by conduction (the air trapped inside the tube is still) and tends to expand. The sudden expansion of the fluid, constrained by the inertia of the unperturbed media, acts as a piston on the rest of the gas, creating a local pressure disturbance which leads to the generation of acoustic waves that propagate along the tube at the speed of sound (thermoacoustic convection) [207, 25, 113, 69]. The acoustic waves generated from the heat source impinge on the walls, and are reflected back with the same sign as the original wave (the theoretical reflection coefficients at the rigid walls, R_0 and R_d, are 1). Subsequently, these waves repeatedly traverse between the boundaries. Given that the acoustic time-scale is an order of magnitude smaller than the pulse duration, these acoustic waves are essentially accumulating while the heating device is active. Once the heating device is switched off, the acoustic energy decays due to losses at the boundaries and viscous and thermal losses within the fluid. For the short tube (black solid line) the maximum pressure is higher and the pressure rises faster than for the long tube (red dashed-dotted line). Indeed, the tube boundaries are closer together, meaning that the acoustic round trip time is shorter, and the acoustic waves are reflected more times during a given time interval than in the long tube configuration. As a result, the acoustic pressure build up in the shorter tube is faster, leading to a higher maximum pressure.

4.4.3 Case C: Accelerated flow (subsonic)

In these experiments, the downstream end of the tube is terminated by the 6.6 mm orifice plate, through which the air flow accelerates. The experimental conditions tested are listed in

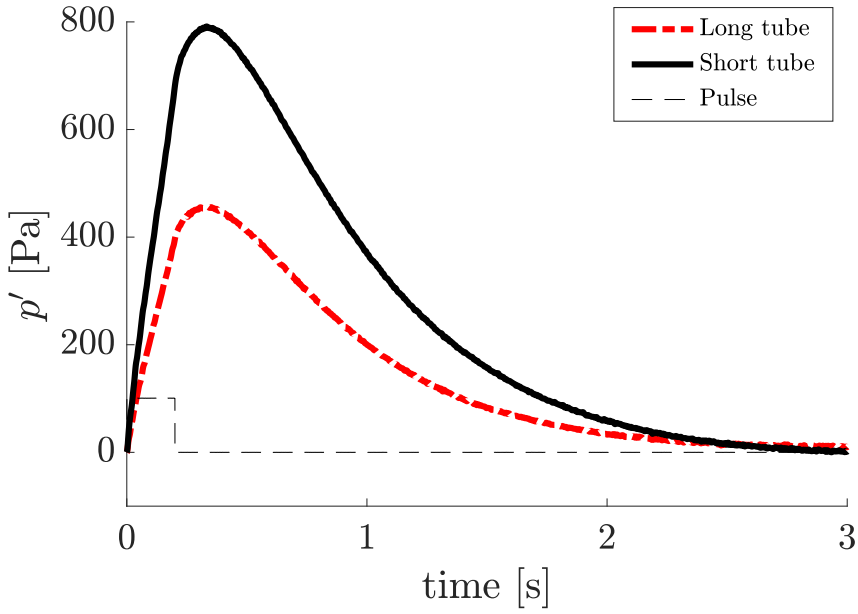

Fig. 4.14 Ensemble-averaged pressure signals obtained after the heating pulse with closed boundaries (rigid wall at the end) for the short (black solid line) and long (red dashed-dotted line) tube configuration.

Table 4.3. It was experimentally determined that the bulk flow velocity required to choke the flow with the 6.6 mm orifice is 4.2 m/s (see Fig. 4.7 in Sec. 4.3.1) therefore the flow through the orifice is subsonic in the test conditions listed.

Long tube

Fig. 4.15 (top) shows the pressure signal obtained 160 mm downstream of the heating module in the long tube configuration. The velocity of the flow is kept low in order to obtain a clear time separation between the heating pulse and the time at which the hot spots arrive at the outlet. Since all the tests are performed by pulsing the heating device at a constant power, increasing the volumetric (and mass) air flow through the heating device decreases the measured temperature rise induced in the flow, as can be seen in Table 4.3. Two thermocouples are located in the orifice to detect the arrival of hot spots at the outlet of the tube. Fig. 4.15 (bottom) zooms in on Case C-3 (Table 4.3) to identify the characteristic components of the acoustic signal.

The air temperature time history in Fig. 4.15 (bottom) is reconstructed from the output of the thermocouple and the anemometer using the method described in Sec. 4.3.3. The data is recorded at three different positions (L_c) downstream of the heating grid: 0.05 m, 0.4 m (end of the short tube) and 1.4 m (end of the long tube). It is assumed that the temperature signal

	$\bar{p}$ $[kPa]$	$\bar{u}$ [m/s]	M_T	ΔT_g $[K]$	ΔT_S $[K]$	ΔT_L $[K]$
1	102.78	0.88	0.1441	26.7	19.1	7.9
2	103.54	1.12	0.1771	21.1	16.1	8.2
3	104.00	1.24	0.1942	19.5	15.1	8.0
4	105.19	1.49	0.2327	15.9	12.5	7.5
5	106.64	1.75	0.2719	13.3	10.9	6.8
6	108.34	1.98	0.3114	11.7	9.9	6.1
7	110.86	2.27	0.3613	10.5	8.5	5.9
8	113.65	2.56	0.4088	9.2	7.6	5.7

Table 4.3 Operating conditions for Case C (accelerated subsonic flow) for the long tube (1.4 m convective length downstream of the heating module) and the short tube (0.4 m convective length). $\bar{p}$: mean pressure at the grid; $\bar{u}$: bulk flow velocity at the grid; M_T: estimated Mach Number at the throat (see Sec. 4.3.1); ΔT_g: measured peak temperature rise of the hot spots at the grid; ΔT_S: measured peak temperature of the hot spots 0.4 m downstream of the heating module (location of the orifice plate for the short tube); ΔT_L: measured peak temperature of the hot spots 1.4 m downstream of the heating module (location of the orifice plate for the long tube)

0.05 m from the heating grid well approximates the temperature signal at the grid. The shape of the temperature signal close to the heating grid has a higher and sharper peak, whilst for longer distances the hot spot spreads out and the temperature signal is more disperse.

From Fig. 4.15 a strong acoustic signal is observed in the tube while the heating device is active: there is a negligible time lag between the driving pulse and the observed pressure pulse. For a distance $L_p = 0.16$ m between the heating grid and the pressure acquisition point, this time lag is $\tau_p = L_p/c \sim 5 \times 10^{-4}$ s, which is of the order of the time resolution of the acquisition system ($\tau_S = 1/8192 \sim 1.2 \times 10^{-4}$ s). In all 8 cases, the pressure reaches a positive maximum at the end of the heating pulse. Therefore, it can be concluded that these positive pressure rises represent the direct noise. When the hot spots arrive at the orifice and are accelerated through it (as detected by the thermocouple signal), smaller negative excursions are observed. As the flow velocity increases (and the convective time decreases), these negative dips occur earlier in time. Therefore, these negative peaks are attributed to the acceleration of hot spots through the orifice plate, the so-called indirect noise. A third contribution to the acoustic signal can be seen in the pressure signal in Fig. 4.15 (bottom): after the direct noise peak, the pressure fluctuation does not return to zero, but becomes negative (negative oscillation labelled P_N). This effect may arise from the mean lower density of the flow, but requires further investigation.

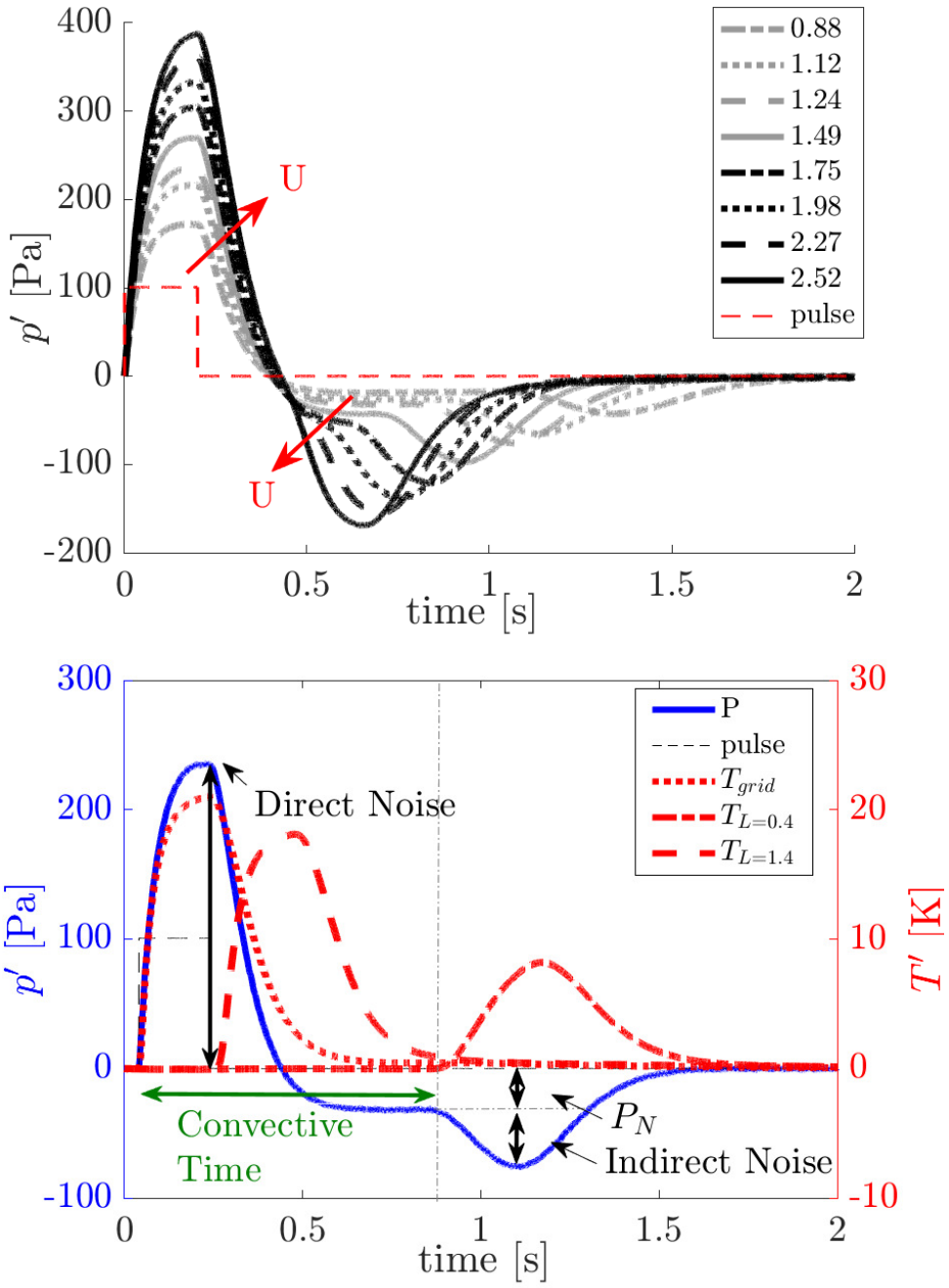

Fig. 4.15 Ensemble-averaged pressure signal acquired by the Kulite transducer 160 mm downstream of the heating module for the cases listed in Table 4.3 (long tube). Legend indicates the magnitude of the bulk velocity ($\bar{u}$) in m/s (top).
Detail of operating condition C-3 ($\bar{u}$ = 1.24 m/s): identification of direct noise, indirect noise, convective time on the pressure trace (solid blue line); and reconstructed air temperature profile acquired at three different convective lengths (L, in m) downstream of the heating module (respectively dotted red line for $L = 0$ m, dashed red line for L =0.4 m and dashed-dotted red line for L =1.4 m) (bottom).

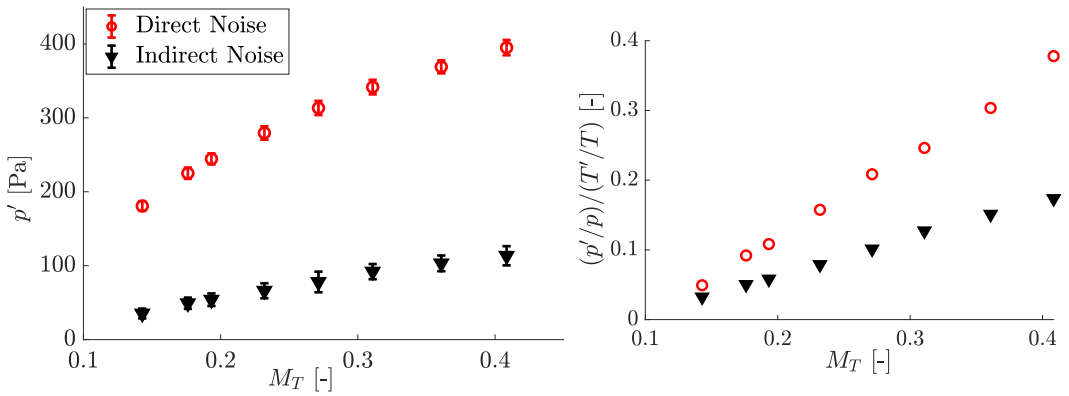

Fig. 4.16 Absolute (left) and normalised (right) values of the peak of the acoustic oscillations of direct and indirect noise *vs.* estimated orifice Mach number in the long tube configuration.

Fig. 4.16 (left) shows the peak values of the direct and indirect noise against the estimated orifice Mach number. The indirect noise peak is evaluated by subtracting P_N from the minimum value of the pressure trace as shown in Fig. 4.15. Both direct and indirect noise peaks increase approximately linearly with the Mach number. The amplitude of the direct noise is nearly four times larger than that of the indirect noise; however, the effect of indirect noise is not negligible. Even at small Mach numbers at the orifice (*i.e.* low accelerations), and for small temperature fluctuations, there is still a clear sign of indirect noise, in contrast to the findings for subsonic conditions in previous experiments [63, 120]. In Fig. 4.16 (right), the maximum absolute values of direct and indirect noise from Fig. 4.16 (left) are normalised by the corresponding peak temperature increase of the air at the grid and at the nozzle (values reported in Table 4.2), and non-dimensionalised by the mean pressure and temperature in the tube. Both the normalised direct and indirect noise are directly proportional to the nozzle Mach number. Considering that the peak temperature at the nozzle is lower than the peak temperature at the heating grid, the normalised indirect noise becomes comparable to the normalised direct noise. However, for higher velocities, the ratio of the hot spot temperature at the nozzle and at the grid becomes smaller, which explains the different slopes of the two curves. This shows that in this experiment the direct noise has a significant influence and cannot be neglected.

The direct noise caused by the heating of the wires always reaches its maximum at the end of the heating pulse (t = 200 ms). As the flow rate (and the velocity) increases, the time separation between the direct and the indirect noise peaks becomes shorter, due to the decrease in the convective time. These results suggest an important issue in the identification of indirect noise: increasing the flow velocity can increase the relative contribution of indirect noise through higher acceleration in the nozzle, yet the convective time of hot spots decreases.

When the convective time becomes similar to the pulse length, direct and indirect noise start merging, and a clear time separation between the two is no longer possible. However, because the direct noise is typically higher (Fig. 4.16), the effect of the indirect noise can not be distinguished in a straightforward way: if the merging effect is not considered, it can be erroneously concluded that there is no indirect noise in the system.

Comparison between the outputs of condenser microphones and piezoresistive pressure transducers

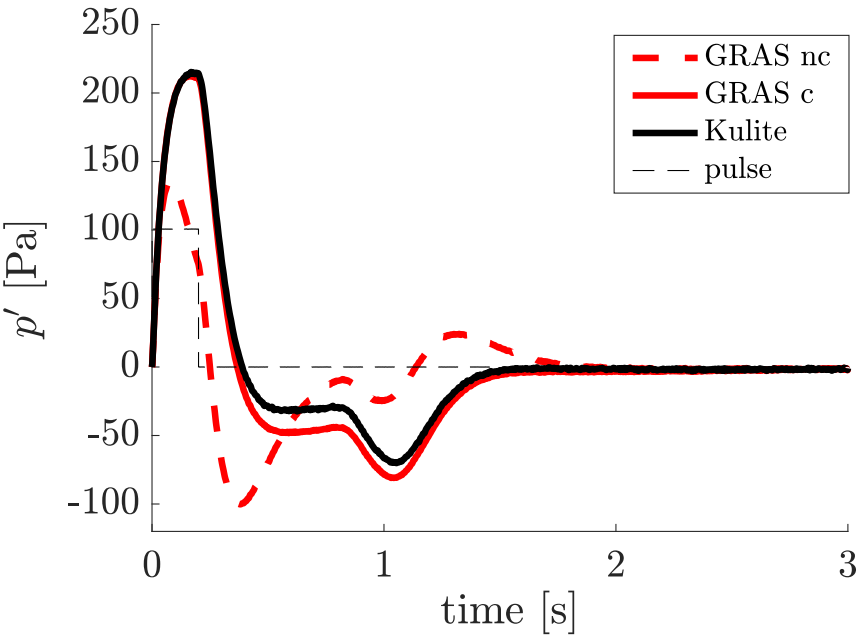

Fig. 4.17 Ensemble-averaged pressure signal acquired 160 mm downstream of the heating module acquired by the Kulite pressure transducer (black solid line) and the G.R.A.S. microphone, before (red solid line) and after (red dashed line) correction using its high-pass filter behaviour at low frequencies (Case C-3, long tube).

A note must be made regarding the usage of capacitive microphones in the present context. Fig. 4.17 compares the pressure signal acquired by a G.R.A.S. microphone (red dashed line) and a Kulite pressure transducer (black solid line) for a bulk flow velocity of 1.24 m/s (M_1 = 0.0036) (case C-3). The signal of the G.R.A.S. microphone is inverted to account for the 180° polarity shift characteristic of a condenser microphone. The signal acquired with the G.R.A.S. transducer is both distorted and attenuated, and shows non-physical ringing caused by the high pass behaviour of the microphone. As expected, once this signal is filtered using

the experimentally determined transfer function (red dashed-dotted line), it nearly matches both the shape and the amplitude of the signal obtained with the Kulite transducer.

Why are the present findings regarding the different types of microphone relevant at all? The amplitude and shape of the pressure signal are essential for understanding the behaviour of the system. A distorted and/or attenuated output can lead to a misinterpretations of the results and a mismatching with the modelling. In prior experiments aimed to generate hot spots and thermoacoustic waves with unsteady electrical heating of thin wires and foils (e.g. DLR EWG [9, 11]), condenser microphones rather than pressure transducers were used, without mentioning if any correction was applied to the output of the microphones. In [13] the issue of the microphone transfer function was brought up. However, the cut-on frequency obtained in [13] from numerical considerations was 12 Hz, 10 times larger than the cut-on frequency experimentally determined in this work and reported in the specifications of G.R.A.S. microphones [2]. Therefore, we suggest that in the future, all such low frequency measurements should to be verified for accuracy according to the calibration suggested here, or that piezo sensors be exclusively used for such low frequency experiments.

Short tube

Fig. 4.18 shows the pressure signal obtained 160 mm downstream of the heating module in the short tube configuration. A convective time $\tau_C \simeq 0.32$ s is estimated for the lowest flow velocity ($\bar{u} = 0.88$ m/s), and $\tau_C \simeq 0.11$ s for the highest flow velocity ($\bar{u} = 2.52$ m/s). As a result of this much smaller difference in characteristic time, direct and indirect noise have merged, and it is no longer possible to analyse the two separately. This merging results in an apparent change both in the shape and the amplitude of the direct and indirect acoustic oscillations. The direct noise appears as a positive increase in the pressure trace, as observed in Fig. 4.15, while the indirect noise brings a negative contribution. However, when they superpose, both the positive and the negative peaks seem to decrease and the slope of the signal changes.

As shown in the case of the long tube (Fig. 4.16), the amplitude of the direct noise is nearly four times higher than that of the indirect noise, and has a dominant effect on the pressure signal. This may lead the indirect noise contribution to be underestimated or neglected altogether. This can be clearly observed in Case C-8 ($\bar{u} = 2.52$ m/s, short tube): the entropy spot reaches the nozzle 0.11 s after the beginning of the heating pulse, when the heating device is still active. The amplitude of the indirect noise peak seems smaller than in the $\bar{u} = 2.27$ m/s case, whereas the direct noise is only slightly higher than in the $\bar{u} = 2.27$ m/s case. However, as observed for the long tube configuration (Figs. 4.15, 4.16) both the direct and indirect noise contributions increase nearly linearly with the Mach number. Thus, the

apparent decrease in the indirect noise amplitude is an effect of the destructive interference of direct and indirect noise. This interaction can also be seen in the shape of the pressure oscillation: the sum of the negative oscillation with the positive direct noise peak effectively increases the decay rate of this positive oscillation.

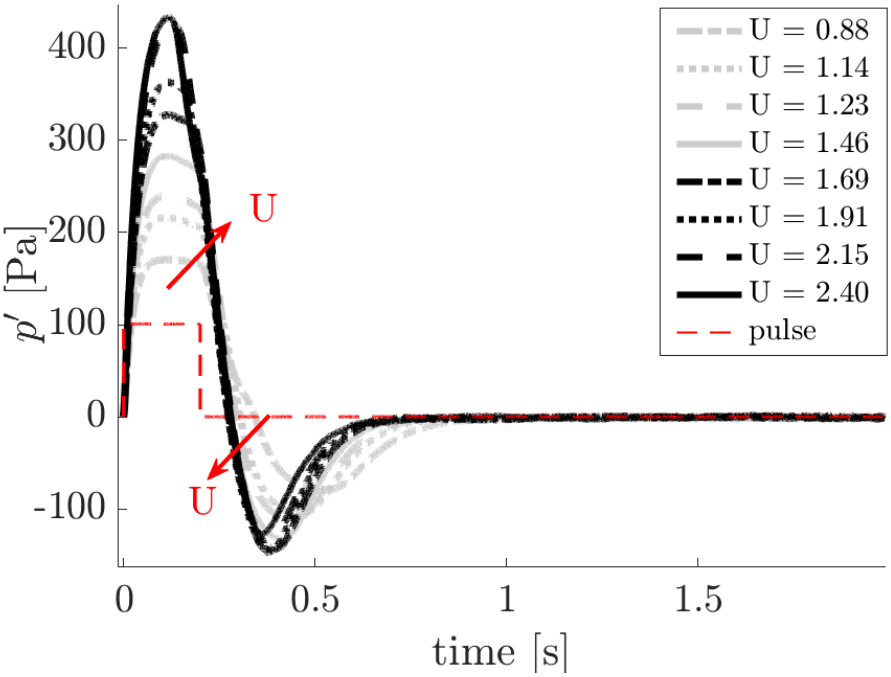

Fig. 4.18 Ensemble-averaged pressure signal acquired by the Kulite transducer 160 mm downstream of the heating module (short tube). Legend indicates the magnitude of the bulk velocity ($\bar{u}$) in m/s.

4.4.4 Case D: Accelerated flow (sonic)

Figs. 4.19 show the pressure signals acquired in choked conditions with the 3 mm diameter orifice (black solid line) in the long and short tube configurations. From Fig. 4.7 the pressure in the duct which corresponds to choked conditions is around 1.9 $\times 10^5$ Pa. These results are compared with the corresponding results in the subsonic configuration (Case C-1, dark grey dashed line), and with the closed tube case (Case B, light grey dotted line). The reflection coefficient of a choked nozzle is comparable to that of a closed end: the velocity is imposed at the throat, which thus nearly behaves as a rigid wall (apart from a small mean flow effect).

The shape of the pressure signal in the choked configuration can be understood by comparing it with the acoustic oscillations in the subsonic and in the closed tube cases. Acoustic waves are created inside the tube when the heating device is active, and undergo repeated reflections at the two ends of the tube. Heat is exchanged from the heating device

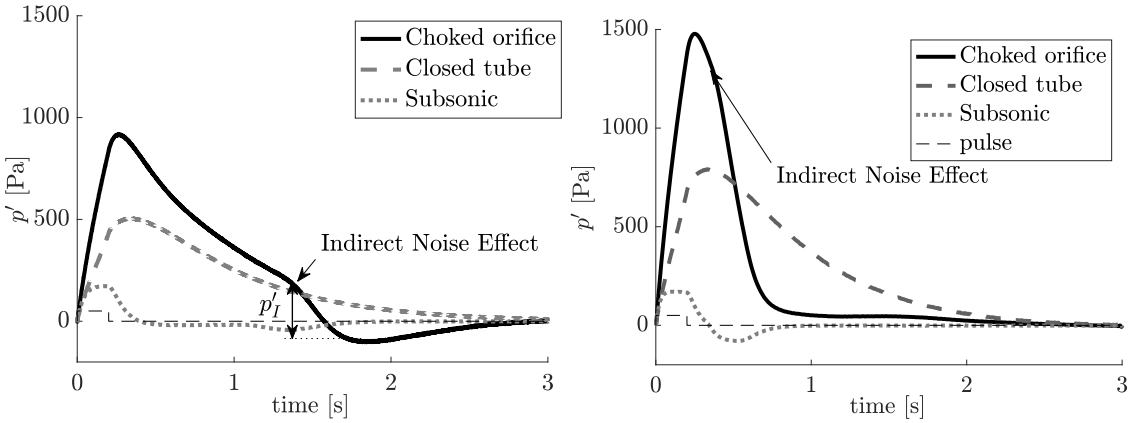

Fig. 4.19 Ensemble-averaged pressure signal acquired by the Kulite transducer 160 mm downstream of the heating module in the long (left) and short (rigth) tube. Black solid lines: choked tube; bulk flow velocity = 0.85 m/s (3 mm orifice); dark grey dashed lines: rigid wall (rigid wall with no flow); light grey dotted lines: subsonic flow, bulk flow velocity = 0.88 m/s (6.6 mm orifice).

to the air via a convective mechanism, which is faster than the conductive mechanism in the closed tube condition, where the air is still. This results in a faster amplification of the acoustic energy in the system. When the heating device is no longer active, the acoustic energy starts to decay. The main difference relative to the closed tube appears due to the entropy waves: when the hot spots are accelerated through the nozzle, negative acoustic waves are generated, so that the slope of the pressure decay changes and becomes steeper. However, the pressure only becomes negative in the case of the long tube configuration. Indeed, the indirect noise generation starts when the acoustic energy of the direct noise has yet to dissipate, and the sum of the positive and negative cases results in the signal shape shown in Figs. 4.19.

For the long tube configuration (Fig. 4.19, left), the amplitude of the indirect noise can be estimated by isolating the negative pressure oscillation from the curve. The amplitude of this oscillation is $p'_I \sim 290$ Pa. Comparing this value with the indirect noise peak for the same bulk velocity in subsonic conditions, the indirect noise in choked conditions is nearly 10 times higher in terms of absolute value and 6 times higher in terms of the normalised value than under subsonic conditions. With the short tube configuration (Fig. 4.19, right), however, the amplitude of the indirect noise cannot be estimated in a straightforward way because the convective time of the entropy is too short and the indirect noise signal can not be extracted from the overall pressure trace, even if its influence as a change of the decay rate of the curve is clear.

4.5 Discussion and further development

A detailed comparison between the experimental measurements and analytical models requires the full characterisation of the tube acoustics at the relevant low frequencies, both regarding the reflection coefficient of the orifice plate as well as the upstream end. Because of the ultra-low frequency range of the present experiments, the calculation of the reflection coefficients is not straightforward. Whereas in general the flow upstream of an orifice plate can be considered as isentropic (as if it was going through a converging nozzle), non-negligible pressure losses occur downstream of the orifice, so the non-isentropicity of the system needs to be characterised for a fully quantitative comparison. Models for the acoustic transfer functions of orifices can be found in the literature, but to the author's knowledge, there has been little information on their behaviour as a source of indirect noise. The entropy-to-sound conversion coefficients for non-isentropic area changes such as orifice plates are introduced in the next chapter.

The present experiments also emphasise one of the major limitations of the current and previous studies: due to the physical behaviour of the wires, experiments can only be run in the ultra-low frequency range. This adds further complications to the understanding and modelling of the system due to the lack of experimental and analytical or numerical data in the infrasonic region. Further, the results are difficult to compare with a real physical situation. This suggests that it may be advantageous to consider alternative configurations capable of excitation/deexcitation frequencies closer to those of interest in real combustors, such as high frequency pulsed injection, even if complications resulting from these alternatives may arise.

4.6 Conclusions

In this chapter we described the design and operation of the Entropy Generator Rig, a modular acoustic rig developed for studying indirect noise in a controlled environment. The experiments described in this chapter measure the backward propagating acoustic signals resulting from accelerating entropy spots generated by electrical heating, into outlet sections operated in subsonic and sonic conditions. The key result is the unambiguous identification of the contribution of direct and indirect noise in the overall noise by time-separating them. The acceleration of entropy spots is shown to generate a significant acoustic signal. A clear identification and separation between direct and indirect noise for the reflected waves had not previously been demonstrated. The indirect noise in a reverberating system as the EGR is isolated by choosing a convective time much longer than the electric pulse length. The indirect noise is then clearly identified by locating thermocouples in the orifice, which

detect the arrival and acceleration of the hot spots: when the thermocouples start detecting an increase in air temperature, a pressure decrease is detected by the pressure transducers. This negative pressure excursion occurs earlier in time as the flow velocity is increased, due to a shorter convective time. We demonstrate that even for small flow accelerations (subsonic conditions), and low values of temperature fluctuations, the indirect noise has a non-negligible contribution to the overall acoustic signal. However, direct noise is found to have a larger effect: when the heating device is active, a large pressure increase is detected by the pressure transducers. This pressure signal is caused by the air expanding due to the heat addition: no time lag is measurable between the heating pulse and this pressure pulse. The peak amplitude of the direct noise is nearly four times higher than that of the indirect noise on average. From these results, it can be hypothesised that one of the reasons why the acoustic trace of entropy noise was not clearly detected in previous experiments is linked to the short convective time associated with the hot spots. In this experiment, a clear time separation between direct and indirect noise can be obtained only at low flow velocities (1-2 m/s) and long convective distances (1.4 m). With higher bulk flow velocities or shorter convective distances, the contribution of the indirect noise merges into the higher direct noise and can no longer be easily identified, even if it may affect the shape and amplitude of the pressure oscillation.

Another important result is the need to carefully account for the response of the pressure transducers at the very low frequencies typical of such rigs, which are limited by the cooling time of the wires. Condenser microphones behave as high pass filters, which significantly attenuate the pressure signal and lead to a phase shift at frequencies below 10 Hz, and are unable to follow static pressure increases or decreases. This high pass filter behaviour generates non-physical ringing in the signal output, which can lead to a misinterpretation of the results. Once the transfer functions of the microphones are taken into account, their outputs can be brought to a good agreement with piezoresistive transducers.

Chapter 5

A generalised model for acoustic and entropic transfer function of nozzles with losses

The low frequency transfer functions for acoustic and entropic perturbations through nozzles and nozzle guide vanes are investigated. Previous theories rely on the isentropic assumption; in real systems, however, pressure losses associated with local friction and flow recirculation may occur, as evidenced by a drop in static pressure. In this chapter we relax the isentropic assumption and derive a parametric model to predict the acoustic and entropic transfer functions of a generic nozzle with subsonic-to-sonic throat conditions in the low frequency domain. For a given geometry and operating conditions, the model can retrieve the acoustic impedance of three limit cases known from the literature, as a function of a pressure loss parameter: the isentropic nozzle, the orifice plate and the converging nozzle terminating a duct. The generalised model is also able to predict the conversion of entropy to sound through orifice plates and non-isentropic nozzles given a measured or estimated static pressure loss parameter. The analytical predictions compare favourably with experimental measurements acquired in the Entropy Generator Rig for circular orifices and nozzles with subsonic-to-sonic throat conditions. The results highlight the need to correctly account for pressure losses in the system in order to properly capture the transfer functions of nozzles, as isentropic predictions differ substantially from the acquired experimental data[1].

[1]The results of this chapter are published in *Journal of Sound and Vibration* [49]

5.1 Introduction

Accurate knowledge of the acoustic and entropic transfer functions of the upstream and downstream boundaries of a combustion chamber or a laboratory rig is needed to correctly evaluate the experimental pressure traces. The acoustic coefficients are often acquired using well-established techniques such as the multi-microphone method [44]. However, at the state of the art there is still no standardised experimental procedure to acquire the entropy-to-sound and composition-to-sound conversion coefficients. These coefficients are therefore evaluated using analytical and numerical models, which have not been experimentally validated yet. These models normally describe the flow in the system as isentropic [147, 145]. Turbine guide vanes and nozzles are often designed to operate as close as possible to isentropic conditions; however, pressure losses and flow recirculations still occur, as evidenced by the drops in the static pressure. Durrieu *et al.* [65] introduced an analytical model based on conservation equations to describe the low frequency acoustic transfer functions of a non-isentropic jump such as an orifice plate. Howe [106], Bechert [14] and Cummings and Eversman [38] modelled the acoustic properties of a subsonic nozzle that terminates a duct, where the flow expands non-isentropically into the atmosphere as a jet. These models were later on extended to higher frequencies, and corroborated by experimental data for the acoustic transfer functions (direct noise) [57, 65, 223, 199, 221, 15]. However, none of these authors included information on the entropy-to-sound conversion in their models. Thus, at the state of the art, the effect of pressure losses to the entropy and composition-to-sound conversion has not yet been investigated.

In this chapter, an analytical model describing the acoustic and entropic transfer functions of generic nozzles with pressure losses is developed and then compared with the experimental data acquired in the Entropy Generator Rig. Acoustic waves are generated from the activation of the pulsating heating grid, while indirect noise is generated from the acceleration of the hot spots through the nozzle (indirect noise). The resulting pressure perturbation signal is the integral of the original pulse combined with the multiple acoustic reflections (reverberation) of the direct and indirect noise arising at the boundaries of the system [175]. For choked conditions at the nozzle, a good match in the acoustic and entropic upstream reflection coefficients was found between calculations and experiments when assuming isentropic flow upstream of the nozzle, both in the case of the direct and indirect noise. However, under subsonic conditions, the analytical predictions did not capture the experimental behaviour [175]. To address this mismatch, in this chapter we introduce a model to predict the acoustic and entropic transfer functions of a generalised nozzle with subsonic-to-sonic throat conditions. We demonstrate how the generalised transfer functions can reduce to previously derived limit cases for (a) an isentropic convergent-divergent nozzle, (b) a non-isentropic

orifice plate, and (c) a convergent nozzle. We show how the isentropic and non-isentropic transfer functions differ substantially in determining the final upstream and downstream pressure perturbations, and how the non-isentropic model is needed to capture the observed experimental behaviour [50]. The outcome is useful not only in understanding the behaviour of instabilities in turbines, but also in the generation of entropic noise in any flow system with flow restrictions.

The chapter is organised as follows: in Section 5.2 we derive an analytical model for the low frequency acoustic and entropic transfer functions of a non-isentropic subsonic nozzle. The experimental configurations used in the experiment are briefly described in Section 5.3. In Section 5.4 the experimental results from the Entropy Generator Rig are compared with the analytical predictions, indicating that the non-isentropicity of the system has to be taken into account to correctly interpret the acquired pressure traces.

5.2 Analytical model

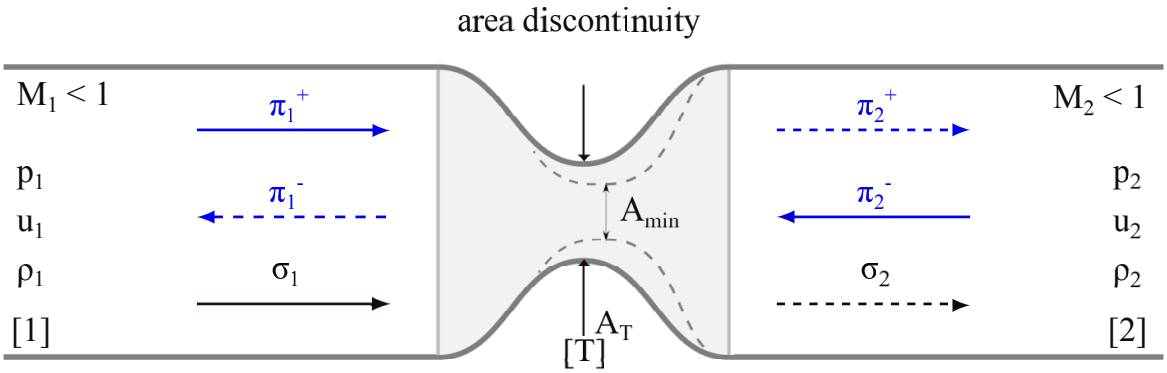

Fig. 5.1 Diagram and state variables for a one-dimensional subsonic nozzle, showing propagating acoustic (π) and entropic (σ) disturbances as impinging waves (solid arrows) and outgoing waves (dashed arrows).

We consider the flow through a generic nozzle, as shown in Fig. 5.1. Although in general the flow is three-dimensional, we consider a quasi-one-dimensional model represented by the upstream and downstream variables indicated in Fig. 5.1. Further, we assume the nozzle to be acoustically compact (Sec. 3.2.3).

The nozzle flow geometry is defined by upstream, downstream and throat cross sections (A_1, A_2 and A_T respectively). As the streamlines of the flow are not able to closely follow sharp angles, the cross-sectional area of the stream tube at the highest mean velocity may be smaller than the geometric area of the throat, so that $A_{min} = \Gamma A_T$, where $\Gamma \leq 1$ is a vena contracta factor. Generally speaking, the accelerating flow upstream of the throat can be

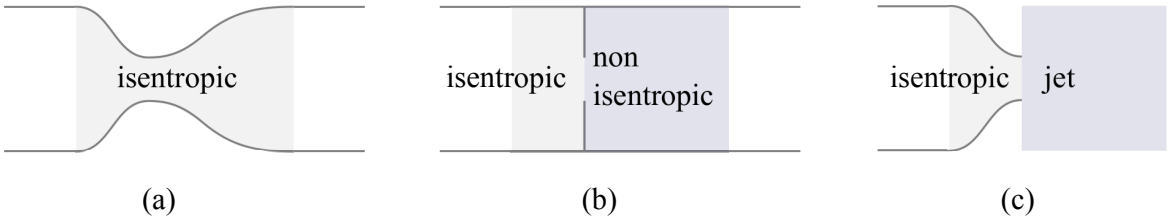

Fig. 5.2 Limit cases considered in previous work: (a) isentropic nozzle [147], (b) orifice plate [65], (c) convergent nozzle terminating a duct [106, 14, 38].

considered to be isentropic as the pressure gradient is favorable for the accelerating flow [65, 59]. However, this is not always the case for an area increase, particularly after abrupt expansions: the pressure gradient acts against the flow velocity and this can generate flow detachment and recirculation zones, which dissipate kinetic energy and generate entropy.

Two limit models can be found in the literature to describe the behaviour of perturbations across an area increase (Fig. 5.2). The first model considers a fully isentropic diverging section [147], *e.g.* with a full pressure recovery through the diffuser (Fig. 5.2(a)). The second model, used for orifice plates and abrupt expansions [59, 65], describes the flow in the expansion region as adiabatic but non-isentropic, wherein the total momentum of the jet is conserved across the jet and expanded area (Fig. 5.2(b)). A converging nozzle which terminates a duct (Fig. 5.2(c)) can be considered as a limit case of the orifice plate model, with the flow expanding into an open environment ($A_2 \to \infty$). A convergent-divergent nozzle with pressure losses is expected to display an intermediate behaviour between the orifice plate and the isentropic nozzle cases. In the diverging section, the flow decelerates and the boundary layer thickens rapidly as the pressure gradient opposes the flow, which may lead to separation or stall, and a net loss of total pressure [16]. In this chapter, we are interested in the propagation of low frequency acoustic and entropic perturbations in such a nozzle with losses. We start by considering the mean flow behaviour, followed by the perturbed flow.

5.2.1 Nozzle transfer functions

In the present one-dimensional model, the mean flow at each section of the duct is characterised by the state variables pressure (p), velocity (u) and density (ρ), and the correspondingly derived Mach number $M = u/c$, where c is the local speed of sound (note that these quantities correspond here to the average values). The degree of non-isentropicity of the flow is related to the pressure drop via an effective area A_j located in the divergent section between the throat and the exit ($A_T \leq A_j \leq A_2$), the notional area where isentropicity ceases. As developed further on, A_j serves as a useful parameter to quantify the degree of static

entropy generation and pressure losses, but should not be identified as a particular *physical* area where flow detachment takes place: the actual process of boundary layer detachment and recirculation is clearly more complex, and is not addressed here. The flow in the nozzle is modelled as isentropic from the inlet A_1 to A_j, followed by a momentum mixing or jet region from A_j to A_2. In the derivation of the transfer functions, a vena contracta factor $\Gamma = 1$ is assumed, although the assumption is relaxed when eventually comparing to the experimental results.

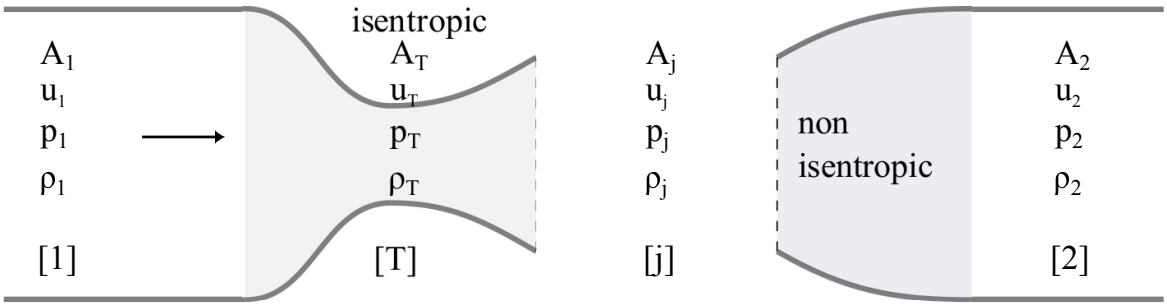

Fig. 5.3 Schematic of the non-isentropic nozzle.

5.2.2 Mean flow

The flow in the nozzle is assumed to be adiabatic, without any external heat, mass or momentum addition. In the experiments described in this chapter, no external gases are injected in the system, so the composition of the flow is constant. Thus, the mass flow rate $\dot{m}$ and the total temperature T_t are conserved through the nozzle.

As discussed in Chapter 3 (Sec. 3.2.3), if the flow is isentropic, the entropy is conserved between two generic area cross sections sections A_m and A_n

$$\left[\frac{p}{\rho^{\gamma}}\right]_n^m = 0 \tag{5.1}$$

If instead the flow is non-isentropic the conservation of momentum needs to be used to describe the flow:

$$\left[A\left(p+\rho u^2\right)\right]_m^n = \int_m^n p\, dA \tag{5.2}$$

where the integral term in Eq. 5.2 represents the pressure forces acting on the sides of the control surface between locations m and n. In a non-isentropic jump, the flow separates or losses due to friction occur, causing losses in the total pressure. This may lead to acoustic-vortical coupling and damping of sound waves [132, 14, 59]. For the case of an orifice plate in a duct, in which the flow leaves at the throat section A_T as a jet oriented purely in the axial

direction, the momentum conservation (Eq. 5.2) between the throat section and section 2 becomes [65, 132]:

$$(p_T - p_2) + \rho_T u_T^2 \frac{A_T}{A_2} = \rho_2 u_2^2 \tag{5.3}$$

The pressure loss for a non-isentropic nozzle falls between the limit cases of the orifice plate and the isentropic nozzle: part of the kinetic energy of the flow in the contraction is recovered as pressure, and the rest is dissipated. In order to analytically capture this phenomenon, one can envision the process as in Fig. 5.3, in which the flow remains isentropic up to a notional location A_j located in the divergent part, beyond which the flow is no longer modelled as isentropic. If $A_j = A_T$, the orifice plate model or jet model is retrieved. If instead, $A_j = A_2$, all the kinetic energy is recovered as pressure towards the isentropic nozzle model. For this non-isentropic nozzle, Eq. 5.3 applied between section j and 2 becomes:

$$(p_j - p_2) + \rho_j u_j^2 \frac{A_j}{A_2} = \rho_2 u_2^2 \tag{5.4}$$

The state variables in one section can be obtained from those in the others, provided that A_j is known. In what follows, a parameter $\beta = A_j/A_2$ is introduced to quantify the pressure losses and entropy gains.

This area ratio β is directly related to the pressure losses occurring in the nozzle. A pressure loss coefficient C_{p0} is used to express the losses in the total pressure p_0 occurring in the nozzle [208, 132]:

$$C_{p0} = \frac{p_{0,j} - p_{0,2}}{\frac{1}{2}\rho_j u_j^2} = \frac{p_j \left(1 + \frac{\gamma-1}{2} M_j^2\right)^{\frac{\gamma}{\gamma-1}} - p_2 \left(1 + \frac{\gamma-1}{2} M_2^2\right)^{\frac{\gamma}{\gamma-1}}}{\frac{1}{2}\rho_j u_j^2} \tag{5.5}$$

To obtain further insight into the relation between of C_{p0} and β, Eq. 5.5 is simplified assuming a low Mach number flow, thus neglecting the compressibility effects ($M << 1$; $\rho_j = rho_2 = \rho$) [132]. In this case, we obtain the Borda-Carnot equation [121], which describes the mechanical energy losses of the fluid due to a (sudden) flow expansion:

$$C_{p0} = \frac{p_{0,j} - p_{0,2}}{\frac{1}{2}\rho_j u_j^2} \simeq \frac{p_j + \frac{1}{2}\rho u_j^2 - p_2 - \frac{1}{2}\rho u_2^2}{\frac{1}{2}\rho_j u_j^2} = (1-\beta)^2 \tag{5.6}$$

Equation 5.6 clearly shows the link between the parameter $\beta = A_j/A_2$ and the losses occurring in the nozzle. When $\beta = \beta_{min} = A_T/A_2$ (orifice plate case), the highest losses occur in the nozzle; when $\beta = 1$ (isentropic nozzle case), $C_{p0} = 0$ and the total pressure is conserved. For $A_T < A_j < A_2$, some pressure losses occur into the nozzle, but part of the kinetic energy of the flow is re-converted into pressure. Thus, the factor β (or conversely

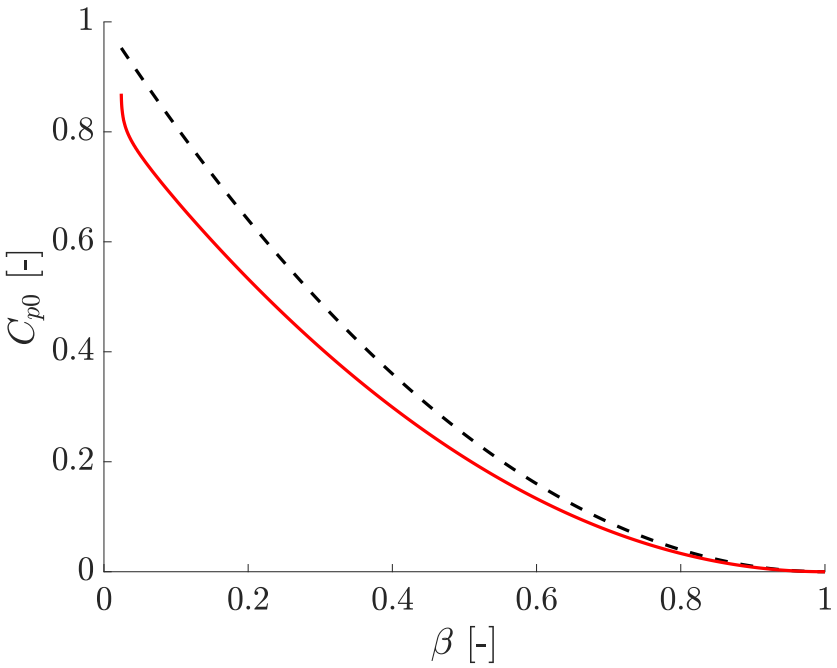

Fig. 5.4 Pressure loss coefficient C_{p0} as a function of the area ratio β: incompressible formulation (dashed black line), and compressible case for choked throat conditions (solid red line).

the non-isentropic area A_j) indicates the level of non-isentropicity of the nozzle. Fig. 5.4 shows the relationship between β and the pressure loss coefficient C_{p0}. The black dotted line corresponds to the incompressible equation (Eq. 5.6). When compressibility is taken into account (red line), the mass flow rate also affects the losses. As the mass flow rate increases, the total pressure losses increase, particularly at high contraction ratio ($\beta << 1$). The red line is obtained from Eq. 5.5, where for each value of β the Mach numbers M_j and M_2 correspond to the condition where the flow is choked at the throat ($M_T = 1$). Clearly, an area ratio of unity ($\beta = 1 \rightarrow C_{p0} = 0$) means that there is zero entropy generation, and for the limit of zero area ratio (expansion into a large area, $A_2 \rightarrow \infty$ or $\beta \rightarrow 0$), the maximum entropy loss arises. The analysis also shows that either C_{p0}, β or any other suitable single valued parameter can be used to describe the degree of non-isentropicity. The choice of β rather than C_{p0} is justified by the simplicity of the equations, and it is in alignment with the previous work of Durrieu *et al.* [65].

There are no universal analytical expressions for the pressure losses in a compressible flow for a nozzle of a given geometry as a function of flow rate parameters, rather only qualitative or semi-empirical models [208, 16, 132]. However, the mean stagnation pressure

loss can be experimentally measured, so that an effective β can be determined from the pressure data, as a measure of the non-isentropicity of a nozzle.

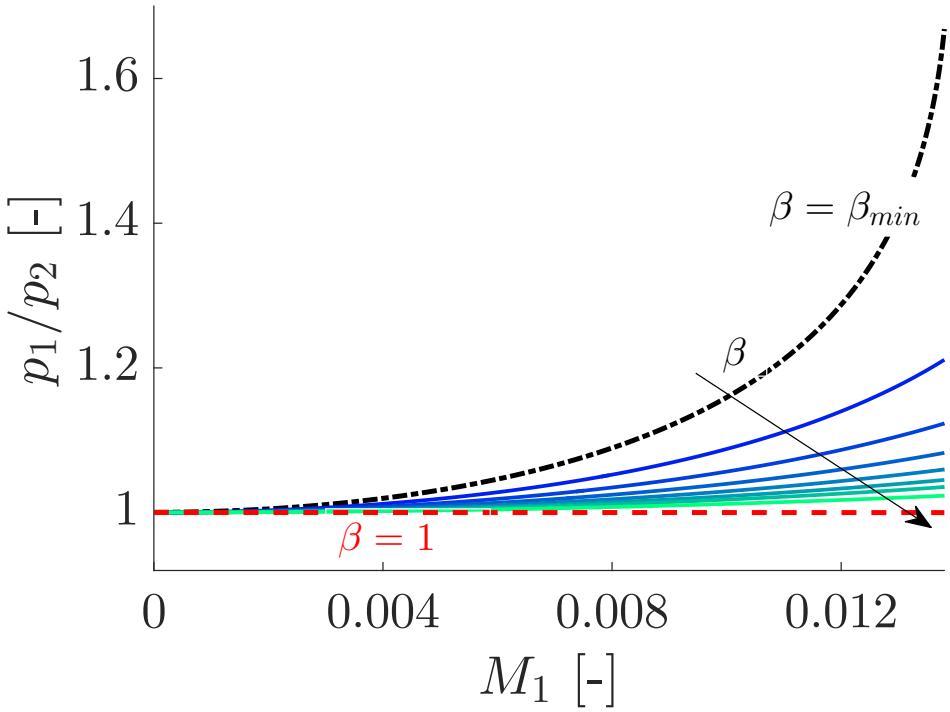

Fig. 5.5 Normalised upstream pressure increase (p_1/p_2) as a function of the upstream Mach number (M_1) for $A_T/A_2 \leq \beta \leq 1$ (calculated using the dimensions of the Entropy Generator Rig for $\Gamma = 1$). Dashed-dotted black line: orifice plate ($\beta = A_T/A_2 = \beta_{min}$); dashed red line: isentropic nozzle ($\beta = 1$); solid lines: non-isentropic nozzles ($\beta_{min} < \beta < 1$).

Fig. 5.5 shows the normalised static upstream pressure ratio p_1/p_2 as a function of Mach number M_1 and the parameter β. For a given geometry, mass flow rate and downstream pressure p_2 at subsonic conditions, the upstream pressure is a unique function of M_1 and of the parameter β. It can be uniquely determined as $p_1/p_T \cdot p_T/p_j \cdot p_j/p_2$ from the isentropic and non-isentropic jump conditions between section jumps $1-T$ (isentropic), $T-j$ (isentropic) and $j-2$ (non-isentropic) respectively. Fig. 5.5 shows that the higher is the dissipation downstream of the nozzle, the higher is the pressure drop. In the limit case of the orifice plate where the area A_j coincides with the throat area A_t ($\beta = \beta_{min}$), the maximum entropy is generated, with the largest relative pressure losses (dashed-dotted black line). Conversely, for $A_j = A_2$ ($\beta = 1$), the diffuser is fully isentropic (dashed red line): the pressure is fully recovered downstream of the throat and, as $A_1 = A_2$, the same mean pressure is measured upstream and downstream of the nozzle ($p_1/p_2 = 1$). At intermediate values of β, the

intermediate situations are covered. In the absence of generalised expressions for the pressure losses, one must rely on experimental relationships for a particular geometry.

For a nozzle of a given geometry, β is expected to vary with the Mach number, as dissipative effects are non-linearly related to flow parameters such as the Reynolds number. In the next section, the parameter β determined from the mean flow measurements of pressure and velocity is used to obtain the acoustic and entropic transfer functions of non-isentropic nozzles.

The equivalent orifice plate model

In Fig. 5.3 the nozzle is divided into four nodes, represented by the areas A_1, A_T, A_j and A_2. As the flow is modelled as isentropic and acoustically compact between A_1 and A_j, the throat section is not required to calculate the flow parameters and transfer functions in subsonic conditions. Thus, a non-isentropic nozzle is acoustically modelled as an *equivalent orifice plate* with orifice throat area A_j. Nevertheless, the throat section A_T is required to determine the base flow, and also defines the lower limit for the parameter A_j. The area A_T determines the choking limit: for a fixed A_j, with $A_j > A_T$, the non-isentropic nozzle with throat area A_T chokes at a lower mass flow rate than an equivalent orifice plate of throat area A_j. This also emphasises the conceptual difference between the effective jet area factor β and the vena contracta factor Γ. The conceptual jet area is larger than the geometric throat area ($A_j/A_T \geq 1$), while the vena contracta area is smaller than the throat area ($A_{min}/A_T \leq 1$).

5.2.3 Linear perturbations

The response of a compact nozzle to acoustic and entropic perturbations is derived by using the small perturbations approach (Sec. 3.1.1). We define the quantities p', ρ', u' and s' as the fluctuating pressure, density, velocity and entropy relative to the mean flow.

The normalised perturbed mass ($\dot{m}$) and energy (or equivalently total temperature, T_t) conservation equations between two generic sections A_m and A_n become:

$$\left[\frac{\dot{m}'}{\dot{m}}\right]_m^n = \left[\frac{1}{M}\frac{u'}{c} + \frac{\rho'}{\rho}\right]_m^n = 0; \tag{5.7}$$

$$\left[\frac{T_t'}{T_t}\right]_m^n = \left[\frac{1}{1+\frac{\gamma-1}{2}M^2}\left(\frac{T'}{T} + (\gamma-1)M\frac{u'}{c}\right)\right]_m^n = 0; \tag{5.8}$$

Between 1 and j, the flow is isentropic, so that Eq. 5.1 reads:

$$\frac{s'_1}{c_p} = \frac{s'_j}{c_p} = \sigma \tag{5.9}$$

Between A_j and A_2, momentum rather than entropy is conserved, and the perturbed momentum conservation (Eq. 5.4) reads

$$\frac{1}{\beta}\frac{c_j}{M_j}\frac{p'_j}{\gamma p_j} + M_j c_j \frac{\rho'_j}{\rho_j} + 2c_j\frac{u'_j}{c_j} = \frac{c_2}{M_2}\frac{p'_2}{\gamma p_2} + M_2 c_2 \frac{\rho'_2}{\rho_2} + 2c_2\frac{u'_2}{c_2} \tag{5.10}$$

where the factor $\beta = A_j/A_2$ again appears as a parameter. Here we are implicitly assuming that the relative *mean* pressure losses are similar to the *perturbed* pressure losses, which holds for the present very low frequency range. This may not be the case for higher frequencies. We can now build transfer functions for the perturbations between the four different sections of areas A_1, A_2, A_T and A_j (Fig. 5.3), keeping β as a representative parameter for the total pressure losses.

5.2.4 Acoustic and entropic transfer function of non-isentropic nozzles

We now model the response of the nozzle to impinging acoustic and entropic disturbances. The upstream ($-$) and downstream ($+$) reflection and transmission coefficients for sections 1 and 2 are defined as as follows:

$$R_+ = \frac{\pi_1^-}{\pi_1^+}; \qquad R_- = \frac{\pi_2^+}{\pi_2^-}; \qquad T_+ = \frac{\pi_2^+}{\pi_1^+}\frac{\gamma p_2}{\gamma p_1}; \qquad T_- = \frac{\pi_1^-}{\pi_2^-}\frac{\gamma p_1}{\gamma p_2} \tag{5.11}$$

The entropy-to-sound conversion coefficients of the nozzle are determined by imposing a convected entropy wave σ_1 entering the nozzle from upstream with velocity u_1. Once this entropy perturbation encounters the velocity gradient in the nozzle, two acoustic waves $\pi_{1,s}^-$ and $\pi_{2,s}^+$ are generated. The entropy-to-sound conversion coefficients for the nozzle are defined as:

$$S_R = \frac{\pi_{1,s}^-}{\sigma_1}; \qquad S_T = \frac{\pi_{2,s}^+}{\sigma_1} \tag{5.12}$$

where the subscript notation $_R$ and $_T$ implicitly defines the reflected and transmitted parts of the acoustic waves. As the generalised nozzle in Fig. 5.3 is divided into four nodes (corresponding to the interfaces A_1, A_2, A_T and A_j), 12 variables are needed to fully characterise the perturbations. Three of these are the imposed impinging perturbations (solid arrows in Fig. 5.1): two incoming acoustic waves (π_1^+ and π_2^-, blue solid arrows) and the entropy perturbation (σ_1, black solid arrow). The remaining 9 unknowns are determined using the 9

jump equations derived in section 5.2.3 (3 jump equations for each area interface), yielding a 9x9 transfer function matrix **M**. In this way, the response of the subsonic nozzle to acoustic and entropic disturbances can be expressed in the compact form

$$\mathbf{M}\cdot\mathbf{X}=\mathbf{a_1}\pi_1^+ + \mathbf{a_2}\pi_2^- + \mathbf{a_3}\sigma_1 \tag{5.13}$$

where

$$\mathbf{M}=$$

$$\begin{bmatrix}
1-\frac{1}{M_1} & -1-\frac{1}{M_T} & -1+\frac{1}{M_T} & 1 & 0 & 0 & 0 & 0 & 0\\
0 & -1-\frac{1}{M_T} & -1+\frac{1}{M_T} & 1 & 1+\frac{1}{M_j} & 1-\frac{1}{M_j} & -1 & 0 & 0\\
0 & 0 & 0 & 0 & 1+\frac{1}{M_j} & 1-\frac{1}{M_j} & -1 & -1-\frac{1}{M_2} & 1\\
\frac{1-M_1}{1+\frac{\gamma-1}{2}M_1^2} & \frac{-1-M_T}{1+\frac{\gamma-1}{2}M_T^2} & \frac{-1+M_T}{1+\frac{\gamma-1}{2}M_T^2} & -\frac{\frac{1}{\gamma-1}}{1+\frac{\gamma-1}{2}M_T^2} & 0 & 0 & 0 & 0 & 0\\
0 & \frac{-1-M_T}{1+\frac{\gamma-1}{2}M_T^2} & \frac{-1+M_T}{1+\frac{\gamma-1}{2}M_T^2} & -\frac{\frac{1}{\gamma-1}}{1+\frac{\gamma-1}{2}M_T^2} & \frac{1+M_j}{1+\frac{-1}{2}M_j^2} & \frac{1-M_j}{1+\frac{\gamma-1}{2}M_j^2} & \frac{\frac{1}{\gamma-1}}{1+\frac{\gamma-1}{2}M_j^2} & 0 & 0\\
0 & 0 & 0 & 0 & \frac{1+M_j}{1+\frac{\gamma-1}{2}M_j^2} & \frac{1-M_j}{1+\frac{\gamma-1}{2}M_j^2} & \frac{\frac{1}{\gamma-1}}{1+\frac{\gamma-1}{2}M_j^2} & \frac{-1-M_2}{1+\frac{\gamma-1}{2}M_2^2} & -\frac{\frac{1}{\gamma-1}}{1+\frac{\gamma-1}{2}M_2^2}\\
0 & 0 & 0 & 1 & 0 & 0 & 0 & 0 & 0\\
0 & 0 & 0 & 1 & 0 & 0 & -1 & 0 & 0\\
0 & 0 & 0 & 0 & c_j\left(\frac{1}{\beta}\frac{1}{M_j}+2+M_j\right) & c_j\left(\frac{1}{\beta}\frac{1}{M_j}-2+M_j\right) & -M_jc_j & -c_2\left(\frac{1}{M_2}+2+M_2\right) & M_2c_2
\end{bmatrix}$$

$$\mathbf{X}=\begin{bmatrix}\pi_1^-\\ P_T^+\\ P_T^-\\ \sigma_T\\ P_j^+\\ P_j^-\\ \sigma_j\\ \pi_2^+\\ \sigma_2\end{bmatrix};\qquad \mathbf{a_1}=\begin{bmatrix}-\left(1+\frac{1}{M_1}\right)\\ 0\\ 0\\ -\frac{1+M_1}{1+\frac{\gamma-1}{2}M_1^2}\\ 0\\ 0\\ 0\\ 0\\ 0\end{bmatrix};\qquad \mathbf{a_2}=\begin{bmatrix}0\\ 0\\ 1-\frac{1}{M_2}\\ 0\\ 0\\ \frac{1-M_2}{1+\frac{\gamma-1}{2}M_2^2}\\ 0\\ 0\\ c_2\left(\frac{1}{M_2}-2+M_2\right)\end{bmatrix};\qquad \mathbf{a_3}=\begin{bmatrix}1\\ 0\\ 0\\ -\frac{\frac{1}{\gamma-1}}{1+\frac{\gamma-1}{2}M_1^2}\\ 0\\ 0\\ 1\\ 0\\ 0\end{bmatrix} \tag{5.14}$$

Transfer functions of the generalised convergent-divergent nozzle

Fig. 5.6 shows the acoustic and entropic transfer functions of the non-isentropic nozzle of Fig. 5.3 obtained by varying β. The transfer functions of the isentropic nozzle ($A_j = A_2$; $\beta = 1$) under subsonic (dashed lines) and sonic (circular markers) conditions are highlighted [147, 152]. The dashed-dotted lines correspond to the reflectivity and transmissivity of an orifice plate [65] ($A_T = A_j$, $\beta = \beta_{min} = A_T/A_2$, with Γ = 1). Under the compact approximation, for a fully isentropic nozzle with $A_1 = A_2$, the transmission coefficient for acoustic waves is unity, and the reflection coefficient is zero. When the nozzle chokes, no perturbations can be transmitted from downstream of the nozzle to upstream, thus $T^- = 0$. On the other hand, the choked throat acts similarly to a velocity node, thus most of the downstream traveling waves are entirely reflected back ($R^+ \simeq 1$), as predicted from [147]. Therefore, the isentropic nozzle transfer functions display a discontinuity for $M_T = 1$. Notably, the flow in a convergent/divergent nozzle has two isentropic solutions for a choked throat, one for a subsonic diffuser and the other one for a supersonic diffuser [8]. For a fixed nozzle geometry and upstream total pressure p_{01}, under choked conditions, the flow follows one or the other depending on the downstream pressure p_2. Generally speaking, the acoustic and entropic reflection coefficients in the upstream subsonic section R_+ and S_R are expected to remain unchanged regardless of the behaviour of the flow in the divergent section, while the remaining transmission coefficients are expected to differ between the two cases. In the current work, as we are concerned about the choking condition as a limit case for a subsonic nozzle, only the subsonic diffuser case is considered.

The present model allows for a continuous transition between a subsonic and choked nozzle, where the loss parameter β enable the accommodation between the two limits (Fig. 5.6). For $\beta \simeq \beta_{min}$ ($A_j \simeq A_T$), the reflection coefficients are highly influenced by the particular value A_j, *i.e.* by the dissipative losses. For $A_j \simeq 10A_T$, the reflection coefficients are practically isentropic, and at the limit $A_j \to A_2$, fully isentropic. From the point of view of combustion instabilities, the behaviour of the upstream propagating waves is of interest, as they may couple with heat release fluctuations. In this context, we note that an opposite behaviour of isentropic and non-isentropic nozzles: the more isentropic the nozzle flow, the lower the reflectivity and the higher the transmissivity. Conversely, while *zero* indirect noise is predicted under isentropic conditions either upstream or downstream of the nozzle, both reflected and transmitted indirect (entropic) noise are *not* negligible for the non-isentropic nozzles. This occurs because under isentropic conditions there is an exact and opposite cancellation of the entropic fluctuations, which is not the case for the asymmetric, non-isentropic situation.

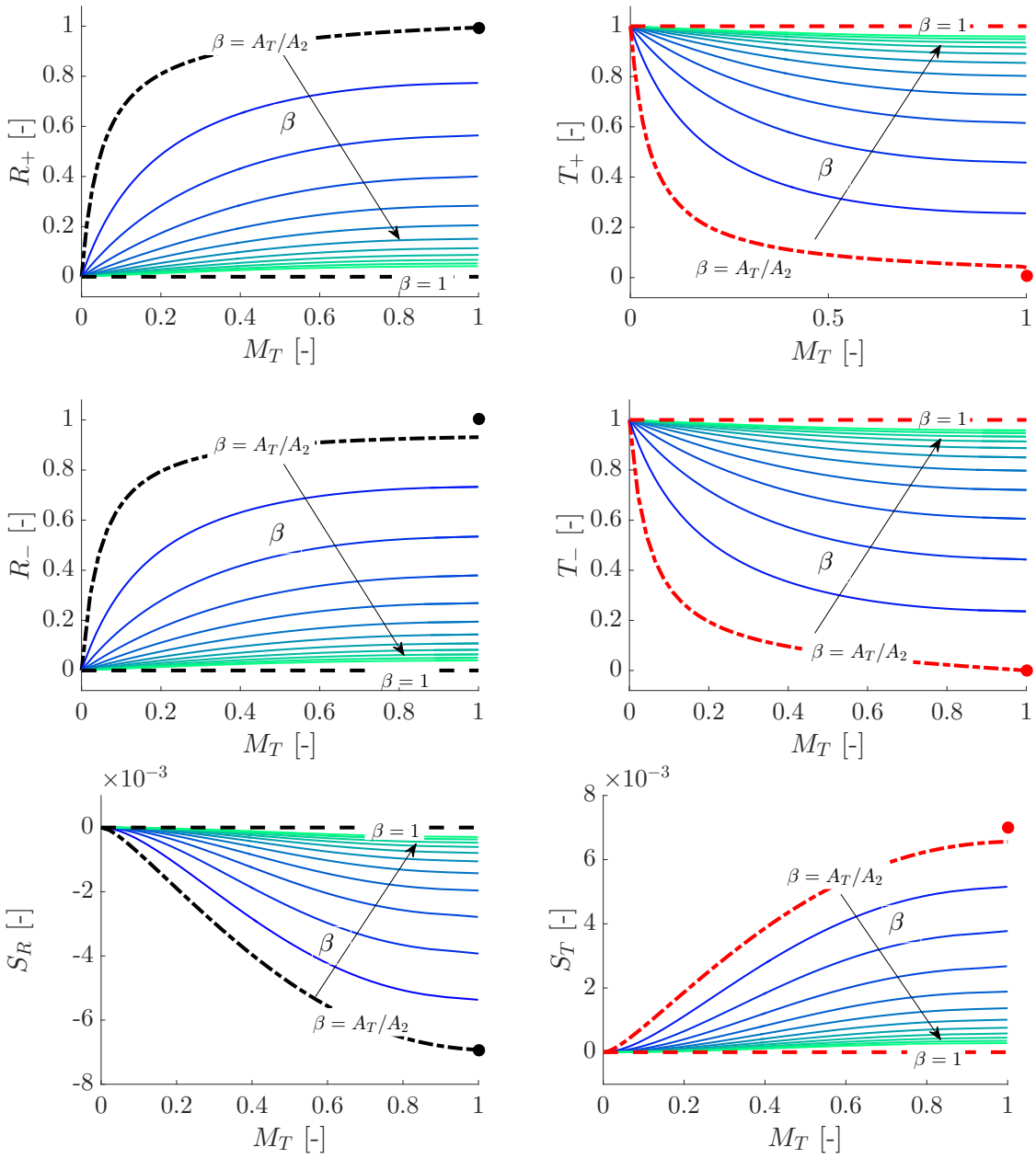

Fig. 5.6 Acoustic (R_+, R_-, T_+, T_-) and entropic (S_R, S_T) transfer functions of the convergent-divergent nozzle with losses. Dashed lines: isentropic subsonic predictions [147] ($A_j = A_2$, $\beta = 1$); circular markers: isentropic choked predictions [147]; dashed-dotted lines: predictions from the orifice plate model [65] ($A_j = A_T$; $\beta = \beta_{min}$); solid lines: results obtained from Eq. 5.13 for values of $A_j/A_T = [2,3,4,5,6,7,8,9,10]$, $\Gamma = 1$.

The convergent-only case

The model for non-isentropic nozzles can be adapted to describe subsonic converging nozzles and diaphragms that terminate a duct, where the flow expands to the atmosphere, by setting $A_2 \to \infty$, with $A_j = A_T$. The acoustic behaviour of a purely convergent nozzle was previously analysed by Howe for incompressible flow using an energy conservation approach [106] and later on by Bechert [14], Cummings [38] and Durrieu [65], which considered only the acoustic reflection. Fig. 5.7 shows the acoustic (left) and entropic (right) reflection coefficients of the convergent-only nozzle. The blue solid lines represent the reflectivity obtained from the transfer matrix (Eq. 5.13) for $A_2 \to \infty$ and $A_j = A_T$. The green dotted line plots the acoustic reflection coefficient derived in previous literature using an acoustic energy balance [106, 14, 65] (Eq. 39 in [65]):

$$R_+ = -\frac{(1-M_1)\left[1-(A_1/A_T)(\rho_1/\rho_T)^2 M_1\right]}{(1+M_1)\left[1+(A_1/A_T)(\rho_1/\rho_T)^2 M_1\right]} \tag{5.15}$$

The prediction from Eq. 5.15 is almost identical to the analytical reflection coefficient obtained from the model developed in Eq. 5.13, which uses the conservation of momentum.

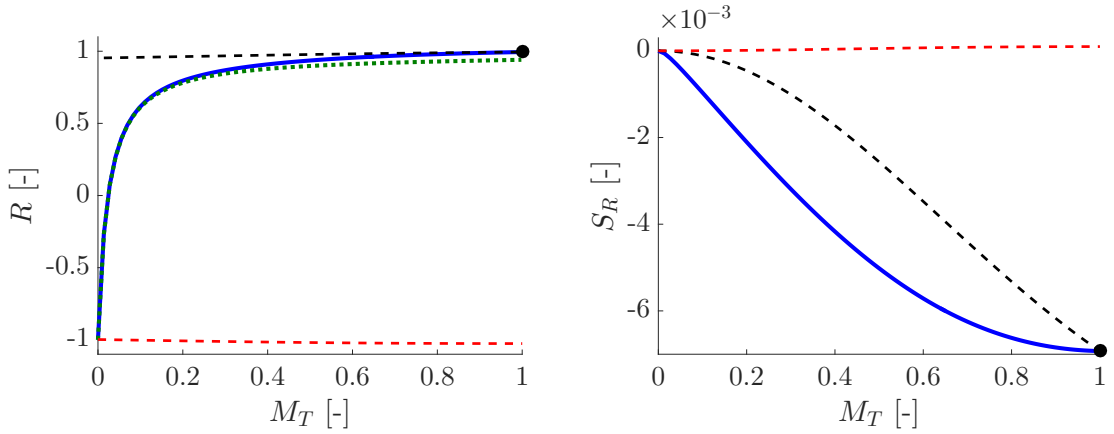

Fig. 5.7 Acoustic (left) and entropic (right) upstream transfer functions for a convergent nozzle terminating in an open jet, as a function of throat Mach number M_T. Dashed lines: predictions for reflected acoustic (left) and entropic (right) waves applying the isentropic relations between A_1 and A_T (dashed black lines) and between A_1 and $A_2 \to \infty$ (dashed red lines); solid blue lines: results of the transfer function of Eq. 5.13 for $A_T = A_j$, $\beta = \beta_{min}$, $A_2 \to \infty$; green dotted line: direct noise reflection coefficient according to [65] (Eq. 5.15).

The dashed lines represent the acoustic (left) and entropic (right) reflected transfer functions calculated using the isentropic subsonic equations in [147]: for the dashed black lines, the isentropic equations are applied between the upstream area A_1 and throat area A_T, while for the dashed red lines the isentropic equations are applied between the upstream

area A_1 and the downstream area $A_2 \to \infty$. Following the definition of the coefficients used in [175], in this work we consider the isentropic formulation between the areas A_1 and A_T (dashed black lines). These isentropic results differ substantially from the non-isentropic coefficients, both for the direct and the indirect noise: the isentropic approximation over-predicts the reflected acoustic wave, and under-predicts the amplitude of the upstream propagating indirect noise. Although the flow through the convergent nozzle is still modelled as isentropic, the non-isentropic expansion of the jet downstream of the throat cannot be neither neglected nor captured with isentropic models.

The change in sign of the acoustic reflection coefficient in Fig. 5.7 (left) has been already observed and discussed in [14, 65, 51]. It is caused by the combination of the positive reflection of the the portion of the wave that impacts the orifice plate solid wall, which acts as a closed end, and the negative reflection of the remaining wave that encounters the open hole [183]. The total reflected wave is the resultant of these in- and out-of-phase waves, leading to low frequency acoustic energy cancellation. Moreover, when the acoustic energy is sufficiently high, part of it is dissipated by the conversion into vortical energy at the edges, where the flow separates. As for a range of Mach numbers, the reflection coefficient becomes zero, this effect has been successfully used to build anechoic terminations [14, 65].

5.3 Experimental configuration

The experimental configuration used in this chapter is shown in Fig. 5.8 and briefly described here. Air flows through the EGR at a controlled rate and passes through the heating grid. Current is pulsed into this heating module to generate a 100 ms long heat release pulse accompanied by a hot spot, which is then advected with the mean flow. As the hot spot is accelerated through the nozzle or orifice plate, it produces indirect noise. The 60-meter-long tube can be attached downstream of the nozzle or orifice plates to prevent immediate reflection of the transmitted sound waves, providing a non-reflecting end termination for the round trip time of a travelling sound wave. This permits the measurement of the transmitted wave. Dynamic pressure measurements are collected at positions downstream of the heating device, upstream and downstream of the nozzle, via flush-mounted pressure transducers, at locations indicated in Fig. 5.8.

Two different experimental configurations are used to compare the experimental data with the analytical predictions in Eq. 5.13. In configuration (i), the flow is accelerated and then decelerated through the convergent/divergent nozzle or the sharp edged orifice plate, characterised by the same throat diameter $d_T = 6.6$ mm (Table 4.1). The nozzle has conical converging and diverging sections, with angles $\alpha_c = 40^\circ$ and $\alpha_d = 4.5^\circ$ respectively. The

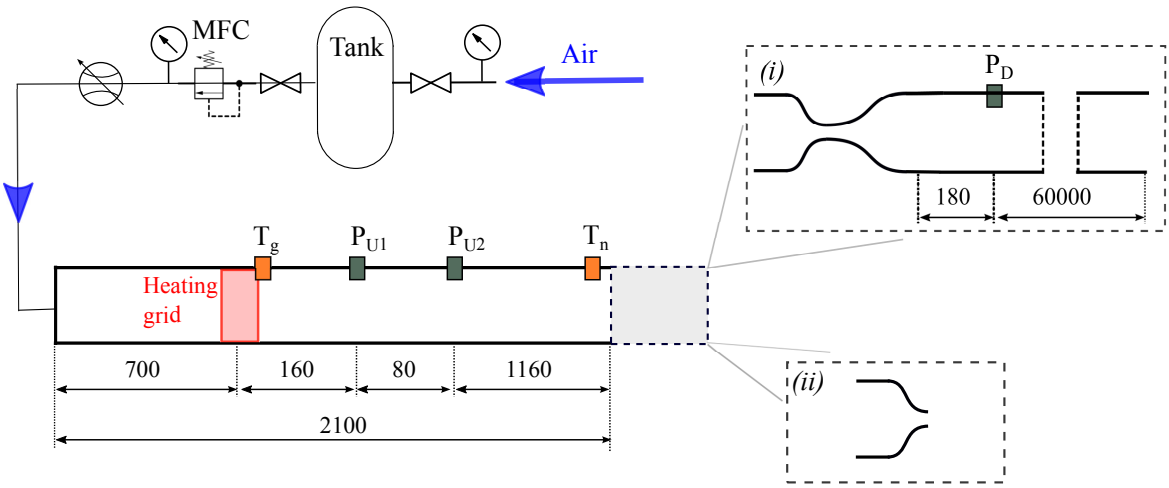

Fig. 5.8 Schematic of the experimental rig: (i) convergent-divergent nozzle configuration; (ii) convergent nozzle-terminated duct. Dimensions in mm. Not to scale.

orifice is a thin sharp edged orifice plate of thickness $t = 2$ mm. Downstream of the area discontinuity, the flow travels through the 60-meter-long tube, allowing the measurements of both the reflected and transmitted sound waves for $t < t_a$. The heating pulse length $t_p = 0.1\ s$ is chosen to be shorter than t_a, so the acoustic waves generated at the heating grid are not superposed with the corresponding reflected ones from the anechoic termination. In configuration (ii) the flow is accelerated through the converging shapes (four nozzles and two orifices described in Table 4.1, Chapter 4) and then expands as a jet in the open environment. The pressure signals are measured upstream of the area discontinuity. These nozzles and orifice plates are all characterised by the same upstream and throat diameters (42.6 mm and 6.6 mm) but different aspect ratios and shapes.

5.4 Experimental results

In this section, the results of the analytical model derived in section 5.2.4 are compared with the corresponding experimental data. Three additional details must be kept in mind regarding the comparisons of theory and experiments. First, the nozzle is compact over the frequency range of the experiment: as shown in Sec. 3.2.3, the characteristic wavelengths of the experiment are at least one order of magnitude longer than the nozzle longitudinal extension (ultra-low frequency range). The quasi-steady assumption holds, thus the transfer functions can be assumed to be real and constant among the frequencies of interest. Traditional frequency-based techniques, such as the two and multi-microphone methods, fail in this ultra low frequency range, as they require a spatial separation of the probes of at least $\lambda/4$ [12, 18],

which is not feasible for the wavelengths of the experiment. Second, the reverberation theory [175] is used to extract the nozzle transfer functions from the time domain pressure traces measured by the pressure transducers. Third, a vena contracta factor $\Gamma < 1$ must be taken into account to correctly capture the experimental behaviour.

5.4.1 Reverberation theory for a compact nozzle

The analytical predictions of the acoustic and entropic reflectivity and transmissivity of the non-isentropic convergent-divergent nozzle, orifice plates and converging nozzle can now be compared with the experimental data.

We recall the upstream and downstream travelling waves π^- and π^+ generated at the heating grid (direct noise). In the time interval considered, the direct noise generated in the upstream section from the activation of the heating grid travels multiple times between the nozzle and the inlet. Therefore, the reverberation of the waves needs to be taken into account to correctly explain the time domain pressure traces and extract the nozzle transfer functions. Rolland [175] has shown that, under acoustically compact conditions, the measured direct noise inside a cavity with inlet and outlet reflection coefficients R_0 and R_+ respectively, where the travelling waves π^+ and π^- generated at the heating grid are allowed to reverberate over a large number of cycles, is:

$$\left(\frac{p'}{\gamma p_1}\right)_u \simeq \frac{(\pi^+ + R_0\pi^-)(1+R_+)}{1-R_0R_+} \tag{5.16}$$

where the subscript $()_u$ indicates that the measurements are taken upstream of the nozzle. For the acoustic measurements downstream of the nozzle $()_d$, the ratio of transmitted to impinging perturbations onto the nozzle has been derived as [175]:

$$\frac{(p'/\gamma p_2)_d}{(p'/\gamma p_1)_u} \simeq \frac{\frac{T_+(\pi^+ + R_0\pi^-)}{1-R_0R_+}}{\frac{(\pi^+ + R_0\pi^-)(1+R_+)}{1-R_0R_+}} = \frac{T_+}{1+R_+}; \tag{5.17}$$

Similarly, for a known impinging entropy spot $\sigma \simeq T'/T$, the reflected entropy-to-sound conversion coefficient (S_R) can be evaluated from the indirect noise measurements upstream of the nozzle p'_s as:

$$\frac{p'_s}{\gamma p_1} = \pi^-_{1,s}\frac{1+R_0}{1-R_0R_+} \qquad S_R = \frac{\pi^-_{1,s}}{\sigma} \tag{5.18}$$

The duct inlet reflection coefficient R_0 has been experimentally determined as $R_0 = 0.97$ [175]. The source wave $(\pi^+ + R_0\pi^-)$, composed of the original plus reflected wave appears

in Eqs. 5.16 and 5.17, so its knowledge is needed to determine the transfer functions. Here, it is measured in a separate experiment using the anechoic termination to isolate it, as explained in Chapter 4 (Sec. 4.3.4). Otherwise, π^+ and π^- can also be determined from the knowledge of the air temperature increase at the heating grid, using the jump conditions of a heating source [63].

5.4.2 Convergent-divergent nozzle & Orifice plate (Configuration (i))

In this section, the experimental transfer functions of the orifice plate and the convergent/divergent nozzle acquired in configuration (i) are compared with the analytical predictions from Eq. 5.13. Each test is performed over a range of 17 mass flow rates, scanning from subsonic to sonic throat conditions. The maximum mass flow rate used in the experiment is determined by the upper limit of the mass flow controller ($\dot{m}_{max} \simeq 10$ g/s).

Base flow and vena contracta factor

Fig. 5.9 compares the measured increase in the mean pressure upstream of the convergent-divergent nozzle (black triangles) and orifice plate (red circles) with analytical predictions. This enables the determination of the vena contracta factor Γ and the jet area ratio β associated with pressure losses in the system for each case. This is important later on, as β is not a fit to the dynamic fluctuations, but the static factor associated with mean pressure loss.

We start determining the vena contracta factor Γ for the orifice plate (Γ_{OP}) and the convergent-divergent nozzle (Γ_{CD}). The asterisk * indicates the flow parameters corresponding to the choking conditions for the nozzle. As the flow in the converging section before the throat is always modelled as isentropic, the upstream Mach number M_1^* corresponding to choked flow only depends on the area ratio between the upstream section and the effective throat area ΓA_T [8]

$$\frac{A_1}{\Gamma A_T} = \frac{1}{M_1^*}\left(\frac{1+\frac{\gamma-1}{2}M_1^{*2}}{\frac{\gamma+1}{2}}\right)^{\frac{\gamma+1}{2(\gamma-1)}} \tag{5.19}$$

For $\Gamma = 1$, ${M^*}_{1,\Gamma=1}$ is the upstream Mach number at choking conditions. The blue dashed-dotted line in Fig. 5.9 refers to expected pressure increase for $\Gamma = 1$. The experimental points asymptote vertically for Mach numbers lower than ${M^*}_{1,\Gamma=1}$, showing that the effective throat area is smaller than the geometric area (*e.g.* $\Gamma < 1$). In addition, the experimental curves of the orifice and the convergent-divergent nozzle do not overlap, as the sharp-edged thin orifice has a lower vena contracta factor ($\Gamma_{OP} < \Gamma_{CD}$).

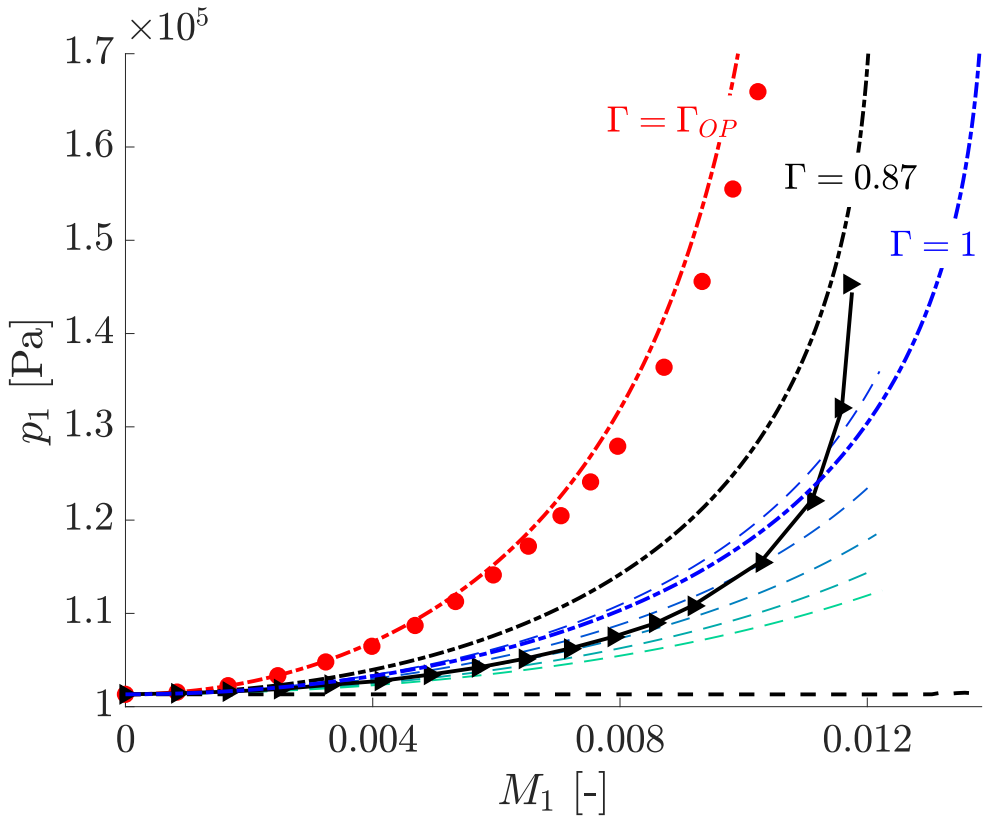

Fig. 5.9 Comparison between experimental and modelled mean upstream pressure increase (p_1) versus Mach number (M_1). Dashed dotted lines: orifice plates curves for different values of Γ. Dashed black lines: isentropic nozzle prediction. Dashed blue-green lines: curves obtained by varying β for $\Gamma = 0.87$. Red circles: experimental pressure increase acquired upstream of the thin orifice plate. Black triangles: experimental pressure increase acquired upstream of the convergent-divergent nozzle. Black solid line: experimental pressure-vs-Mach number curve used to determine the value β at each mass flow rate for the convergent/divergent nozzle.

Durrieu [65] provides a Mach-dependent formulation of the expected vena contracta factor Γ_{OP} for a sharp-edged thin orifice plate:

$$\Gamma_{OP} = \frac{1}{1+\sqrt{0.5\,(1-A_T/A_1)}} + 0.13M_T^2 \tag{5.20}$$

where M_T corresponds to the Mach number at the vena contracta section. In the current experimental set-up, $0.59 < \Gamma_{OP} < 0.72$. The experimental point at the highest Mach number acquired with the orifice plate corresponds to the choked throat condition ($M_T = 1$). Using $\Gamma = \Gamma_{OP}$, the analytical prediction for the pressure increase upstream of the orifice plate (red dashed-dotted curve) predicts well the experimental data (red dots).

For the convergent-divergent nozzle (black triangles) in Fig. 5.9, the curve formed by the black triangles and solid line suggests that the flow chokes at the throat for the highest mass flow rate, as the slope of the curve tends to infinity. Also in this case, $\Gamma_{CD} < 1$, as the curve becomes asymptotic to a vertical line at $M^*_{1,CD} < M^*_{1,\Gamma=1}$.

Few results can be found in the literature to model the vena contracta factor of a convergent-divergent nozzle, which are usually limited to incompressible flow. Hollinshead reports a vena contracta coefficient at low Mach number $\Gamma_{CD} = 0.90 - 0.95$ [104], and all authors agree on the geometry and flow dependence of Γ_{CD} [208, 16]. In order to estimate a value for Γ_{CD}, we use the experimental point at the highest mass flow rate in Fig. 5.9, corresponding to choking conditions. Using Eq. 5.19, the value Γ_{CD} is determined, as $\Gamma_{CD} \simeq 0.87$. This Γ value is assumed to be constant for all mass flow rates used. The dashed-dotted black line in Fig. 5.9 corresponds to the pressure increase for an orifice plate ($\beta = \beta_{min}$) with a constant $\Gamma = 0.87$. The dashed black line, instead, shows the pressure increase for an isentropic convergent-divergent nozzle with $A_1 = A_2$. As expected, the experimental points for the nozzle lie between those two cases, consistent with the expected lower pressure losses with respect to the orifice plate and higher pressure losses with respect to the isentropic nozzle. The dashed lines are obtained by varying the β factor: each of these lines corresponds to a different value of β. The variable values of β correspond to different degrees of pressure loss. The value β at each flow rate is determined from the experimental data by minimising the error between experimental and predicted static pressure loss. The black solid line connects the points resulting from this minimisation process. The corresponding values of β determined with this algorithm from the mean flow quantities are used in Section 5.4.2 to predict the transfer functions of the nozzle.

Acoustic transfer functions

Fig. 5.10 (top) shows examples of ensemble-averaged (over 90 traces) pressure traces acquired upstream (p'_u, dashed lines) and downstream (p'_d, solid lines) of the convergent-divergent nozzle (black) and the orifice plate (red) for a mass flow rate $\dot{m} = 1.4$ g/s, generated by the activation of the heating grid. The anechoic time $t_a = 0.36$ s is marked by the vertical dashed-dotted grey line. After t_a, the downstream end ceases to be silent as the travelling waves reflected at the downstream open end reach the transducers. The direct noise upstream and downstream of the nozzle reaches a maximum at the end of the heating pulse (for $t = t_p = 0.1$ s). The acceleration of the entropy spot, instead, occurs for $t > t_a$, so the indirect noise is *combined* with the direct noise reflected from the end of the anechoic termination for $t > t_a$. Therefore, only the direct noise is compared with the model in this section.

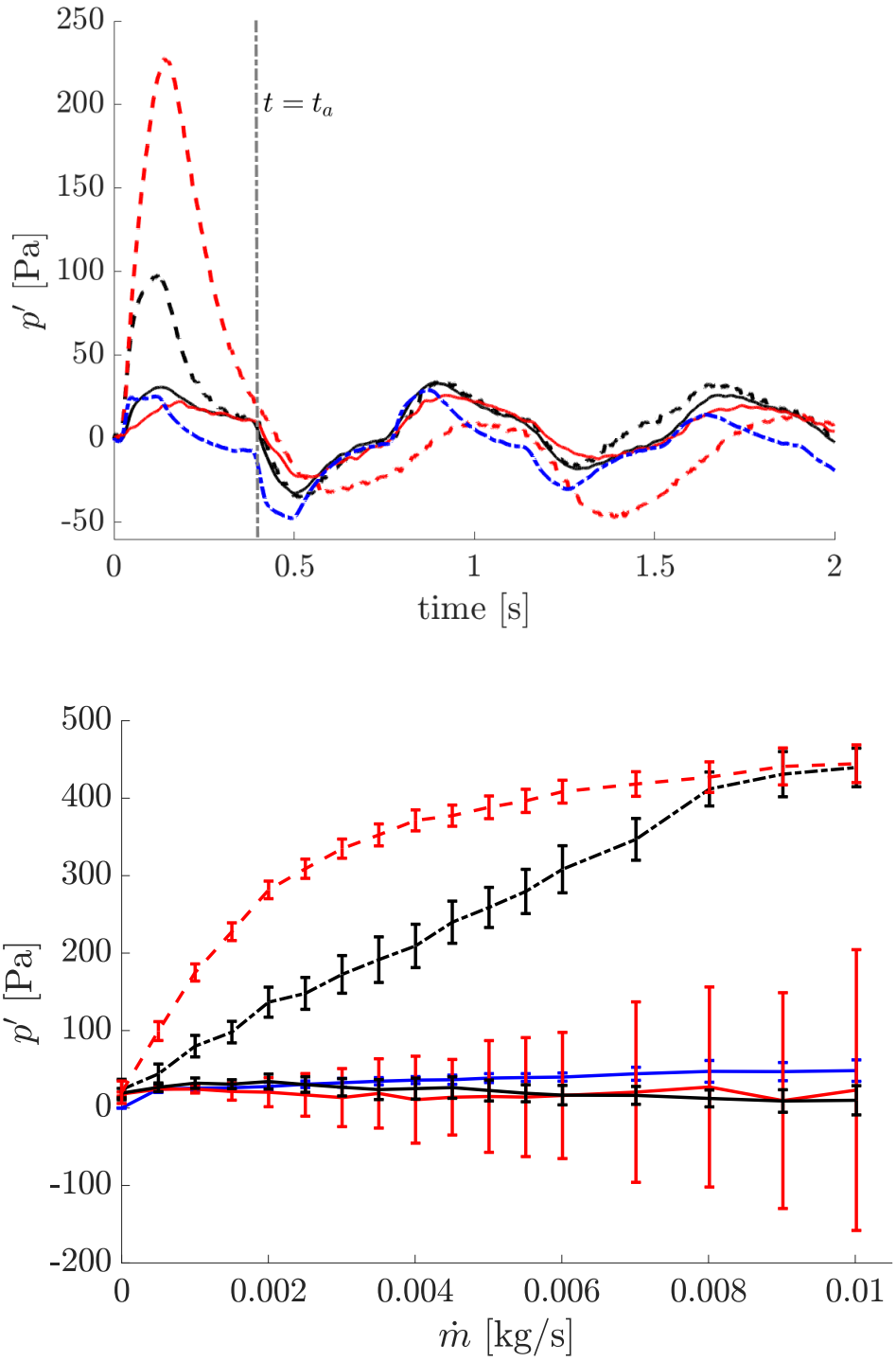

Fig. 5.10 Ensemble-averaged pressure traces acquired upstream (dashed lines) and downstream (solid lines) of the convergent-divergent nozzle (black) and orifice plate (red). Blue dashed-dotted line: source wave $(\pi^+ + R_0\pi^-)\gamma p_1$ determined using the anechoic termination. Mass flow rate $\dot{m} = 1.4$ g/s (top).
Direct noise pressure peaks acquired upstream (dashed line) and downstream (solid line) of the convergent-divergent nozzle (black) and orifice plate (red). Blue line: direct noise peak of the source wave $(\pi^+ + R_0\pi^-)\gamma p_1$ (bottom).

As explained in Sec. 5.4.1, the knowledge of the input source wave $(\pi^+ + R_0\pi^-)\gamma p_1$ is needed to determine the nozzle transfer functions. Here, we experimentally isolated this source wave with a separate experiment using the anechoic termination, as explained in Chapter 4 (Sec. 4.3.4). In configuration (i), the nozzle was removed and the 60-meter-long tube was attached directly to the rig, so that the rig is terminated with a 61-meter-long open end. When the heating source is activated, the travelling wave $(\pi^+ + R_0\pi^-)\gamma p_1$ is immediately acquired by the pressure transducers, then it travels through the 60 meter long tube until it is negatively reflected back at the open end, and is acquired again after $t = t_a$. Thus, for $t < t_a$, the pressure transducers measure the single travelling wave $(\pi^+ + R_0\pi^-)\gamma p_1$ (blue dashed-dotted line in Fig. 5.10 (top)). The same measurements (upstream and downstream pressure traces and source wave) were repeated for the 17 mass flow rates. The peaks in the upstream (dashed lines) and downstream (solid lines) pressure traces and of the source wave (blue) acquired for $t < t_a$ are plotted in Fig. 5.10 (bottom). These normally correspond to the peak in the direct noise trace. The large standard deviations in the measurements of the transmitted sound waves downstream of the orifice plate (red solid line) are attributed to the noise generated by the jet. Indeed, by increasing the mass flow rate, the non-coherent noise generated by jet exiting from the orifice increases substantially. The flow noise which is uncorrelated with the low frequency pulse is removed by cycle averaging the pulse sequence, which acts as a low frequency filter. In this way, transmitted sound waves generated by the heating grid can be isolated. From these measured averaged peak values, we obtain the experimental values of $(\pi^+ + R_0\pi^-)\gamma p_1$, p'_u and p'_d and we can determine the reflection R_+ and transmission T_+ coefficients of the orifice and nozzle using Eq. 5.16 and 5.17.

The measurements downstream of the nozzle display a lower signal-to-noise ratio and higher background noise level, so the transmission coefficients T^+ are less accurate than the reflection coefficients R^+, especially for the orifice plate. This suggests that the measurements upstream of the nozzle constitute a more accurate way to determine the acoustic properties of a non-isentropic nozzle, as multiple reflections enhance the signal, obtaining a standard deviation of $std_{R^+}/R_+ \simeq 16-18\%$. However, the reliability of the transmission coefficients determined with the averaged data in Fig. 5.10 (bottom) can be verified from an acoustic intensity balance.

$$R_+ + T_+\frac{p_1}{p_2} \leq 1 \tag{5.21}$$

The experimental reflection (black) and transmission (red) coefficients for the orifice plate (circles) and the nozzle (triangles) are shown in Fig. 5.11, top and bottom respectively, and compared with the analytical predictions (lines). Fig. 5.11 (top) shows that the experimentally determined transfer functions for the orifice plate agree well with the analytical predictions

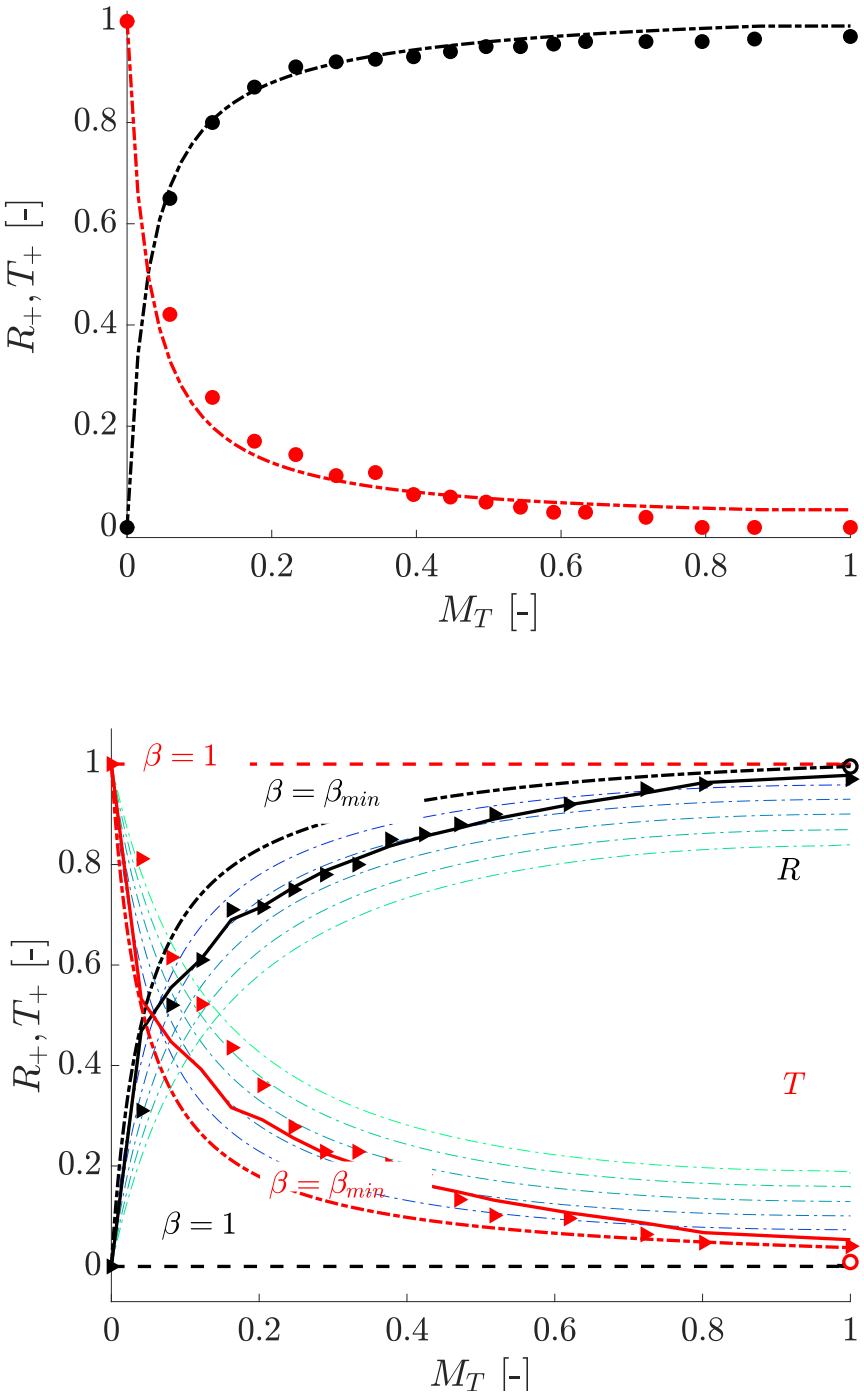

Fig. 5.11 Orifice plate: comparison between experimental reflectivity (black circles) and transmissivity (red circles) with the analytical predictions (dashed-dotted lines) [65] (top). Convergent-divergent nozzle: comparison between experimental reflectivity (black triangles) and transmissivity (red triangles) with the analytical predictions. Dashed lines: isentropic predictions ($\beta = 1$), dashed-dotted lines: orifice plate transfer functions ($\Gamma = 0.87$, $\beta = \beta_{min}$), dashed-dotted blue-green lines: non-isentropic nozzle transfer functions (each corresponding to a $\beta = const.$ pressure line in Fig. 5.9). Solid line: predicted transfer functions using the β determined from the mean flow behaviour (bottom).

(black and red dashed dotted line). For the convergent/divergent nozzle (Fig. 5.11 (bottom)), the isentropic model (dashed line) predicts zero reflections (black), and full transmissivity (red), except at the point of choking (circular markers), which clearly does not represent the experimental behaviour.

The black and red dashed-dotted lines correspond instead to the equivalent orifice plate ($\Gamma = 0.87$, $\beta = \beta_{min}$) reflectivity and transmissivity. As expected from the mean pressure behaviour, the experimentally determined reflectivity (black triangles) and transmissivity (red triangles) lie between the orifice plate and the isentropic nozzle transfer functions. The black and red solid lines correspond to the predicted acoustic reflectivity and transmissivity from Eq. 5.13, using the values of β determined from the mean pressure increase in Sec. 5.4.2. Overall, good agreement is obtained between the non-isentropic predictions and the experimental transfer functions, once both the equivalent jet factor β and vena contracta factor Γ are evaluated. Again, Fig. 5.11 shows that the isentropic predictions may differ substantially from the actual transfer functions of a nozzle in the presence of pressure losses.

5.4.3 Convergent only nozzle (Configuration (ii))

The experimental data acquired in configuration (ii) with converging nozzles are here compared with analytical predictions. Fig. 5.12 shows the expected (lines) and measured (markers) static upstream pressure increase by using six converging terminations (see Table 4.1 for the meaning of the symbols). The four nozzles and the thick orifice plate have similar behaviour, while the thin orifice plate generates a much higher increase in the upstream pressure, owing its lower vena contracta factor. The lines in Fig. 5.12 correspond to the modelled upstream pressure increase for a sharp edged orifice plate with $\Gamma = \Gamma_{OP}$ from Eq. 5.20 (red solid line) and a nozzle with $\Gamma = 0.9$ (blue solid line). These values of Γ are used in the determination of the nozzle transfer functions in Sec. 5.4.3.

Acoustic and entropic transfer functions

The experimental acoustic and entropic reflected transfer functions for the converging terminations are here compared with the analytical predictions. Figures 5.13 show the maximum and the minimum pressure peaks measured for 14 different mass flow rates. As discussed in Chapter 4 (Sec. 4.4), the maximum of the oscillation always corresponds to the direct noise peak, while the minimum does not necessarily coincide with the peak of the indirect noise, due to the partial merging with the direct noise at the higher flow rates. However, the reverberation model is able to properly account for the merging. In order to determine the entropy-to-sound conversion coefficient R_s, the amplitude of the impinging entropy spot

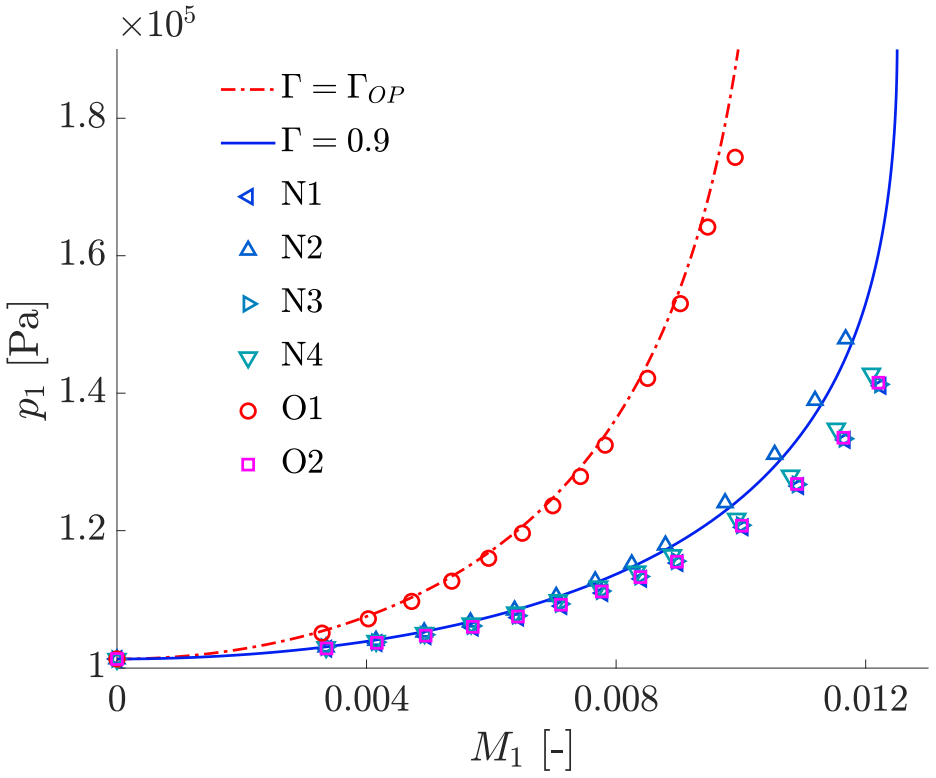

Fig. 5.12 Upstream pressure increase versus mass flow rate for the six converging shape terminations. Circle: thin orifice plate; square: thick orifice plate; triangles: converging nozzles (see Table 4.1 for the meaning of the symbols). Solid red line: prediction from the orifice plate model, $\Gamma = \Gamma_{op}$, solid blue line: prediction from the orifice plate model, using $\Gamma = const. = 0.9$.

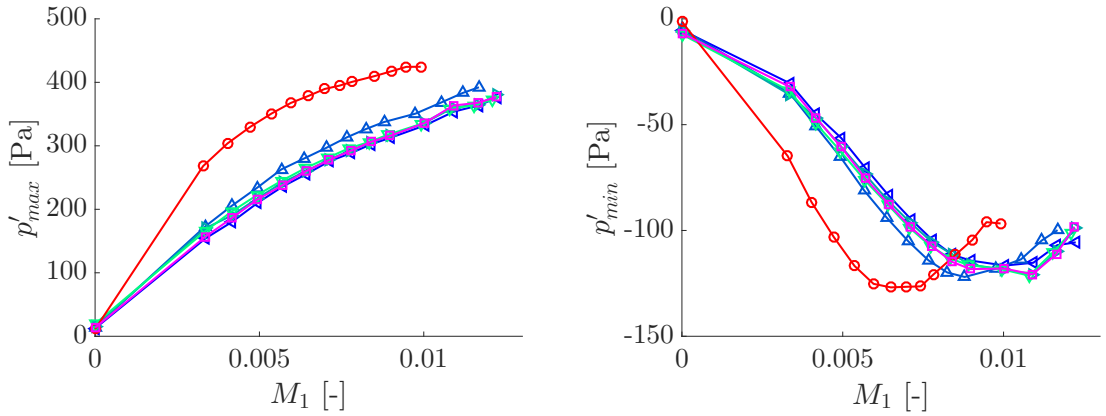

Fig. 5.13 Measured peak of the pressure traces for the direct (left) and indirect noise (right) with the six converging shapes. Circle: thin orifice plate; square: thick orifice plate; triangles: converging nozzles (see Table 4.1 for the meaning of the symbols).

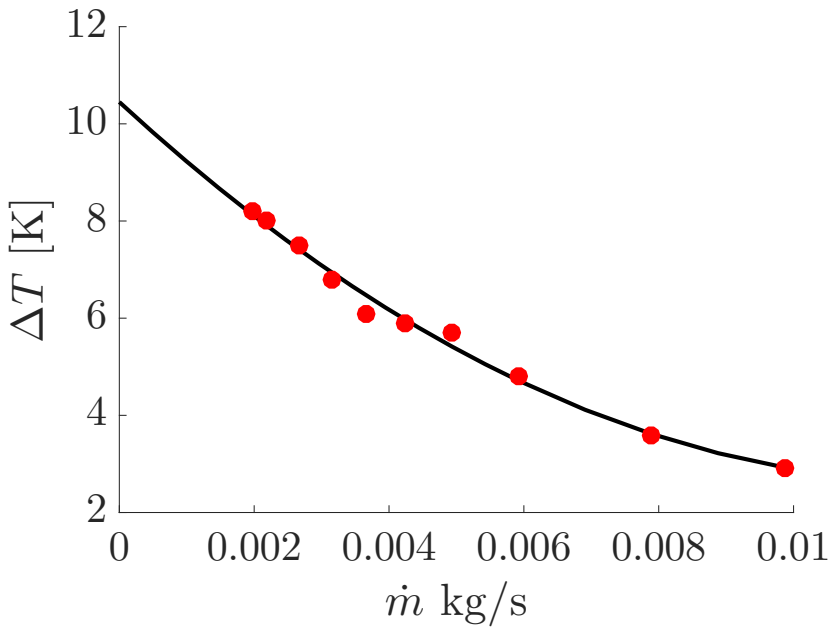

Fig. 5.14 Hot spot temperature at the acceleration point versus mass flow rate: experimental points (dots) and best fit curve (black line).

$\sigma \simeq T'/T$ is needed (Eq. 5.18). The temperature increase in the flow T' generated by the heating grid is obtained from thermocouple measurements at the nozzle (Fig. 5.14) after correcting the thermocouple output for the time response as described in Chapter 4 (Sec. 4.3.3).

Fig. 5.15 compares the analytical predictions with the experimental direct (top) and indirect (bottom) transfer functions for the different nozzles (triangles) and orifices plates (square and circle) determined using the reverberation formula in Sec. 5.4.1. The solid lines are obtained from the non-isentropic model of Eq. 5.13 with $\Gamma = \Gamma_{OP}$ (red lines) and $\Gamma = 0.9$ (blue lines) ($A_j = \Gamma A_T$ and $A_2 \to \infty$). The dashed lines are obtained from the isentropic formula applied between the upstream and the throat sections. A good match is obtained between the non-isentropic predictions and the experimental data, both for the direct and the indirect noise. In contrast, the isentropic model overpredicts the acoustic reflection coefficients, while it underpredicts the amplitude of the entropy-to-sound conversion coefficient. These results suggest that the mismatch between the isentropic theory and the experimental data in [175] is due to the non-isentropicity of the system. The flow can be considered as isentropic up to the throat, but the non-isentropic expansion of the jet needs to be accounted in subsonic conditions to correctly capture the experimental results. Once the non-isentropicity of the system is taken into account, a good match between experimental results and analytical predictions is obtained.

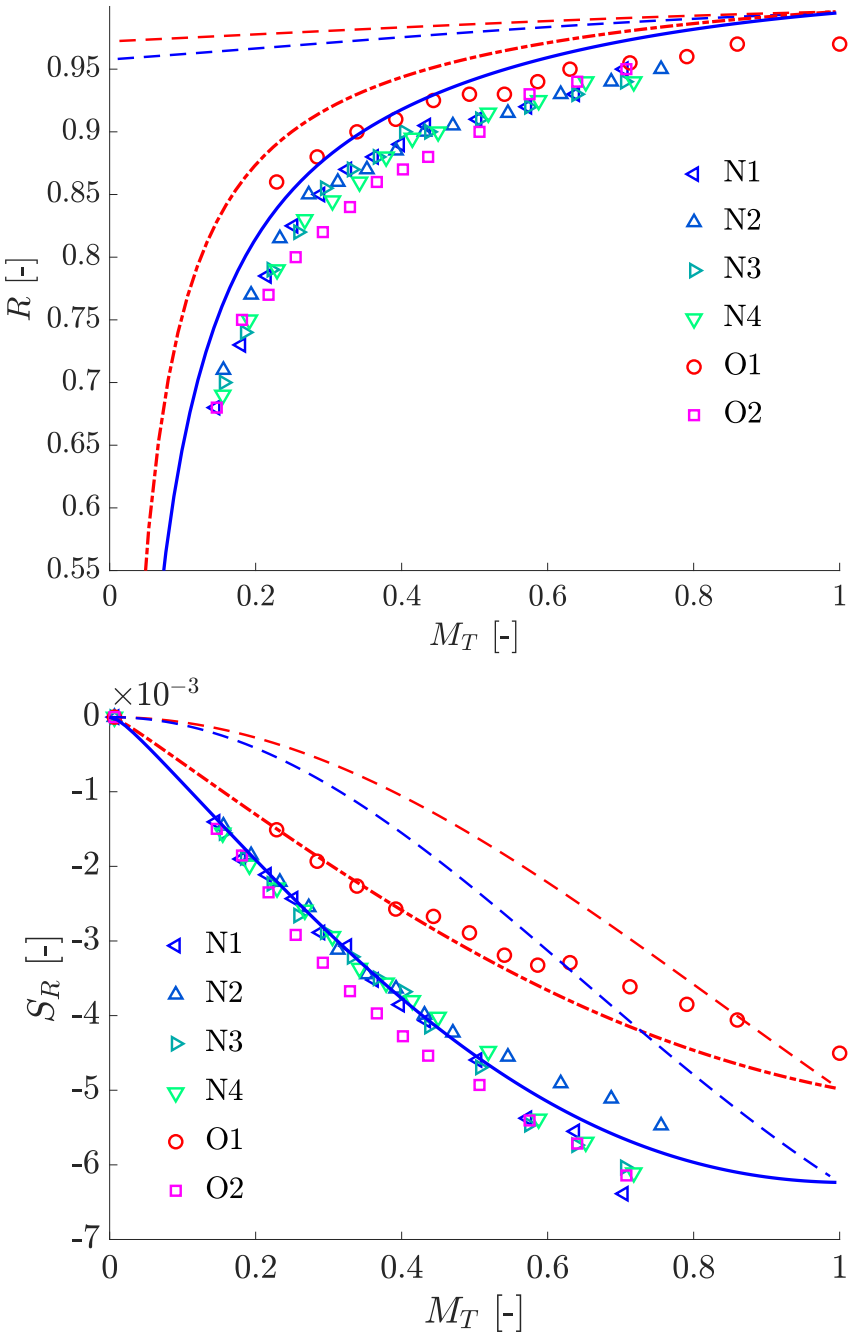

Fig. 5.15 Reflected direct (top) and indirect noise (bottom) in a converging shape termination. Experimental points: orifices (circles) and convergent nozzles (triangles) (see table 4.1 for the meaning of colours and symbols). Solid lines: non-isentropic nozzle predictions; dashed lines: isentropic nozzle predictions ($\Gamma = \Gamma_{op}$ for the red lines and $\Gamma = 0.9$ for the blue lines).

5.5 Discussion and further development

The results of this chapter demonstrate how losses in a nozzle should be taken into account to correctly predict its acoustic and entropic transfer functions. Due to the low frequency response of the excitation source, only the quasi-steady case is considered here. The zero-frequency case captures the physics of the phenomena, but results at frequencies closer to the characteristic frequencies of combustion chambers are needed to understand the importance of indirect noise in real systems. Previous analytical, numerical and experimental studies had already validated both the isentropic and non-isentropic acoustic transfer functions of jump conditions, at low and high frequency [65, 199, 119]. However, there was still no description in the literature of the entropy-to-sound conversion occurring in non-isentropic acceleration/deceleration regions. Thus, this is the first description of indirect noise generated in a nozzle with losses.

This model can be extended to higher frequencies by discretising the nozzle domain into smaller segments, as previously done for the isentropic cases in [155, 62]. However, fluid dynamic simulations might be needed to properly capture the actual flow behaviour and obtain realistic values for the pressure and velocity of the flow in the non-isentropic section. In fact, low order models might not be able to describe the development of pressure losses and flow recirculation zones. In addition, the current model considers only subsonic-to-sonic nozzles. Aero-engines normally operate with subsonic to sonic flow; however, there might be some applications in which the flow is accelerated to supersonic speed. Extending the model to supersonic isentropic nozzle flows is relatively straightforward [147], but, if shock waves develop, the analytical description of supersonic nozzles becomes more complicated [147, 110]. In particular, both shock waves and pressure losses will arise in the divergent part of the nozzle, making the behaviour of the flow complex to predict and analyse. The quasi-one dimensional hypothesis might no longer be valid, and more sophisticated 2D or 3D simulations might be required to properly capture the acoustic and entropic transfer functions of the system.

The major complication still remains the validations of these models against experimental data. It is extremely challenging to probe entropy spots after they enter the acceleration region, as there are no experimental tools to visualise what happens to the entropy blob once it starts being accelerated in a nozzle. Indeed, the phase and amplitude characteristics of the generated indirect sound is closely related to the amplitude and shape of the incoming entropy spots.

This will be the focus of the upcoming chapters.

5.6 Conclusions

In this chapter, we introduce a parametric model to predict the quasi-steady acoustic and entropic transfer functions of nozzles with pressure losses. This model extends the isentropic formulation to non-isentropic flow behaviours in subsonic-to-sonic throat conditions. Three cases known in the literature are recovered as limit conditions of the model: the isentropic nozzle (area jump without losses in the total pressure), the orifice plate (area jump with the highest level of total pressure losses in the diffuser section), and the convergent nozzle terminating a duct, which can be treated as a orifice plate expanding in an open environment. The analytical formulation of the entropy-to-sound conversion coefficient for isentropic nozzles can be found in the literature, however, the entropy-to-sound conversion under dissipative conditions (orifice plates and converging shapes) was not previously investigated.

The present model covers the intermediate situations between an isentropic nozzle and a non-isentropic orifice plate, where the flow in the diffuser is not fully isentropic. Measured static pressure losses are used to determine the dynamic parameter for isentropicity in a nozzle subjected to low frequency perturbations. The non-isentropic model not only captures the experimental results well, but also succeeds in bridging the subsonic to sonic transition regime across the nozzle, where the isentropic predictions fail. In the specific geometry analysed, the isentropic theory grossly underestimates the amplitude of the indirect noise generated, and overestimates the reflected direct noise. These results emphasise how the dissipation of the acoustic energy in a system should be accounted for to correctly predict the nozzle behaviour in a non-isentropic environment. These considerations become important in understanding how to attribute and remedy instabilities in real systems, where direct and indirect noise are mixed in the acquired pressure traces. The present approach suggests a more accurate method for estimating the actual reflected and transmitted indirect noise under the quasi-steady assumption.

Chapter 6

Laser-based time resolved measurements of temperature and density

Many fundamental processes in gas dynamics, such as supersonic/hyper-sonic flow, combustion, turbulence, aero-acoustics, and plasma physics, occur on time scales of microseconds or less. This poses significant challenges for making accurate measurements of the quantities of interest, as repetition rates of the order of 10^4-10^6 Hz are needed to capture the relevant dynamics. Optical and spectroscopic techniques, in particular laser-based, are normally used to perform non-intrusive, in-situ diagnostics. In the last decades, the improvement in the instrumentation has opened up for temporally and spatially resolved measurements of extreme dynamics and complexities. Robust lasers with high pulse energy, ultra-short pulse duration, and high repetition rate, along with ultra-fast, high sensitivity cameras and detectors have been developed. Unfortunately, high speed measurements of species, temperature, and density in turbulent combustion and high-speed reactive flows are extremely challenging, so that only a few techniques are capable to probe these scalars with the needed accuracy and precision. As illustrated by the previous chapters, one example appears in the need for measuring the passage of entropy or compositional spots with millisecond resolution in order to identify the source of indirect noise. This thesis contributes to the development of Laser-Induced Grating Spectroscopy (LIGS) as a non-intrusive, high repetition rate technique to time and space resolve temperature and composition variations in reacting flows. Our goal is to demonstrate that LIGS is a suitable candidate to probe the amplitude and strength of the unsteady entropy and composition spots produced at the flame location and then accelerated through the gas turbine in a combustion chamber.

6.1 High repetition rate diagnostics for temperature and density measurements in reacting flows

Modern research into turbulent and unsteady combustion relies on the physical, mathematical and numerical modelling of the underlying processes. Experimental data is eagerly sought to assess, validate and improve these models. Techniques that do not employ lasers are normally simpler and cheaper, but they are often less versatile and more intrusive. Laser based techniques, instead, allow non-intrusive time and space resolved measurements with more accuracy and precision. Different techniques can be performed simultaneously to correlate the scalar and vectorial quantities of interest. However, laser diagnostics often require more complex and expensive experimental set-ups and data analysis and a clear optical access to the flow.

For the purpose of measuring entropy and composition spots in reacting flows, a technique that can detect and time resolve temperature and composition variations in high pressure-high temperature environments is needed. The characteristic frequencies typical of indirect noise are of the order of hundreds of Hertz, therefore sampling rates of at least 1 kHz are necessary to properly capture the phenomena. The goal of this chapter is to consider and lay out Laser-Induced Grating Spectroscopy (LIGS) as a potential candidate. In this introductory chapter, we give a brief overview on the main techniques suitable to probe unsteady temperature and composition variations, listing their advantages and disadvantages and highlighting their relevant previous applications in combustion diagnostics (Sec. 6.1.1 and 6.1.2). LIGS is then introduced and discussed more in detail. After a brief literature overview (Sec. 6.2), we describe the signal formation, the alignment procedure and the data analysis (Sec. 6.3) more in depth.

6.1.1 Non laser-based diagnostic techniques

Temperature and composition measurements in reacting flows without using lasers are usually simpler and cheaper, but the data is normally less accurate and less precise. Various techniques have been employed to detect temperature and density variations in combustion environments; here we recall thermocouple and anemometer measurements, acoustic attenuation measurements and scattering and shadowgraphic measurements. Physical probes, such as thermocouples and anemometers, are inexpensive and easy to use, but they might significantly alter the measurement region due to their obstruction to the flow. Moreover, probes suffer from limited time response due to their inertia [11, 84] and might not survive the elevated temperatures. Acoustic source-receiver measurements have been employed

for detecting the passage of entropy spots, allowing a tomographic reconstruction of the temperature field [212, 211], but they involve a complex set-up with many microphones and electrodes connected to a combustor section. Scattering and shadowgrafic measurements (such as schlieren, background oriented schlieren, etc.) can detect density changes in the flow with good time resolution, but they only offer qualitative line-of-sight measurements. Further, such methods significantly degrade within turbulent combustion environments [68], even if recent improvements to background oriented schlieren have demonstrated capabilities to deliver more quantitative information in high temperature or compressible flows [169, 213].

6.1.2 Laser-based diagnostic techniques

Various laser diagnostics techniques can probe temperature, density and composition in reacting flows with different level of spatial resolution, precision and accuracy. A distinction is commonly made between the so-called *linear* and *non-linear* techniques. This nomenclature arises from the interaction of the incident light with the medium under investigation. Generally speaking, the polarisation $P(\omega)$ induced in the medium by the incident electric field $E(\omega)$ can be expressed as:

$$P(\omega) = \varepsilon_0 \left(\chi E(\omega) + \chi^2 E(\omega)^2 + \chi^3 E(\omega)^3 + ..\right) \tag{6.1}$$

where ε_0 is the permittivity of the free space and χ^n is the n^{th} order in the expansion of the electric susceptivity of the medium. Linear techniques normally rely on the interaction between the medium and a single incident photon, which is typically either absorbed or scattered. This effect is usually obtained for a low amplitude of the incident electric field. Instead, non-linear techniques require the interaction of multiple photons with the medium simultaneously, as described by the higher order terms of the induced polarisation. The second order term becomes zero as gaseous molecules have their centre of symmetry at their centre, and only the third order term is relevant. This means that the electric fields of three incident photons (E_1, E_2 and E_3) are mixed and they induce a polarisation which radiates a *signal* photon (E_4). Therefore, non-linear effects are only seen for very high field strengths, or when a resonance enhances the signals. Higher order effects (>3) are not typically observed.

The most popular linear techniques suitable to time resolve temperature, density or composition variations in reacting flows are Tunable Laser Diode Absorption Spectroscopy (TDLAS), Laser-Induced Fluorescence (LIF), Spontaneous Raman and Rayleigh scattering; while the main non-linear techniques are Coherent Anti-Stokes Raman Spectroscopy (CARS) and Laser-Induced Grating Spectroscopy (LIGS).

Linear techniques

Methods using continuous wavelength lasers, such interferometric and laser absorption techniques, derive the local temperature and composition from the attenuation of one or more laser beams through a medium. They can achieve good temporal resolution but lack of spatial resolution for being line of sight measurements [92, 7, 66, 91, 136].

Laser-induced fluorescence is a widely used technique for imaging of concentration or temperature fields. It is based on the excitation of the molecules of a tracer to a higher electronic energy state. When they de-excite, they fluoresce, releasing light at a longer wavelength, whose intensity can be related to the local concentration or the temperature after proper calibration. Spatially and temporally resolved measurements can be obtained [115, 82], but they offer a limited dynamic range and a limited accuracy over a wide temperature range. Moreover, these measurements often require the seeding of a fluorescing species and are affected by radiation trapping.

Rayleigh scattering probes the local number density of molecules in the gas, by scattering a signal which is proportional to the concentration of the species [54]. Provided that the composition is known, the local temperature can be determined. Rayleigh signals are weak: after the laser excites the molecules in the medium, the light is scattered in all directions, so the receiver collects only a small percent of the total energy. High frequency Rayleigh scattering measurements have been made, but they were characterised by a low signal-to-noise ratio [210, 23, 170]. More importantly, reflections by surfaces and particles limit the accuracy, so that measurements in sooty or enclosed environments are severely challenged. Filtered Rayleigh Scattering (FRS) [150] has been developed to suppress the background noise: the light is filtered using a cell containing a vapour (such as iodine for 532 nm wavelength), which absorbs the stray light coming from the reflections on particles and surfaces. FRS allows measurements in enclosed environments, but it requires a highly energetic and narrow line laser.

Spontaneous Raman scattering measures the local concentration of the major species and, if combined with temperature measurements via Rayleigh scattering, the mixture fraction [66, 187]. Raman scattering is characterised by very weak signals, as the Raman cross section is usually three orders of magnitude smaller than the Rayleigh cross section. As a result, Raman experiments often require long acquisition times under exposure and high pulse energies to achieve enough signal-to-noise. Therefore, the data is often phase locked to resolve the features of interest [60], which impedes capturing unsteady phenomena if their characteristic frequencies are not known a priori. The development of pulse burst lasers, which deliver pulses at high energies and at high repetition rate (see Chapter 9) has allowed

single shot, time resolved planar LIF [204], Raman [77] and Rayleigh [164] measurements in reacting flows.

Non-linear techniques

Non-linear optical techniques, such as CARS and LIGS offer local measurements and good signal-to-noise ratio, as they are characterised by coherent (beam-like) signals. To date, CARS is the best established technique for point measurements of temperature and minor species concentration in reacting flows [66, 177]. CARS employs multiple photons to excite the molecular vibrations, and the local temperature is obtained from the CARS scattered signal by fitting a model to its spectrum. In certain cases, spectral information can also provide concentration or number density. CARS measurements have several advantages, such as spectral sensitivity, directionality, low absorption of energy between the lasers and the medium and high spatial resolution. The use of pico- and of femto-second mode-locked lasers has recently allowed the extension of CARS to high repetition rate measurements (up to 100 kHz) [140, 178, 192, 53, 151]. However, CARS requires a complicated and expensive set up, with three narrow-line lasers of different wavelengths carefully aligned, and a complex data analysis. In addition, the accuracy of the measurements deteriorates in pressurised environments, as the generation of spectral lines at pressure is not completely understood, so the model for fitting the CARS spectrum is inherently less accurate.

In contrast, LIGS requires a much simpler set-up and data analysis than CARS, still offering good accuracy and precision. LIGS measures the local speed of sound via a change in the local density induced by opto-acoustic effects, from which temperature and composition can be derived. However, to date, LIGS is not yet well established as a diagnostic technique for pressurised reacting flows. Until the present experiments, there had been no attempts to perform high repetition rate LIGS measurements in flames, due to the lack of suitable instrumentation and limited general understanding of the potential and limitations of the technique. In this thesis, high repetition rate LIGS (1-100 kHz) has been developed, showing its capability to time resolve temperature and composition changes in reacting and non-reacting flows. For the first time, a pulse burst laser is used for LIGS diagnostics, and the advantages and the disadvantages of this application are discussed.

6.2 Laser-Induced Grating Spectroscopy: an overview

Laser-Induced Grating Spectroscopy (LIGS) is a non-linear laser diagnostic technique which measures the local speed of sound using the modulation frequency detected from probing a laser-induced transient grating. LIGS signals are based on opto-acoustic effects which

arise from the interaction of the local medium with a stationary grating generated from the interference of two pulsed laser beams [39]. LIGS signals can be generated either by a resonant (wavelength coincident with an absorption line) or a non-resonant process. The non-resonant process arises from an electrostrictive interaction named Laser-Induced Electrostrictive Grating Scattering (LIEGS), whereas the resonant process arises from resonant absorption of the radiation energy, leading to Laser-Induced Thermal Grating Scattering (LITGS). In the presence of strongly absorbing molecules, the energies required to generate the thermal gratings are normally one order of magnitude lower than those needed to generate the electrostrictive gratings. Although LITGS typically offers a higher signal-to-noise ratio than LIEGS, its main limitation is the need for sufficiently large concentrations of a resonant species at the available pump laser wavelength.

6.2.1 LIGS: literature review

Laser-induced spectroscopy using transient gratings was initially developed in crystallography to probe excited states in the bulk of molecular crystals [181, 182, 161]. Later, LIGS was applied to the condensed phase to detect a wide variety of chemical, physical and biological processes [70]. LIGS was used in biological fluids (vitreous, eye lens, blood) to measure thermal diffusivity, speed of sound, temperature and attenuation coefficient [28, 125, 148, 87].

However, LIGS has found most of its applications for diagnostics in the gas phase. One of the first uses of picosecond grating detection in gases was performed by Rose et al. [176] in sodium vapour, demonstrating the potential of the technique for combustion and plasma diagnostics. Govoni et al. [88] obtained transient resonant and non-resonant LIGS signals in an air-water mixture. By varying the pump laser wavelength, the laser line could be tuned to and away from one absorption line of the mixture, obtaining thermal and electrostrictive gratings, respectively. After these first experimental studies, more rigorous models of the signal were developed, and LIGS started being applied to hypersonic and reacting flows. Cummings et al. [39, 40] derived and experimentally validated an analytical model for LIEGS based on the linearised equations of hydrodynamics and light scattering, while Paul et al. [165] described the theory underlying the formation and evolution of LITGS. Electrostrictive measurements were made in non-reacting flows to probe the local gas temperature [189, 191], species concentration [39] and flow velocity [98, 99]. Furthermore, simultaneous measurements of temperature and flow velocity [98, 93, 123] were obtained successfully. LIEGS was later applied to probe mixing of jets [72] as well as the gas temperature in supersonic wind tunnels [184].

For diagnostics in reacting flows, thermal LIGS (LITGS) is usually preferred to electrostrictive LIGS, due to lower pump laser energies normally required and the higher signal-

to-noise ratio achievable. To date, LITGS has been demonstrated in reacting flows to measure temperature, pressure, velocity and species concentration [126, 209, 193, 215]. Thermal LIGS requires either tuning the laser wavelength to an absorption line of the flow or adding an absorbing species to the mixture. On the one hand, many tracer species might not survive the high temperatures of the combustion environment, or they might perturb the flow if added in a non-negligible amount. On the other hand, matching the pump wavelength to an absorption line of the flow poses stricter requirements on the lasers that can be used in the experiments. Only few pulsed lasers have both a suitable wavelength to excite species surviving in reacting flows and a suitable pulse shape and energy for LITGS. The use of dye lasers increases the wavelength flexibility, but also the complexity and cost of the optical set-up. A common LIGS application is the use of a dye laser at 308 nm as pump to excite the OH radicals produced by hydrogen or methane flames [216, 126, 94]. Fourkas et al. [74] seeded sodium atoms into hydrogen and methane flames and employed two picosecond lasers at 589.6 and 589.0 nm to resonantly probe the flow. Williams et al. [215] measured the temperature in a firing GDI optical engine using the fourth harmonic (266 nm) of a Nd:YAG laser, by adding acetone to the combusting flow. Luers et al. [141] used the second harmonic of a Nd:YAG laser to probe temperature of NO_2 doped flames in a self-pressurised vessel. Adding tracer molecules to the flame, however, usually limits the applicability of the technique: for example, acetone does not survive at elevated temperatures, while experiments with NO_2 are dangerous. Ideally, one would like to use the molecules naturally produced by the flames to simplify the measurements. Water is naturally present in the burnt gases of many flames, but its absorption lines are difficult to access. Hell et al. [95, 96] utilised the weak absorption band of water around 1 μm to obtain LITGS in a hydrogen/air flame at atmospheric pressure using the fundamental output of a Nd:YAG laser. Energies of 110 mJ per pulse were required (one order of magnitude more than those normally used for thermal LIGS measurements), but the acquired signals had a low signal-to-noise ratio and only few peaks that were damped out almost immediately. The small number of peaks did not allow a frequency based analysis, so a calibration algorithm was developed to fit a modelled signal to the acquired time traces. Hemmerling et al. [97], instead, took advantage of the ro-vibrational transition of water around 820 nm with a dye laser as pump. Sahlberg et al. [179] accessed the strong absorption lines of water and hydrocarbons at 3 μm in ethylene/air flames. They started from a 1064 nm Nd:YAG laser and utilised a series of dye and doubling crystals until reaching a pulse wavelength of 3 μm and a pulse energy of 7 mJ. Another suitable natural absorber in flames is soot, which acts as a black body and can absorb the laser energy and generate the thermal grating if sufficiently high energies are delivered by the pulses [26, 100].

However, a systematic investigation of LIGS in sooty environments has not yet been carried out.

Towards high repetition rate LIGS measurements

One of the main limitations of the LIGS experiments described above is the lack of temporal resolution. Relatively high pump pulse energies were used to generate the gratings, which could be delivered only by low repetition rate lasers. In fact, there is a trade-off between the energy per pulse that a laser can deliver and the frequency of the pulses, due to the necessity of cooling the internal parts. Lower pulse energies are usually delivered at higher repetition rates (order of kHz), while higher pulse energies can be delivered only at low repetition rates (order of Hz). Initially, it was believed that the pulse energies of high repetition rate lasers were not sufficiently high to generate detectable thermal LIGS signals. However, Forster et al. [73] demonstrated LITGS at 10 kHz in a transient non-reacting flow using 8 mJ per pulse delivered by the second harmonic of a high speed Nd:YAG PIV laser. They seeded the flow with NO_2, which absorbs 532 nm light, and measured the unsteady changes in the temperature due to a sudden gas expansion. This work opened up the possibility of high repetition rate LIGS to detect and time resolve unsteady phenomena in flows. At the state of the art, however, high repetition rate LIGS measurements have not been applied yet to thermoacoustics and reacting flows. The main issue is the requirement of lasers delivering short pulses (less than 10 ns) with sufficiently high energies and a wavelength matching an absorption line of the flow. In this work we demonstrate that this can be achieved by using the weak absorption line at 1064 nm of water and a pulse burst Nd:YAG laser in the fundamental harmonic.

6.3 LIGS: operating principles and experimental methods

This section presents details of the operating principles and experimental approach of LIGS. A general overview of the optical geometry and essential experimental requirements for LIGS measurements (including a typical optical geometry and signal acquisition equipment) are given, along with details of the alignment procedure and data processing approach employed in this work. The specific optical parameters and essential features of the equipment used in each experiment are presented in greater depth in the corresponding chapters.

6.3.1 Signal generation

In this section we describe the generation of LIGS signals (Fig. 6.1). In a typical LIGS experiment, two parallel, polarised, coherent pulsed pump laser beams from the same laser source are crossed at an angle θ to generate an interference pattern within the crossing volume, called a grating, of spacing Λ (Fig. 6.1a). The value of Λ is determined by the crossing angle and the laser wavelength λ:

$$\Lambda = \frac{\lambda/2}{\sin(\theta/2)} \tag{6.2}$$

The interaction between the medium and the radiation in the interference pattern generates, in general, both resonant and non-resonant processes (Fig. 6.1b). The non-resonant process arises from an electrostrictive interaction and leads to LIEGS, whereas the resonant process arises from resonant absorption of the radiation energy, leading the generation of a thermal grating, thus enabling LITGS. The electrostrictive interaction involves the polarizability of the molecules such that they are driven towards the regions of higher electric field intensity. The work done by the electric field compresses the flow adiabatically, and the resulting pressure perturbation drives two oppositely propagating acoustic waves, which form a travelling density perturbation oscillating in time at a frequency determined by the transit time of the sound waves across the grating wavelength. The variation of density associated with an acoustic wave (i.e. the adiabatic density modulation), causes a variation of the real part of the complex refractive index which acts as a phase grating [39, 40, 109, 190]. The resonant process requires that the wavelength of the incident pump light corresponds to a spectral absorption in some molecular species of the gas. Molecular excitation is higher in corresponding regions of high field intensity in the interference (grating) pattern. The absorbed energy is subsequently released by collisional quenching processes, resulting in localised perturbations in the temperature and density in the form of a thermal grating. The latter modulation is also accompanied by associated pressure and density waves, which interact periodically in and out of phase with the temperature grating, and can be detected as a locally varying field. The matter of which the resonant or non-resonant processes dominate depends upon the properties of the incoming light and of the species present in the interaction region. In strongly absorbing media (with respect to the pump laser wavelength used), the thermal grating process usually dominates, leading to LITGS signals which can usually be observed using relatively low pump energy pulses (1 to 10 mJ) [184]. Electrostrictive gratings do not require an absorbing species, and can be induced by non-resonant wavelengths, but since they are normally orders of magnitude weaker than the thermal gratings, much higher energy pulses (around 100 mJ) are required to obtain detectable scattered signals [39, 184].

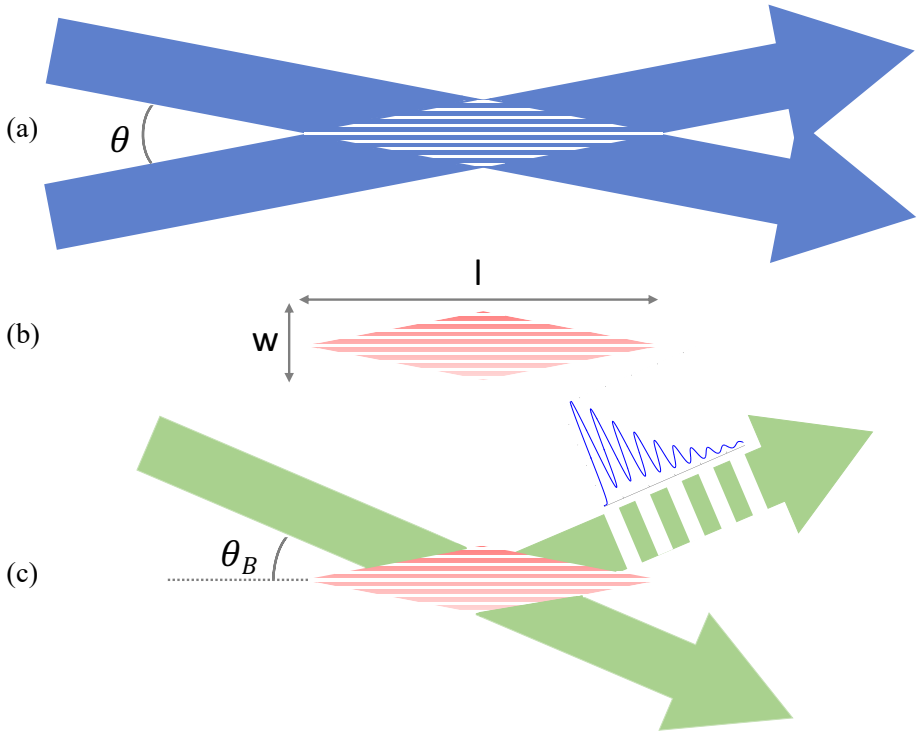

Fig. 6.1 Formation of the LIGS signal: generation of the stationary grating (a); interaction between the stationary grating and the medium (b); Bragg-scattering of the probe beam encoding the signal (c). θ: crossing angle; θ_B: Bragg angle; l: probe volume length; w: probe volume width.

Electrostrictive signals can often be distinguished by their prompt appearance, in contrast to thermal gratings, which have a time lag as they are only generated following the transfer of stored electronic energy to heat. Although the LITGS technique offers significantly higher signal-to-noise ratio than LIEGS, its main limitation is the need for a sufficient concentration of a resonant species at the available wavelength. Both techniques benefit from the higher densities available in experiments at higher pressures.

The signal generated in the probe volume is extracted by a coherent probe beam of wavelength λ_{pr} incident at the appropriate Bragg angle θ_{B} to the grating:

$$\theta_{\mathrm{B}} = \sin^{-1} \frac{\lambda_{\mathrm{pr}}}{2\Lambda} \tag{6.3}$$

The Bragg-scattered light encodes the LIGS signal, which oscillates with the frequency modulating the grating density (Fig. 6.1c).

As the propagating waves in the grating move at the local speed of sound c, the modulation frequency of the scattered signal is determined as:

$$f = n\frac{c}{\Lambda} = 2n\frac{c}{\lambda}\sin\frac{\theta}{2} \tag{6.4}$$

where the factor $n = 1$ for thermal gratings and $n = 2$ for electrostrictive gratings, depending on whether the process is non-adiabatic (thermalisation) or adiabatic (electrostriction). The speed of sound is related to the local temperature and mixture bulk properties. Assuming an ideal gas equation of state, the local temperature can be obtained from the oscillation frequency of the LIGS signal as:

$$c^2 = \frac{1}{n^2}f^2\Lambda^2 = \frac{\gamma RT}{W} = \frac{\gamma p}{\rho} \tag{6.5}$$

where γ is the ratio of specific heats, R the universal gas constant, W the bulk molecular weight of the mixture, and p, T, and ρ the local pressure, temperature, and density, respectively. From Equation 6.5, the local speed of sound is proportional to the measured frequency. Further information about the local pressure, density and concentration of the absorbing species can be extracted from other features of the signals [165, 40, 116, 26]. For example, the decay rate of the grating, and therefore the total number of ringings, depends on the diffusion rate of the molecules, which acts to equilibrate the initial density perturbation, so it can be related to the local pressure and density. For thermal gratings, the local concentration of the absorber determines the amount of energy absorbed in the probe volume. Greater heat deposition leads to higher density modulation, causing stronger signals. Instead, the quenching characteristics of the absorber (e.g. time needed to release the stored energy) influence the initial rising slope and contrast of the signals. In hybrid LIGS signals in a propane/air non-reacting mixture (signals displaying both the electrostrictive and thermal contributions), Kiefer et al. [116] showed that the ratio of the thermal to electrostrictive peaks is correlated with the local concentration of propane, which weakly absorbs 1064 nm wavelength light. In this thesis, with a similar analysis, we determine the local water concentration in the products of non-sooty flames using the signals generated with 1064 nm light (Chapters 8-9). All this information is useful to evaluate the contribution of temperature or composition variations in complex flows when they change simultaneously. However, a set-up dependent calibration is needed to relate these features of the signals to physical quantities, as shown in Chapters 8-9. In fact, also the shape, amplitude and duration of the pump pulses affect the rising time, amplitude and contrast of the signals [190]. The analytical expressions describing how these effects influence the formation of LIGS signals can be

found in previous work [40, 165, 190, 214]. As they go beyond the scope of this thesis, they are not shown here.

6.3.2 Lasers and optical layout

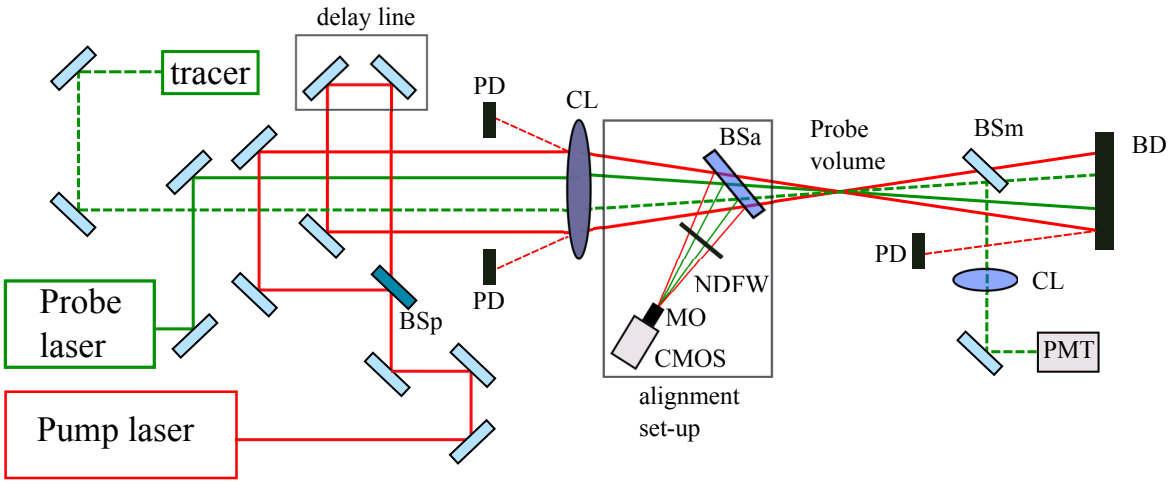

Fig. 6.2 Generic optical layout of a LIGS experiment. BSp: beam splitter; CL: crossing lens; BD: beam dump; BSa: beam sampler; NDFW: neutral density filter wheel; MO: microscope objective; CMOS: CMOS Camera; BSm: harmonic beam splitter; PMT: photomultiplier; PD: photodiode.

The LIGS experiments described in this thesis were done using three different optical tables, which are briefly described at the beginning of each chapter before the respective results. The main hardware components of the apparatus used in each experiment are summarised in Table 6.1. Fig. 6.2 shows a generic LIGS optical table, resembling the one used for the experiments in Chapter 8 and 9, where the beams are crossed in a folded boxcars forward arrangement. Two laser sources are needed: a pulsed laser is used as pump to generate the stationary grating, while a continuum wave laser is used as probe and scatters off the grating, producing the LIGS signal. Alternatively, a pulsed beam can be used as probe [193, 217]. A tracking beam, usually generated from a low power diode laser, identifies the Bragg-scattering direction for aligning the collection optics.

To generate the crossing geometry in Fig. 6.1, the pump beam is at first directed through a 50/50 beam splitter (BSp), creating two beams of equal intensity. High reflective mirrors are used to make these two beams parallel. As a first step, the two beams should be synchronised in time to ensure that they reach the probe volume simultaneously. Stampanoni-Panariello

	Chapter 7	**Chapter 8**	**Chapter 9**	**Appendix A**
pump laser	Edgewave IS200-2-L	Continuum Powerlite DLS9010	QuasiModo Spectra Physics	Edgewave/ Continuum Surelite III-10
λ pump	355 nm	1064 nm	1064 nm	355 nm
pump frequency	0.5-1 kHz	10 Hz	100 kHz	10 Hz - 1 kHz
probe laser	CNI MLL-III-671	Coherent Verdi G	Coherent Verdi G	CNI MLL-III-671
λ probe	671 nm	532 nm	532 nm	671 nm
oscilloscope	LeCroy 6104A	Keysight DSOS804A	Keysight DSOS804A	LeCroy 6104A
photomultiplier	Hamamatsu H6780-20	Hamamatsu H10721-20	Hamamatsu H10721-20	Hamamatsu H6780-20

Table 6.1 Summary of the hardware components used in the LIGS experiments described this thesis.

[190] demonstrated that the coherence of the two beams strongly affects the amplitude of the signals. A time delay of 20 pico-seconds between two 10-ns width Gaussian beams reduces the intensity of the stationary grating by one order of magnitude and, consequently, the strength of the signal. Thus, the time and phase shift between the two pulses should be minimised, especially for multimode beams, which have a shorter coherence length. In Figure 6.2 an adjustable delay line is added in the path of one of the two beams, allowing an accurate control of the synchronisation. Two co-planar photodiodes (PD), connected to an oscilloscope, are used to monitor the beams at the crossing lens location. The delay line is manually adjusted in real time by looking at the outputs of the photodiodes on the oscilloscope, until reaching a good time overlap of the crests of the two beams. A simpler, but less accurate, synchronisation strategy consists in the addition of delay compensator lenses in the path of the pump beams (Chapter 7). This might not lead to a perfect time overlap, but improves the compactness of the optical table, reducing the number of mirrors needed.

After synchronising the two pumps, the four beams have to be mutually positioned, which is achieved by using two identical masks (Fig. 6.3). These masks are positioned in the near

field and far field with respect to the measurement zone, acting initially as alignment guides to obtain four parallel beams in the desired configuration. The beams are mutually crossed using a crossing lens (CL), generating the probe volume. Pump and probe beams are then damped, while the signal beam is collected with a detector. The alignment masks used the experiments of this thesis are shown in Fig. 6.3: one for experiments with a 355 nm pump and a 671 nm probe lasers (Chapter 7 and Appendix A); the other one for experiments with 1064 nm pump and 532 probe lasers (Chapter 8 and 9). To determine the layout of these masks, at first the distance d_{pu} between the two pump beams is chosen. The crossing angle θ becomes $\theta = \tan^{-1} d_{\mathrm{pu}}/f_l$, where f_l is the focal length of the crossing lens. From the knowledge of θ, the grating spacing Λ is determined from Eq. 6.2, while the corresponding Bragg angle θ_B is determined from Eq. 6.3. This defines the horizontal position of the probe beam on the mask which ensures that the beam hits the grid at the Bragg direction. This distance d_{pb} of the probe beam from the centre of the mask is evaluated as $d_{\mathrm{pb}} = f_l\, tan(\theta_B)$, where f_l is the focal length of the lens. The vertical position of the probe beam on the mask is instead a free parameter. In the first mask (355 nm pump-671 nm probe), the pump and the probe beams are non-coplanar. This layout complicates the alignment of the beams through curved surfaces, such as cylinders and tubes, as the direction of non-planar beams might be significantly distorted when passing through the curved walls. However, it simplifies the separation between signal beam and pump beams in the collection plane, as the two pumps can be dumped in a lower plane without blocking the signal beam. Instead, the pump and probe beams are co-planar in the second mask (1064 nm - 532 nm). A selective beam splitter (reflection of 532 nm light, transmission of 1064 nm light, BSm in Fig. 6.2) is needed to separate the signal beam from the pump beams after the measurement location. The signal beam is re-collimated with a converging lens CL and then sent to a photomultiplier (PMT). Whilst it is possible to use fast-response photodiodes for acquiring strong signals [215], PMTs are preferred as they offer a much higher signal-to-noise ratio. PMTs are also advantageous as they are composed of sufficiently large active collection areas, such that the whole signal can be collected without employing a focusing lens to collimate the signal onto a small detection region. This reduces the amount of scattered light entering the detector. Whilst the wavelength of the probe beam is selected to be different to that of the pump beams in order to spectrally isolate the signal, the PMT is normally sensitive to both wavelengths. Hence, filters are placed in the path of the signal beam to block scattered light from the pumps. The acquisition of the signals with the oscilloscope is triggered by the laser pulses, which are acquired with a fast response photodiode. The signals are stored in the oscilloscope in binary form, which was found to be the fastest way to save them and read them with Matlab, used for processing the data.

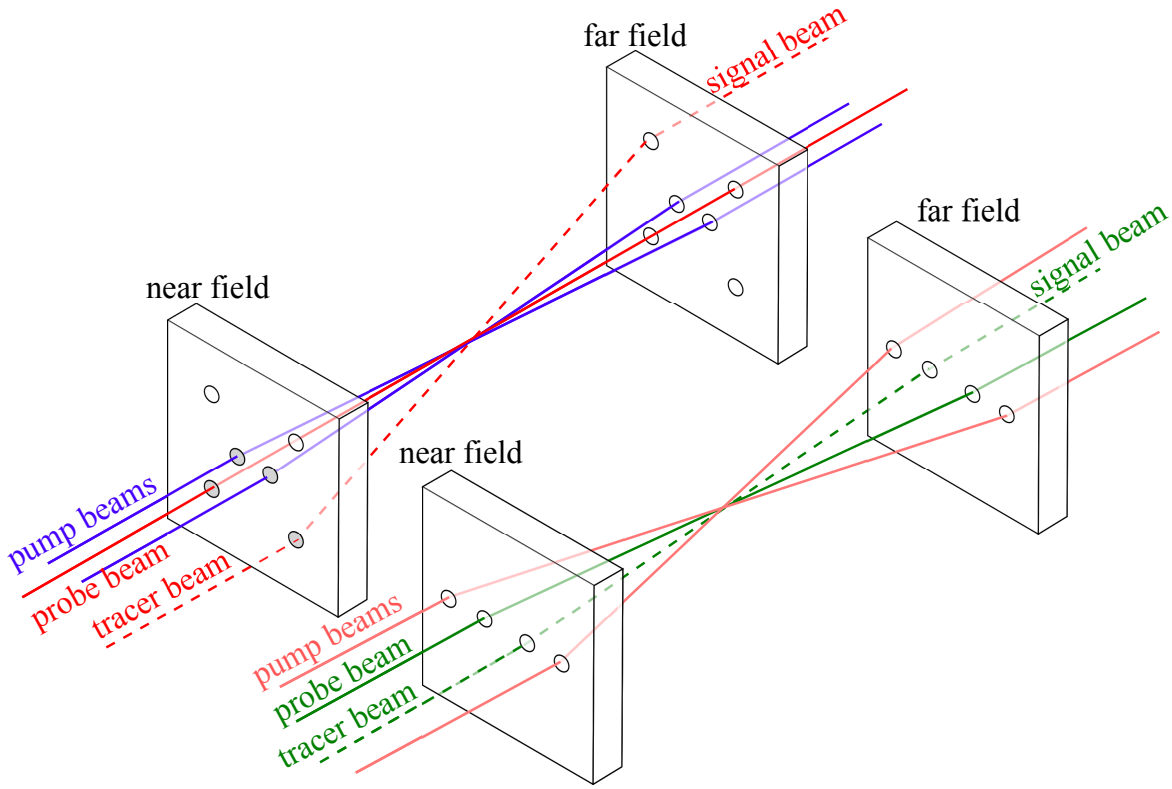

Fig. 6.3 Illustration of the geometry of the beams crossing at the probe volume with the masks used in the experiments described in this thesis: 355 nm pump - 671 nm probe, non-coplanar beams (left); 1064 nm pump - 532 nm probe, co-planar beams (right).

6.3.3 Alignment of the beams in the probe volume

Careful alignment is required to obtain good spatial overlap between the two pump and the probe beams, ensuring that the grating is produced in the intended measurement location and that the probe beam scatters off the grating at the Bragg angle. Here we describe the complete alignment procedure recommended to obtain strong and stable LIGS signals (Note that variations of this procedure were followed in each experiment described in this thesis). As a first step, the mutual position of the beams has to be adjusted after they are crossed to overlap them, due to the chromatism of the crossing lens,: beams of different wavelengths have their focus and their intersection at slightly different axial locations. A pinhole on a two-axis manual traverse stage is positioned at the crossing point of the two pump beams to define the location of the probe volume. Initially, the probe and tracer beam do not pass through the pinhole, so their far field mirrors are adjusted until they pass through it. This roughly ensures that the four beams meet at the same point. However, to fine-tune their overlap, the probe volume should be imaged using a system of mirrors, lenses, filters and

Fig. 6.4 Stationary grating generated by the pump beams imaged by the CMOS camera. Grid spacing is approximately $\Lambda = 16\ \mu$m.

a camera. In the set-up shown in Fig. 6.2, a 10:90 reflection/transmission beam sampler (BSa) attached to a magnetic base is inserted in the path of the four beams, right before the probe volume, to mirror the crossing point while reducing the intensity of the beams. The sampled beams are further attenuated using neutral density filters (NDF). The reflected probe volume is then enlarged via a microscope objective (Edmund Optics-10 X) and imaged using a CMOS Camera (Thorlabs DCC1545M) connected to the computer. This procedure has several advantages: at first, the spatial resolution can be improved by ensuring that the pump beams cross exactly at their waist (the point where the converging beams have their smaller diameter), obtaining a smaller probe volume. Further, it allows one to quickly check the overlap of the beams before starting any new acquisition: the mirror on the magnetic base can be easily added/removed before starting a new experiment, without affecting the alignment.

Probe volume characteristics

Figure 6.4 shows the stationary grating imaged by the CMOS camera. The grating is generated from the overlap of the two 1064 nm pump beams with a crossing angle $\theta \simeq 3.81°$, obtaining a grating spacing of approximately $\Lambda = 16\ \mu$m.

Following the Gaussian approximation, the beam diameter at the focal point is:

$$d_f = M^2 \frac{4 f \lambda}{\pi d_0} \tag{6.6}$$

where d_0 is the initial beam diameter before the converging lens and M^2 takes the divergence of the beam into account. If we initially neglect the Gaussian shape of the beams at the crossing location, we obtain the three dimensions of the probe volume as follows (See Fig. 6.1):

$$l = \frac{2d_f sin\left(\frac{\pi}{2} - \frac{\theta}{2}\right)}{sin\theta}; \qquad w = \frac{2d_f cos\left(\frac{\pi}{2} - \frac{\theta}{2}\right)}{sin\theta}; \qquad h = d_f \tag{6.7}$$

where l, w and h are the length, width and thickness of the probe volume respectively. The total probe volume can be computed as:

$$V = 0.5lwh \tag{6.8}$$

However, the intensity of the stationary grating is stronger at the core of the rhomboidal intersection, due to the Gaussian shape of the beams. To account for this, we evaluate the length of the probe volume as $l' = 0.8l$ (where the value 0.8 is used as it is typical of four wave mizing experiments). This length should be large enough to obtain signal, but sufficiently small to avoid spatial averaging of the temperature over inhomogeneous regions and ensure that measurements are accurate (see Appendix A). In the experiments described in this thesis, the flow properties in the probe volume are assumed to be uniform. In addition, the PMTs used for acquiring the LIGS signal have a cross section of 8 mm and integrate all the incident light. Instead, Willman et al. [218] demonstrated that, by using an optical fiber array, the spatial distribution of the speed of sound along the length of the probe volume can be detected, despite the measurements losing accuracy for the reduced signal-to-noise ratio.

6.3.4 Extraction of the oscillation frequency

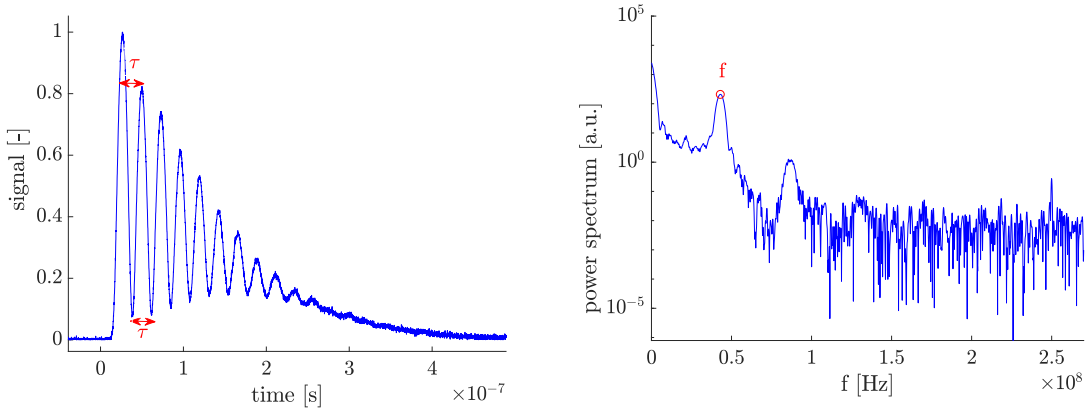

Fig. 6.5 LIEGS signal in air obtained for a grid spacing $\Lambda = 16\mu$m (left) and corresponding power spectrum (right).

Figure 6.5 shows a LIEGS signal corresponding to the speed of sound in air at room temperature and grating spacing of 16 μm (generated from the stationary grating shown in Fig. 6.4). The oscillating behaviour can be clearly identified in the time trace. Three different strategies have been used in the literature for extracting the oscillation frequency from the signals to determine the local speed of sound: evaluation of the time separation between peaks and valleys of the signal, extraction of the frequency from the power spectrum of the signal and data fitting.

The average time separation $\bar{\tau}$ between the peaks and the valleys in the signal can be used to compute the LIGS frequency as $f = 1/\bar{\tau}$. However, this time separation might not be fully representative of the frequency of the oscillations, as other harmonics might sum up and distort the overall shape. Stampanoni-Panariello et al. [190], Lowe et al. [139] used a peak finding algorithm to determine the LIGS frequency, claiming a precision of 0.5 % for strong, clear signals. However, such an approach becomes less robust for weaker signals with lower signal-to-noise ratios and uncertainties in determining the exact time location of the peaks. Moreover, it can be shown that the peak-to-peak and valley-to-valley time separations in the same LIGS signal usually slightly differ from each other. These values are averaged to determine the frequency, but this might lead to inaccuracies if the signal displays a small number of oscillations or if it is highly distorted by noise or misalignment effects.

For signals displaying several ringings, the LIGS frequency can be clearly identified as a peak in its power spectrum obtained with a Fast Fourier Transform (Fig. 6.5, right). The literature indicates that the FFT is the most accurate tool for determining the frequency of a signal . This is the strategy used in this thesis. Each single shot is padded with zeros (more than 2^{21} points) to enhance the frequency resolution in the power spectrum, and a Hanning window is used to smooth out the corners and improve the Fourier transform of the signal[1]. The analysis in the frequency domain is effective when signal-to-noise levels are low and when the uncertainty in determining exact peak locations becomes significant [217]. However, this method can lead to inaccurate results in situations when the signal decays rapidly, displaying only a limited number of oscillations, or the noise has frequencies close to the LIGS oscillation frequency. Accurate measurements in the frequency domain rely on identifying a distinct peak in the power spectrum, which can be broadened by noise or weakened if signals only have a few oscillations. For example, LIGS signals in reacting flows at atmospheric pressure usually decay almost immediately, due to the low density in the probe volume, as shown in Chapter 8. In this case, the power spectrum is ineffective of extracting any frequency information. As both the signal amplitude and the number of ringings increase with the density [39, 190, 165], signals in pressurised environments usually

[1]The Matlab data analysis routine used in this work was partially developed by B.A.O. Williams [214]

display a sufficient number of oscillations to allow an accurate extraction of the frequency using the FFT.

Methods extracting the oscillation frequency only give information about the local speed of sound, while the knowledge on the local composition is needed to determine the temperature. Fitting of the LIGS signal to a theoretical model [165, 40], instead, allows us to determine not only the speed of sound, but also the local temperature, pressure and composition (Sec. 6.3.1), with an achievable precision claimed to be of order 0.1 % [214]. However, fitting routines are computationally expensive and normally require some previous knowledge of the gas in the probe volume. Data fitting algorithms are normally needed for signals which display only few oscillations, as described in Luers et al. [96, 141, 180]. In unsteady or turbulent flows, where the mixture in the probe volume changes substantially from shot to shot, the high uncertainties in the composition of the flow decrease the accuracy in the determination of the flow parameters from a LIGS signal by using fitting algorithms.

6.3.5 Sources of error

In this section we briefly discuss the main sources of error in LIGS diagnostics. The accuracy of LIGS measurements inherently depends on the accuracy in the determination of the oscillation frequency:

$$c \propto f; \qquad T \propto f^2 \tag{6.9}$$

Any uncertainties or systematic errors in the evaluation of this frequency translates into errors in the derived speed of sound and temperature. When the oscillation frequency is extracted from the power spectrum, a sufficient number of ringings in the signal are needed to accurately identify this frequency. It can be demonstrated [55] that the width of the peak representing the LIGS frequency in the Fourier transform Δf is linked to the length of the signal τ_s as:

$$\Delta f \cdot \tau_s \geq \frac{1}{4\pi} \tag{6.10}$$

which gives a conservative estimation on the expected accuracy. In a signal displaying N oscillations (where $\tau_s \simeq N/f_{\mathrm{LIGS}}$), Eq. 6.10 can be re-written as

$$\Delta f \frac{N}{f_{\mathrm{LIGS}}} \geq \frac{1}{4\pi} \rightarrow \frac{\Delta f}{f_{\mathrm{LIGS}}} \geq \frac{1}{4\pi N} \tag{6.11}$$

If a signal has 6 oscillations, $\Delta f / f_{\mathrm{LIGS}} \simeq 1.33\%$. This is a conservative result that can be enhanced by peak fitting on the FFT. However, a short number of oscillations with poor contrast might also lead to a systematic bias in the FFT [55] which cannot be corrected for.

Therefore, care must be taken to use the FFT to analyse LIGS signals with a small number of ringings.

Once the LIGS frequency is extracted, the calibration parameter Λ is required to determine the speed of sound (Eq. 6.4). Λ depends on the focal length, on the distance between the pump beams and on the pump laser wavelength (Eq. 6.2), but pure geometrical evaluation does not allow us to determine the crossing angle and the grating spacing with the required accuracy. The focal length f_l and distance between the pump beams d_{pu} can only be measured with millimetre accuracy, leading to a rough determination of the crossing angle θ and, consequently, of Λ (from Eq. 6.3). It is common practice to perform a calibration LIGS measurement using a gas with a known speed of sound c_{cal} (known temperature and composition). The grating spacing Λ can be derived from the calibration frequency f_{cal} as $\Lambda = c_{cal}/f_{cal}$. This value of Λ is then applied to the measurements with the reasonable assumption that the pump alignment is not altered over the course of the experiments (in Chapter 9 we show a situation in which Λ varies due to the unsteadiness of the laser). Using this calibration, the accuracy of LIGS reflects the accuracy in the knowledge of the calibration speed of sound and in the frequency recovery technique. In LITGS calibration experiments, the effects of the addition of an absorber to the flow should be carefully evaluated, as discussed in Appendix A: even small quantities of the absorbing species can significantly affect the local properties of the flow or can lead to a non-negligible temperature increase (thermalisation) in the probe volume.

Finally, to translate the speed of sound into temperature, the local composition is needed to determine the γ and c_p. These values are commonly extracted from flame simulations, but, in unsteady and turbulent flames, this evaluation might not be straightforward due to the rapid changes of the mixture in the probe volume. Composition uncertainties (W_{der}, γ_{der}) shift the derived LIGS temperature T_{der} from the actual value T_{real} as:

$$T_{\text{der}} = \frac{W_{\text{der}}}{\gamma_{\text{der}}} \frac{\gamma_r}{W_r} T_{\text{real}} \tag{6.12}$$

A final source of error are non-uniformities in the properties of the gas in the probe volume. The folded boxcars arrangement often generates long probe volume in the axial direction, so that they may cover regions with multiple temperature or gas composition. These various contributions are averaged with their relative amplitudes from the detector, as it integrates all the collected light. This averaging effect might lead to substantial misinterpretation of the actual properties of the flow in the probe volume, as shown in Appendix A.

Chapter 7

Measurements of temperature and composition spots with LITGS

In this chapter, LITGS is applied to detect and time-resolve the passage of temperature and composition spots in the Entropy Generator Rig. A 355 nm wavelength PIV laser is operated at 0.5 - 1 kHz to generate the stationary grating. Biacetyl, which absorbs 355 nm wavelength light, is used as an absorber in trace amounts to generate the thermal grating. In an open laminar jet, a feasibility study shows that small ($\simeq 3\%$) fluctuations in the mean flow properties are well captured with LITGS. However, corrections of the mean flow properties by the presence of biacetyl are necessary to properly capture the fluctuations. The actual density and temperature variations in the flow are determined using a calibration procedure validated in the laminar jet flow. Finally, travelling entropy and composition spots in the Entropy Generator Rig are directly measured at different locations along the quartz tube section, obtaining good agreement with the expected values. This study demonstrates that LITGS can be potentially used as a technique to obtain instantaneous, unsteady temperature and density variations in a combustion chamber, requiring only limited optical access[1].

7.1 Introduction

Information about the generation, transport and acceleration of entropy and composition variations in combustion chambers are essential to evaluate the entropy-to-sound conversion and consequently the contribution of indirect noise to the overall combustion noise (Chapter 2). However, there is still little quantitative evidence of the behaviour of travelling entropy and composition spots in reacting flows due to the lack of experimental data [58, 154]. This

[1]The results of this chapter are published in *Journal of Engineering for Gas Turbine and Power* [48]

is mainly linked to the scarcity of techniques capable to probe unsteady temperature and composition changes with the accuracy required for model validation. In this chapter, we demonstrate high repetition rate Laser-induced thermal grating spectroscopy as a technique capable to detect and time-resolve temperature and composition variations in the Entropy Generator Rig. In the experiments described in this chapter, a 355 nm high repetition rate laser is used as pump laser to generate the signal. This laser was the only high speed laser available in the laboratory with the required characteristics: a short pulse width ($<$10 ns) and a sufficiently high energy per pulse (up to 4 mJ per pulse). Biacetyl was found to be the substance which could absorb 355 nm light without being particularly harmful for the human health (apart from producing an unpleasantly strong odour of popcorn which propagated everywhere in the laboratory). The mean flow in the Entropy Generator Rig was seeded with biacetyl, so that travelling entropy and composition spots could be detected with LITGS. The measured LITGS frequency is proportional to the local speed of sound (Eq. 6.5), and it can be related both to perturbations in temperature and density. In this work, LITGS is used to probe both aspects of the flow fluctuations. The results obtained in this chapter suggest that LITGS could be used as a diagnostic technique to time-resolve unsteady changes in the temperature and composition inside a combustor.

This chapter is organised as follows: a brief description of the experimental set-up and optical table is given in Sec. 7.2. A calibration procedure to extract density and temperature information from the LITGS signals is developed and then validated using a laminar jet, demonstrating that small steady and unsteady changes in the flow composition and temperature can be well time-resolved with LITGS (Sec. 7.3). Finally, LITGS is successfully applied in the Entropy Generator Rig to detect the passage of composition and temperature spots, using the quartz tube to visualise the flow (Sec. 7.5).

7.2 Experimental set-up

7.2.1 Optical layout

The optical layout of the experiment is sketched in Fig. 7.1. An Edgewave IS200-2-L laser generates pulsed laser beams with a wavelength $\lambda = 355$ nm, delivering 0.5-4 mJ per pulse. The frequency of the laser can be varied up to 10 kHz and in the present experiments the frequencies are between 0.5 and 1 kHz. All the optics are pre-aligned and placed over a 410$\times$550 mm movable breadboard box[2], where the probe laser is also located. Thus, this LIGS table is compact, portable and versatile: the movable breadboard allows the LIGS optics

[2]This breadboard and the optics inside it belong to B.A.O. Williams, who designed and assembled it

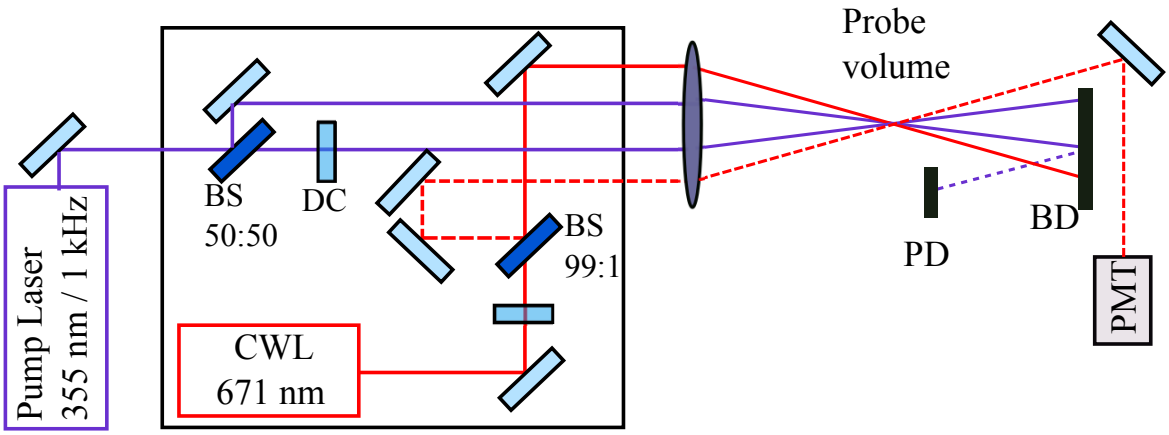

Fig. 7.1 Optical layout of the experiment. PL: 355 nm pulsed edgewave laser; CWL: continuous solid state laser; PD: photodiode; PMT: photomultiplier; HRM: highly reflective mirror; CLT: converging lens for telescopic arrangement; BS: beam splitter; BD: beam dump; CL: crossing lens; DC: delay compensator plate; S: signal; T: trigger.

to be quickly transported and placed in front of an alternative pump laser source. By using guiding pinholes located on the path of the pump beam, the new pump laser can be aligned with the LIGS optics. Inside the box, a 50/50 beam splitter divides the 355 nm pump beam into two identical beams and a 12 mm thick quartz plate compensates for the optical delay between them. The two beams, separated by 12 mm, are crossed by a 300 mm focal length crossing lens, resulting in a crossing angle $\theta \simeq 2.3°$, producing a grating of spacing 8.7 μm. Convex lenses along the path of the beams before the crossing lens ensure that the beams at the probe volume are collimated, without allowing the crossing lens to also focus them at the crossing point. This generates a probe volume with length and width of approximately 40×1 mm. This has two benefits. Firstly, the diameter of the interaction region is kept large enough to ensure that the signal does not decay as a result of the short transit time of the acoustic waves away from the probe volume, and that the signal oscillations are maintained within a time limited only by the long-lived diffusion and viscous damping effects. Secondly, this arrangement produces a collimated signal beam that can propagate to the detector efficiently without requiring a re-collimating lens near the interaction region, where it would be prone to collect scattered light, reducing the signal-to-noise ratio [215]. The continuous probe beam is produced by a CNI MLL-III-671 diode-pumped solid state laser ($\lambda = 671$ nm, power = 300 mW, diameter $\sim$ 1 mm) and sampled via a 99:1 splitter. The weaker beam (1%) is used as a tracer to track the direction of the signal beam and position the collection optics. The scattered signal is detected using a Hammamatsu photomultiplier (H6780-20). A photodiode

(DET210) provides a trigger signal for the data acquisition using the pump light scattered from the beam dump. The signals are recorded using a 4-channel LeCroy 6104A oscilloscope (sampling rate 10 Gs/s, 1 GHZ bandwidth, 40 million points maximum real time memory) in sequential mode, for 1 μs (10000 points) per signal. Oscilloscope memory limitations mean that a maximum of 4000 shots can be sequentially recorded and stored in one sequence. Once the memory buffer is filled, a few seconds are needed to store the buffer and start a new acquisition.

7.2.2 Experimental layout

The experiments are run in two different configurations. An open laminar jet is used for calibration (Fig. 7.2), while the Entropy Generator Rig with optical access (Fig. 7.3) is used to detect the passage of entropy and composition spots in a weakly turbulent flow.

The laboratory air supply system provides filtered air, and Alicat mass flow controllers regulate the flow: two 250 slpm ($\pm$0.8% accuracy, $\pm$1% full scale) and one 20 slpm ($\pm$0.8% accuracy, $\pm$1% full scale). The mean flow is seeded with biacetyl (2,3-butanedione; 99%; Acros Organics CAS: 431-03-8, Fisher Scientific UK LTD) using two Dreschel bottle bubblers with sintered heads (a 0.25 l bottle for flow rates lower than 20 slpm and a 0.5 l bottle for higher flow rates from Soham Scientific). The bubblers are kept at ambient temperature, and deliver nearly saturated mixtures of biacetyl, which are diluted downstream. Density and mixture fraction variations are induced in the air flow by adding carbon dioxide, argon or helium (See Table 7.1 for the specific heat capacity and molecular mass). The gases are pulsated into the tube using the fast response solenoid valve (Sec. 4.2.3).

	Air	CO_2	Ar	He	Biacetyl
W [g/mol]	28.97	44.01	39.948	4.002	86.09
$\bar{c}_p$ [J/mol/K]	29.115	37.144	20.78	20.77	120.97

Table 7.1 Molecular mass and specific heat capacity ratio of air, carbon dioxide, argon, helium and biacetyl.

Laminar jet

A laminar air jet (Fig. 7.2) is used for calibration. It consists of a 21 mm diameter, 150 mm long stainless steel tube (30 mm diameter jet for temperature calibration). The LITGS beams cross about 2 mm above the tip of the tube. The main gas line which passes through the bubbler is connected to a secondary dilution line 1 metre downstream of the bubbler. The jet tube has two ports: the air line (bubbler and dilution) is connected at port A. The second port

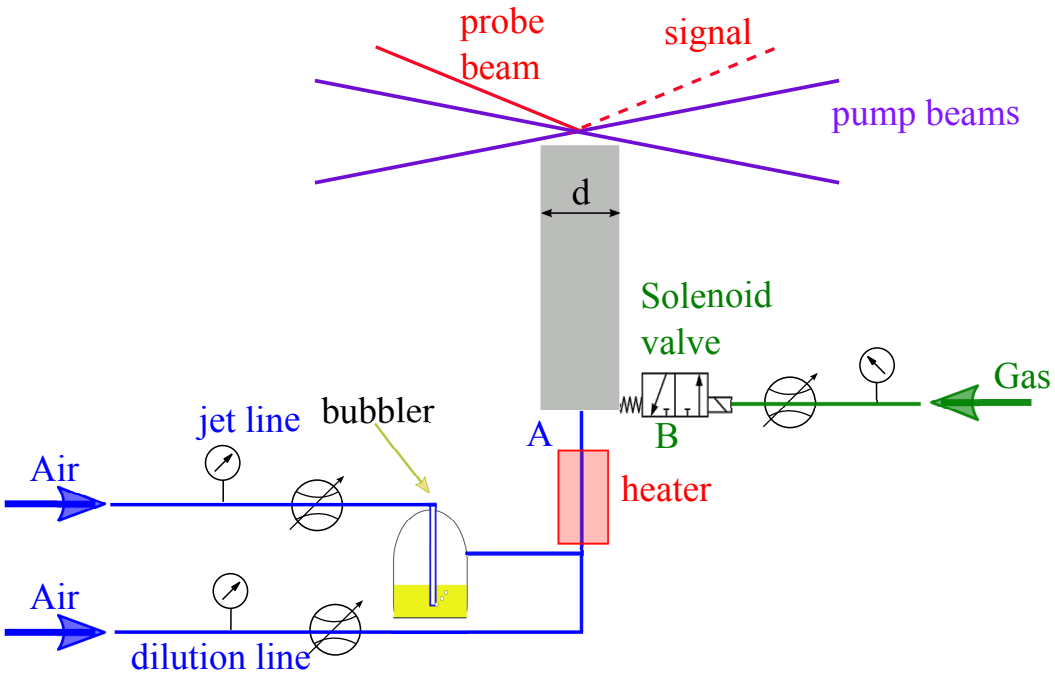

Fig. 7.2 Schematic of the jet experiment set-up. Not to scale. d = 21/30 mm.

B is used for the pulsated flow. An in-line heater (AHP-7562 Omega Engineering, 240 V, 750 W, 140 mm heated length) can be added to the flow line for increasing the temperatures of the gas.

Entropy generator

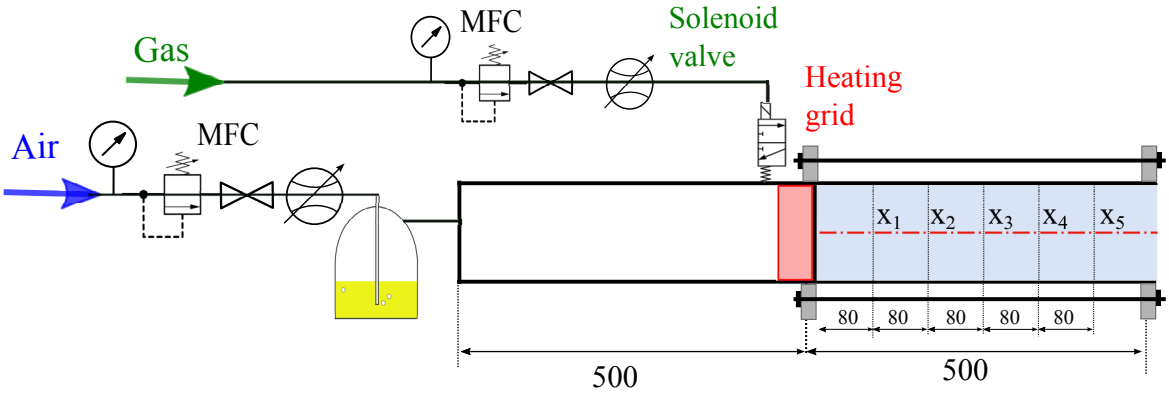

Fig. 7.3 Schematic of the entropy wave generator with an optical access window. Dimensions in mm. Dimensions not to scale.

Entropy and composition spots are generated via pulsed power to the heating grid or pulsed injection of a different gas (here helium, carbon dioxide or argon) (Chapter 4). The Entropy Generator is adapted with the quartz tube section, to provide optical access to the flow downstream of the entropy source. The rig is positioned on a 3-axis traverse, driven by three stepper motors controlled via a Labview interface. The LITGS probe volume is aligned to the centreline of the duct at different locations, marked 1 to 5 in Fig. 7.3. As pump and probe beams are not co-planar in this experiment, adjustment of the probe beams is needed to maximise the strength of the signals. In this experiment, the downstream end of the rig is left open to the atmosphere. This simplifies the experimental conditions, as the rig does not have to be pressure tested for leakages and also allows the use of flow rates lower than the ones needed to pressurise and choke the rig.

7.3 Calibration: mixture fraction and temperature measurements

In this section, we investigate how accurately frequency measurements with LITGS can be converted into temperature or mixture fraction fluctuations. For the calibration experiments, a flow of 5 slpm of air with saturated biacetyl forms a vertical laminar jet (Fig. 7.2), whilst the LITGS probe volume is located at the centreline of the jet at about 2 mm from the tube rim. A total of 1000 shots of 10000 points at 10 Gs/s are acquired. The raw voltage signal is padded with zeros up to 2^{21} samples (approximately 200 times longer) prior to taking its Fast Fourier Transform. The frequency of the oscillation corresponds to the highest peak in the power spectrum (Sec. 6.3.4). In what follows, the standard deviation in the frequency is denoted as σ_f, and is shown as error bars in the experimental plots.

7.3.1 Trade-off between intrusiveness and precision

LITGS is based on the generation of a local density change by absorption of energy, and it is therefore slightly intrusive, unless the product of pump beam energy and the concentration of the absorber are kept low [218, 139]. On the other hand, the signal itself, proportional to the square of the density perturbation [193], needs to be sufficiently high to provide suitable signal-to-noise for an assessment of the frequency. This might require the addition of a non-negligible quantity of a resonant species to the mean flow and the use of sufficiently high pump laser energies, which can potentially perturb the flow characteristics. To avoid thermalisation effects in the probe volume, the laser fluence must be kept low. A compromise should be achieved between increasing the diameters of the beams at the crossing point to

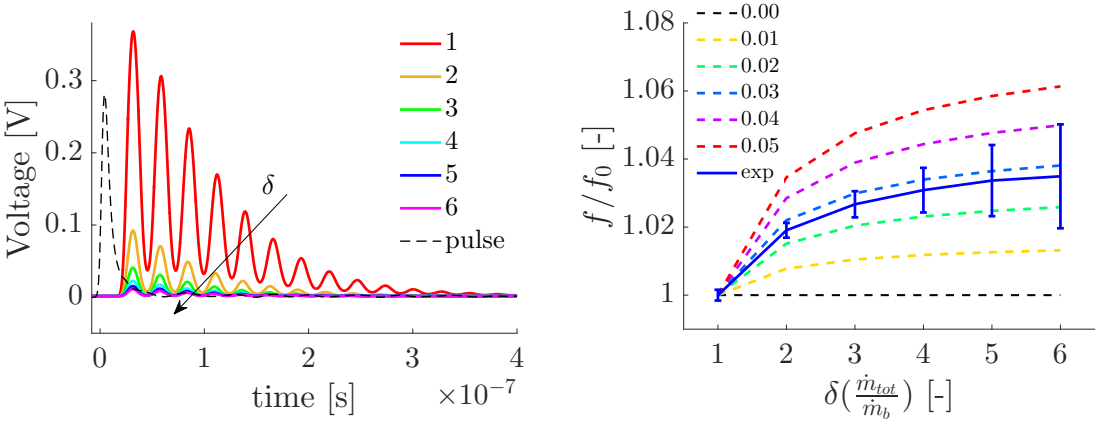

Fig. 7.4 Ensemble averaged LITGS time traces obtained by increasing the dilution ratio $\delta = \dot{m}_{tot}/\dot{m}_B$ (left); Frequency peaks for each dilution ratio, normalised by the frequency at zero dilution. Blue solid line: experimental data; dashed lines: values predicted for a given molar concentration of saturated undiluted biacetyl X_v; black line: normalised LITGS frequency for $X_b = 0$ (no biacetyl in the mean flow) (right).

reduce the fluence and obtain low thermalisation, and the need for spatial resolution in the longitudinal direction. Also, low concentration of a seeding species with properties similar to the mean flow should be used to avoid variations in the mean flow properties due to the added substance. This trade-off between intrusiveness and spatial resolution of the technique is discussed more in detail in Appendix A.

For the purpose of calibration, in this section we show how seeding the mean flow with an absorber in trace amounts might affect the mean flow properties and therefore the extracted frequency of the signals. Fig. 7.4 shows how variations in the dilution ratio of the biacetyl stream cause a decrease of the amplitude (left) and shift in the frequency (right) of LITGS signals. A constant mass flow rate of 5 slpm (approximately 0.1 g/s) flows through the bubbler. This main stream is diluted by adding extra air with the dilution line downstream of the bubbler, for dilution ratios $\delta = \dot{m}_{tot}/\dot{m}_{bub}$ between the total mass flow rate and the bubbler flow rate between δ =1 (undiluted) and δ =6. The signals decrease in strength from the undiluted to the most diluted mixture, as expected from the proportionality with the density change by absorption. The experimental plot (solid line) of the frequency f obtained for the signal at each dilution ratio, normalised by the undiluted conditions f_0 is shown in Fig. 7.4 (right). The measured peak frequencies increase with increasing dilution, and so do the corresponding standard deviations. The change in frequency (gradient of the plot) decreases with increasing dilution, until the values reach an approximately asymptotic value.

Clearly one wishes to have high signals and low standard deviations, but with a single value for the frequency, representing the true speed of sound (no added biacetyl to the mixture

and no temperature increase in the probe volume due to the laser). An optimum dilution ratio must be used for which the signal is sufficiently strong, the standard deviation sufficiently low and the energy of the pump laser does not increase the probe volume temperature. Any corrections due to the changes in properties produced by the tracer biacetyl must be taken into account. The following development explains the underlying theory to resolve the issues.

When an absorber (denoted as species b) is added to the flow of air (species a) with a molar concentration X_b , the frequency of the LITGS signal depends on the corresponding property of the mixture:

$$f^2 = \frac{1}{\Lambda^2}\frac{\gamma RT}{W} = \frac{1}{\Lambda^2}\frac{\left(1-\frac{R}{\bar{c}_{p,a}(1-X_b)+\bar{c}_{p,b}X_b}\right)^{-1}R}{W_a(1-X_b)+W_bX_b}(T_a+\Delta T) \tag{7.1}$$

Eq. 7.1 takes into account both changes in the local composition (and the corresponding changes in the molecular weight and specific heat capacity ratio), and the expected local temperature rise by absorption, ΔT. For the low laser fluences characteristic of the current experiment (collimated crossing beams), it can be demonstrated (See Appendix A) that the laser pulses induce negligible thermalisation ($\Delta T \ll T_a$ in Eq. 7.1). However, Fig. 7.4 (right) clearly shows that the change in biacetyl concentration has a non-negligible effect on the local speed of sound: biacetyl has a significantly different heat capacity and molecular mass with respect to air (Table 7.1). Accurate measurements of the molar fractions of biacetyl X_b in the flow after the bubbler are challenging in the absence of absolute standards. However, from the knowledge of the vapour pressure of biacetyl at a given bubbler temperature $p_s(T)$, the ideal maximum concentration of biacetyl in saturated conditions can be estimated as $X_{b,s} = p_s/p_0$, where p_0 is the total pressure in the bubbler, which, in this case, is atmospheric pressure. From [160] the vapour pressure of biacetyl at room temperature is $p_s = 0.058$ bar, thus $X_{b,s,\max} = 0.058$.

A calibration procedure is introduced to estimate the actual molar concentration of biacetyl in the mean flow, and the necessary correction to the frequency. From Eq. 7.1, the ratio of frequencies between two biacetyl mole fractions $X_{\delta 1}$ and $X_{\delta 2}$ can be expressed as:

$$\left(\frac{f_{\delta 2}}{f_{\delta 1}}\right)^2 = \frac{\left(1-\frac{R}{\bar{c}_{p,a}(1-X_{\delta 2})+\bar{c}_{p,b}X_{\delta 2}}\right)^{-1}}{\left(1-\frac{R}{\bar{c}_{p,a}(1-X_{\delta 1})+\bar{c}_{p,b}X_{\delta 1}}\right)^{-1}}\frac{W_a(1-X_{\delta 1})+W_bX_{\delta 1}}{W_a(1-X_{\delta 2})+W_bX_{\delta 2}} \tag{7.2}$$

where the total molar fraction of biacetyl X_δ for each dilution ratio δ is:

$$X_\delta = \frac{X_b}{(1-X_b)\delta + X_b} \tag{7.3}$$

The dashed lines in Fig. 7.4 (right) represent the frequency ratio f_2/f_1 calculated from Eq. 7.2 by varying the concentration of biacetyl X_b. The value $X_b = 0.028$ solves Eq. 7.2. The black line corresponds to the limit case where no biacetyl is added to the flow (X_b =0), so that an increase in the total mass flow rate does not change the bulk flow properties (in this case thermal gratings can not be generated).

Fig. 7.4 (right) shows that even for low biacetyl concentrations ($X_b = 0.01$), the frequency change for saturated conditions relative to no dilution ($\Delta f_{max}/f_0 = 2\%$) is non-negligible. On the other hand, in order to obtain high signal-to-noise ratios and low standard deviations, a relatively high concentration of biacetyl is required. As in these experiments we use a concentration of biacetyl $X_b \simeq 3\%$, the change in the mean flow properties must be accounted for.

7.3.2 Relative speed of sound in different gases

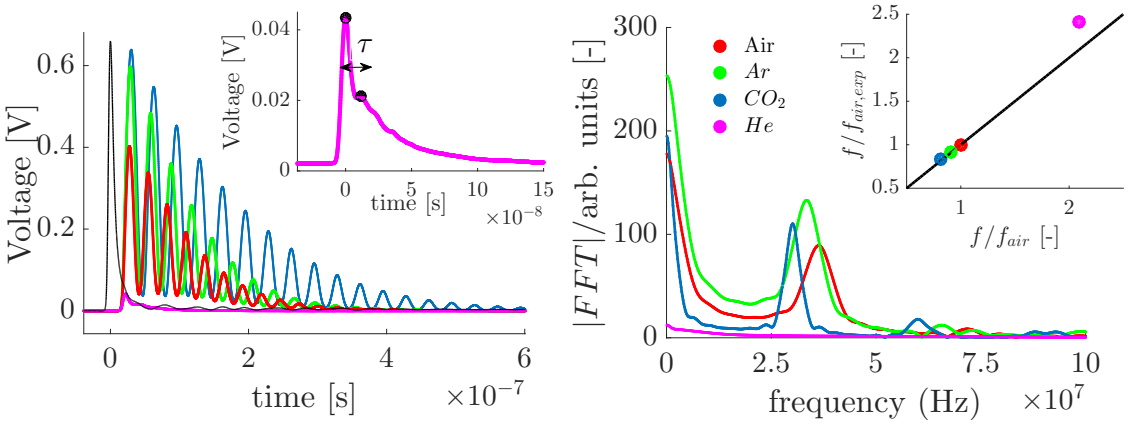

Fig. 7.5 Ensemble-averaged LITGS signals acquired in jets of biacetyl-saturated air, argon, carbon dioxide and helium. Inset: zoom on the helium signal (left). Corresponding Fourier Transform of the signals. Inset: ratio between the peak frequencies obtained with different gases, normalised by that with air (right).

In this section, we deploy LITGS to measure the changes in the speed of sound in different gases, using pure jets of air, carbon dioxide, argon and helium seeded with biacetyl. Mass flow rates of 5 slpm of air, CO_2, Ar and 10 slpm of He are passed through the 250 ml bubbler with no further dilution.

Fig. 7.5 shows the ensemble averaged LITGS signals in the four gases, in the time (left) and in the frequency domain (right). The speed of sound in carbon dioxide and argon is lower than in air, so the corresponding LITGS oscillation frequencies are lower. For helium, however, the speed of sound is much higher, and, as the quenching efficiency and density are

low, the amplitude of the LITGS signal in helium is weak compared to the other gases, and only two peaks can be observed in time (inset in Fig. 7.5, left). Therefore, in this specific case of pure helium, the corresponding frequency can not even be identified in the power spectrum (Fig. 7.5, (right)), but is instead evaluated from the time separation between peaks as $f = 1/\bar{\tau}$. As seen in Chapter 6, the evaluation of the LITGS frequency from the time separation of few peaks might decrease the accuracy of the measurements. In the inset of Fig. 7.5 (right), the expected oscillation frequencies in the three gases, normalised by that of air f_0 are compared with the experimental values. Good agreement is found between predictions and experimental data. As expected, the value for helium displays a higher error, probably also caused by the large difference in molecular mass between biacetyl and helium, for which the diffusivity of biacetyl in helium is lower, causing a lower concentration of biacetyl in the jet of pure helium.

7.3.3 Steady composition variations

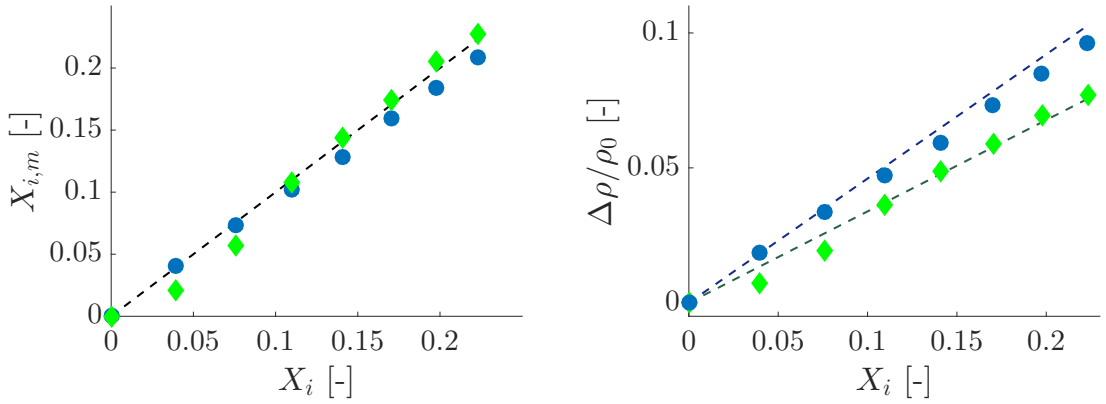

Fig. 7.6 Measured mean molar concentrations of CO_2 (blue dots) and argon (green diamonds) in a jet of air (left) and mean density variations using LITGS, relatively to the expected concentrations based on dilution ratios (right).

LITGS can be used to detect relatively small changes in the composition of a flow under steady conditions (Fig. 7.6). A secondary flow of CO_2 and Ar is steadily added (port B, no solenoid valve) to the base laminar jet flow (Fig. 7.2 with undiluted vaporised air and biacetyl flow, port A). The flow at the measurement point is assumed to be homogeneous, given the long mixing length relatively to the diameter. The addition of the secondary flow changes both the specific heat capacity and the molecular mass of the flow passing through

the probe volume. The molar concentration of the secondary gas X_i is calculated using:

$$\left(\frac{f_i}{f_0}\right)^2 = \frac{\left(1-\frac{R}{\bar{c}_{p,i}X_i+\bar{c}_{p,0}(1-X_i)}\right)^{-1}}{\left(1-\frac{R}{\bar{c}_{p,0}}\right)^{-1}} \frac{W_0}{W_iX_i+W_0(1-X_i)} \tag{7.4}$$

where the base flow of air and biacetyl ($_0$) is used as a reference. The pressure p and temperature T are assumed to be constant in the jets with ($[-]_i$) and without ($[-]_0$) the addition of the secondary flow:

$$p = \frac{\rho_0 RT}{W_0};\ p = \frac{\rho_i RT}{W_i} \rightarrow \frac{\rho_0}{W_0} = \frac{\rho_i}{W_i} \tag{7.5}$$

Therefore, the density variation in the mean flow due to the addition of the secondary flow is computed as

$$\frac{\Delta\rho}{\rho_0} = \frac{\Delta W}{W_0} = \frac{W_iX_i+W_0(1-X_i)}{W_0} - 1 \tag{7.6}$$

These results in Fig. 7.6 show that small changes in the mean flow properties can be detected with LITGS, provided that the determination of the oscillation frequency is sufficiently accurate and precise.

7.3.4 Temperature measurements

In what follows we derive a calibration procedure to correctly evaluate the temperature increase from the LITGS data in the presence of a seeded absorber. A base flow of 40 slpm of air passes through the bubbler (no dilution), is warmed up by the in-line resistance heater by varying the applied voltage, and forms a jet in the 30 mm tube. A thermocouple is used to monitor the temperature increase, using a flow of 40 slpm of *pure air* (no biacetyl) while the resistance warms up until the temperature stabilises, to reduce the biacetyl consumption. The data recorded with the thermocouple (dashed line in Fig. 7.7) refers to air-only case. Once the recorded temperature is stable, the same mass flow rate of air is passed through the bubbler and the heater and LITGS traces are recorded over the tracer-laden laminar jet, at the same location where the thermocouple was located. Once the LITGS signal is recorded, the air flow is switched from the bubbler and the voltage on the resistance is increased, repeating the same procedure for the next temperature acquisition.

The temperature increase ΔT_{ab} in the air and biacetyl flow (magenta circular markers in Fig. 7.7) is obtained from the LITGS oscillation frequency as:

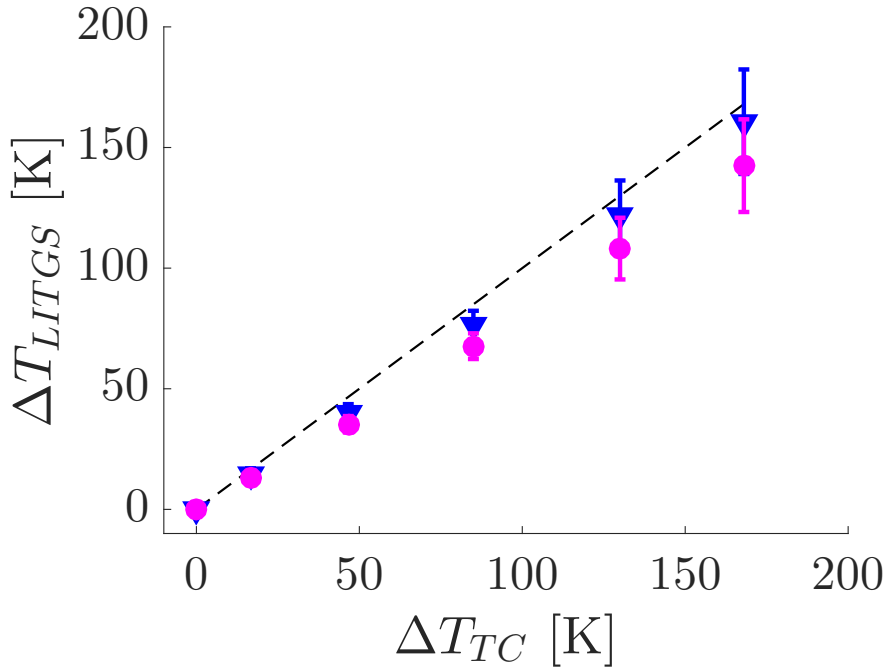

Fig. 7.7 Measured temperature rise from ambient using LITGS, plotted against the thermocouple measurements. Dashed line: thermocouple measurements in the pure air jet; magenta dots: LITGS measurement in the air and biacetyl jet; blue triangles: equivalent temperature increase in the pure air jet from the LITGS measurements.

$$\Delta T_{ab} = \left[\left(\frac{f_{ab}}{f_0} \right)^2 - 1 \right] T_0 \tag{7.7}$$

where $T_0 = 294$ K is the ambient temperature and f_0 is the corresponding frequency. Part of the discrepancy between the LITGS and the thermocouple measurements can be explained by the different molecular mass and specific heat of the flows with and without biacetyl. The heater delivers a constant power Q to the flow, so the relation between the temperature increase in the flow with (ΔT_{ab}) and without (ΔT_a) biacetyl is

$$\frac{\Delta T_a}{\Delta T_{ab}} = \frac{\frac{Q}{c_{p,a}\dot{m}_a}}{\frac{Q}{c_{p,ab}\dot{m}_{ab}}} = \left(1 + \frac{X_b}{1 - X_b} \frac{\bar{c}_{p,b}}{\bar{c}_{p,a}} \right) \tag{7.8}$$

The measured temperature rise in the mixture with air is higher than that measured in air plus biacetyl for a given heating power. Once this factor is accounted for, the two measurements agree within 2% (blue symbols in Fig. 7.7). For high temperature variations, the temperature dependency of c_p should be also taken into account in Eq. 7.8.

7.4 Time-resolved composition variation measurements in a laminar jet

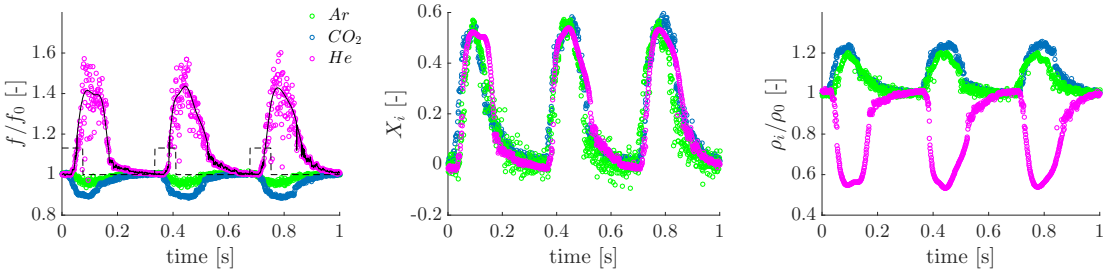

Fig. 7.8 Normalised time-resolved frequency variation obtained from LITGS measurements in a laminar jet pulsated with a secondary gas of helium, argon or carbon dioxide (left); corresponding time-resolved molar fraction of the pulsated gas (centre); corresponding relative measured density variation (right).

Since we demonstrated that LITGS can resolve the difference between different speeds of sound, it is possible to use it as a marker of the mixture fraction in an unsteady binary mixture, where the molecular weights of the mixing streams are different. In this section we show that LITGS can time-resolve density and composition perturbations generated by the unsteady injection of argon, carbon dioxide and helium in an air jet. A steady mass flow rate of 24 slpm of air is used as base flow in the laminar jet (Fig. 7.2): half of the flow passes through the bubbler and the other half through the dilution line, for a mean flow velocity u = 1.15 m/s and a Reynolds number Re = 1558. Periodic spots of the secondary gas are injected at the bottom of the jet (port B), using the fast response valve. The pressure in the gas tank upstream of the injection line is regulated to about 3 bar. The frequency of the pulses is set to 3 Hz, with a duty cycle of 20%. The repetition rate of the laser is set to 1 kHz. Fig. 7.8 (left) shows the time-resolved (non averaged) LITGS frequency traces acquired within 1 s, corresponding to three cycles of the valve, normalised by the base flow frequency f_0. The shape and amplitude of the gas pulses can be clearly identified in the frequency traces, including the characteristic rise and decay time. While the pulses of carbon dioxide and argon are well defined, the helium pulses are more spread out at the end of the pulse, when the highest quantity of helium is injected into the flow, causing a shorter signal with a smaller number of oscillations, as shown in Fig. 7.5. Thus, the helium data is interpolated with an envelope determined using the RMS of 30 consecutive points. The molar fraction X_i of the injected gas corresponding to each LITGS frequency is determined using Eq. 7.4, and plotted in Fig. 7.8 (centre). The volumetric flow rates injected by the valves for the three gases are similar for the different gases, as expected. From the molar fraction X_i , the density variation

at each point is obtained from Eq. 7.6. As the density of helium differs substantially from the air, the variation of density after the helium pulses is much higher than for CO_2 and Ar, as shown in Fig. 7.8 (right).

7.5 Time-resolved composition variation measurements in the Entropy Generator Rig

The aim of the calibration and validation measurements reported in the previous sections is to enable accurate unsteady measurements of entropy and composition spots through a duct, so as to map out their convection and dispersion. Here these are demonstrated along the optically accessible Entropy Generator Rig. The small diameter of the cylinder poses a particular problem when aligning the beams into the quartz tube, as small-out-of-plane misalignments of the rig can easily deflect the three beams towards different directions whereas they need to cross at exactly the same point. The probe beam is mainly affected by this deviation, as it enters the probe volume at an angle with respect to the horizontal plane. The duct height was adjusted using the traverse until the centreline of the cylinder was coplanar with the the two pump beams. A few iterations were required to maintain the crossing of the two pump and the probe beams along the same plane across the cylinder centreline. The larger the radius of curvature of the quartz tube, the less severe is this problem, and flat windows or co-planar beams solve the issue.

The mass flow rate of air in the experiment is set to 80 slpm (1.57 g/s), which corresponds to an upstream velocity of about 1 m/s and a Reynolds number of Re = 2800, so the flow is in a nearly turbulent regime. Air flows nearly saturated with biacetyl are used (low or no dilution), and this is the main factor limiting the maximum flow velocity achievable. The maximum flow rates are limited by the consumption rate of biacetyl and the volume of the bubbler: relatively high mass flow rates lead to lower biacetyl molar fractions, as the bubbler becomes less effective. Ye,t the flow rates could not be increased above 100 slpm without causing spillages of biacetyl from the bubbler. An alternative vaporisation method or a laser wavelength tuned to a more strongly-absorbing region of the molecular spectrum would allow higher flow rates to be achieved.

Under these conditions, using 0.5 mJ of energy in the pump beams, a typical base flow signal in the rig had an average amplitude of 200 mV, versus the 350 mV in the open jet. The standard deviation over 1000 points in the LITGS signal of the base flow was $\sigma_f = 3.5 \times 10^5$, so $\sigma_f / f_0 = 1\%$. This corresponds to a standard deviation of $\sigma_T = 5$ K. It was therefore decided to increase the pump pulse energy to 4 mJ. Indeed, for this higher energy, the

amplitude of the signal became 400 mV, and the standard deviation decreased to $\sigma_f \simeq 10^5$, so $\sigma_f / f_0 < 0.3\%$, which corresponds to a standard deviation of $\sigma_T \simeq 1$ K. It was experimentally verified that such energies still generated negligible thermalisation in the measurements (Appendix A). The repetition rate of the laser pulses in the present experiment was limited to 500 Hz, so as to allow the acquisition of longer periods of time in the data set due to the limited space in the memory buffer of the oscilloscope. No difference was found regarding either the laser pulses shapes and amplitudes, or in the signal characteristics (mean frequency and standard deviation) between the higher and lower repetition rates used.

7.5.1 Detection of composition spots

Composition spots were detected using LITGS in the quartz tube at the five centreline positions indicated in Fig. 7.3. The different gases (CO_2, Ar, He; first, second and third column respectively) were injected at a frequency of 1 Hz and a duty cycle of 20%. At each point, the passage of about 30 spots was recorded, then the rig was moved from one place to the other using the traverse.

Figs. 7.9 (first row) shows the instantaneous time-resolved traces at five of the locations for CO_2, Ar and He pulses. The passage of the spots the can be clearly identified in these signals. In order to decrease the standard deviation and obtain more accurate measurements, the energy of the laser pulses was set to 4 mJ. The consumption of biacetyl in the bubbler generates a small shift of the base flow frequencies. When the level of biacetyl in the bubbler drops, the vaporisation becomes less efficient, the concentration of biacetyl decreases and the corresponding mean flow frequency increases (Fig. 7.4). The change in concentration of biacetyl has to be taken into account to properly evaluate the mean flow properties at each location. The mean flow has a dilution $\delta = 1.33$, as 60 slpm of air pass through the bubbler and 20 slpm of air bypass it. The molar concentration of biacetyl in the point with the highest biacetyl concentration is $X_b = 0.013$, determined with the procedure described in Sec. 7.3.1. The biacetyl concentration for the other flow rates is then evaluated from the mean flow frequency using Eq.7.4 and 7.6.

Once the mean flow properties for each location are determined, the mole fraction and density variation due to the passage of the composition spots are determined using Eq. 7.1. An error in the evaluation of the biacetyl concentration in the mean flow of $\Delta X_b = 0.01$ (e.g. if X_b =0.023 instead) would lead to an error in the evaluation of the density variation $\Delta\rho_i/\rho_i < 1\%$, thus the quantitative results are reliable. The 30 composition spot pulses are phase averaged to obtain clearer information on the shape and amplitude of the spots, reducing the scatter of the measurements (third and fourth rows). However, the features of the injected pulses can be observed directly from the instantaneous measurements (non

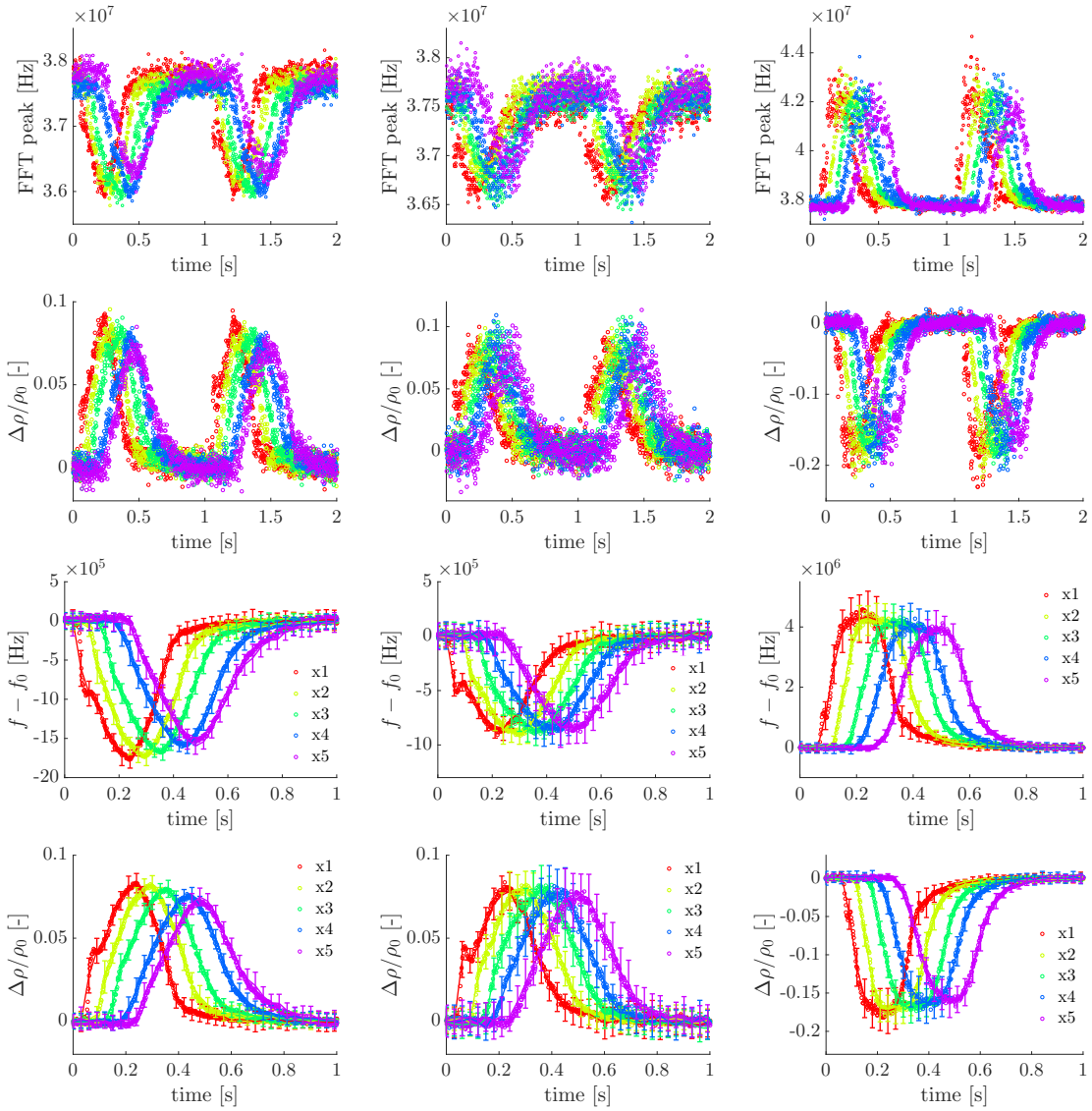

Fig. 7.9 Detection of composition spots (from left to right column: CO_2, Ar, He) at five locations along the quartz tube. Injection pulse frequency: 1 Hz; duty cycle: 20%. Row 1: time-resolved LITGS traces (peak frequency); row 2: time-resolved normalised density variations; row 3: ensemble-averaged (30 pulses) LITGS traces (frequency variation from the mean); row 4: ensemble-averaged (30 pulses) normalised density variations.

averaged). For example, the signals acquired in position x_1 display a small hump in the first few milliseconds, which corresponds to the first bounce of the composition spot off the opposite wall after being injected, a feature which disappears in the following positions. Some effects of dispersion can be observed in the pulses, despite the short distance within the five measurement locations. The spots at x_1 have a sharper shape, while at x_5 they are more spread out. For the helium, as expected, the signals are more noisy relatively to CO_2 and Ar. Diffusive effects have a higher impact on helium, as it is a smaller and lighter molecule, with a higher diffusion coefficient.

7.5.2 Detection of temperature spots

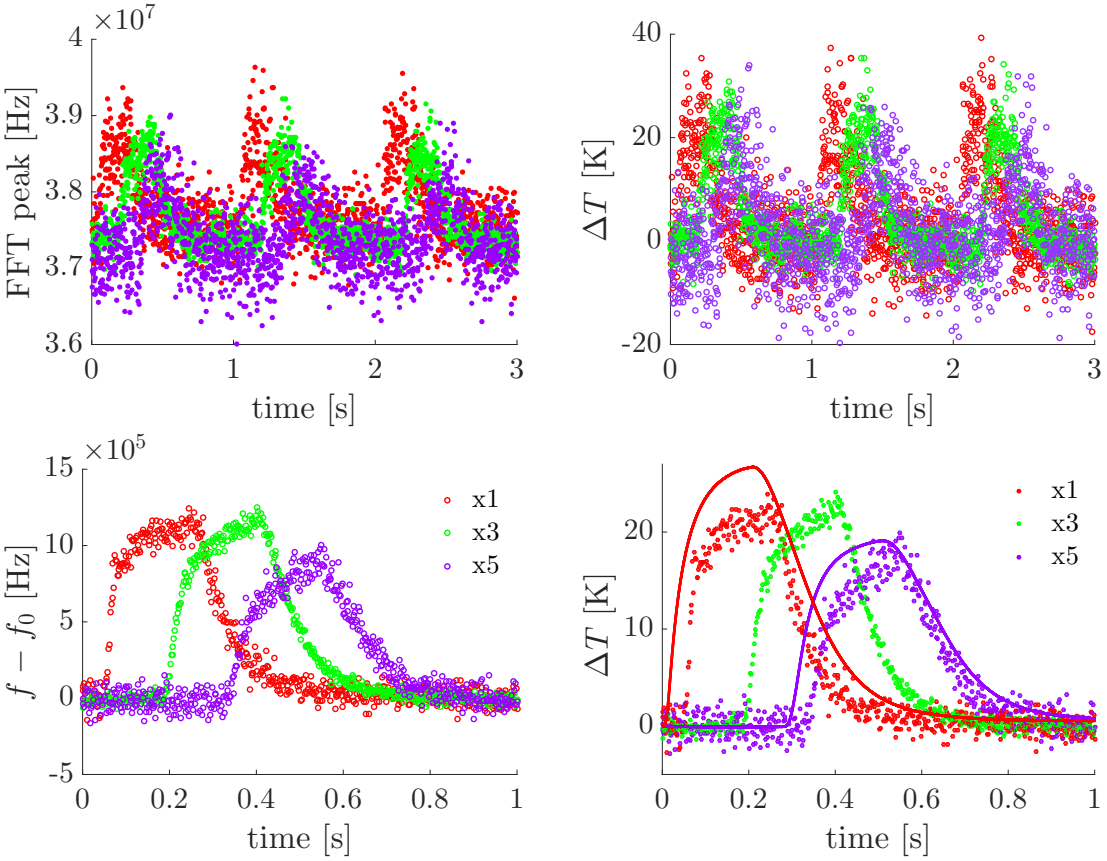

Fig. 7.10 Measured time-resolved temperature fluctuations: frequency (top-left); temperature deviation from initial value (top-right); averaged frequency variation (bottom-left); ensemble-averaged temperature obtained with LITGS (circles) and with anemometer and thermocouples (lines) (see Sec. 4.4.3 (bottom-right)).

This section describes the results of LITGS measurements applied to detect temperature variations generated in the via the heating grid, and advected and dispersed along the rig,

where they are acquired with LITGS at locations x_1, x_3 and x_5 in Fig. 7.3. The experimental conditions are chosen to be comparable to the experimental case C1 reported in Chapter 4 (Sec. 4.4.3) to compare the LITGS results with the temperature data previously acquired with thermocouples and anemometers. The heating grid delivers pulses of τ =200 ms, with an input power of 35 V $\times$ 21 A, to resemble the experimental conditions of Chapter 4. The mass flow rate and duct dimensions are chosen to be similar: here, a mass flow rate of 80 slpm (with dilution δ=1) runs into the 42 mm-inner-diameter rig; in Sec. 4.4.3, a mass flow rate of 78 slpm flows into the 42.6 mm-inner-diameter rig. The temperature measurements are acquired at similar locations too. In table 4.3 (Chapter 4), the maximum amplitude temperature of the entropy spot at the grid and 40 mm downstream as measured using corrected thermocouple measurements are reported to be $\Delta T = 26.6$ and 21.1 K, respectively.

Fig. 7.10 (top-left) shows the time-resolved frequency traces obtained with LITGS. To reduce the scatter, the signal is averaged over 30 phase-locked traces (Fig. 7.10 (bottom-left)). After taking the base flow frequency shift into account, the temperature increase ΔT is determined using the calibration procedure described in Sec. 7.3.4 (Fig. 7.10 (top-right)) The averaged temperature traces (Fig. 7.10 (bottom-right)) obtained in this way are compared with the measurements in Sec. 4.4.3. The comparisons between the thermocouple and LITGS measurements are very favourable, even though the measurements are acquired in different facilities with different flow rates at slightly different positions. In Sec. 4.4.3 the thermocouple measurements are corrected using a faster hot-wire, and some inaccuracy is also expected, of the order of 1-2 K. Overall, the rise and fall of the temperature perturbation is very well captured, and the variations should be attributed to differences in the experimental set-up, including the fact that the heating grid losses may be slightly different in the two set-ups, as the pipe materials varied.

7.6 Discussion and further development

In this chapter we demonstrate the potential of LITGS as a technique capable to detect the unsteady passage of entropy and composition spots, using a simplified experiment as the Entropy Generator Rig. There are very few techniques capable of detecting temperature variations of such small magnitude at high frequencies, so the present technique may be useful across other areas as well. In the present work, the upper limit of the measurement frequency has not been explored in order to save the mirrors and the quartz tube from damage. However, measurements can exceed 1 kHz frequency under suitable conditions [73]. If deployed to model combustors or a gas turbines, time-resolved measurements of unsteady temperature and composition changes may allow the detection of the amplitude of the entropy

and composition fluctuations surviving through the chamber and entering into the nozzle, and help quantify the indirect noise generated from their acceleration. The main barrier to perform these measurements is finding a good match between available absorbing species and laser wavelengths. Candidates exist for the fundamental harmonic of the Nd:YAG laser (*e.g.* water, as shown in Chapter 8-9, and propane); for quadrupled Nd:YAG frequencies 266 nm (*e.g.* toluene, which is also present in the fuel), or even oxygen in the deeper UV excitement range (172 nm). In the absence of absorbing species, high power lasers can be used to generate electrostrictive gratings, from which temperature and composition can be detected as well. However, electrostrictive gratings normally require energies too high to be delivered at high frequency by common PIV lasers. The one option currently available is the pulse burst laser. The application of a pulse burst laser to LIGS is described in Chapter 9.

7.7 Conclusions

LITGS is applied to make time-resolved measurements of temperature and composition variations ($< 1-3\%$ in amplitude) in non-reacting flows. LITGS is a relatively simple technique which requires only limited optical access and simple data analysis, and therefore is a good candidate to detect unsteady temperature and composition variations in combustion chambers. In this experiment, biacetyl is used as a tracer in the flow to absorb the 355 nm laser light and generate the thermal grating. It is demonstrated that the addition of biacetyl generates non-negligible property changes to the local mixture. A calibration procedure is developed to evaluate the concentration of biacetyl, and thus recover the real temperature and composition from the oscillation frequency. A further validation experiment in unsteady conditions demonstrates that LITGS can time-resolve unsteady perturbations. Finally, LITGS is successfully applied to detect the passage of entropy and composition spots in the Cambridge Wave Generator, showing that the technique is suitable to analyse the generation, dissipation and dispersion of entropy spots. These measurements should allow the characterisation of the strength and amplitude of the entropy and composition spots surviving through a combustion chamber and entering into the nozzle, and help to quantify the indirect noise generated from their acceleration.

Nevertheless, this study highlights some of the limitations of the technique. The main complication lies in the requirement of the presence of an absorbing species in the flow at the specific wavelength of the laser, which may be achieved by seeding the flow, thus altering the mean flow properties. Alternatives to the seeding of the flow are explored in Chapters 8-9. The second disadvantage is the trade-off between perturbing the temperature in the robe

volume by using tightly focused beams and degrading the spatial resolution. This issue is explored more in depth in Appendix A.

Chapter 8

Temperature and water measurements in flames using 1064 nm LIGS

In this chapter, Laser-Induced Grating Spectroscopy (LIGS) is applied to premixed CH_4/ air laminar flat flames under operating pressures of 1 to 6 bar. For the first time, temperature and water molar fractions are acquired simultaneously in a pressurised reacting flow environment using LIGS. A 1064 nm pulsed laser is used as a pump to generate a temporary stationary intensity grating in the probe volume. Water molecules in the flame products absorb the laser energy and generate a thermal grating if sufficiently high energies are delivered by the laser pulses, here more than 100 mJ per pulse. Such energies allow the electric field to polarise the dielectric medium, resulting in a detectable electrostrictive grating as well. This creates LIGS signals containing both the electrostrictive and the thermal contributions. The local speed of sound is derived from the oscillation frequency of the LIGS signals, which can be measured from the power spectrum of the single shots. Data shows that the ratio between the electrostrictive and the thermal peak intensities is an indicator of the local concentration of the absorbing molecule. This information can be used to infer the relative local water concentration, as well as the temperature. The measured values of speed of sound, temperature, and water concentration in the flames examined compare favourably with flame simulations with Chemkin, showing an estimated accuracy of 0.5 to 2.5% and a precision of 1.4-2%. These results confirm the potential for 1064 nm LIGS-based thermometry for high-precision temperature measurements of combustion processes[1].

[1]The experiments described in this chapter were done at the Clean Combustion Research Center at King Abdullah University of Science and Technology. The results described in this chapter are published in *Combustion and Flame* [46]

8.1 Introduction

Accurate and precise measurements of gas temperature in reacting flows are desirable for model validation and for effective and fast design of low emission internal combustion engines and gas turbines. However, the hostile environment of combustion chambers makes these measurements extremely challenging, so that only a few experimental techniques are able to probe the temperature without perturbing the flow. In this chapter, Laser-Induced Grating Spectroscopy (LIGS) is demonstrated as a promising technique to measure the local temperature and water concentration in high pressure combustion environments. LIGS (LIEGS + LITGS) measurements are performed in premixed CH_4/air laminar flat flames under operating pressures of 1 to 6 bar. The thermal grating is generated by the weak absorption of 1064 nm light by the water vapour present in the reaction products. Hell et al. [95, 96] also took advantage of the weak absorption band of water to obtain LITGS in a hydrogen/air flame at atmospheric pressure using a 1064 nm pump. However, the acquired signals only had few peaks and a low signal-to-noise ratio, reducing the accuracy in the measurements and making the frequency based analysis impractical. A calibration algorithm had to be developed to fit a modelled signal to the acquired time traces, which made the signal analysis much more complicated and subjected to error. Thus, a particular novelty of the work described in this chapter has been the demonstration of the technique without the use of an added absorber for accurate measurements in flames at pressure, which simplifies the data analysis procedure. The first harmonic of the Nd:YAG laser at 1064 nm is ideal to achieve the high energy outputs (more than 100 mJ per pulse) required to produce LITGS using water as an absorber. Such energies also generate non-negligible electrostrictive signals. Since the LITGS signal intensity is expected to depend on the water concentration while the LIEGS signal intensity does not, combined LITGS and LIEGS should allow measuring water concentration.

The chapter is organised as follows: after a brief description of the optical set-up and the experimental facilities (Sec. 8.2), the experimental procedure is explained (Sec. 8.3.1), with a particular focus on the effects of operating pressure (Sec. 8.3.2) and pump laser energy (Sec. 8.3.3) on the amplitude and oscillation frequency of the LIGS signals. Then, the experimental results obtained for flames at a pressure of 4 bar are described in more details and compared with burner-stabilised, lean premixed methane/oxygen/nitrogen flames at high pressure simulated using a chemical kinetic model with Chemkin. Comparisons are based on speed of sound, temperature and water concentration (Sec. 8.3.4).

8.2 Experimental set-up

8.2.1 Optical layout

The optical layout of the experiment is sketched in Fig. 8.1, and resembles the one described in Chapter 6. A seeded pulsed Nd:YAG laser (Continuum Powerlite DLS9010) generates a laser beam with a wavelength $\lambda = 1064$ nm at a repetition rate of 10 Hz. The Q-switch delay is adjusted to deliver pulses of 12 ns duration with a total energy of 1 J. The pulse energy is then adjusted in the range from 75 to 350 mJ by manually rotating a half wave plate (HWP) placed before a polarizer beam splitter cube (PBSC). The beam level is raised to 1.20 m via a periscope tower to reach the height of the windows of the high-pressure vessel. Beyond the periscope, the beam has horizontal polarization.

A 50/50 beam splitter plate optimised for 1064 nm divides the beam into two identical beams. A delay line (DL) created by two mirrors on a translation stage is located in the path of one of the two beams to ensure that the two beams are in phase at the probe volume. The two parallel beams, separated by 50 mm, are crossed using a 75-mm diameter bi-convex crossing lens (CL) with a 750-mm focal length, resulting in a crossing angle $\theta \simeq 3.81°$. This arrangement produces a grating of 16 μm spacing in a probe volume of length and width of approximately 5 mm and 200 μm, respectively. These dimensions are evaluated from Eq. 6.6 with $M^2 = 2$, and the crossing geometry described in Sec. 6.3.3. The continuous probe beam is generated by a continuous wave solid state laser (Coherent Verdi G) operating at 532 nm with a maximum power output of 17 W and a diameter of ~ 2 mm. A guide beam, also at 532 nm, produced by a diode laser (Thorlabs CPS532) is used as a tracer to identify the direction of the scattered signal and facilitate positioning of the collection optics. These four beams (two pump, the probe, and the tracer beams) are coplanar and alignment masks are used to adjust their respective positions. Details about the alignment procedure of the beams can be found in Sec. 6.3. A dichroic harmonic beam splitter (Thorlabs HBSY12) reflects the LIGS signals (532 nm) and transmits the pump beams (1064 nm), which are then trapped in beam dumps (BD). The LIGS signals are re-collimated with a second 75-mm diameter bi-convex crossing lens (CL) with a 750-mm focal length, then travel for 1.5 m to reject spurious signals, and are finally collected by a PMT (Hamamatsu H10721-20, rise time: 0.57 ns). Two 550 nm low pass filters (T: 99.9% at 532 nm, T: 0.08% at 1064 nm) are mounted in front of the PMT to improve the rejection of background scattered light. The operation parameters of the PMT were selected to guarantee operation in the linear range. An infrared photodiode (Thorlabs DET210) detects the pump pulses and triggers acquisition of the LIGS signals. The signals are recorded using an oscilloscope (Keysight DSOS804A, 10 Gs/s sampling rate, 8 GHz bandwidth).

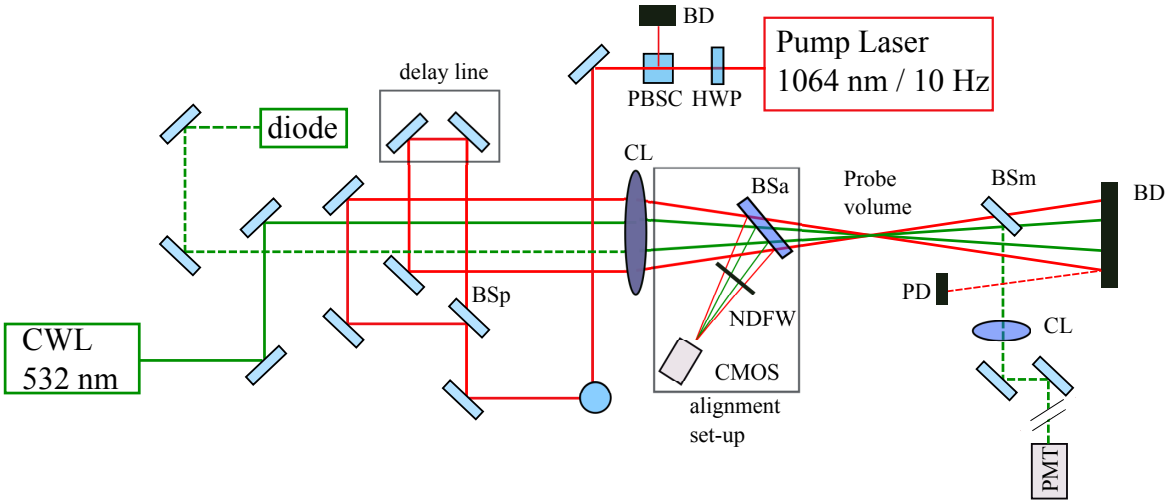

Fig. 8.1 Optical layout of the experiment. Pump Laser: 1064 nm pulsed laser; CWL: Continuous Wavelength Laser; diode: tracer beam; BSp: beam splitter (for 1064 nm); PT: periscope tower; CL: crossing lens; BD: beam dump; PBSC: polarising beam splitter cube; HWP: half wave plate; BSa: beam sampler; NDFW: neutral density filter wheel; CMOS: CMOS camera; BSm: harmonic beam splitter (transmits 1064 nm and reflects 532 nm); PMT: photomultiplier.

8.2.2 Experimental rig

LIGS measurements are performed in laminar premixed methane/air flat flames located in a vertically-oriented pressure vessel operated from 1 to 6 bar. This vessel is designed for continuous operation and features a 127×127 mm^2 square cross-section chamber of 350 mm height. Resistance to pressure and temperature is achieved with 9-mm thick and air cooled stainless steel walls. Pressure is controlled with a manual needle valve and a dome-loaded back-pressure regulator (Equilibar GS2-NR-SS316) installed in parallel downstream of the exhaust port of the vessel. Pressure is first adjusted roughly by progressively closing the needle valve and fine adjustments are then made by tuning the back-pressure of the regulator using pressurised nitrogen. The vessel has four extension tubes mounted at 90 degrees to each other in the horizontal plane. These extension tubes terminate with 25.4-mm thick, 85-mm aperture diameter BK-7 windows (with a overall window diameter of 127 mm), providing optical access into the vessel. One window is used to pass the pump beams and the opposite window allows relaying the LIGS signals outside the vessel. The two remaining windows, mounted at 90 degrees, are used to monitor the flame. Jets of air continuously impinge on the four windows and prevent water from condensing on them. The flame is stabilised on a sintered-bronze porous plug burner (McKenna burner), which is water-cooled and has a diameter of 60 mm. A concentric porous ring that surrounds the porous plug can

provide a steady co-flow of nitrogen or air but it was not used in these experiments because flame stability was impaired. The burner is mounted inside the vessel on a three-axis traverse system, which allows positioning of the probe volume on the centre line of the burner, and at different heights above the porous surface. Flow rates of methane and air are regulated using thermal mass flow controllers (Brooks SLA series). These units are calibrated with air using gas flow calibrators (MesaLabs FlexCal series) before the experiments to maintain an accuracy better than 1% for all conditions. The flame is ignited at atmospheric pressure by inserting a gas lighter through one of the side windows. The desired pressure set-point is then reached by slowly increasing pressure in the presence of the flame. The pressure is monitored by a pressure gauge (Omega Engineering) with a 0.25% accuracy. A S-type thermocouple (Pt/Rh) with a bead diameter of $d = 58$ μm is inserted in the vessel to measure the temperature of combustion products at the probe volume location for comparison with LIGS measurements.

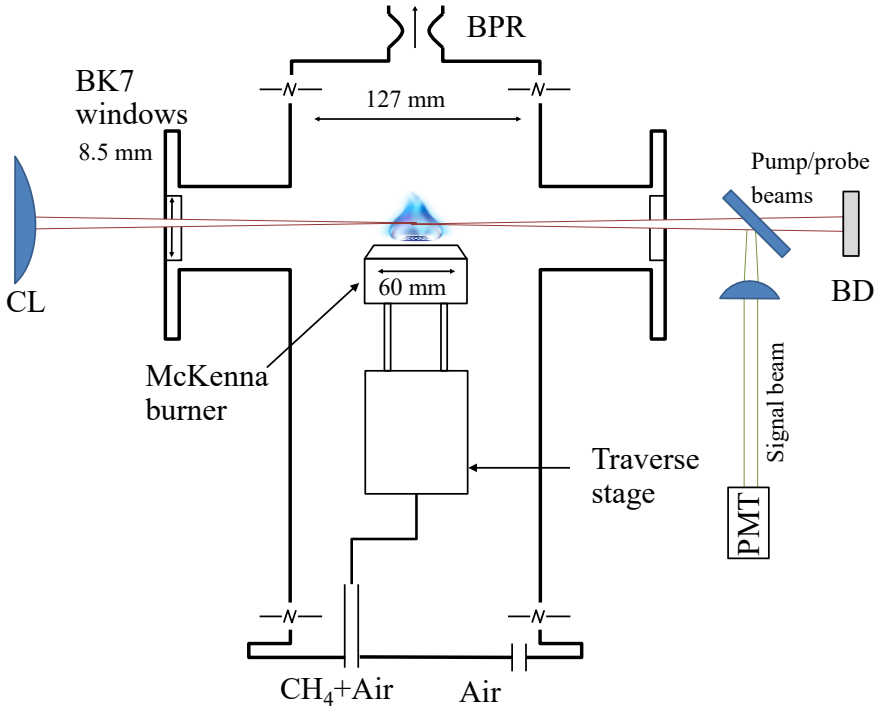

Fig. 8.2 Schematic of the pressure vessel used in the experiments, including the McKenna burner inside the enclosure. CL: crossing lens; BPR: back pressure regulator; BD: beam dump.

8.3 Results and analysis

LIGS measurements were conducted in pressurised premixed methane/air flames using the 1064 nm Nd:YAG laser as a pump for energies higher than 100 mJ per pulse. As a consequence, the signal obtained is the sum of contributions from the non-resonant (electrostrictive) process and the resonant (thermal) process due to the weak absorption of 1064 nm light by water molecules naturally present in combustion products. The LIGS signal oscillation frequency, and the corresponding speed of sound, is extracted from the power spectrum of the signal, while it is demonstrated that the relative amplitude of the electrostrictive and thermal peaks is an indicator of the local water concentration. LIGS temperature results are also compared to thermocouple measurements as well as simulations of burner-stabilised laminar premixed flames that include effects of conductive and radiative heat losses.

8.3.1 Signal description

Fig. 8.3 shows two examples of ensemble-averaged LIGS signals acquired in the vessel: the blue dotted line is a signal in laboratory air at room temperature and atmospheric pressure inside the vessel, and the red solid line is a signal in a flame at 4 bar. The pump laser pulse energy is set to 170 mJ and the probe power to 2 W. This combination of pump energy and probe power yields good signal-to-noise ratio and low standard deviations. The signal at room temperature and atmospheric pressure derives from electrostriction exclusively, because air molecules do not absorb radiation at the 1064 nm wavelength. The grating wavelength Λ of Eq. 6.2 is determined from this electrostrictive signal, for which the composition and temperature within the probe volume are known. A value of $\Lambda = 16\ \mu$m is found. The spacing Λ of the stationary grating is the same both in the air and in the flames, apart from the small distortion of the laser beams generated by the flame[2]. The red solid line shows the signal acquired in the products of a nearly stoichiometric flame at an equivalence ratio of $\phi = 0.95$ at 4 bar. The water molecules in the flame products absorb the 1064 nm light only weakly: the absorption cross section of water molecules at 1064 nm is around two orders of magnitude smaller than that of common absorbers used for LITGS, such as toluene and acetone at 266 nm ($\sigma \simeq 10^{-22}$ cm^2 for water versus $\sigma \simeq 4\ 10^{-20}$ cm^2 for acetone [33, 203] and $\sigma = \simeq 0.7\ 10^{-20}$ cm^2 for biacetyl [105]). Thus, more energetic pump pulses are needed to generate a detectable thermal grating in the flame. More than 100 mJ per pulse are required for water, compared to 1-10 mJ for acetone and toluene in [215]. With such high energies, a non-negligible electrostrictive grating is also generated, as can be observed in the first few nano-seconds of the signal (inset in Fig. 8.3). While the electrostrictive process is prompt,

[2]This effect has been evaluated to be nearly negligible for the flames analysed.

the thermal process is slower, and the onset of the LITGS occurs after an induction period associated with thermalisation of the absorbed radiation [165], so that the two contributions are separated by a time delay. A closer look at the first oscillations of the signal (inset in Fig. 8.3) shows that the electrostrictive contributions in air and in the flame yield a first electrostrictive peak within a few nanoseconds after the laser pulse (marked E) while the much larger thermal contribution in the flame signal appears after a longer time delay of roughly 15 ns (marked T).

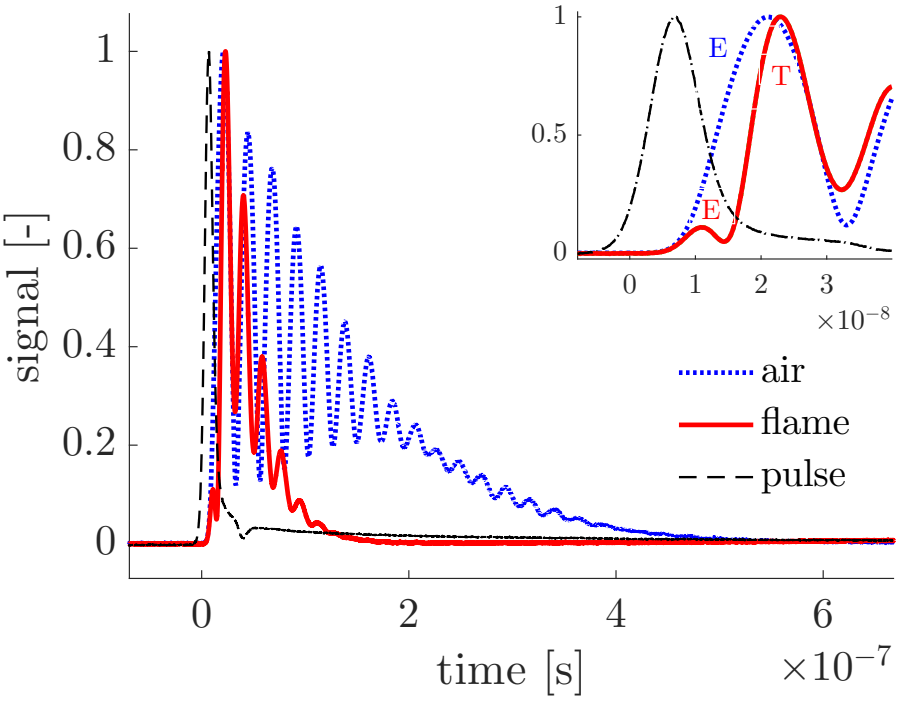

Fig. 8.3 Normalised LIGS signals ensemble-averaged over 1000 shots. Electrostrictive signal acquired in air at room temperature and atmospheric pressure (blue dotted line) and thermal+ electrostrictive signal in the products of a premixed CH_4/air flame with equivalence ratio $\phi = 0.95$ at 4 bar (red solid line). Black dashed-dotted line shows the pump laser pulse which triggers acquisition of the LIGS signals. Inset shows early times. Labels E and T refer to electrostrictive and thermal processes, respectively.

The top left panel of Fig. 8.4 shows a typical single-shot LIGS signal acquired in the combustion products of the flame with $\phi = 0.95$ at 4 bar. The contributions of the electrostrictive and thermal processes to the LIGS signal are clearly visible, but, as already noticed in Fig. 8.3, the amplitude of the thermal peak is much larger than the amplitude of the electrostrictive peak. The top right panel of Fig. 8.4 shows the power spectrum corresponding to this single-shot LIGS signal. In this power spectrum, only the peak associated with

the thermal contribution can be clearly identified, with an oscillation frequency of $f_T = 53.3$ MHz. This suggests that, while a first peak is detectable, the electrostrictive process does not contribute significantly to the LIGS signal as a whole. This happens because the electrostrictive contribution is immediately damped out. This effect has been reported earlier [190] and is due the cut-off frequency imposed by the laser pulse duration. As shown in [190], if the LIGS oscillation frequency is higher than the laser pulse cutoff frequency, the diffraction efficiency of the grating decreases due to the destructive interference between the acoustic waves generated at different times during the long excitation pulse. The laser pulse duration used in this study is $\tau_L = 12$ ns, defining a system cut-off frequency of $f_{co} \simeq 1/\tau_L = 83$ MHz, which is smaller than the electrostrictive frequency of this signal $f_E = 2 \times f_T \simeq 106.6$ MHz. Thus, the electrostrictive signal decays immediately after the first peak is generated, and its contribution cannot be further identified in the power spectrum. The bottom row of Fig. 8.4 shows the single-shot LIGS signal (left) and the corresponding power spectrum (right) for another flame at 4 bar that features a lower equivalence of $\phi = 0.60$. In this case, both contributions of the LIEGS and LITGS signals can be identified in the time (single-shot signal) and frequency (power spectrum) domains. This is attributed to the lower temperature experienced in this flame (due to a larger excess of air), which yields a smaller speed of sound and a smaller electrostrictive oscillation frequency of $f_E \simeq 78$ MHz $< f_{co} = 83$ MHz. In this case, the electrostrictive oscillations do not dissipate immediately, and the overlap of thermal and electrostrictive oscillations can be observed in time trace. Depending on pressure and equivalence ratio, the relative contributions of the LIEGS and LITGS signals vary. However, it should be noted that such contributions can always be distinguished clearly at early times. In this case, the amplitude of the thermal and electrostrictive peaks are similar: less water is produced by the flame due to the lower equivalence ratio, and this decreases the peak amplitude of the thermal contribution. Therefore, Fig. 8.4 shows that the ratio between the intensity of the first thermal (I_T) and electrostrictive (I_E) peaks is a function of the equivalence ratio. This ratio, $R_W = I_T/I_E$, has a value $R_W = 8.3$ for the example with $\phi = 0.95$, and a much smaller value, $R_W = 1.2$, for $\phi = 0.60$. Since the LITGS signal intensity is expected to be proportional to the water concentration, while the LIEGS signal intensity does not, the ratio R_W can provide a measure of the water concentration. Following this argument, the LIGS signals shown in Fig. 8.4 suggest that the water concentration is much larger in the products of the flame with $\phi = 0.95$ than that with $\phi = 0.60$. This is the expected result based on simple equilibrium calculations.

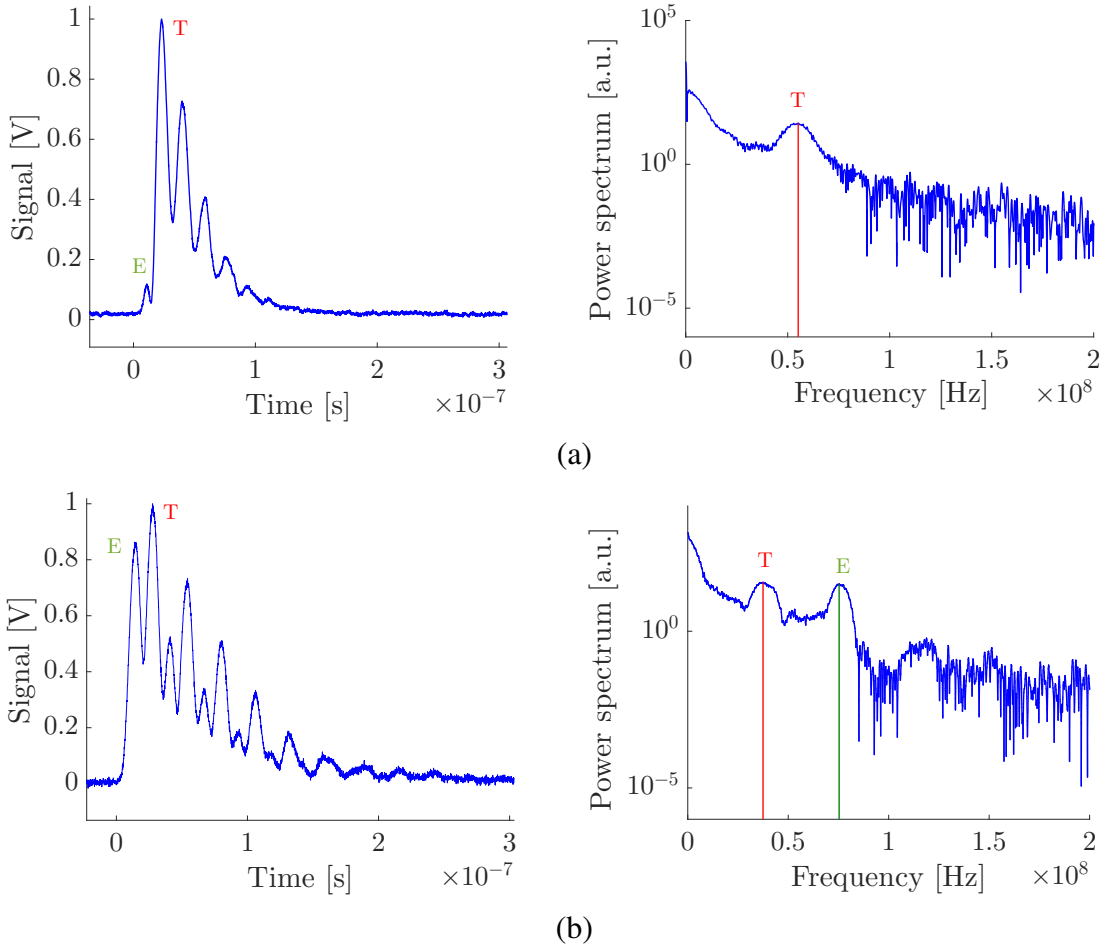

Fig. 8.4 Sample LIGS single shots acquired in the 4 bar flame. Time trace (left) and power spectrum (right). Nearly-stoichiometric flame, $\phi = 0.95$, 5 mm above the surface of the burner (a) and lean flame, $\phi = 0.60$, 10 mm above the surface of the burner (b). The vertical red and green lines in the spectrum indicate the peaks for thermalisation (T) and electrostriction (E) (in the time and in the frequency domains).

Calibration from reference conditions

Let $f_{E,0}$ be the electrostriction frequency in air and c_0 the corresponding speed of sound at room temperature T_0 used for calibration. The LIGS oscillation frequency in flames $f_{T,f}$ (taken here equal to that of the LITGS contribution f_T in the power spectrum of Fig. 8.4) is extracted from the power spectrum of the signals. From Eq. 6.5, assuming a negligible distortion of the beams due to the flame, the corresponding speed of sound c_f was obtained as:

$$c_f = 2\frac{f_{T,f}}{f_{E,0}}c_0 \tag{8.1}$$

The factor of 2 arises from the electrostriction index. Using a perfect gas equation and Eq. 8.1, the temperature in the combustion products T_f is determined as:

$$T_f = 4\frac{f_{T,f}^2}{f_{E,0}^2}\frac{\gamma_0}{\gamma_f}\frac{W_f}{W_0}T_0 \tag{8.2}$$

where W_0 and W_f stand for the air and combustion products molar mass, respectively.

Fig. 8.4 illustrates how the LITGS oscillation frequency $f_{T,f}$ can be extracted from the power spectrum of the flame signals, without relying on complex fitting algorithms. However, Eq. 8.2 shows that inferring the combustion product temperature requires the knowledge of the combustion product molar mass, which is *a priori* unknown. Normally, molar mass and specific heat capacity ratio are extracted from flame simulations or from complex models of LIGS signals (Sec. 6.3.1). The hybrid thermal-electrostrictive LIGS technique, reported here for the first time, may allow us to reduce uncertainties in determining the local composition by providing a simple relative measure of the water concentration. Indeed, the experimentally determined water concentration extracted from LIGS signals could be compared to simulated values to validate or improve the predictions on the local composition. Details on how this is achieved are shown in Sec. 8.3.4.

8.3.2 Pressure effects

Fig. 8.5 shows LIGS signals acquired in combustion products for a fixed equivalence ratio $\phi = 0.95$ and at different pressures. At atmospheric pressure, the LIGS signal has low amplitude and decays promptly. As the pressure increases, the signal amplitude and the number of peaks increase. Indeed, Stampanoni-Panariello et al. [190] showed that the signal intensity, I, and the rate of decay of the peak intensities, Γ, are both a function of the mixture density, ρ, as follows:

$$I \propto \rho^2 = \left(\frac{PW}{RT}\right)^2; \qquad \Gamma \propto \frac{1}{\rho} = \frac{RT}{PW} \tag{8.3}$$

thus increased densities lead to higher signal amplitudes and lower decay rates, both of which are desirable for robust LIGS measurements. The number of ringings in the signals increase with pressure, so that signals at 4 bar already display 6/7 oscillations, which lead to a maximum error in the frequency determination from the power spectrum $\Delta f/f < 1.2\%$ (See Sec. 6.3.5). In the product region of flames, the signals at ambient pressure have a low amplitude and decay almost immediately, due to the high temperature and low density. On the other hand, at higher pressures, effects of beam steering due the density and temperature gradients are more pronounced. This could have a detrimental effect on spatial resolution. Various techniques have been suggested to mitigate the issue, such as enlarging one of the two pump beams to obtain an elliptically-shaped beam, which provides a more robust overlap despite the steering caused by the flame [143]. This technique has not been implemented here because only laminar flames are examined and temporal fluctuations of density are small, limiting beam steering.

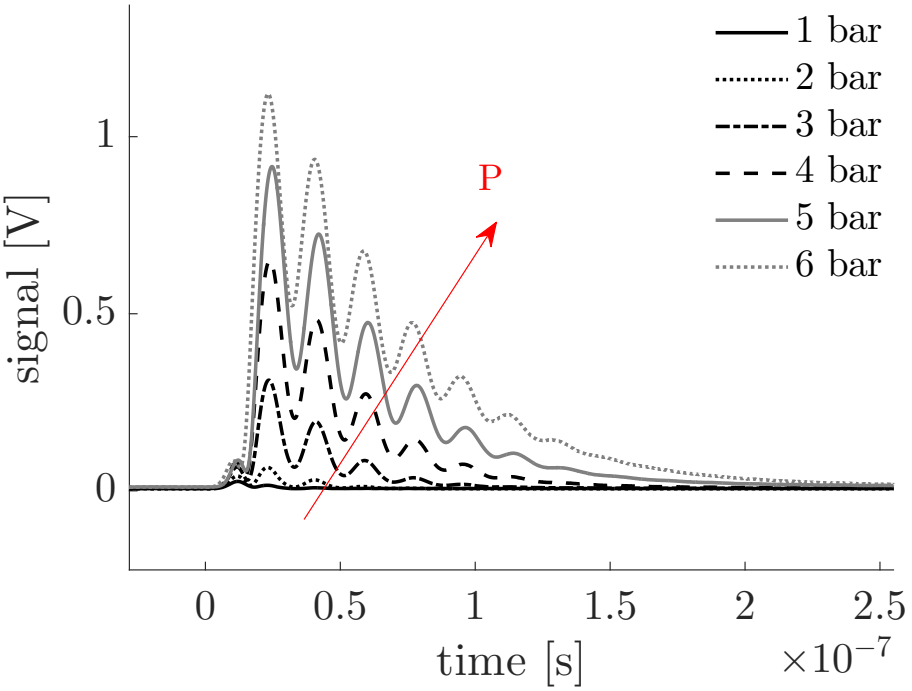

Fig. 8.5 Ensemble-averaged LIGS signals acquired in the products of nearly stoichiometric flames ($\phi = 0.95$) at different pressures, 5 mm above the surface of the burner.

8.3.3 Pump energy effects

Fig. 8.6 (left) shows ensemble-averaged LIGS signals acquired for pump pulse energies ranging from 75 to 350 mJ. A larger pump laser irradiance (*e.g.* energy per unit time per unit area) yields LIGS signals of larger amplitude owing to the stronger thermal grating generated. The measured LIGS oscillation frequency remains constant for the different energies considered (Fig. 8.6 (right)), indicating that the gas mixture within the probe volume is not being significantly heated due to the energy delivered by the pump beams. For thermal LIGS, this test is needed to verify the non-intrusiveness of the technique [94] (See Appendix A). A large absorption cross section of the resonant molecule typically increases the risk of introducing excessive thermal energy to the probe volume. Because the absorption cross section of water at 1064 nm is not large, this effect is less likely to occur, and this is confirmed by Fig. 8.6 (right). The same figure shows that the standard deviation (thus the precision) of the measurements does not change for energies higher than 125 mJ, thus it is optimal to operate using energies in the range 125-350 mJ for the current optical set-up.

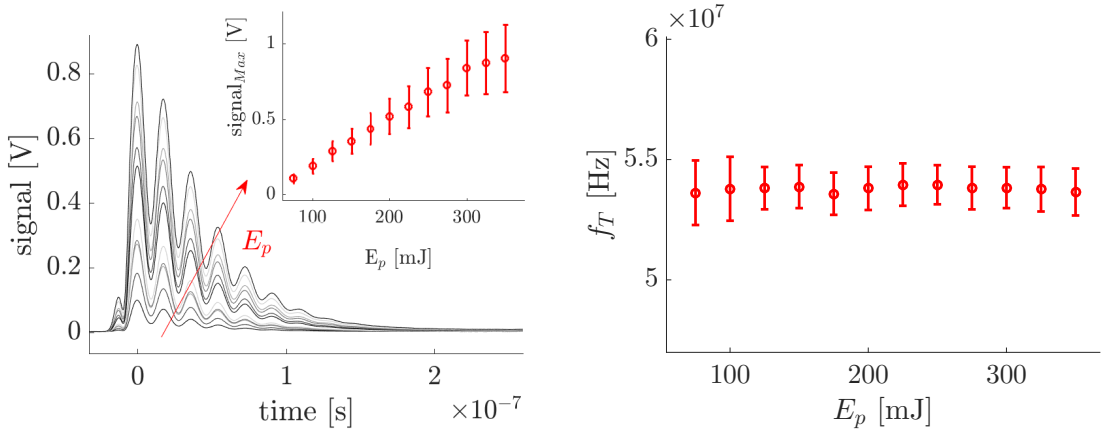

Fig. 8.6 Ensemble-averaged LIGS signals acquired in the products of a nearly stoichiometric flame ($\phi = 0.95$) for a pressure of 4 bar and increasing pump pulse energies from 75 to 350 mJ. Inset shows the average signal amplitude for each pump energy level. Error bars represent plus/minus one standard deviation in the measurements (left). Measured LIGS oscillation frequency as a function of pump energy (right).

8.3.4 Measurements in flames at 4 bar

LIGS was used to determine the local speed of sound, water concentration, and temperature in the products of lean-to-rich premixed methane/air flames at 4 bar. The measurements shown here were conducted 5 mm above the surface of the burner, in the product zone. The equivalence ratio was varied from $\phi = 0.73$ to $\phi = 1.30$ by varying the fuel mass flow

rate while keeping the air mass flow rate constant. For each flame, 1000 LIGS shots were acquired. The pump laser pulse energy was set to 170 mJ and the probe power to 2 W.

Speed of sound measurements

Fig. 8.7 compares the speed of sound inferred from LIGS measurements (based on Eq. 8.1) with predictions obtained with stabilised flame simulations.

The premixed flame species and temperature are modelled using the Chemkin software suite [5] using the burner-stabilised flame module with gas radiation, which accounts for heat losses to the surroundings. The required boundary conditions are the fresh reactant mass flow rate (which is prescribed in the experiments and, therefore, known) and the porous surface temperature (which was measured with a thermocouple). The GRI MECH 3.0 detailed chemistry mechanism (specifically the C2-NOx chemistry mechanism) [188] was used to define chemical reactions and reaction rates, thermodynamic properties, and transport properties because it is known to perform well for methane fuel over wide ranges of equivalence ratio and pressure. The radiation heat loss to the environment from gas products in the flame and post-flame region is also included using the radiation heat-transfer model and an optically-thin limit for both gas and dispersed phase [202]. The molecular weight used to determine the temperature from the speed of sound corresponds to those calculated in the product region of the flame, in the region where heat losses are still insignificant, as determined above. Nevertheless, in general, a potentially better route for model validation is to directly compare sound speeds obtained from LIGS rather than temperatures. The error bars in Fig. 8.7 represent plus/minus one standard deviation (σ_c) in the measurements. The precision of the measurements, evaluated as $\sigma_c/\bar{c}$ is 1.4-1.7%. The agreement between simulations and experiments is very good at rich equivalence ratios, with discrepancies limited to 0.5%. For lean flames, the measured speed of sound is larger than the calculated speed of sound by up to 2.5%. A similar mismatch between experiments and simulations has been reported in [95] for lean flames at atmospheric pressure, also stabilised with a McKenna burner and using a data fitting algorithm to post-process LITGS signals in the time domain. The mismatch may therefore be inherent to inaccuracies of the simulations.

Temperature measurements

Fig. 8.8 shows the temperature of the combustion products derived from the oscillation frequency measurements using Eq. 8.2. The mixture values of specific heat capacity ratio γ and molecular mass W of the flame products are extracted from the outputs of the burner-stabilised flame Chemkin simulations. Good agreement is obtained between experiments

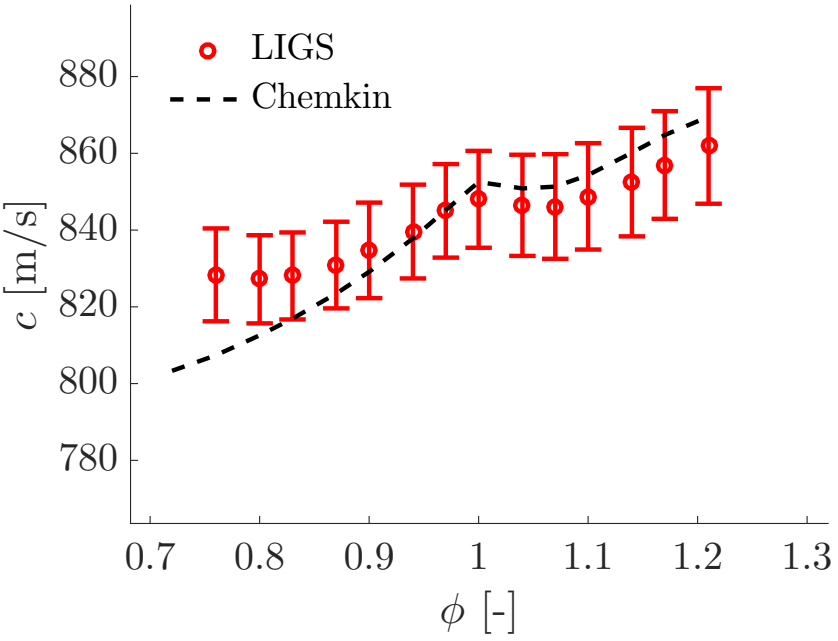

Fig. 8.7 Speed of sound c as a function of equivalence ratio ϕ for flames at 4 bar. Dashed lines show calculated values of speed of sound from stabilised flame simulations using Chemkin. Error bars represent plus/minus one standard deviation in the measurements.

and simulations for nearly stoichiometric and rich conditions. For lean flames, the measured values are larger than the simulated ones by about 4.5%, echoing the mismatch observed in the speed of sound. To further investigate this mismatch, additional thermocouple measurements were made using a S-type thermocouple in a separate experiment in which LIGS was not activated and the thermocouple bead was placed at the exact same location as the LIGS the probe volume. The temperatures measured by the thermocouple (TC) are considerably lower than the measured LIGS and simulated Chemkin values and this is due to large radiative heat losses occurring at the bead of the thermocouple. The radiative heat losses can be corrected for, but the accuracy of the correction depends on the accuracy of the heat exchange model used [128]. Due to the complexity of the inner geometry of the vessel, as well as the difficulties in defining the emissivity of the various surfaces and their temperature, it is only possible to provide an interval of confidence within which the actual combustion products temperature is expected to be. This interval is confined by an upper (TC h, dashed-dotted line) and a lower limit (TC l, dotted line), which are calculated by considering two extreme scenarios. The higher limit refers to a condition where the thermocouple is modelled as a small sphere in a cold vessel, without accounting for the proximity of the burner surface. For the lower limit, the burner surface is included in the heat exchange model. These two limits

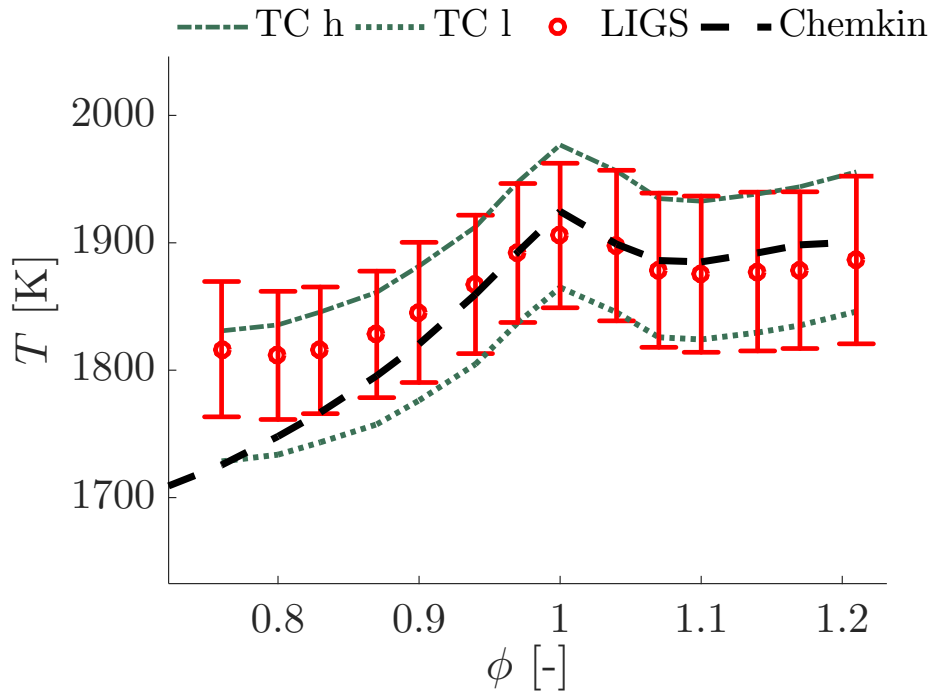

Fig. 8.8 Temperature of the combustion products measured 5 mm above the burner surface as a function of the equivalence ratio for flames at 4 bar. LIGS measurements (red circles), Chemkin simulations (dashed line), thermocouple measurements corrected for radiative heat losses: lower limit (dotted line) and upper limit (dashed-dotted line).

define an interval of approximately 100 K that brackets the LIGS measured and simulated temperatures. Although uncertainties in the thermocouple measurements, the slope of the temperature profile from thermocouple at low equivalence ratio matches better the LIGS output than the Chemkin simulations, further lending evidence for the possibility that the Chemkin model might be inadequate at lower equivalence ratio. The comparison offers further proof that the LIGS configuration used in this study allows measuring accurately the temperature in the products of lean-to-rich premixed flames at a pressure of 4 bar.

Water concentration measurements

Fig. 8.9 demonstrates a suggested calibration procedure to obtain water concentrations from the ratio of the thermalisation first peak amplitude I_T to the electrostriction first peak amplitude I_E. The amplitude (in Volts) of the first electrostrictive LIEGS peak, I_E, is proportional to the pump energy E_p while the amplitude of the first thermal LITGS peak, I_T, is proportional to the product of the pump energy and the mole fraction of water, $E_p X_w$. Therefore, the ratio I_T/I_E is expected to be linearly proportional to the water mole fraction ($I_T/I_E \propto X_w$) but,

as this value is set-up dependent, it requires calibration. A linear correlation between the peak amplitude ratio and the water concentration is demonstrated in Fig. 8.9 (left), where the experimentally determined ratio I_T/I_E is plotted against the water concentration X_W obtained from Chemkin simulations:

$$\frac{I_T}{I_E} = \alpha X_W + \beta \tag{8.4}$$

For this set-up, the values $\alpha = 120.2$ and $\beta = -14.1$ are obtained from the experimental data in Fig. 8.9 (left) using a least squares linear fitting, determining the interpolation line. Using these values α and β, the local value X_W can be extracted from the ratio I_T/I_E for any LIGS signals, and Eq. 8.4. Fig. 8.9 (right) compares the experimentally determined X_W with the output of Chemkin simulations for each equivalence ratio ϕ. Agreement between measurements and simulations is good, confirming that the hybrid LIGS configuration used in this study allows the accurate measurement of water mole fractions in the products of lean-to-rich premixed flames at a pressure of 4 bar, as long as the set-up dependent calibration data is provided. Experimentally determined water mole fractions in the probe volume can be used to verify the predicted values from flame simulations and improve the overall accuracy of LIGS by confirming the mixture composition. A correlation between the relative amplitude of the thermal and electrostrictive peaks and the absorber concentration was first shown for a propane - air non-reacting mixture [116]. We demonstrate here for the first time the applicability of such method in reacting flows and at elevated pressure using water as an absorber.

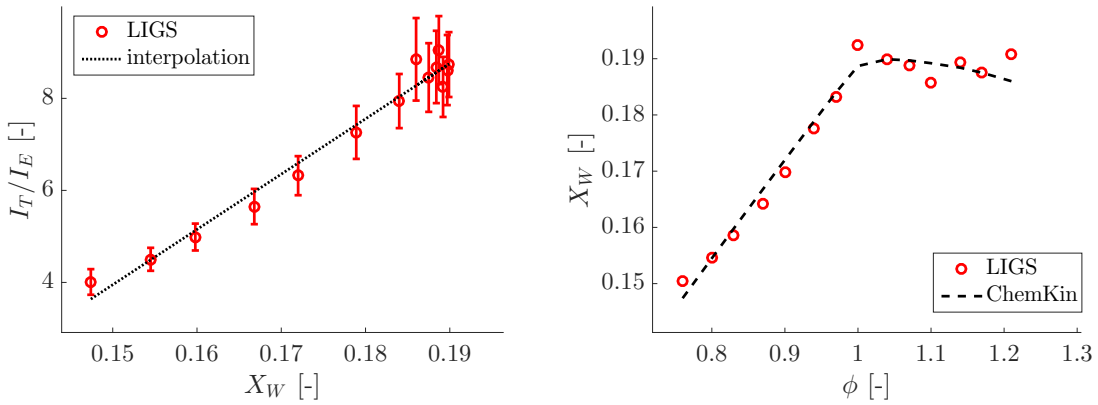

Fig. 8.9 Relationship between water concentration X_W and thermal-to-electrostrictive peak intensity ratio I_T/I_E for flames at 4 bar (markers). Dotted line shows the linear interpolation of the data (left). Water concentration versus equivalence ratio: experimentally derived from LIGS measurements (markers) and calculated using Chemkin simulations (dashed line) (right).

8.4 Discussion and further development

In this chapter, we show that LIGS using the widely available 1064 nm wavelength is a versatile and robust technique to detect the local speed of sound, temperature, and composition in a pressurised combustion environment. Water naturally produced from combustion absorbs the 1064 nm light and generates the thermal grating: no external tracers have to be added to the flow. Since water lines at 1064 nm are relatively weak, the energies required to obtain detectable thermal LIGS are sufficiently high to generate a non-negligible electrostrictive signal as well. The electrostrictive signals acquired in air are used for calibration. In most of the flames data acquired in the products zone, the combination of pulse width, temperature and grating spacing makes the electrostrictive signal decay after the first oscillation. Clearly detectable electrostrictive signals in flames might be obtained, for example, by using a pump laser wavelength not resonant with the flame products. By using a 1064 nm pump laser at energies higher than 100 mJ, as described in this chapter, cold reactants or colder regions of incomplete mixing (electrostriction) and hot product regions (electrostriction and thermalisation) can be probed. However, the main limitation of these measurements is the lack of time resolution, as the pump laser is pulsed at 10 Hz, allowing only the acquisition of averaged values of the flame properties. In Chapter 9 we demonstrate the use of a 1064 nm pulse burst laser, which can deliver 133 mJ at 100 kHz, to obtain high repetition rate LIGS measurements. However, pulse burst lasers are extremely expensive, unstable and can only generate bursts of 10 ms, after which they need a cooling time of several seconds. Thus, other strategies are needed to obtain more affordable and more versatile high repetition rate LIGS measurements in reacting flows.

8.5 Conclusions

In this chapter, LIEGS and LITGS measurements using 1064 nm pump wavelengths have been demonstrated in laminar premixed CH_4/air flames at elevated pressure. We showed that for moderate pulse energies (around 100 mJ per pulse), the LIGS signal consists of a combination of effects from the electrostrictive and the thermal contributions associated with low absorption by water molecules. At atmospheric conditions, the high temperature in the flames causes a nearly immediate dissipation of the transient grating, so that the LIGS signals acquired at 1 bar have a low amplitude and are insufficient to clearly identify the oscillation frequency. At increased pressures, the density of the gas in the probe volume increases and sufficiently strong signals are generated. For pressures larger than 3 bar, LIGS signals have a large enough number of oscillations and good signal-to-noise ratio to clearly

allow measurements of their oscillation frequency. Experiments conducted in combustion products of different equivalence ratios at 4 bar showed that the ratio between electrostrictive and thermal peaks is related to the water concentration in the probe volume. For the first time, temperature and water concentration measurements are obtained simultaneously from LIGS signals in pressurised flames. The experimentally determined values of speed of sound, temperature, and water concentration are shown to compare well with the simulated values using Chemkin. This work demonstrates that 1064 nm LIGS is a suitable and versatile technique to perform temperature and composition measurements in high pressure/high temperature reacting flows. As water is a common product of flames, this technique is particularly suitable to diagnose flames of industrial interest, as it does not require the addition of any absorbers to the flow, and it is significantly less complicated than CARS. Since LIGS is a relatively simple technique which requires limited optical access to the measurement volume and offers simple data analysis, it is a good candidate detect temperature and composition simultaneously with time and space resolution in combustion chambers. In summary, the work described in this chapter opens up the possibility of temperature and water measurements in regions of challenging optical access, such as high pressure gas turbines, engine combustion chambers and reactors by using relatively inexpensive light sources and optics.

Chapter 9

Use of a pulse burst laser for tracer-free LIGS measurements at 100 kHz

This chapter shows the first application of a burst laser for laser-induced grating spectroscopy. A Nd:YAG pulse burst laser is used as pump laser to perform high repetition rate (100 kHz) LIGS in non-reacting and reacting flows. Thermal gratings are obtained in the products of a premixed laminar methane/air flame from the absorption of 1064 nm light by weak water vapour lines and compared with data at 10 Hz, showing good agreement. It is also verified that soot particles, acting as black bodies, can absorb 1064 nm laser light and generate detectable thermal gratings for the pump energies delivered by the burst laser (E_p= 133 mJ per pulse). These results suggest that a pulse burst laser can potentially allow high-repetition rate, tracer-free LIGS measurements both in sooty and non-sooty reacting flow environments. The highly energetic pulses also allow the generation of a detectable laser-induced electrostrictive grating. Time-resolved, high repetition rate LIEGS measurements are demonstrated for the first time using an air/helium jet modulated with a loudspeaker. However, some issues of such application due to the high energies involved are highlighted[1].

9.1 Introduction

A significant shortcoming of the available pulsed laser systems is the trade-off between maximum repetition rate and energy per pulse that they can deliver. The repetition rate is primarily limited by the thermal loading of the laser components, which need to be cooled down by circulating water or air. Highly energetic pulses ($E_p > 100$ mJ), necessary for LIEGS, are usually only obtained from low repetition rate systems (10 Hz). High repetition

[1]The results of this chapter are published in *Optics Express* [47]

rate PIV lasers, instead, can operate at 10 kHz, but they deliver pulse energies too low to generate detectable electrostrictive gratings. For these reasons, to date there have been no high repetition rate LIEGS measurements. The recently developed pulse burst laser can generate highly energetic pulses ($E_p \simeq 100$ mJ) at high repetition rates (0.1-1 MHz). However, the laser can only fire for a window of time (a burst lasts 10-100 ms), and then it needs to cool down for about 10-20 s.

In this chapter, for the first time, a Nd:YAG pulse burst laser is used as pump laser for LIGS. Using the fundamental harmonic at 1064 nm, the energy of each pulse, around 133 mJ, is sufficiently high to generate detectable thermal gratings in flames and electrostrictive gratings. As a proof of concept, LIGS signals at 100 kHz are obtained while probing the product region of the premixed methane/air flames at 4 bar already analysed in Chapter 8, where thermal LIGS signals are obtained by the absorption of 1064 nm light by weak water vapour lines. The 100 kHz data compares well with the measurements previously obtained at 10 Hz (Sec. 9.3). We also show that soot particles, acting as black bodies, can absorb the laser light and generate detectable thermal gratings for such pulse energies (Sec. 9.4). Finally, high repetition rate-time-resolved electrostrictive LIGS measurements are obtained in a sinusoidally-modulated helium/air jet (Sec. 9.5). In this simplified configuration, we demonstrate how the high energies involved can generate some issues, such as a drift of the beams. These results suggest that 100 kHz LIGS diagnostics using pulse burst lasers can be potentially applied to reacting flows to detect unsteady phenomena, but corrections due to the behaviour of the lasers are needed.

9.2 Experimental set-up

9.2.1 Pulse burst lasers

A pulse burst laser is a laser which can deliver short pulses (less than 10 ns width) at high repetition rate (0.1-1 MHz), over bursts of 10-100 ms, followed by a cooling time of 10-20 s. The first burst laser was developed by Huntly [112] and Grace et al. [89] in the nineties. This ruby laser delivered pulses of hundreds of mJ at 500 MHz for about 140 μs, but it needed to cool down for minutes. A new generation pulse burst laser was constructed by Lempert et al. [129], and further developed by Wu et al. [219]. This Nd:YAG laser generated pulses of 1 mJ at rates up to 1 MHz. Thurow et al. [205] improved the system, building a second generation burst laser delivering 99 pulses of 100 mJ with a maximum repetition rate of 1 MHz. Further upgrades [206] increased the uniformity, flexibility and stability of the pulses.

In this latter design, which is referred to as "third generation" system, the burst is initially generated at low power using a master oscillator power amplifier made by a continuum wavelength Nd:YAG laser. Acoustic-optical modulators (AOM) are used to slice pulses of light, forming a burst of low-energy pulses, which are then amplified by a factor of 10^5 by a chain of three flash lamp-pumped double-pass Nd:YAG rod amplifiers cooled with water.

The Nd:YAG pulse burst laser used in the experiments (Spectral Energies Quasi-Modo), delivers 7 nanosecond long pulses of 133 mJ each in the fundamental harmonic. Each burst lasts a maximum of 10 ms, for a total of 133 J per burst at 100 kHz, and is followed by a waiting time of 10-20 s.

9.2.2 Optical layout

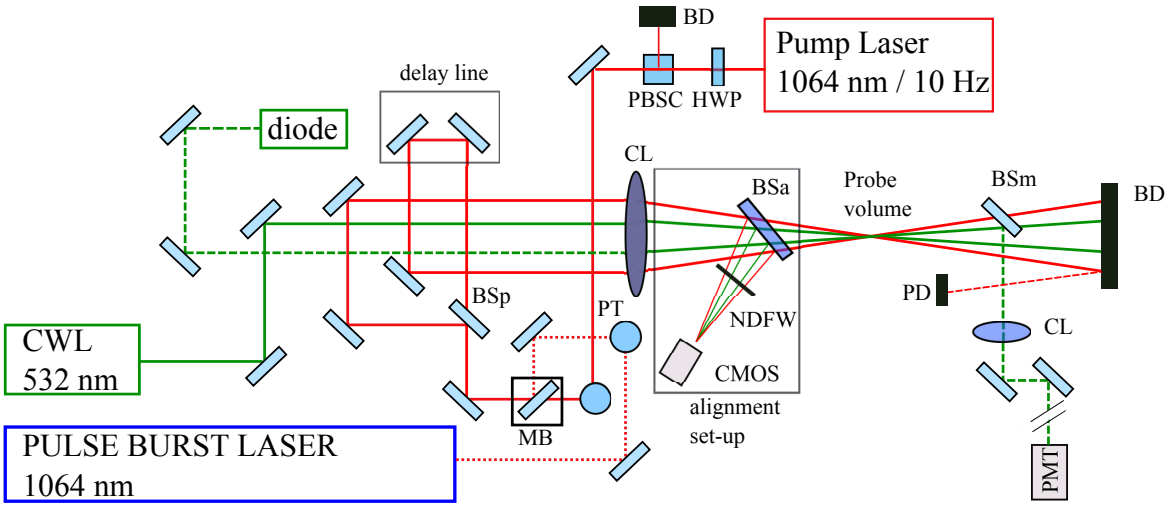

Fig. 9.1 Optical layout of the experiment. For the meaning of the terms see Fig. 8.1. MB: magnetic base.

The optical layout of the experiment is sketched in Fig. 9.1. This experiment shares the same optical table with the low-frequency set-up described in Chapter 8 (Sec. 8.2). A magnetic base (MB) allows a swap between the low and the high repetition rate pump beams. Three pinholes are placed in the beam path to adjust the overlap between the 10 Hz and the 100 kHz beams. The pulse burst laser is seeded, which means that light from a

single-frequency CW laser is injected into the pulsed beam at the beginning of the buildup period. As the seeding beam perfectly overlaps with the pulsed beam, it can be used for aligning the laser, so the operator does not need to wait for the bursts.

9.3 LIGS in flames using water as an absorber

In this section we aim to demonstrate the applicability of the pulse burst laser to LIGS diagnostics in a reacting flow environment. We compare the speed of sound and water concentration from LIGS signals using the 100 kHz pulse burst laser and the 10 Hz laser. The measurements were only performed in steady laminar flames due to limitation of the pressure vessel, which was too small to sustain the flow rates and power required by turbulent/unsteady flames. As the two lasers share the same optical arrangement, the alignment parameters (such as grating spacing) are nominally the same. The measurements were conducted at the same location, 5 mm above the surface of the burner, in the product zone. A total of 200 pulses of 133 mJ each were delivered at 100 kHz from the pulse burst laser. This burst duration (2 ms) was chosen to reduce the thermal load on the windows of the vessel.

9.3.1 Signal characterisation

Fig. 9.2 shows ensemble averaged LIGS signals acquired in the the methane/air flame (with an equivalence ratio of $\phi = 0.95$) obtained with the high (black) and low (red) repetition rate lasers. The thermal (T) and electrostrictive (E) peaks are marked on the figure. The two signals display the same oscillation frequency and the same number of peaks, but they differ in their contrast (*e.g.* peaks vs valley amplitude ratio). This is linked to the pump laser pulse duration: the longer the pulse, the higher the destructive interference between the sound waves generated in the probe volume, which reduces the contrast in the signal. Indeed, the pulse width (dashed line) of the burst laser is shorter than that of the 10 Hz laser, yielding a better signal contrast. Previous work [190] demonstrated that the contrast and decay rate of LIGS signals provide information about the local density and composition, but it depends on the characteristics of the pump laser pulse, as shown in Fig. 9.2. Thus, a specific calibration is needed prior using the signal shape to infer information about the gas in the probe volume. The pulse width of the laser is linked to the laser settings, such as the Q-switch level. Therefore, different signal contrasts might occur even using the same laser if the settings are changed during the experimental campaign.

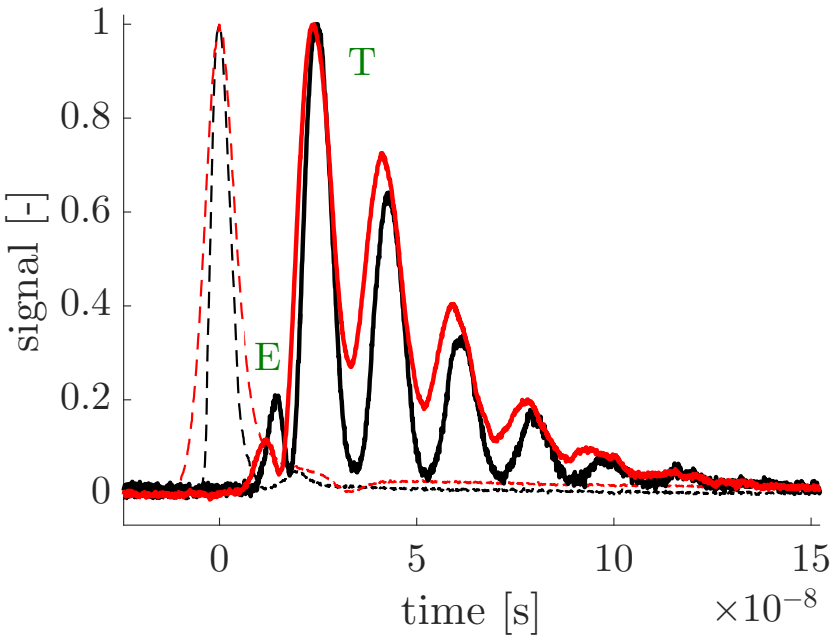

Fig. 9.2 Comparison between 100 kHz (black) and 10 Hz (red) LIGS signals in premixed methane/air flames at 4 bar. Normalised LIGS signals (solid line) and laser pulses (dashed lines).

9.3.2 Speed of sound, temperature and water measurements

The equivalence ratio in the flames was varied from $\phi = 0.73$ to $\phi = 1.30$ by varying the fuel mass flow rate while keeping the air mass flow rate constant, as done at 10 Hz in Chapter 8. Fig. 9.3 (left) compares the speed of sound obtained from LIGS signals with the 100 kHz (black) and the 10 Hz (red) lasers and with the predictions from burner-stabilised flame simulations using Chemkin (dashed blue line). The speed of sound is extracted from the oscillation frequency of the signals, according to Eq. 6.5. Then, the temperature is derived by using the molecular mass and specific heat capacity ratio from Chemkin simulations (Fig. 9.3, right), as discussed in Chapter 8.

The water concentration (Fig. 9.4, left) is derived after calibration (Fig. 9.4, right) using the intensity ratio between the thermal and electrostrictive peaks in the signal, as explained in Sec. 8.3.4. The calibration curves obtained for the low and high repetition rate laser sources are shifted and this is attributed to the different signal contrasts. After calibration, results at high and low frequency agree by 0.2-1.2% for the speed of sound and by 0.2-1.7% for the water concentration, suggesting that high repetition rate measurements of temperature and

water concentration can be made in reacting flows using a 1064 nm pulse burst laser and water as an absorber.

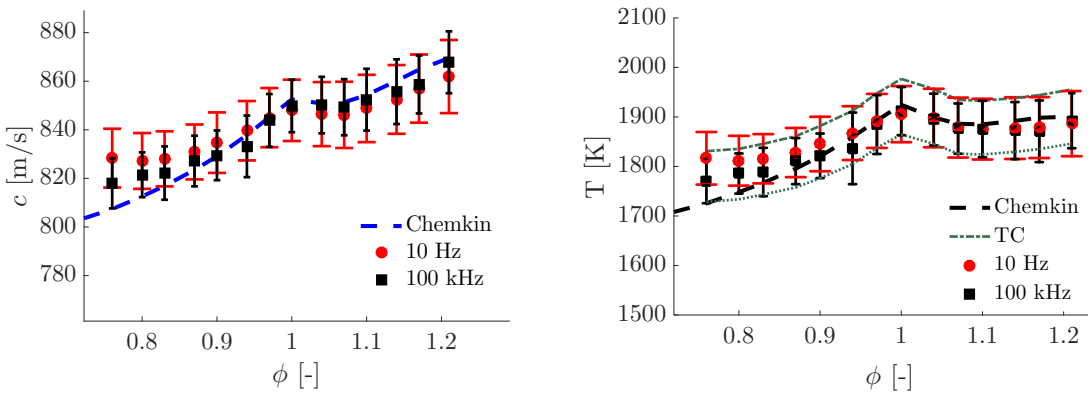

Fig. 9.3 Comparison between 100 kHz (black squares) and 10 Hz (red dots) LIGS measurements in premixed methane/air flames at 4 bar. Measured speed of sound and comparison with Chemkin results (dashed line) (left); temperature derived from LIGS and comparison with Chemkin results (dashed line) and thermocouple measurements (dotted lines) (right).

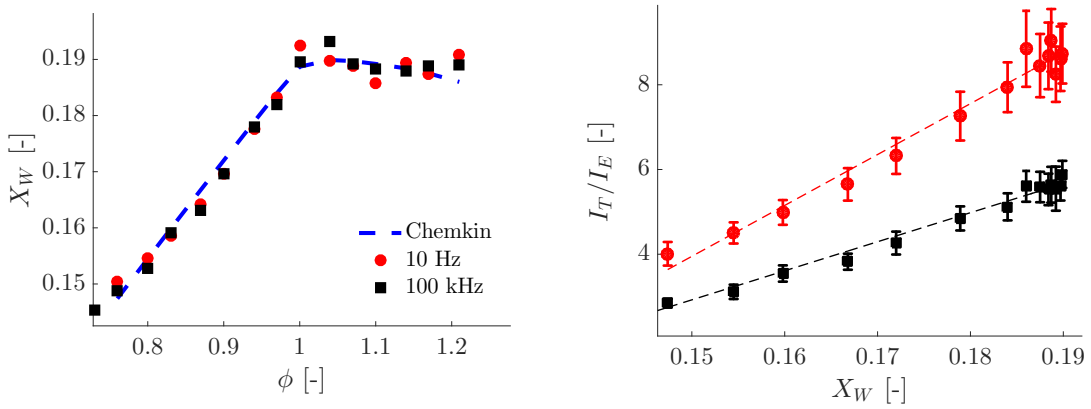

Fig. 9.4 Water concentration from LIGS measurements at 10 Hz (red dots) and 100 kHz (black squares) and comparison with Chemkin (dashed line) (left). Calibration curves derived with the procedure described in Sec. 8.3.4 (right).

9.4 LIGS in flames using soot as an absorber

Fig. 9.5 shows the normalised averaged (over 170 shots) LIGS signal obtained in a sooty C_2H_2/air flame with equivalence ratio $\phi = 2$ (yellow), compared with the signal obtained using water as an absorber in the premixed CH_4/air flame of Fig. 9.2 (blue). It was

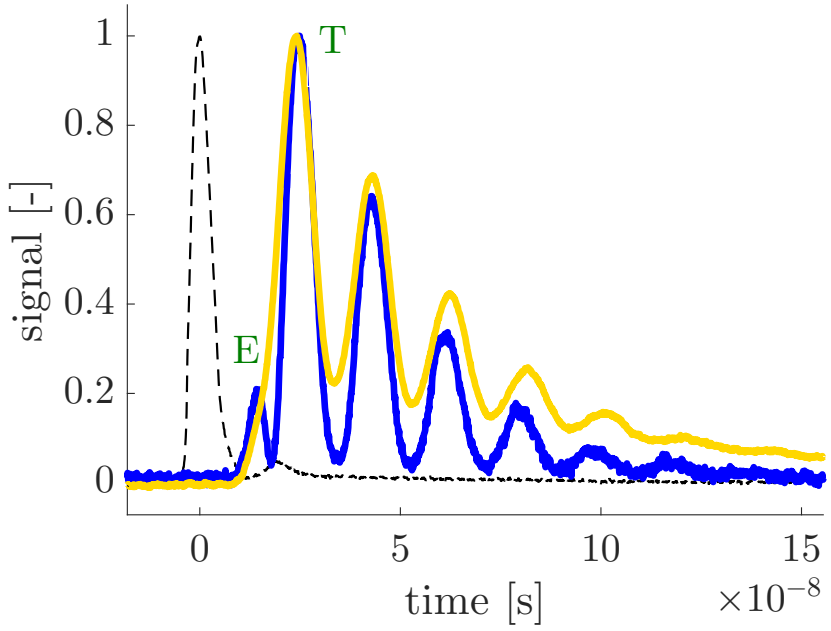

Fig. 9.5 Comparison between LIGS signals in the flame products for a non-sooty CH_4/Air flame, $\phi = 0.95$ (blue) and a sooty C_2H_2/Air flame, $\phi = 2$ (yellow) at 4 bar.

demonstrated [26, 100] that soot particles, acting as a black body, can also absorb laser light and generate a detectable thermal grating for sufficiently high laser pulse energies. The contrast and rising/decay rates of the two signals are different, due to the different quenching characteristics of soot and water. This data seems to confirm that seeding-free thermal LIGS measurements can also be performed in the sooty regions of a flame using the 1064 nm laser source and pulse energies of the order of 100 mJ. However, soot particles can be burnt and or made incandescent by the highly energetic pump laser pulses. The incandescence generates light with a broad wavelength spectrum (LII signal), which propagates in all directions and is therefore also collected by the PMT, causing a shift in the baseline of the signals. This effect is shown in Fig. 9.6. On the left, we plot the LIGS single shots acquired every 0.1 ms during a burst (each burst is 1.7 ms long). The baseline voltage of the signals (V_1) shifts in time, rising in the first shots, and then slowly decreasing and finally it stabilises to zero. The change in the baseline is shown in Fig. 9.6 (right), where the baseline voltage (V_1) of the LIGS signal is plotted versus time during a burst. The evolution of the baseline voltage V_1 resembles the characteristic shape of a LII signal. When, instead, the soot particles are completely burnt by the laser, sparks of light, which distort the signal and can saturate the PMT, might be generated. These effects are worsened by the high energy/high repetition rate pulses of the burst laser, which do not leave enough time to the medium for releasing the

absorbed energy between one shot and the other (for water, this is not an issue as the energy absorbed in a pulse is quickly released before the beginning of the next pulse). Thus, soot might be used as an absorber for LIGS, but care must be taken to verify the non intrusiveness and the saturation limit of the measurements. As there is no information about these issues in the literature, further investigations are ongoing.

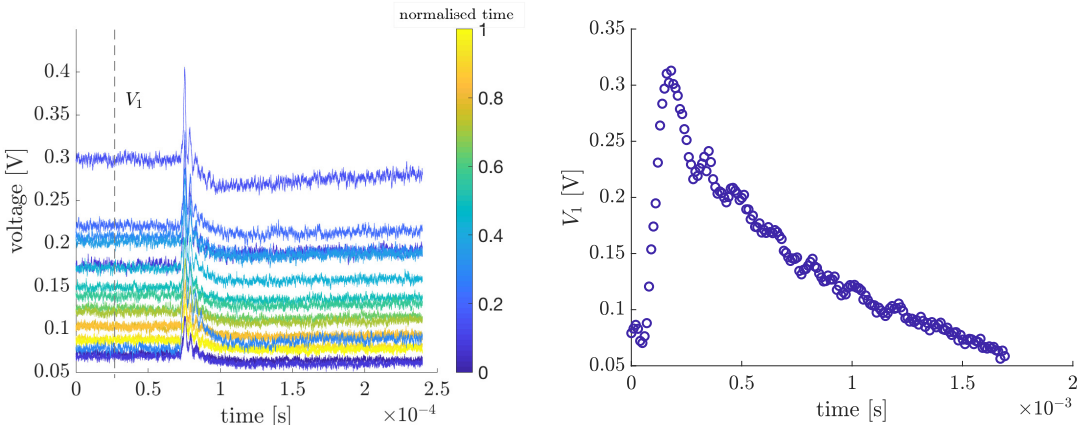

Fig. 9.6 Evolution of the LIGS signals during a 1.7 ms burst using soot as an absorber, with single shots displayed every 0.1 ms (left); shift in the baseline due to the straight light generated in the probe volume (right).

9.5 LIEGS at 100 kHz in a modulated helium/air jet

9.5.1 Experimental set-up

LIEGS measurements are performed in a sinusoidally modulated jet of helium and air (Fig. 9.7). A flow of helium (5 slpm) is continuously delivered into a plenum, which is then connected to a 3/8" vertical pipe. A loudspeaker driven at 300 Hz modulates the helium flow entering the pipe. At a distance of 200 mm downstream of the exit of the plenum, a steady flow of air from a choked valve (10 slpm) is added to the helium flow using a T-junction. The air-helium mixture then travels through the metal pipe for 200 mm before exiting into the room. The probe volume is located in the centre of the jet, 3 mm above the exit of the pipe.

9.5.2 Results: time-resolved electrostrictive LIGS

We discuss advantages and disadvantages of the use of a pulse burst laser as pump for LIGS measurements in a simplified experiment using the helium/air jet (Fig. 9.7). The pulse burst

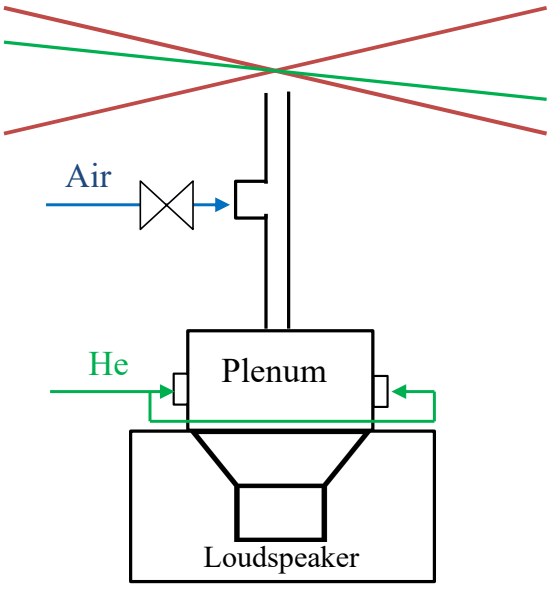

Fig. 9.7 Schematic of the air/helium jet used in the experiment. Not to scale.

laser is operated at a repetition rate of 100 kHz, delivering 1000 pulses of 133 mJ each per burst. The cooling time between bursts is set to 20 s.

Measurements in the steady flow

We initially performed LIGS in a steady flow of air (10 slpm) and in a steady mixture of helium (5 slpm) and air (10 slpm), where the concentration of helium is 6.3% by mass. The goal of this experiment was to investigate the behaviour of the system and evaluate the evolution of the LIGS signal during the burst. As the helium and air molecules do not absorb 1064 nm radiation, no thermal gratings were formed, thus the signals were generated only from electrostriction. Fig. 9.8 shows the two normalised single shot LIEGS signals obtained in the jets with different compositions: the red signal was acquired in pure air, while the black signal was acquired in the steady mixture of air and helium. Helium has a lower density than air, thus both the speed of sound (and consequently the LIGS oscillation frequency) and the damping rate of the sound waves are higher, as already noticed for the thermal LIGS signals (Sec. 7.3.2, Chapter 7).

Fig. 9.9 (left) shows the evolution in the frequency of the LIEGS signals for the 1000 consecutive single shots of one burst (*i.e.* for a time of 10 ms). A drift in the acquired frequency can be observed in both tests. This was not caused by a physical change in the density of the jet, but by a change in the spatial location of the probe volume, as discussed in the following session.

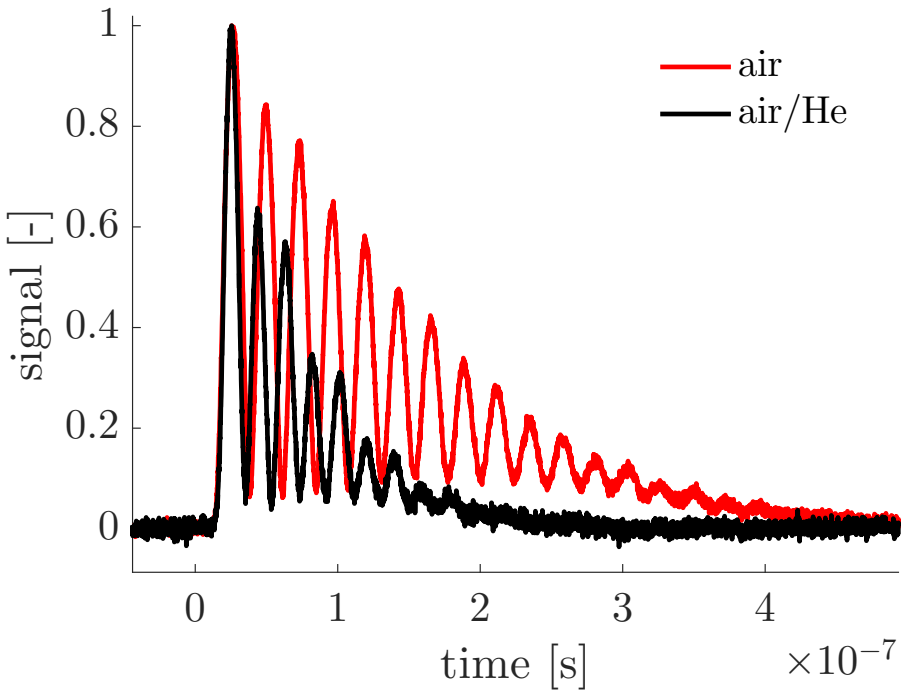

Fig. 9.8 Normalised single shot LIEGS signals recorded at 100 kHz in the steady jets of air (red) and helium and air (black).

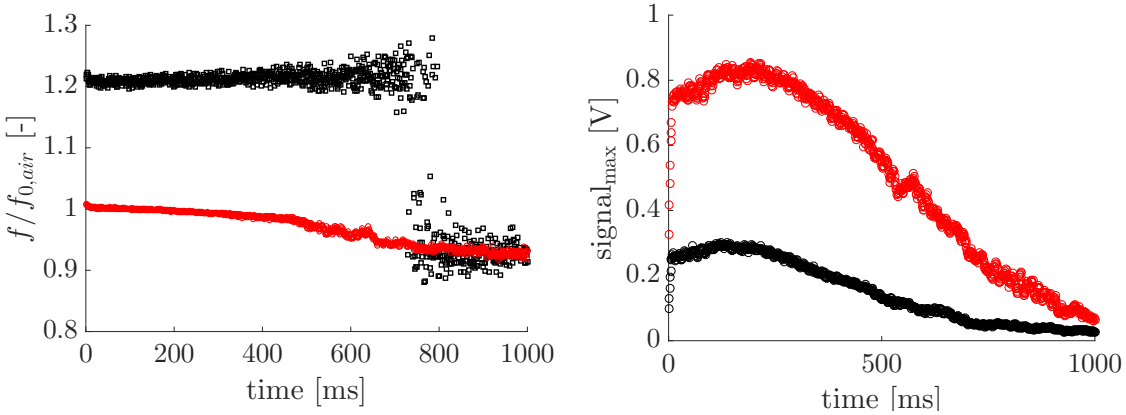

Fig. 9.9 Evolution of the frequency of the LIEGS signals during a burst: jet of pure air (red circles), modulated jet of helium and air (black circles) (left); evolution of the amplitude of the LIEGS signals acquired in air (red) and in the steady jet of air and helium (black) during a burst (right).

Drift in the probe volume

In this section we discuss the origin of the drift in the inferred density derived from the LIGS signals over the burst (Fig. 9.10). The behaviour of the signals during the burst suggests that such a drift was not caused by a physical change in the local conditions owing to e.g. laser-induced thermalisation. For the signal in air (red dots) the derived density shows an apparent positive increase during the burst, which would correspond to a local temperature decrease that can not attributed to any external changes caused by the laser. The apparent change in density was instead caused by a drift in the spatial location and crossing angle of the beams forming the probe volume. In fact, images of the laser beam during the burst reveal that the beam is affected by a spatial drift, becoming also somewhat defocused. This effect is attributed to the high radiation energy and the consequent thermal loading that a burst generates on the amplifiers and optics (both inside and outside the laser). As the two beams travel for about 2 m before crossing in the probe volume, even small initial shifts can be highly amplified along the path, and this can substantially affect the crossing angle and consequently the grating spacing, as well as the spatial location of the probe volume.

Images of the beam revealed that its drift is consistent from burst to burst, so that, in principle, the effect of changes in the crossing angle can be removed from the data by using a calibration in steady air. As the speed of sound in steady air c_a can be assumed to be constant, the variation of the LIGS frequency $f_{a,i}$ at each shot $()_i$ should only reflect the variation of the crossing angle θ_i and consequently of the grating spacing Λ_i:

$$f_{a,i} = \frac{c_a}{\Lambda_i} = c_a \frac{\sin(\theta_i/2)}{\lambda/2} \tag{9.1}$$

This quantity Λ_i can be used to obtain the *correct* speed of sound $c_{E,i}$ in each shot during the burst as:

$$c_{E,i} = \Lambda_i f_{E,i} \tag{9.2}$$

From Eq. (9.1), the crossing angle had changed by 5% between the beginning and the end of the burst. The data is also more scattered at the end of the burst: the overlap between the three beams (two pump and probe beams) had deteriorated, making the quality of the signal poorer. In particular, the biggest variation occurs after $t = 5$ ms, thus, this effect might be mitigated by reducing the duration of the burst.

After applying the correction of Eq. (9.2), only the variation of the crossing angle has been considered, but not the spatial change in the position of the probe volume. The beam drift had moved the probe volume away from the centre of the jet, therefore the data at the beginning and at the end of the burst were not acquired at the same location. In this

experiment, this movement is particularly evident in the last milliseconds of the burst in the helium/air jet (black dots in Fig. 9.9 (right)): the probe volume had travelled out of the jet completely until it reached the still air, as evidenced by the acquired density which corresponds to air. Additionally, for the sinusoidally-modulated flow, in the first two periods of oscillations generated by the speaker, the acquired density variation has a clearer shape, while in the last one it is distorted. Variations in the length and location of the probe volume might also change the overall composition of the mixture inside it (higher or lower percentage of helium). This could explain why the opposite behaviour in the derived density is observed in the jet of pure air and helium and air: the concentration of helium in the probe volume may vary between the beginning and the end of the burst. This reduces the spatial resolution that can be achieved with the measurements and hinders the acquisition of local phenomena occurring at a specific point. Care must be taken while choosing the experimental target, which has to be large enough to ensure that the probe volume remains inside it during a burst and has uniform properties in the measurement plane (or at least in the area where the probe volume is expected to move).

This simple experiment shows how the data acquired with a burst laser should be carefully evaluated to ensure that variations due to the misalignment of the system are not erroneously confused with physical changes in the properties the flow. As final remark, it has to be clarified that this is not an inherent limitation of the technique, but of the current state of the art of the lasers. Improvements in the instrumentation, such as a better stability of the burst laser, and more robust optical components might help to reduce this issue.

Measurements in the sinusoidally-modulated flow

After evidencing all the problems linked to the use of the pulse burst laser, this section aims to show the potential of high repetition rate LIEGS to time-resolve the changes of the sound speed in the probe volume. In this experiment, the concentration of helium is periodically modulated at 300 Hz by using the loudspeaker. The loudspeaker was driven with a sinusoidal wave input but, due to the rather large input amplitude used, the modulated flow did not display a perfect sinusoidal shape. Variations in the concentration of helium in the jet change, in turn, both the specific heat capacity ratio and the molecular mass of the mixture, and therefore the local speed of sound in the flow passing through the probe volume. Fig. 9.10 shows the density variation determined from about 850 consecutive LIEGS single pulses (*i.e.* over a time of 8.5 ms). The bursts were not synchronised with the speaker period, thus the laser started firing at different instants along the speaker cycle, so that only 850 shots can be used for averaging the LIEGS signals over the 40 bursts. Each blue circle shows the time-resolved (non-averaged) single shot density variation (normalised to the density of pure

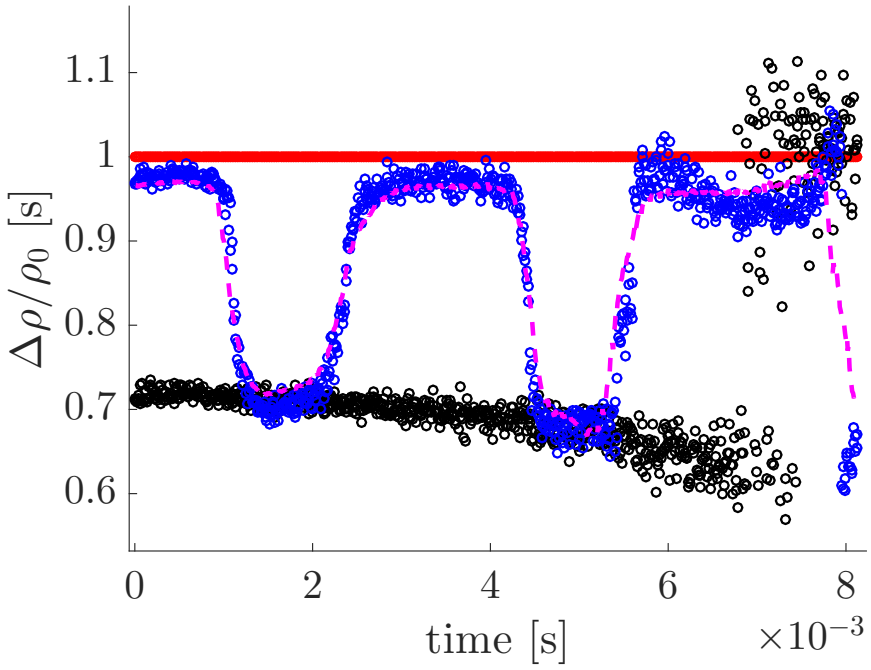

Fig. 9.10 Evolution of the acquired density of the LIEGS signals during a burst. Dots: density derived from single shots LIGS signals: jet of pure air (red circles); steady mixture of helium and air (black circles); modulated jet of helium and air (blue circles); magenta line: averaged signal over 40 bursts.

air) in a burst, determined from the frequency of the LIEGS signal, while the magenta line shows the averaged value (over the 40 bursts). A similar procedure to the one described in Chapter 7 (Sec. 7.3.3) is used in this chapter to determine the density variations in the jet from the LIEGS signals. In this case, however, no corrections due to the presence of a seeded absorbing molecule or thermalisation effects are needed, which is one of the advantages of LIEGS over LITGS.

Let $f_{E,0}$ be the calibration frequency, which is acquired for the LIEGS signals in pure air. For each LIEGS signal $()_i$ in the modulated mixture, the instantaneous molar concentration of helium in the probe volume X_{He} is determined from its frequency $f_{E,i}$:

$$\left(\frac{f_{E,i}}{f_{E,0}}\right)^2 = \frac{\left(1-\frac{R}{\bar{c}_{p,a}(1-X_{He})+\bar{c}_{p,h}X_{He}}\right)^{-1}}{\left(1-\frac{R}{\bar{c}_{p,a}}\right)^{-1}} \frac{W_a}{W_a(1-X_{He})+W_{He}X_{He}} \tag{9.3}$$

where $()_a$ refers to pure air, $()_{He}$ to pure helium. Assuming constant temperature, the knowledge of X_{He} allows the determination of the instantaneous density ρ_i, as follows:

$$\frac{\rho_i}{\rho_a} = \frac{W_i}{W_a} = \frac{W_a(1-X_{He}) + W_{He}X_{He}}{W_a} \tag{9.4}$$

The variations in the density during the helium cycle can be precisely captured: the non-averaged trace follows closely the averaged one, and even the small variations in the density between two consecutive shots are captured. However, while the first two speaker periods have a clearer shape, the last one is distorted, due both to the spatial drift in the probe volume and the changes in the probe volume dimensions.

9.6 Discussion and further development

In this chapter, we demonstrate the application of LIGS at 100 kHz using a pulse burst laser as pump. The energies delivered by the pulse burst laser are sufficiently high to obtain LIGS signals without the addition of any tracer molecules to the flow in non-reacting and reacting flows: both electrostrictive gratings and thermal gratings using the water in the flame products as absorber can be generated. In addition, it is shown that soot particles, acting as black bodies, can also absorb 1064 nm laser light and generate a thermal grating under specific circumstances. Thus, seeding-free LIGS measurements may be performed both in sooty and non-sooty flames, making hybrid LIGS a suitable candidate to probe reacting flows in hostile environments. In a combustion chamber, the same pump laser at 1064 nm, delivering around 100 mJ per pulse, can be used to perform LIGS both in the cold reactants with electrostriction, and in the hot products with thermalisation using soot or water. The high repetition rate of the burst laser can potentially allow time-resolved measurements of unsteady phenomena. However, complications may arise from the use of such lasers. As discussed in Sec. 9.5, the high energies used to pump the laser amplifiers cause a drift in the direction of the laser beam, which manifests itself as a drift in the acquired frequency of LIGS signals, limiting the useful burst duration. In addition, high burst energies might damage the mirrors and the optical access to the flow, especially as the beams at the optical windows location are often converging, so their fluence increases. With the available technologies, pulse energies higher than 100 mJ per pulse at 100 kHz (which are typically required to generate electrostrictive signals using folded boxcars arrangements) can be delivered only by burst lasers, while high repetition rate PIV lasers reach a maximum of 40 mJ per pulse at 1 kHz, which is not enough to obtain detectable LIGS signals using water or soot. Thus, the pulse burst laser remains the only available option for high repetition rate, tracer free LIGS measurements in reacting

flows, at least using 1064 nm light. Another significant issue of such application is the cost of a burst laser, which is two orders of magnitude higher than that of a high speed PIV laser. The results of this chapter suggest that the technology of the available lasers is the main obstacle for deploying high speed LIGS to reacting flows. Improvements in the instrumentation will allow a wider applicability the technique.

9.7 Conclusions

For the first time, tracer-free LIGS measurements are demonstrated at rates of 100 kHz using a pulse burst laser. The energies delivered by its fundamental harmonic (around 130 mJ per pulse) allow the generation of detectable electrostrictive gratings. The potential of the technique in reacting flows is demonstrated by comparing high and low repetition rate LIGS measurements in premixed methane/air flames at 4 bar. Thermal gratings are generated using the water vapour naturally produced by the flame as absorber. The speed of sound, temperature and water concentration measurements at 100 kHz show good agreement with results at 10 Hz. The use of soot as an absorber can potentially extend the use of LIGS to sooty flames. In the second part of this chapter, we present the first time-resolved LIEGS measurements in a sinusoidally modulated, non-reacting helium/air jet. However, we also point out some drawbacks of the application linked to the behaviour of the burst laser: small initial spatial drifts in the beam are largely amplified along the optical table, affecting the geometric characteristics of the probe volume. A calibration procedure to partially correct for this issue is introduced. This chapter demonstrates that 100 kHz LIGS can be used as a tool to detect and time-resolved unsteady changes in turbulent reacting flows, but issues due to the unsteadiness of the burst laser might arise.

Chapter 10

Conclusions and future work

The goal of this thesis has been to shed a light on the behaviour of accelerating entropy spots. Two pieces of information are needed to correctly interpret and quantify the entropy-to-sound conversion occurring in combustion chambers: the strength of the accelerating entropy spots and the characteristics of the pressure (sound) waves generated by their acceleration. This dissertation addresses both aspects. In the first part of the work, we describe the development of an experimental rig (the Entropy Generator Rig) aimed to experimentally validate and further develop analytical models for the entropy-to-sound conversion. With this rig, we unambiguously identify and time-separate the indirect noise generated by accelerating entropy spots for the first time. This allows a comparison between clear experimental data and analytical models. In the second part of the thesis, we demonstrate that Laser Induced Grating Spectroscopy (LIGS) is a suitable tool to detect and time-resolve the passage of unsteady entropy and composition spots travelling in combustion chambers. The main findings and conclusions of this work are presented here, along with possible avenues for future work.

10.1 Entropy-to-sound conversion mechanisms

10.1.1 Conclusive remarks

An acoustic flow system, the Entropy Generator Rig was built to conduct investigations on direct and indirect noise in a simplified and controlled environment (Chapter 4). The Entropy Generator Rig is a gas flow rig in which synthetic entropy and composition spots are generated with a pulsated heating grid of thin wires or pulsated injection of different gases. These entropy and composition spots are carried by the air flow and are finally accelerated through a nozzle located at the end of the duct, producing a strong acoustic signature (indirect noise). A quartz section downstream of the entropy source allows for visual access to

the flow to perform laser diagnostic measurements of the scalar changes associated with thermal or compositional perturbations. This set-up is designed to mimic the thermoacoustic behaviour of a combustor in a more controlled environment, which is ideal for obtaining well characterised data for model validation. The contribution of the indirect noise generated by entropy spots and compositional inhomogeneities can be easily identified and isolated in the acquired pressure traces, allowing a direct comparison between experimental data and analytical models. Prior to the present work, the experimental data had been largely unable to validate indirect noise models: the generation of the downstream-propagating entropic and vortical noise had been demonstrated experimentally [11, 120], but quantitative comparisons with theoretical predictions were not usually carried out or the results were inconclusive [63, 138, 110, 13]. Moreover, the upstream-propagating entropic noise had yet to be measured.

The data acquired in the EGR is the first measurement that clearly identifies and isolates the upstream- and downstream-propagating acoustic signatures of indirect noise generated by subsonic and sonic nozzles and orifice plates. These measurements demonstrate that previous entropy-to-sound conversion models significantly underestimate the indirect noise produced in the Entropy Generator Rig (Chapter 5). These models describe the flow that passes through the nozzle as isentropic (no losses), while in real systems (and in the Entropy Generator Rig), drag, friction and flow re-circulation might occur, generating losses in the total pressure, which affect the propagation of the acoustic waves. In order to correctly capture the conversion of scalar perturbation to sound, we introduce a revised model describing the acoustic and entropic transfer functions of non-isentropic nozzles. These results show that non-isentropic effects significantly affect the nozzle behaviour, so they must be taken into account in the attribution and mitigation of noise and instabilities in systems with losses. In particular, the amplitude of the indirect noise contribution might be comparable to or even exceed the direct noise in non isentropic nozzles. This highlights the importance of experimental validation while developing solutions to mitigate the occurrence and effects of indirect noise.

10.1.2 Future work

The present work shows that direct and indirect noise can be generated, separated and measured in model conditions, with results consistent with analytical models for one-dimensional compact nozzles, once corrected for losses. The analytical framework and experimental methods developed in this work can be used to obtain further insight into indirect noise mechanisms, but additional developments are needed to extend the current analysis to more realistic conditions and export these results to real combustion chambers.

Realistic nozzles

The analytical and experimental investigations of this thesis (Chapter 4-5) only consider the noise generated in one dimensional compact nozzles with subsonic-to-sonic throat conditions. However, in some practical applications, the flow might reach supersonic speeds in the turbine. The model for the acoustic and entropic transfer functions of non-isentropic nozzles (Chapter 5) should be extended to supersonic nozzles with and without a shock in the diffuser. Further, a one dimensional model might not be fully representative of annular combustion chambers, so the circumferential behaviour of the system should be modelled by introducing a radial coordinate θ [58]. Finally, the frequency dependent behaviour of the nozzle transfer functions should be taken into account by relaxing the compactness hypothesis. Previous models for non-compact systems have demonstrate that the amplitude and the phase of the reflected and transmitted waves can be substantially affected by the frequency of the impinging perturbations. Analytically, approaches such as the Magnus expansions [62] or the nozzle equivalent length [85] can be used to determine the nozzle transfer functions, while CFD simulations might be useful to correctly capture the behaviour of the non-isentropic mean flow along the nozzle. Experimentally, the generation of synthetic entropy spots at high frequency adds further complexity to the system. Fast response micro-solenoid valves can be operated up to 600 Hz, but it is difficult to ensure that there is no merging between two consecutive entropy spots. Moreover, there are still no straightforward methods to unambiguously identify and time separate the direct and indirect noise contributions in pressure traces when they are merged.

Indirect noise in reacting flows

The results of this thesis are obtained in a low Reynolds number non-reacting flow rig operated at low frequency. In this simplified configuration, the indirect noise generated by small entropic perturbations is shown to have a non-negligible contribution in the overall sound generated by the rig. However, the findings of this investigation should be extended to high frequency perturbations to high Reynolds number reacting flows. The amount of indirect noise generated strongly depends on the strength of the accelerating entropy and composition perturbations, on the flow parameters and on the geometric characteristics of the combustor. At the state of the art, it is still unclear how the combination of these effects influence the indirect noise, and consequently it is difficult to draw a general conclusion on the role of indirect noise in the overall sound generated in a combustor. A first limitation is the lack of quantitative correlations between the amplitude and strength of the accelerating entropy spots that have survived along the combustion chamber and the amount of indirect

noise consequently generated. This thesis suggests that LIGS can be a suitable candidate to detect and time-resolve unsteady entropy and composition spots, to quantify their strength before the acceleration region and allow the validation of dissipation and dispersion models. At the state of the art, techniques to isolate the acoustic signature of accelerating entropy spots still need to be developed. The time resolved temperature traces acquired with LIGS might be used to extract the indirect noise from the pressure via a coherence analysis. The lack of quantitative experimental evidence and of general understanding has translated into an absence of solutions to reduce or eliminate the effects of indirect noise in aeroengines and gas turbines. Only after gaining a better insight of the mechanisms driving the generation of indirect noise, remedies to mitigate its influence and effects can be developed.

10.2 LIGS for time-resolving the passage of entropy spots

10.2.1 Conclusive remarks

Only few experimental techniques are capable of detecting and time resolving unsteady temperature and composition changes in high pressure environments. Laser-Induced Grating Spectroscopy (LIGS) is a developing optical technique for the diagnostics in the gas phase, requiring only limited optical access to the flow and a relatively simple and inexpensive optical arrangement. LIGS measures the local speed of sound, temperature and composition of a mixture (Chapter 6). LIGS signals can be generated either by a resonant or a non-resonant process in the interaction between the medium and the stationary grating obtained by two crossing pump laser beams. The non-resonant process arises from an electrostrictive interaction named Laser-Induced Electrostrictive Grating Scattering (LIEGS) whereas the resonant process arises from resonant absorption of the radiation energy, leading to Laser-Induced Thermal Grating Scattering (LITGS). In the presence of strongly absorbing molecules, the energies required to generate the thermal gratings are normally one order of magnitude lower than those needed to generate the electrostrictive gratings. Although LITGS typically offers a higher signal to noise ratio than LIEGS, its main limitation is the need for sufficient concentrations of resonant species at the available pump laser wavelengths. In the past, LIGS was applied only as a low frequency (10 Hz) diagnostic technique. In this work, high repetition rate lasers (1-100 kHz) are used to obtain LIGS measurements at high frequency. This enables time resolved measurements to be conducted, a requirement to capture unsteady phenomena such as the passage entropy and composition spots and turbulence.

A first feasibility study is conducted on the Entropy Generator Rig, where high repetition rate LITGS (0.5-1 kHz) is successfully applied to detect and time-resolve travelling entropy

and composition spots along the tube (Chapter 7). In this experiment, biacetyl is seeded in the flow to absorb the 355 nm light of a high speed PIV laser and generate the thermal grating. Results obtained suggest LITGS is a suitable technique to analyse the generation, dissipation and dispersion of entropy spots, but the use of biacetyl as an absorber limits this application to non-reacting flows only, as biacetyl burns at relatively low temperature. When LIGS is applied to reacting flows (Chapter 8), a particular novelty of the development is to demonstrate the technique in a pressurised environment using the fundamental harmonic the popular Nd:YAG laser, without adding tracers to the flow to generate LITGS signals, but instead taking advantage of water molecules which are common products of the combustion and absorb the 1064 nm wavelength light. This simplifies the measurements and allows for realistic use of the technique for industrial environments.

The 1064 nm wavelength LIGS is initially applied at 10 Hz to premixed methane-air flames, using a burner installed in a pressurised, optically accessible vessel. At atmospheric conditions, the high temperature in the flames causes a nearly immediate dissipation of the transient grating, whereas at higher pressures, the density of the gas in the probe volume increases and sufficiently strong signals can be generated. For moderate pulse energies (around 100 mJ per pulse), the LIGS signal consists of a combination from the electrostrictive grating and the thermal contributions associated with the low absorption by water molecules. Features of the signal can be used not only to determine the local speed of sound, but also the local water concentration. The results obtained show that tracer-free LIGS can be easily employed to identify unburnt reactants, burnt gases and soot particles, which makes it a versatile technique for gas turbine environments. However, the energies required for such measurements (100 mJ) are too high to be delivered at high repetition rate by common high speed PIV lasers, due to overheating of the internal components. At present, only the newly developed pulse burst lasers can generate pulses with sufficiently high energies and pulse duration suitable for LIGS.

In this work, a pulse burst laser is used for the first time as pump laser to perform LIGS at a repetition rate of 100 kHz. We obtain both thermal measurements in reacting flows and electrostrictive measurements in unsteady non-reacting flows (Chapter 9). However, this laser has some limitations due to the ultra-high energies involved, such as short burst duration and long waiting time in between bursts for cooling. We also demonstrate that the beam drifts during the burst, reducing the accuracy and spatial resolution of the measurements. However, these results still suggest the potential of LIGS for ultra-high repetition rate diagnostics in reacting flows: the drift can be calibrated to increase the accuracy, while further developments in the pulse burst laser might improve its stability. To conclude, the results of this thesis suggest that LIGS is a suitable candidate to time and space resolve entropy and composition

spots in unsteady reacting flows. As it requires a relatively inexpensive and simple set-up (if standard lasers are used), it is ideal for commercialisation. Improvements in the technique can contribute to obtain a new generation of diagnostics which can deliver high accuracy/precision gas-phase temperature measurements in high-pressure/high temperature flows.

10.2.2 Future work

This thesis demonstrates that LIGS is a suitable candidate to detect entropy and composition spots in combustion chambers. LIGS can been used to overcome the complexity of CARS, while still offering accuracy and precision. LIGS measurements in the gas phase have been made for more than 40 years, but improvements are still needed to fully establish the technique, to enhance its robustness and to convince the community that LIGS is a suitable and cheaper candidate to replace CARS as the golden standard for temperature measurements.

Measurements in turbulent reacting flows

To date, LIGS has not yet been applied to detect and time-resolve temperature and/or composition variations in turbulent reacting flows. The results of this thesis and of most of the previous work are limited to laminar flames only. In reacting flows, thermal LIGS is often preferred to electrostrictive LIGS, because it offers higher signal levels and because the oscillations of the induced-grating are not damped by destructive interference during the laser pulse (Sec. 8.3.1). On the other hand, thermal LIGS requires the presence of species which absorb light at the pump laser wavelength. The present work demonstrates that tracer-free LITGS in reacting flows can be performed using either water or soot naturally present in the flame products as absorbers. In both cases, the energies required to generate the thermal grating (around 100 mJ) can be easily delivered by common low frequency pulsed lasers. However, there are no high repetition rate standard lasers which can deliver such energies and have a suitable pulse duration (5-10 ns). PIV lasers can deliver maximum energies of 40 mJ per pulse at 1 kHz, but they are usually set to deliver visible light via a cavity configuration, so they cannot be easily converted to the first harmonic. Other common products of flames are water, CO_2 and some hydrocarbons. These molecules have a large absorption cross section in the infrared region (1.9-2.4 μm), so small energies (1-10 mJ) are required for obtaining strong LITGS signal [180]. However, at the state of the art there are no high repetition rate IR lasers with a pulse shape suitable for LIGS.

Chapters 8-9 suggest two possible avenues to obtain tracer free, high repetition rate LIGS measurements in reacting flows. The intensity and the damping rate of the signals improve with density (Sec. 8.3.2, Chapter 8), thus, if the pressure in the system is raised to higher values ($p > 10$ bar), the pulse energies of high repetition rate PIV lasers at 1064 nm might be sufficient to obtain detectable thermal LIGS measurements. Nevertheless, higher pressures in turbulent flows increase beam steering, which might cause a worse overlap of the three beams and consequently weaker signals, and even some missed shots. To mitigate the issue, one of the two beams can be enlarged to an elliptical shape, as was done for CARS [143]: this strategy increases the the overlap region without affecting the length of the probe volume. However, as the crossing location of the two pumps varies from shot to shot, the measurements lose spatial resolution.

Otherwise, the pulse burst laser can be used for high repetition rate LIGS in turbulent reacting flows, with an application similar to the one described in Chapter 9 for laminar flames. The repetition rates of 100 kHz allow the detection of unsteady turbulent features; however, as a burst lasts only for 10 ms, low frequency phenomena (frequencies lower than 100 Hz) might not be captured using this laser. Entropy spots, usually generated at low frequencies (50 Hz - 100 Hz), might not be detected by such short bursts. Another complication lies in the imperfect behaviour of the burst systems. The extremely high energies delivered cause some issues in stability of the lasers, such as variations in the energy from burst to burst and drift and defocusing of the beam. As pulse burst lasers are a relatively new technology, further developments are likely to improve the quality of their output, obtaining systems which can deliver longer and more stable bursts. These considerations highlight how the development of LIGS is currently limited by the technology of the available lasers and not by shortcomings in the technique.

Use of soot as an absorber

Soot, acting as a black body, can absorb the laser energy and generate the LIGS signal, as demonstrated by Brown et al. [26], Hemmerling et al. [100] and by the preliminary results of Fig. 9.5 (Chapter 9). However, there are still no systematic investigations of the effects that soot concentration, flow characteristics, energy and wavelength of the pump laser have on the LIGS signals. In particular, the intrusiveness of the technique has not yet been evaluated. Focused beams in the probe volume might break the soot particles, generating a non-negligible temperature increase, as well as sparks of light which can saturate the PMT. Further, a systematic modelling of the generation of the thermal grating in sooty environments has yet to be carried out. Thus, LIGS in sooty flames still requires fundamental investigation prior its application to reacting flows. An interesting future application might

be the simultaneous acquisition of the LII signal from the CW beam passing through the probe volume and of the LIGS signal from the Bragg scattered light, to measure of both the speed of sound and the soot concentration simultaneously.

Improvements in the technique

A shortcoming of LIGS has been its relatively low spatial resolution when using the standard experimental procedure. The most common optical layout for LIGS is a folded boxcar arrangement using a single lens (50-70 mm diameter, 300-1000 mm focal length) for crossing the four beams into a single point. In such arrangement, only a small optical access to the flow is needed, as the beams travel close to each other beyond the lens. However, this arrangement only allows small crossing angles between the pump beams ($\theta < 5^\circ - 6^\circ$ for focal length $f_l = 0.3 - 1$ m), which generate long overlap regions e.g. long probe volumes. Using a single lens, a shorter probe volume can only be obtained by reducing the beam diameter at the crossing location. Results in Appendix A show that this might generate an excessive increase of the laser fluence in the probe volume, inducing a non-negligible thermalisation, which translates into an erroneous reading of the local temperature. This poses a threshold on the minimum beam diameter that can be used for LITGS (electrostrictive measurements are not affected by thermalisation). In CARS, the spatial resolution was improved by using two different bi-convex lenses to cross the pump beams with a wider angle and reduce the length of the interaction region [142]. Such optical arrangement implies having a wider distance between the beams. Thus, this layout is unpractical for applications in enclosed environments which normally are provided only with a limited optical access. Moreover, a shorter probe volume reduces the number of oscillations in the LIGS signals and consequently the accuracy in the determination of the local speed of sound. Thus, for application in enclosed environments and combustion chambers, the trade-off between the achievable spatial resolution and precision and accuracy in the measurements implies that probe volume length might not be reduced below 2-3 mm in the transverse directions using conventional lasers (delivering beams with diameters at the laser port of 7-12 mm). Moreover, the PMTs commonly used for acquiring the signals have a circular cross section of 8 mm diameter, and integrate all the scattered light impinging on them, averaging any spatial variations in the signals. If arrays of sensors or cameras are used to image the different portions of the scattered light, space resolved measurements might be obtained, despite a lower signal to noise ratio.

A second shortcoming of LIGS is the absence of a general experimental procedure: much of the previous work has reached conclusions which are often only set-up dependent (e.g. they are only valid for a specific combination of laser wavelength/absorber, local pressure,

probe volume length). General guidelines for calibration, signal acquisition, data processing and analysis are needed. Comprehensive algorithms should be developed, not only to extract the local speed of sound, but also the temperature and species concentration from LIGS measurements. This is a significant requirement, which can be considered in the light of the commercialisation efforts by Dantec. Dantec is launching a small portable LIGS box, which can be placed in front of the flow system of interest to obtain LIGS measurements. General instructions on the working principle, calibration procedure, data analysis and on the advantages and disadvantages of the technique can help to distribute this set-up faster, making LIGS an established and accessible technique for temperature measurements in reacting flows.

Appendix A

Trade-off between thermalisation and spatial resolution with LITGS

Thermal LIGS measurements are often advantageous with respect to electrostrictive LIGS measurements, as they normally need pump laser energies one order of magnitude lower to generate detectable signals. On the other hand, LITGS requires the presence of an absorber in the flow and relies on a non-adiabatic process (e.g. there is a net energy transfer between the laser pulses and the molecules), which might induce a non-negligible temperature increase in the probe volume. This thermalisation effect might be reduced by increasing the size of the probe volume, which however deteriorates the spatial resolution. In this Appendix, we investigate this trade-off between spatial resolution and thermalisation. LITGS measurements are performed in non-reacting jets of air, using biacetyl as an absorber. Two different pulsed pump lasers (10 Hz and 1000 Hz) tuned to 355 nm are used in the experiments. For a fixed pulse energy and crossing angle, good spatial resolution can be achieved by using small beam diameters at the crossing point. However, as the energy per unit area increases, the thermalisation of the probe volume induced by the laser pulse might lead to a non-negligible local temperature increase. We show that for small beam diameters at the crossing point (in this case $d_{cp} < 50$ μm), the thermalisation of the probe volume can generate errors of the order of 35% of the estimated absolute temperature, and must be corrected for. For larger (e.g. $d_{cp} > 1$ mm) beam diameters at the crossing point, the thermalisation effect becomes negligible, but the probe volume length increases substantially, decreasing the spatial resolution of the measurements[1].

[1]The results of this chapter were presented in the 19^{th} International Symposium on the Application of Laser and Imaging Techniques to Fluid Mechanics [52]

A.1 Experimental set-up

A.1.1 Optical layout

LITGS signals are generated at low (10 Hz) and high repetition rate (1000 Hz) using two different laser sources (and optical layouts). In both optical set-ups, the pump lasers have a wavelength $\lambda = 355$ nm, the probe lasers have a wavelength $\lambda = 671$ nm, and the beams are crossed in a forward folded boxcars arrangement. The low speed set-up (Fig. A.1) is more flexible, as the mirrors and lenses are positioned on a wider optical table, and therefore the alignment can be more easily modified. The high speed set-up is the compact LIGS box described in Chapter 7 (Fig. 7.1). The two set-ups share the acquisition hardware: the signals are recorded using the 4-channel LeCroy 6104A oscilloscope (sampling rate 10 Gs/s, 1 GHZ bandwidth, 40 million points maximum real time memory) in sequential mode, for 1 μs (10000 points) per signal.

Low speed set-up

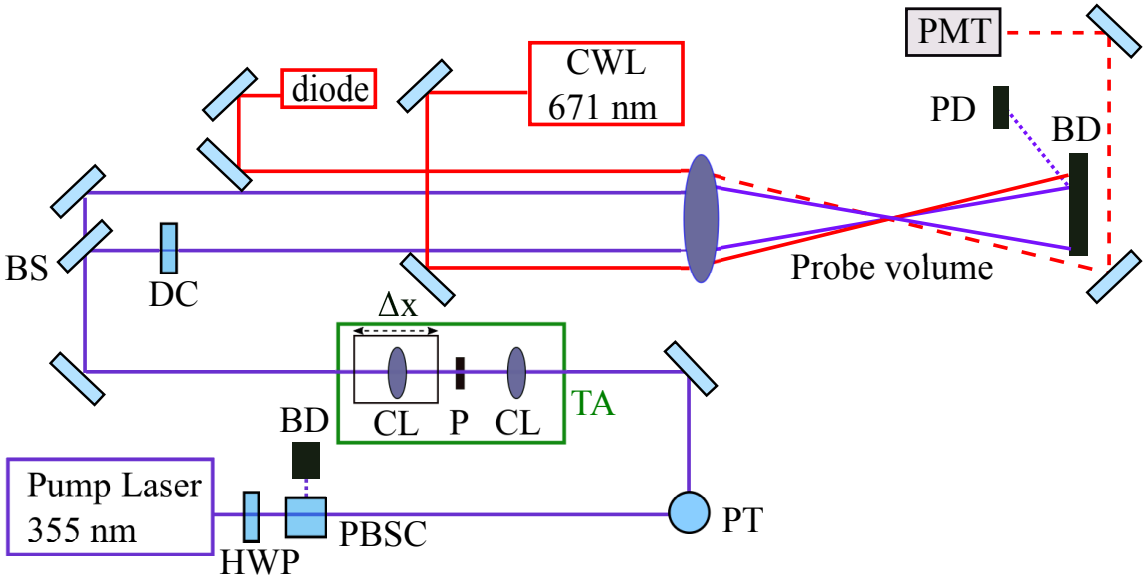

Fig. A.1 Optical layout of the experiment. PL: pump laser, CWL: continuous wavelength probe laser; diode: tracing beam; PD: photodiode; PMT: photomultiplier; HWP: half wave plate; PBSC: polariser beam splitter cube; PT: periscope tower; TA: telescopic arrangement; CL: crossing lens; P: pinhole; BS: beam splitter; DC: delay compensator plate; BD: beam dump.

In the low speed set-up, pump pulses of 10 ns duration are generated from a frequency tripled Nd:YAG laser (Continuum Surelite III-10). The laser crystals and Q-switch are

adjusted to deliver the maximum energy output ($E_p \simeq 120$ mJ at the laser port) to increase the stability and improve the shape of the pulse. The pulse energy is then adjusted in the range from 1.5 to 20 mJ by using a half wave plate (HWP) and a polariser beam splitter cube (PBSC) at the exit of the laser. A telescopic arrangement formed by two 250 mm focal length convex lenses (CL) and a pinhole (P) cleans up the beam profile. The position of the second lens can be incrementally varied up to 15 mm along the beam path using a traverse stage. In this way, the divergence of the beam can be incrementally modified, which changes the location of the beam waist with respect to the crossing point by varying the value M^2 in Eq. 6.6. A 50/50 beam splitter divides the 355 nm beam into two identical beams, and a 15 mm thick quartz plate is added to the shortest path to compensate for the phase shift between them. The two pump beams, separated by 15 mm, are focused and crossed by a 2-inch 500 mm focal length crossing lens, resulting in a crossing angle $\theta \simeq 1.8^\circ$ and a grating spacing $\lambda = 11.83$ μm. After the probe volume, they are blocked with a beam dump (BD). The continuous probe beam is produced with a pumped solid state laser (CNI MLL-FN-671 LD, $\lambda = 671$ nm, maximum power = 1 W, diameter d $\simeq 2$ mm). The tracing beam is generated with a collimated laser diode module (λ=635 nm, power = 1.2 mW). The LITGS signal is detected using a Hamamatsu H6780-20 photomultiplier, with a gain set to 0.55 V for a sensitivity of 80 mA/W. A photodiode (DET10A) pointed at the beam dump (BD) detects the pump pulses providing the trigger signal for the acquisition.

High speed set-up

The high speed set-up is described in the Chapter 7 (Sec. 7.2) and uses the portable LIGS optical table with the 355 nm high speed PIV laser.

A.1.2 Experimental layout

The experiments are run in heated open laminar and turbulent jets (Fig. A.2), similar to the one described in Chapter 7. The laboratory air supply system provides filtered air, and the flow is seeded with biacetyl using two 0.5 l Dreschel bottle bubblers with sintered heads. The bubblers are kept at room temperature, and deliver nearly saturated mixtures of biacetyl, which can be diluted downstream. The air jets consist of 8, 21 and 30 mm diameter 150 mm long stainless steel tubes. These jets are placed in the centre of a metallic cylinder with a diameter of 200 mm. Secondary air may be injected at the bottom of the cylinder via three swirl plugs to obtain a co-flow around the main jet. A honeycomb flow straightener and a metallic mesh ensure that the co-flow is laminar and straight when it reaches the top of the cylinder. To increase the temperature of the flow coming out from the jet, an in-line heater

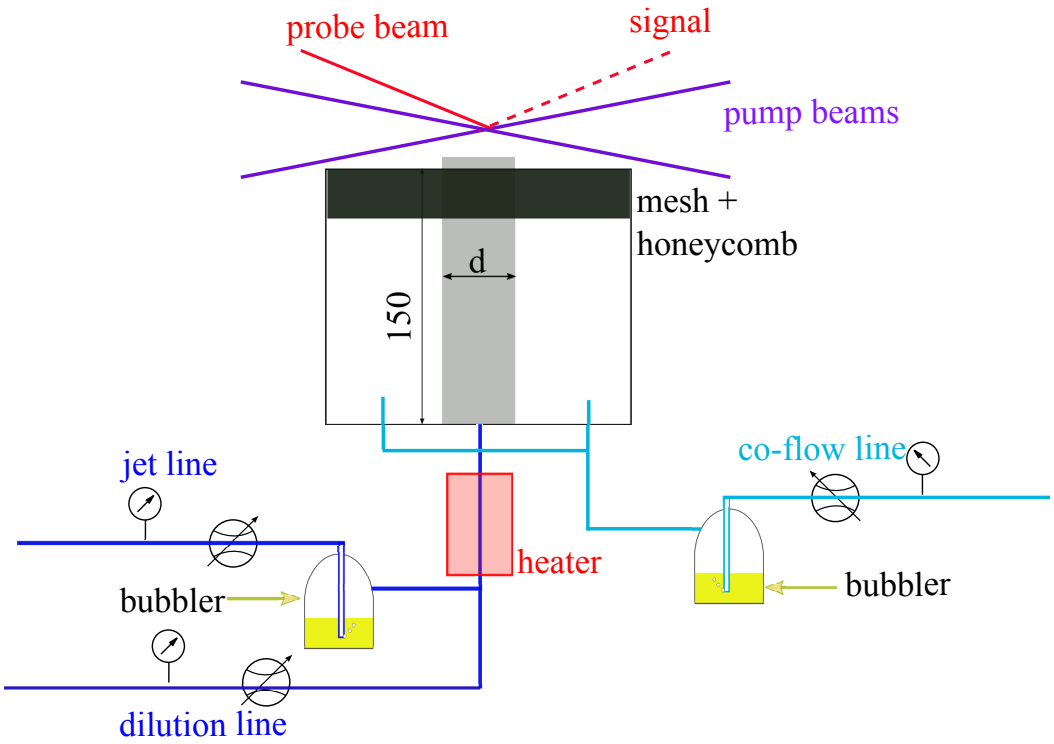

Fig. A.2 Schematic of the jet experimental set-up.

(AHP-7562 Omega Engineering, 240 V, 750 W, 140 mm heated length) can be added to the jet flow line.

A.2 Trade-off between intrusiveness and precision

Thermal LIGS is based on the generation of a local density change from the absorption of the pump pulse energy by the medium in the probe volume, and therefore might be intrusive under some circumstances. In this Appendix, we discuss this issue, demonstrating that the laser pump pulses might perturb the local temperature unless the product of the pump beam fluence and the concentration of the absorber are kept low. On the other hand, the signal itself, proportional to the square of the density perturbation, needs to be sufficiently high to provide suitable signal-to-noise ratio for an assessment of the frequency. The signal amplitude can be increased by either raising the pump laser energy or the absorber concentration in the probe volume.

If the target flow does not contain any molecules that absorb the specific laser wavelength, an external substance must be added in small quantities to the main flow to generate the thermal grating. However, if this absorber has different molecular properties from the

mean flow (such as in the case of biacetyl, see Table 4.1), the bulk flow properties can be substantially altered even for small concentrations, as shown in Chapter 7. Moreover, at high laser fluence, the flow in the probe volume may also be consistently thermalised by the absorption of the pump laser energy. In this Appendix, we explore this effect.

From an energy balance, the induced temperature increase in the probe volume ΔT (Eq. 7.1) may be modelled as [139]:

$$\frac{\Delta T}{T_0} = \eta \frac{E_p}{A_{cp}} \frac{\sigma_{cs} N_A}{\bar{c_p} T_0} X_V \tag{A.1}$$

where η is a coefficient representing the thermalisation efficiency, E_P is the pump pulse energy, $A_{cp} \simeq d_{cp}^2 \pi/4$ is the beam area at the crossing point (thus E_p/A_{cp} is the laser fluence), σ_{cs} is the absorption cross section of the tracer, N_A Avogadro's number, $\bar{c}_p$ the molar specific heat of the mixture, and T_0 the unperturbed temperature. Eq. A.1 shows that, due to the presence of the absorber, the pump laser energy always induces a positive change in the local temperature. This change might be negligible at low laser fluence, or for weak absorbers in a small quantity, as in the experiments described in Chapter 7.

In this Appendix, we demonstrate a situation in which the thermalisation is non negligible, using the jet seeded with biacetyl ($[-]_b$ in the equations), in a molar fraction X_b. As seen in Eq. 7.1, the acquired LITGS frequency f_1 may differ from the true frequency f_0 of the unseeded and unperturbed air jet (subscript $[-]_a$) due to thermalisation of the probe volume and changes in molecular weight and specific heat capacity ratio of the mixture. Using Eq. A.1, we re-write Eq. 7.1 as:

$$f_1^2 = \frac{1}{\Lambda^2} \frac{\gamma_1 R T_1}{W_1} = \frac{1}{\Lambda^2} \frac{\left(1 - \frac{R}{c_{p,a}(1-X_b)+c_{p,b}X_b}\right)^{-1} R \left(T_{0,a} + \eta \frac{E_p}{A_{cp}} \frac{\sigma_{cs} N_A}{\bar{c_p}} X_b\right)}{W_a(1-X_b) + W_b X_b} \tag{A.2}$$

which can be re-arranged as:

$$\frac{f_1}{f_0} = \left[\frac{\left(1 + X_b \frac{c_{p,b} - c_{p,a}}{c_{p,a}}\right) \left(1 + X_b \eta \frac{E_p}{A_{cp}} \frac{\sigma_{cs} N_A}{\bar{c_p}} X_V\right)}{\left(1 + X_b \frac{c_{p,b} - c_{p,a}}{c_{p,a} - R}\right) \left(1 + X_b \frac{W_b - W_a}{W_a}\right)} \right]^{1/2} \tag{A.3}$$

Fig. A.3 shows the calculated changes in the frequency of the LITGS signals from Eq. A.3. The biacetyl molar fraction is fixed to X_b=1%, while the laser fluence is varied by both changing the diameter of pump beam at the crossing point d_{cp} and the energy delivered by the pump E_p. The thermalisation efficiency is here assumed as $\eta = 5\%$, as was found by Lowe [139]. Fig. A.3 shows that, for typical pump beam energies used in LITGS experiments (1-25 mJ), a significant variation in the frequency is obtained when the diameter of the beams at

the crossing point d_{cp} is lower than d_{cp} = 100 μm. In this case, the energy delivered per unit area significantly thermalises the probe volume, which reflects in an induced increase in the local speed of sound and, consequently, in the LITGS frequency. This thermalisation effect can be significantly reduced by increasing the beam diameter at the crossing point (in this case, for beam diameters $d_{cp} > 100\ \mu m$) . However, larger beam diameters produce poorer spatial resolution, as the length of the probe volume l is directly proportional to the beam diameter d_{cp}, as seen in Eq. 6.7). Thus, for small crossing angles θ between the pump beams, there is a trade-off between the thermalisation effects and the achievable spatial resolution.

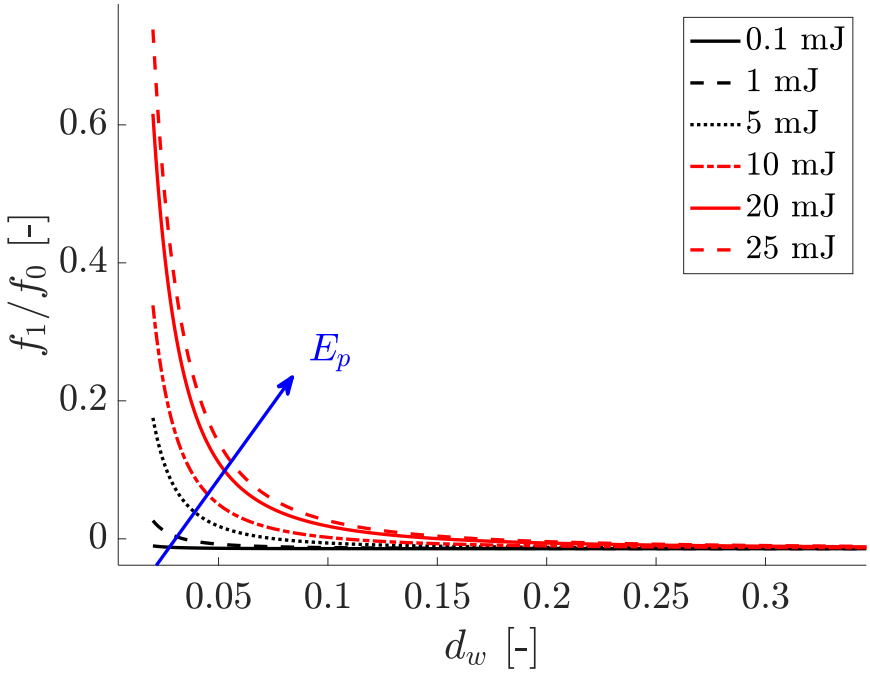

Fig. A.3 Predicted change in the LITGS oscillation frequency obtained by varying the fluence of the laser E_p/A_{cp} for a fixed biacetyl concentration of $X_b = 1\%$, assuming a thermalisation efficiency $\eta = 5\%$. Legend: energy per pulse delivered by the pump beam E_p.

In the current experiment, the beams in the low speed set-up are focused at the crossing point. The diameter of the low frequency pump beam was measured at the laser port as d_0 = 7 mm using a knife-edge method. By assuming a perfectly collimated Gaussian beam, with a focal length f_l = 500 mm, the waist diameter of the beam can be estimated from Eq. 6.6 as $d_{cp} = 32.2\mu m$. Fig. A.3 suggests that for such a diameter, the thermalisation induced by the laser might not be neglected, as we experimentally demonstrate in this Appendix. In the high-frequency set-up, however, the defocused geometry generates collimated beams

at the crossing point (d_{cp} = 1 mm). This ensures that the measurements are not affected by thermalisation, but generates an overlap region of length l = 40 mm (Chapter 7).

A.2.1 Determination of the unperturbed speed of sound

In this section, we explore the effects that the presence of an absorber might have on the determination of the true speed of sound of the unperturbed medium from LITGS signals. For small concentrations of the absorber ($X_b \to 0$), Eq. A.3 can be linearised as

$$\frac{f_1}{f_0} = 1 + \frac{1}{2} X_b \left[\eta \frac{E_p}{A_{cp}} \frac{\sigma_{cs} N_A}{\bar{c_p} T_0} - \left(\frac{W_b - W_a}{W_a} + \frac{R(c_{p,b} - c_{p,a})}{c_{p,a}(c_{p,a} - R)} \right) \right] + o(X_b^2) \qquad \text{(A.4)}$$

The acquired LITGS frequency f_1 coincides with the unperturbed frequency f_0 if the second term on the right hand side of Eq. A.4 is negligible. This happens if either $X_b \to 0$ (which normally leads to a poor quality of the signal), or when the term in the square brackets is negligible. The latter occurs when the thermalisation is negligible and the absorber has a similar properties to the mean flow ($W_b \simeq W_a$ and $c_{p,b} \simeq c_{p,a}$). When $X_b \neq 0$, the sign of the term in the square brackets depends on the balance between thermalisation and change in properties of the bulk mixture due to the tracer (difference between the specific heat and molecular mass of the tracer and of the main flow). When the thermalisation effect is higher (high laser fluence E_P/A_{cp} and high absorbing cross section σ_{cs}) the term in the square brackets has a positive sign, and the frequency f_1 increases with the molar concentration of the absorber X_b. Conversely, if the specific heat ratio of the absorber and its molecular mass differ substantially from the mean flow properties (as in the current case of biacetyl, where both $c_{p,b}$ and W_b are higher than the corresponding properties of air) and the thermalisation is negligible, the term in the square brackets has a negative sign and the frequency f_1 decreases with the concentration X_b. There might be significant errors in the evaluation of some of the quantities of the perturbation term of Eq. A.4, such as the energy effectively transferred to the flow ηE_p, the actual cross section area of the probe volume A_{cp} and the actual specific heat capacity $\bar{c}_p$ for a given temperature. However, Eq. A.4 suggests a way to determine the real frequency f_0 without the knowledge of the terms in the square brackets: by varying the concentration of the absorber X_b (in this case by adding dilution air to the saturated jet leaving the bubbler) while keeping the set-up and pump energy constant, the perturbed frequency f_1 depends linearly on X_b, multiplied for a coefficient that can be assumed as fixed for different dilution ratios (the term in the square brackets). By varying the concentration of the absorber X_b, this unknown term can be evaluated, and the unperturbed frequency f_0 can be obtained from the intersection of the experimental points with the $X_b = 0$ axes (in the frequency versus concentration plot). A similar procedure is applied in Chapter 7.

Accurate knowledge of the real unperturbed frequency f_0 is needed to correctly calibrate the LITGS measurements: the geometric grating spacing Λ is usually determined from a calibration experiment (Sec. 6.3.5). However, if the presence of the absorber in the mean flow and the thermalisation effects are not properly accounted for, the parameter Λ can be wrongly evaluated, leading to substantial errors in the actual LITGS measurements.

A.3 Results: intrusiveness of LITGS

A.3.1 Demonstration of the trade-off between thermalisation and spatial resolution

In this section, we experimentally demonstrate how the energy delivered from the pump laser pulses can generate non-negligible temperature increases in the probe volume after a certain threshold of laser fluence. The experiments are run using the 10 Hz laser set-up (Fig. A.1) and the 21 mm diameter jet, with an air flow of 40 slpm, of which 10 slpm are bypassed through the bubbler with biacetyl, for a fixed dilution ratio $\delta = \dot{m}_{tot}/\dot{m}_{bub} = 4$ (biacetyl molar fraction $X_b = 0.01$). The energy delivered by the pump laser E_p is set to 11 mJ and is kept constant during the experiment. In order to vary the laser fluence in the probe volume (E_P/A_{cp}), the beam size at the intersection point (and therefore the cross section and volume of the interaction region) are changed by varying the position of the beam waist with respect to the crossing location. The divergence of the pump laser beam (the term M^2 in Eq. 6.6) is varied by incrementally changing the position of the re-collimating lens in the telescopic mount, moving the traverse stage by Δx (Fig. A.1). When the lens is exactly located at the focal distance from the focal point P, the beam is perfectly re-collimated after the telescopic mount. If instead the lens is shifted from this nominal position by Δx, the beam leaving the telescopic mount becomes slightly converging or diverging. For perfectly collimated beams at the crossing lens, the beam waist nominally coincides with their crossing location. However, if they are slightly converging/diverging at the crossing lens, the beam waist no longer occurs at the crossing location, so that the length of the probe volume is effectively changed. In this experiment, the position of the second lens is incrementally shifted in steps of $\Delta x = 1$ mm from the focal-distance location ($\Delta x = 0$) to a maximum shift of $\Delta x = 14$ mm beyond it, generating a divergence in the beam leaving the telescopic mount. This results in an incrementally larger beam diameter at the crossing point and a corresponding lower laser fluence.

Figure A.4 plots the normalised frequency shift $\Delta f = f - f_{min}$ for each position of the second lens, normalised by the minimum value of the frequency f_{min} (which corresponds to

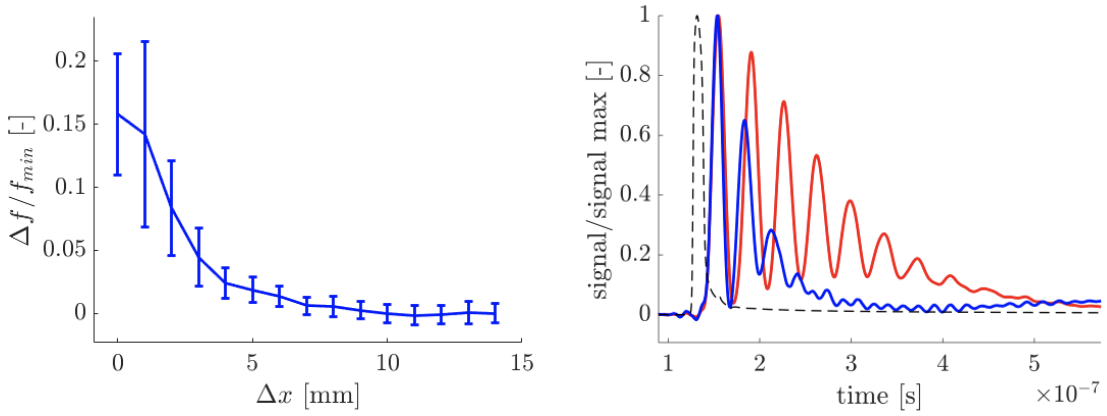

Fig. A.4 Change in the oscillation frequency of the LITGS signal due to the thermalisation of the probe volume caused by an increase of the laser fluence E_P/A_{cp} at the crossing point. The pump energy E_P is fixed to 11 mJ and the cross sectional area A_{cp} is varied by changing the location of the beam waist with respect to the crossing location (left). Ensemble-averaged normalised LITGS signals obtained for highly focused beam (high laser fluence as the beam waist correspond to the crossing point, $\Delta x = 0$, solid blue line) and low laser fluence (beam waist approximately 20 mm from the crossing point, $\Delta x = 14$ mm, solid red line). Dashed line represents the pump laser pulse (right).

the *unperturbed* local speed of sound). Figure A.4 shows that, after a certain threshold, the frequency of the LIGS signal starts increasing due to the induced thermalisation. When $\Delta x =$ 0 mm, the beam have their smallest size at the crossing point, thus the highest fluence. In this case, all the laser energy is released within a small region and the induced thermalisation of the probe volume becomes non negligible, generating a significant change in the local temperature and therefore in the acquired frequency. When the beam diameter and the corresponding area at the crossing point increase, the pulse energy becomes spread over a bigger volume, leading to negligible thermalisation, as predicted in Fig. A.3. Due to these effects, the speed of sound corresponding to the LITGS frequency becomes 17% higher than the *unperturbed* speed of sound, which is obtained for negligible thermalisation ($\Delta x = 14$ mm). This results in an error of 35% on the evaluated temperature. As the biacetyl concentration and the pump pulse energy are kept constant during the experiment, the change in the oscillation frequency observed in Fig. A.4 (left) is only due to the change in the beam diameter d_{cp}. The shape of the acquired signals also differs considerably (Fig. A.4, right): a smaller interaction region leads to a shorter signal with fewer peaks (blue solid line), as the sound waves quickly leave the smaller probe volume region. For a larger interaction region, the signal lasts longer (red solid line), as diffusion and viscous damping effects have a smaller influence on the signal.

A.3.2 Effect of the dilution and determination of the unperturbed speed of sound

In this section, we demonstrate the effect of the change in biacetyl concentration X_b on LITGS signals. We experimentally validate the behaviour theoretically predicted by Eq. A.3 and A.4, and further validate the calibration procedure outlined in Chapter 7 for estimating the actual biacetyl concentration $X_{b,s}$ as well as the unperturbed speed of sound in the gas in the measurement volume. In the experiment, a constant flow of 15 slpm passes through the biacetyl bubbler, and the biacetyl concentration in the flow exiting from the 21 mm diameter jet is incrementally decreased by adding unseeded air through the dilution line. The same experiment is run both in the low frequency and high frequency set-up.

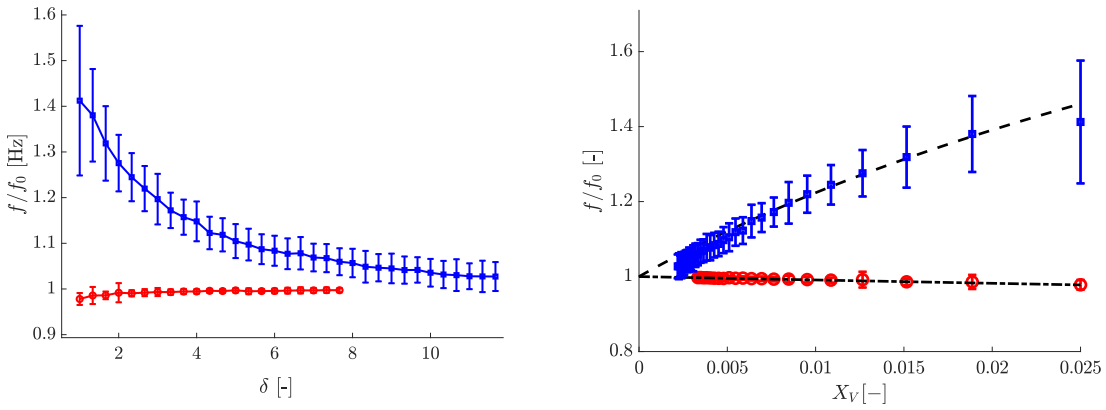

Fig. A.5 Change in the LITGS oscillation frequency due to the dilution of biacetyl in the mean flow at a constant laser fluence (red circles: low laser fluence, blue squares: high laser fluence), plotted versus the dilution factor $\delta = \dot{m}_{tot}/\dot{m}_{bub}$ (left); estimated molar concentration of biacetyl X_b (right). Data acquired using the 10 Hz laser, at a fixed energy Ep = 11 mJ. Dashed lines: modelled behaviour (right).

Figure A.5 (left) shows the experimental points acquired with the 10 Hz laser (markers), plotted versus the dilution factor δ. The two curves are obtained for two different laser fluence levels: the blue square points are acquired with the beam focusing at the crossing point (corresponding to Δx =0 mm in Fig. A.4, the highest laser fluence), while the red circular markers are acquired with the beam waist shifted of 20 mm from the crossing point (corresponding to Δx =14 mm, the lowest laser fluence). As predicted from Eq. A.4, two different trends are observed in the frequency of the LITGS signals when increasing the dilutions: for high laser fluence ($\Delta x = 0$, small beam diameter at the crossing point), the thermalisation of the probe volume has a dominant effect over the change in the flow properties due to biacetyl. The term in square brackets in Eq. A.4 has a positive sign and

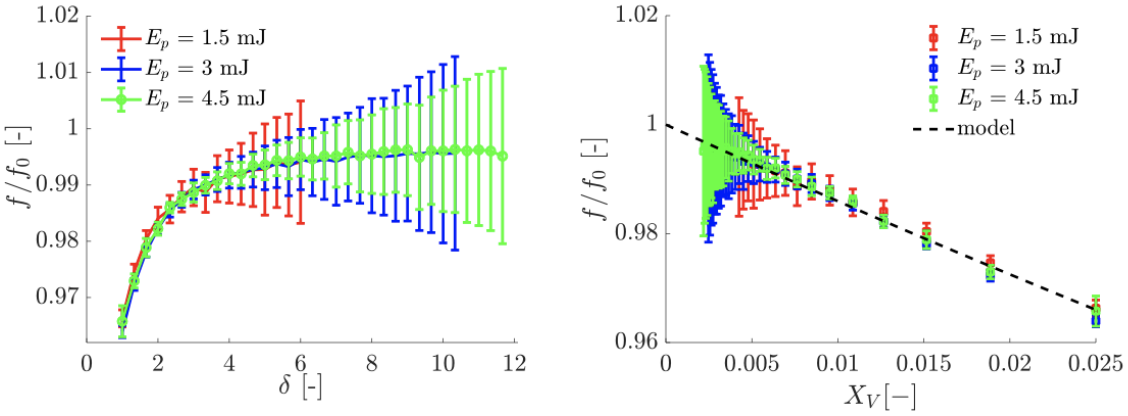

Fig. A.6 Change in the LITGS oscillation frequency due to the dilution of biacetyl in the mean flow, plotted versus the dilution factor $\delta = \dot{m}_{tot}/\dot{m}_{bub}$ (left) and the estimated molar concentration of biacetyl X_b (right). Data acquired using the 1 kHz laser, for pump energies of 1.5, 3 and 4.5 mJ. Dashed line: modelled behaviour.

the frequency increases with higher concentrations of biacetyl (lower dilution). Instead, for low laser fluence ($\Delta x = 14$, larger beam diameters at the crossing point), the change in the flow properties has a dominating effect as the thermalisation is negligible. The term in the square brackets in Eq. A.4 becomes negative and the frequency decreases by increasing the concentration. To accurately predict and/or model this behaviour, an accurate knowledge of the terms in Eq. A.4 would be needed, which is difficult to achieve. By using a fitting algorithm on the experimental LITGS data in a dilution curve, both the concentration of biacetyl in the flow leaving the bubbler $X_{b,s}$ and the effective laser fluence $\eta E_p/A_{cp}$ can be estimated: Eq. A.3 must be valid at each dilution δ using the measured change in frequency between two operating conditions m and n. The real frequency f_0, corresponding to the unperturbed speed of sound c_0, can then be determined from Eq. A.3. In Figure A.5 (right), the experimental points are plotted as a function of the molar fraction X_b, which is determined after fitting, and the dashed lines represent the fitted curves. For low values of biacetyl concentration (X_b <1%), the linear behaviour expected from Eq. A.4 is observed.

In Fig. A.6, the dilution experiment is repeated with the high speed laser at 1 kHz, for three different pulse energies (due to the compact arrangement of the optics, the divergence of the beams could not be modified in this set-up). As the beams are collimated in the crossing location (large diameters), the laser fluence at the crossing point has a low value, the thermalisation is negligible and the frequency changes only due to the change in the mean flow properties: the experimental curves obtained for the three energies are superposed. It can be concluded that the thermalisation has a negligible effect in the experiments run with the high frequency set-up. This result is used in Chapter 7.

The experiments described in Figs. A.5 and A.6 demonstrate that the addition of small quantities of an absorber, as well as the thermalisation due to high laser fluence, can significantly affect the acquired LITGS frequency. These effects have to be properly taken into account while evaluating the LITGS signal, especially in the calibration tests aimed to evaluate the geometric grating spacing Λ: if the potential intrusiveness of the measurements is not verified, the calibration parameter is wrongly evaluated, leading to systematic errors in the processing and analysis of experimental data. For thermal LIGS experiments, when an absorber is added to the mean flow (such as acetone, toluene, biacetyl, etc.) we suggest to perform a dilution experiment to evaluate the intrusiveness of the measurements and determine the unperturbed speed of sound prior to taking further measurements.

A.4 Results: effect of spatial resolution on LITGS signals

In this section, we use a heated jet seeded with biacetyl to investigate the accuracy of the LITGS measurements. Comparing the temperatures derived from LITGS signals with thermocouple measurements, we demonstrate that LITGS can precisely and accurately detect temperature in a heated flow, provided that the temperature is uniform inside the probe volume: spatial averaging along the direction of the beam propagation can have a major impact on the accuracy.

A flow of 40 slpm passes through the bubbler, and onward through a 30 mm diameter jet (Re = 1800, laminar case) or 8 mm diameter jet (Re = 26000, turbulent case). Each jet is co-annular with a 200 mm diameter metallic cylinder, through which a co-flow of air seeded with biacetyl is supplied. LITGS is used to scan the temperature profile along the diameter of the laminar heated jet (Fig. A.7, left) and turbulent heated jet (Fig. A.7, right). The blue circles show the measurements obtained with the co-flow seeded with biacetyl, while red squares show the measurements obtained without the co-flow. The resulting LITGS measurements are compared with thermocouple values (dashed line). Without the seeded co-flow (red circles), the thermocouples and LITGS compare favourably, as the thermal grating forms only in the heated jet with biacetyl and the real temperature is captured by LITGS. However, once the room temperature co-flow is switched on, the acquired frequency is affected by averaging effect: the measurement volume contains not only the heated flow, but also the colder co-flow, both seeded with biacetyl. The PMT integrates all the scattered signals impinging into the sensitive area, but signals from the colder areas have a higher intensity, and therefore have a dominant effect. For this reason, LITGS and thermocouple measurements differ, as the LITGS signals are averaged along the probe volume, while thermocouple only measures the temperature in a point. This effect is more marked in the

turbulent jet, which has a diameter of 8 mm, considerably smaller than the probe volume length ($l \simeq 40$ mm). Only a small part of the probe volume is filled with the heated jet, while the rest of it is filled with the colder co-flow air. The intensity of the signal is higher at lower densities, therefore the presence of heated air is only barely captured from the LITGS measurements (blue circles). In the case of the wider laminar jet, whose diameter of 30 mm is similar to the probe volume length, the averaging effect has a lower impact, as most of the probe volume is filled with heated air. However, spatial averaging still occurs: LITGS measurements with the co-flow (blue circles) are lower than thermocouple measurements, especially for the points at the sides of the jet. This demonstrates that the effective probe length is longer than 30 mm and that the spatial averaging has a major impact on the acquired signal. In the high speed set-up, in which the collimated beams lead to a 40 mm long probe volume, the LITGS measurements lack of spatial resolution in the axial direction and lead to undue averaging, in spite of the advantage of low thermalisation for the low laser fluence.

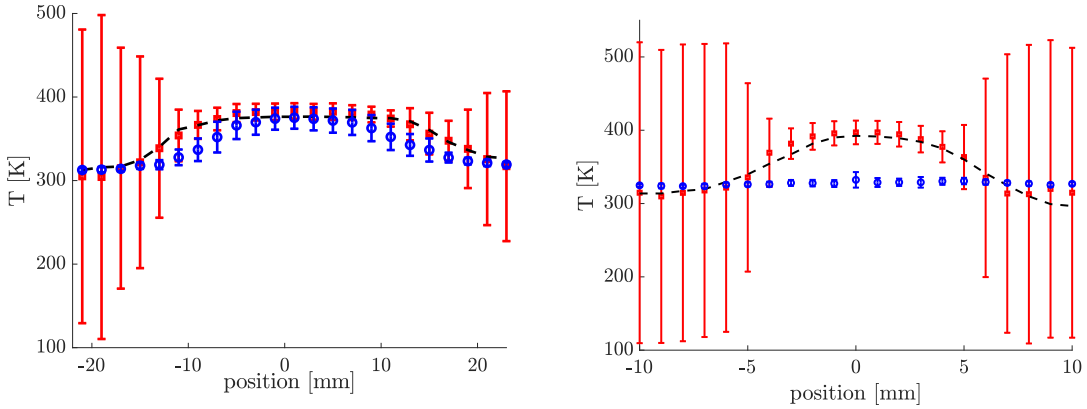

Fig. A.7 Measure LITGS temperature profile for the heated laminar (left) and turbulent (right) jet flow as a function of local radius, with (red squares) and without (blue circles) co-flow, and comparison with thermocouple measurements (dashed lines).

A.5 Conclusions

In this Appendix, we analyse the trade-off between spatial resolution and intrusiveness in the LITGS measurements using a low (10 Hz) and high speed (1 kHz) pump laser tuned at 355 nm. Biacetyl is added to the mean flow to absorb the 355 nm laser light and generate the thermal grating. We show that the addition of biacetyl at levels compatible with good signal-to-noise ratio changes the properties of the mean flow in a non-negligible way, and that the induced changes in molecular mass and specific heat capacity in the flow must be taken into account to correctly evaluate the local temperature. For sufficiently high laser

fluence (high pulse energies and low crossing areas), the absorption of laser energy from the biacetyl generates a non negligible temperature increase in the probe volume, shifting the LITGS frequency by 17% and therefore the acquired temperature by 35%. To mitigate the thermalisation effect while still maintaining good quality signals, the diameter of the pump beams at the crossing point can be increased, either by moving the beam waist far from the crossing point or by using collimated beams. However, a larger beam at the crossing point increases the probe volume length, thus deteriorates the spatial resolution. The principle is demonstrated in an experiment with heated laminar and turbulent jets seeded with biacetyl. The experiment shows a trade-off between intrusiveness and spatial resolution: increasing the beam diameter at the crossing location reduces the laser-induced thermalisation but leads to a longer probe volume, and a poorer spatial resolution. Techniques are suggested to both assess the effects and select a suitable set of experimental parameters.

References

[1] (1960). Nasa Glenn Research Center, Rocket Engine Test Facility (RETF) https://www1.grc.nasa.gov.

[2] (2016). Gras 26AC https://www.gras.dk.

[3] (2018). Advisory Council for Aviation Research and Innovation in Europe (ACARE) https://www.acare4europe.org/.

[4] (2018). Aviation Environment Federation (AEF) https://www.aef.org.uk.

[5] (2018). Chemkin Pro 18.2 (Reaction Design).

[6] (2018). International Civil Aviation Organization (ICAO) https://www.icao.int.

[7] Allen, M. G. (1998). Diode laser absorption sensors for gas-dynamic and combustion flows. *Measurement Science and Technology*, 9:545–562.

[8] Anderson, J. (2004). *Modern Compressible Flow with Historical Perspective*. McGraw-Hill, third edition.

[9] Bake, F., Kings, N., and Roehle, I. (2008). Fundamental mechanism of entropy noise in aero-engines: experimental investigation. *Journal of Engineering for Gas Turbines and Power*, 130(1):011202.

[10] Bake, F., Michel, U., and Roehle, I. (2007). Investigation of entropy noise in aero-engine combustors. *Journal of Engineering for Gas Turbines and Power*, 129(2):370.

[11] Bake, F., Richter, C., Muhlbauer, B., Kings, N., Rohle, I., Thiele, F., and Noll, B. (2009). The Entropy Wave Generator (EWG): A reference case on entropy noise. *Journal of Sound and Vibration*, 326(3-5):574–598.

[12] Banks-Lee, P. and Peng, H. (1989). Length error analysis for impedance tube measurements. *The Journal of the Acoustic Society of America*, 85:1769–1772.

[13] Becerril, C., Moreau, S., Bauerheim, M., Gicquel, L., and Poinsot, T. (2016). Numerical investigation of combustion noise: the Entropy Wave Generator. In *22nd AIAA/CEAS Aeroacoustics Conference, Lyon, France*, pages 1–18.

[14] Bechert, D. (1980). Sound absorption caused by vorticity shedding, demonstrated with a jet flow. *Journal of Sound and Vibration*, 70(79):389–405.

[15] Bellucci, V., Flohr, P., and Paschereit, C. O. (2004). Numerical and experimental study of acoustic damping generated by perforated screens. *AIAA Journal*, 42(8):1543–1549.

[16] Blevins (1984). *Applied fluid dynamic handbook*. Wokingham: Van Nostrand Reinhold.

[17] Bloy, A. W. (1979). The pressure waves produced by the convection of temperature disturbances in high subsonic nozzle flows. *Journal of Fluid Mechanics*, 94(03):465–475.

[18] Boden, H. (1986). Influence of errors on the two-microphone method for measuring acoustic properties in ducts. *The Journal of the Acoustical Society of America*, 79(2):541–549.

[19] Bohn, M. (1977). Response of a subsonic nozzle to acoustic and entropy disturbances. *Journal of Sound and Vibration*, 52(2):283–297.

[20] Bohn, M. S. (1976). *Noise produced by the interaction of acoustic waves and entropy waves with high speed nozzle flows*. PhD thesis, California Insitute of Technology.

[21] Bohn, M. S. and Zukoski, E. E. (1976). Effect of flow on the acoustic reflection coefficient at a duct inlet. *Journal of the Acoustical Society of America*, 59(6):1497–1499.

[22] Bonciolini, G. and Noiray, N. (2019). Synchronization of thermoacoustic modes in sequential combustors. *Journal of Engineering for Gas Turbines and Power*, 141(031010):1–9.

[23] Bork, B., Bohm, B., Heeger, C., R, C. S., and Dreizler, A. (2010). 1D high-speed Rayleigh measurements in turbulent flames. *Applied Physics B*, 101:487–491.

[24] Bragg, S. L. (1963). Combustion Noise. *Journal of the Institute of Fuel*, 36:12–16.

[25] Brown, M. A. and Churchill, S. W. (1995). Experimental measurements of pressure waves generated by impulsive heating of a surface. *Aiche Journal*, 41(2):205–213.

[26] Brown, M. S. and Roberts, W. L. (1999). Single-point thermometry in high-pressure, sooting, premixed combustion environments. *Journal of Propulsion and Power*, 15(1):119–127.

[27] Bruun, H. (1995). *Hot Wire Anemometry: Principles and Signal Analysis*. Oxford University Press Inc., 1 edition.

[28] Butenhoff, T. J. (1995). Measurement of the thermal diffusivity and speed of sound of hydrothermal solutions via the laser-induced grating technique. *Internation Journal of Thermophysics*, 16(I):1–9.

[29] Candel, S. (1972). *Analytical studies of some acoustic problems of jet engines*. PhD thesis, California Institute of Technology.

[30] Candel, S. (2002). Combustion dynamics and control: progress and challenges. *Proceedings of the Combustion Institute*, 29:1–28.

[31] Candel, S., Durox, D., Ducruix, D., Birbaud, A. L., Noiray, N., and Schuller, T. (2009). Flame dynamics and combustion noise: progress and challenges. *International Journal of Aeroacoustics*, 8(1-2):1–56.

[32] Carter, S., Ned, A., Chivers, J., and Bemis, A. (2010). Selecting piezoresistive vs. piezoelectric pressure transducers (AN 102). Technical report, Kulite Semiconductor Products, Inc.

[33] Chaplin, M. (2019). Water Absorption Spectrum (http://www1.lsbu.ac.uk/water/water_vibrational_spectrum.html).

[34] Chu, B. T. and Kovasznay, L. C. G. (1958). Non-linear interactions in a viscous heat-conducting compressible gas. *Journal of Fluid Mechanics*, 3:494–514.

[35] Conrad, E. W., Bloomer, H. E., Wanhainen, J., and Vincent, D. W. (1968). Interim summary of liquid rocket acoustic-mode instability studies at a nominal thrust of 20 000 pounds. Technical report, NASA.

[36] Crighton, D. G., Dowling, A. P., Ffowcs Williams, J., Heckl, M., and Leppington, F. G. (1992). *Modern methods in analytical acoustics, lecture notes*. Springer-Verlag London.

[37] Culick, F. and Yang, V. (1995). Overview of combustion instabilities in liquid-propellant rocket engines. In *Liquid Rocket Engine Combustion Instability. Progress in Astronautics and Aeronautics.*, pages 3–37. American Institute of Aeonautics and Astrophysics.

[38] Cummings, A. and Eversman, W. (1983). High amplitude acoustic transmission through duct terminations: theory. *Journal of Sound and Vibration*, 91:503–518.

[39] Cummings, E. B. (1994). Laser-induced thermal acoustics: simple accurate gas measurements. *Optics Letter*, 19(17):1361–1363.

[40] Cummings, E. B., Leyva, I. A., and Hornung, H. G. (1995). Laser-induced thermal acoustics (LITA) signals from finite beams. *Applied optics*, 34(18):3290–3302.

[41] Cumpsty, N. and Marble, F. (1977a). The interaction of entropy fluctuations with turbine blade rows; a mechanism of turbojet engine noise. *Proceedings of the Royal Society*, 357(1690):323–344.

[42] Cumpsty, N. A. (1979). Jet engine combustion noise: pressure, entropy and vorticity perturbations produced by unsteady combustion or heat addition. *Journal of Sound and Vibration*, 66(4):527–544.

[43] Cumpsty, N. A. and Marble, F. E. (1977b). Core noise from gas turbine exhausts. *Journal of Sound and Vibration*, 54(2):297–309.

[44] Dalmont, J. (2001). Acoustic impendance measurement, part I: a review. *Journal of Sound and Vibration*, 243(3):427–439.

[45] Darecki, M., Edelstenne, C., Enders, T., Fernandez, E., Hartman, P., Herteman, J.-P., Kerkloh, M., King, I., Ky, P., Mathieu, M., Orsi, G., Schotman, G., Smith, C., and Wörner, J.-D. (2011). Flightpath 2050. Technical report, European Commission.

[46] De Domenico, F., Guiberti, T. F., Hochgreb, S., and Roberts, W. L. (2019a). Temperature and water measurements in flames using 1064 nm Laser-Induced Grating Spectroscopy (LIGS). *Combustion and Flame*, 205:336–344.

[47] De Domenico, F., Guiberti, T. F., Hochgreb, S., Roberts, W. L., and Magnotti, G. (2019b). Tracer-free laser-induced grating spectroscopy using a pulse burst laser at 100 kHz. *Optics Express (submitted)*.

[48] De Domenico, F., Lowe, S. M., Fan, L., Williams, B. A. O., and Hochgreb, S. (2019c). High frequency measurement of temperature and composition spots with LITGS. *Journal of Engineering for Gas Turbines and Power*, 141(031003):1–11.

[49] De Domenico, F., Rolland, E., and Hochgreb, S. (2019d). A generalised model for acoustic and entropic transfer function of nozzles with losses. *Journal of Sound and Vibration*, 440:212–230.

[50] De Domenico, F., Rolland, E. O., and Hochgreb, S. (2017a). Detection of direct and indirect noise generated by synthetic hot spots in a duct. *Journal of Sound and Vibration*, 394:220–236.

[51] De Domenico, F., Rolland, E. O., and Hochgreb, S. (2017b). Measurements of the effect of boundary conditions on upstream and downstream noise arising from entropy spots. In *Proceedings of ASME Turbo Expo 2017: Turbomachinery Technical Conference and Exposition, Charlotte, NC, USA*, pages 1–13.

[52] De Domenico, F. D., Fan, L., Lowe, S. M., Weller, L., and Hochgreb, S. (2018). Trade off between thermalisation and spatial resolution for LITGS. In *19th International Symposium on the Application of Laser and Imaging Techniques to Fluid Mechanics, Lisbon, Portugal, July 16-20, 2018*, pages 1–24.

[53] Dennis, C. N., Slabaugh, C. D., Boxx, I. G., Meier, W., and Lucht, R. P. (2016). 5 kHz thermometry in a swirl-stabilized gas turbine model combustor using chirped probe pulse femtosecond CARS. Part 1: Temporally resolved swirl-flame thermometry. *Combustion and Flame*, 173:441–453.

[54] Dibble, R. and Hollenbach, R. (1981). Laser Rayleigh thermometry in turbulent flames. *Proceedings of the Combustion Institute*, 18(1):1489–1499.

[55] Dolan, D. H. (2010). Accuracy and precision in photonic Doppler velocimetry. *Review of Scientific Instruments*, 81(053905):1–7.

[56] Dowling, A. (1993). The calculation of thermoacoustic oscillations. *Journal of Sound and Vibration*, 180(4):557–581.

[57] Dowling, A. P. (1992). Sound absorption by a screen with a regular array of slits. *Journal of Sound and Vibration*, 156:387–405.

[58] Dowling, A. P. and Mahmoudi, Y. (2015). Combustion Noise. *Proceedings of the Combustion Institute*, 35(1):65–100.

[59] Dowling, A. P. and Stow, S. R. (2003). Acoustic analysis of gas turbine combustors. *Journal of Propulsion and Power*, 19(5):751–764.

[60] Duan, X. R., Meier, W., Weigand, P., and Lehmann, B. (2005). Phase-resolved laser Raman scattering and laser Doppler velocimetry applied to periodic instabilities in a gas turbine model combustor. *Applied Physics B*, 396:389–396.

[61] Ducruix, S., Schuller, T., Durox, D., and Paris, E. C. (2003). Combustion dynamics and instabilities: elementary coupling and driving mechanisms. *Journal of Propulsion and Power*, 19(5):722–734.

[62] Durán, I. and Moreau, S. (2013). Solution of the quasi one-dimensional linearized Euler equations using flow invariants and the Magnus expansion. *Journal of Fluid Mechanics*, 723:190–231.

[63] Durán, I., Moreau, S., and Poinsot, T. (2013). Analytical and numerical study of combustion noise through a subsonic nozzle. *AIAA Journal*, 51(1):42–52.

[64] Durán, I. and Morgans, A. S. (2015). On the reflection and transmission of circumferential waves through nozzles. *Journal of Fluid Mechanics*, 773:137–153.

[65] Durrieu, P., Hofmans, G., Ajello, G., Boot, R., Aurégan, Y., Hirschberg, A., and Peters, M. C. (2001). Quasisteady aero-acoustic response of orifices. *The Journal of the Acoustical Society of America*, 110(4):1859–1872.

[66] Eckbreth, A. (1996). *Laser diagnostics for combustion temperature and species*. CRC Press, first edition.

[67] Eckstein, J., Freitag, E., Hirsch, C., and Sattelmayer, T. (2006). Experimental study on the role of entropy waves in low-frequency oscillations in a RQL combustor. *Journal of Engineering for Gas Turbines and Power*, 128(2):264–270.

[68] Elsinga, G. E., Oudheusden, B. W. V., Scarano, F., and Watt, D. W. (2004). Assessment and application of quantitative schlieren methods: calibrated color schlieren and background oriented schlieren. *Experiments in Fluids*, 36:309–325.

[69] Farouk, B., Lin, Y., and Lei, Z. (2010). Acoustic wave induced flows and heat transfer in gases and supercritical fluid. In Cho, Y. and Greene, G., editors, *Advances in Heat Transfer (Vol.42)*, pages 1–136. Elsevier.

[70] Fayer, M. D. (1982). Dynamics of molecules in condensed phase: picosecond holographic grating experiments. *Annual Review of Physics and Chemistry*, 33:63–87.

[71] Ffowcs Williams, J. E. and Howe, M. S. (1975). The generation of sound by density inhomogeneities in low Mach number nozzle flows. *Journal of Fluid Mechanics*, 70(03):605–622.

[72] Förster, F. J., Baab, S., Steinhausen, C., Lamanna, G., Ewart, P., and Weigand, B. (2018). Mixing characterization of highly underexpanded fluid jets with real gas expansion. *Experiments in Fluids*, 59(44):1–10.

[73] Förster, F. J., Crua, C., Davy, M., and Ewart, P. (2017). Time-resolved gas thermometry by laser-induced grating spectroscopy with a high-repetition rate laser system. *Experiments in Fluids*, 58(87):1–8.

[74] Fourkas, J. T., Brewer, T. R., Kim, H., and Fayer, M. (1991). Picosecond polarization-selective transient grating experiments in sodium-seeded flames. *The Journal of Chemical Physics*, 95(8):5775–5784.

[75] Franzelli, B., Riber, E., Gicquel, L. Y. M., and Poinsot, T. (2012). Large Eddy Simulation of combustion instabilities in a lean partially premixed swirled flame. *Combustion and Flame*, 159(2):621–637.

[76] Franzoni, L. P. and Elliott, C. M. (1998). An innovative design of a probe-tube attachment for a 0.5-in. microphone. *Journal of the Acoustical Society of America*, 104(5):2903–2910.

[77] Gabet, K. N., Jiang, N., Lempert, W. R., and Sutton, J. A. (2010). Demonstration of high-speed 1D Raman scattering line imaging. *Applied Physics B*, 101:1–5.

[78] Gaetani, P. and Persico, G. (2019). Transport of entropy waves within a high pressure turbine stage. *Journal of Turbomachinery*, 141(031006):1–9.

[79] Gaetani, P., Persico, G., and Spinelli, A. (2015). Entropy Wave Generator for indirect combustion noise in a high-pressure turbine. In *Proceedings of the 11th European Conference on Turbomachinery Fluid Dynamics and Thermodynamics*.

[80] Giauque, A., Huet, M., and Clero, F. (2012). Analytical analysis of indirect combustion noise in subcritical nozzles. *Journal of Engineering for Gas Turbines and Power*, 134(111202):1–8.

[81] Giauque, A., Huet, M., Clero, F., Ducruix, S., and Richecoeur, F. (2013). Thermoacoustic Shape Optimization of a Subsonic Nozzle. *Journal of Engineering for Gas Turbines and Power*, 135(102601):1–9.

[82] Giezendanner, R., Keck, O., Weigand, P., Meier, W., Meier, U., and Stricker, W. (2002). Periodic combustion instabilities in a swirl burner studied by phase-locked planar laser-induced fluorescence. *Combustion Science and Technology*, 175:721–741.

[83] Giusti, A., Magri, L., and Zedda, M. (2019). Flow inhomogeneities in a realistic aeronautical gas-turbine combustor: formation, evolution, and indirect noise. *Journal of Engineering for Gas Turbines and Power*, 141(011502):1–11.

[84] Giusti, A., Worth, N. A., Mastorakos, E., and Dowling, A. P. (2017). Experimental and numerical investigation into the propagation of entropy waves. *AIAA Journal*, 55(2):446–458.

[85] Goh, C. S. and Morgans, A. S. (2011). Phase prediction of the response of choked nozzles to entropy and acoustic disturbances. *Journal of Sound and Vibration*, 330(21):5184–5198.

[86] Goh, C. S. and Morgans, A. S. (2013). The influence of entropy waves on the thermoacoustic stability of a model combustor. *Combustion Science and Technology*, 185:249–268.

[87] Gojani, A. B., Danehy, P. M., Alderfer, D. W., Saito, T., and Takayama, K. (2004). Development of laser-induced grating spectroscopy for underwater temperature measurement in shock wave focusing regions. In *Proceedings of SPIE - The International Society for Optical Engineering*, pages 1–10.

[88] Govoni, D. E., Booze, J. A., Sinha, A., and Crim, F. F. (1993). The non-resonant signal in laser-induced grating spectroscopy of gases. *Chemical Physics Letters*, 216(3):525–529.

[89] Grace, J. M., Nebolsine, P. E., Goldey, C. L., Chahal, G., Norby, J., and Heritier, J. (1998). Repetitively pulsed ruby lasers as light sources for high-speed photography. *Optical Engineering*, 37(8):2205–2212.

[90] Hajialigol, N. and Mazaheri, K. (2018). The dissipation and dispersion of the entropy wave caused by a turbulent lean premixed flame in a combustor. *Applied Thermal Engineering*, -:1–17.

[91] Hanson, R. K. and Davidson, D. F. (2014). Recent advances in laser absorption and shock tube methods for studies of combustion chemistry. *Progress in Energy and Combustion Science*, 44:103–114.

[92] Hanson, R. K., Kuntz, P. A., and Kruger, C. H. (1977). High-resolution spectroscopy of combustion gases using a tunable IR diode laser. *Applied Optics*, 16(8):2045–2048.

[93] Hart, R. C., Balla, R. J., and Herring, G. C. (2001). Simultaneous velocimetry and thermometry of air by use of nonresonant heterodyned laser-induced thermal acoustics. *Applied Optics*, 40(6):965–968.

[94] Hayakawa, A., Yamagami, T., Takeuchi, K., Higuchi, Y., Kudo, T., Lowe, S., Gao, Y., Hochgreb, S., and Kobayashi, H. (2018). Quantitative measurement of temperature in oxygen enriched CH4/O2/N2 premixed flames using Laser Induced Thermal Grating Spectroscopy (LITGS) up to 1.0 MPa. *Proceedings of the Combustion Institute*, 37(2):1427–1434.

[95] Hell, A., Förster, F., Rosenko, E., and Weigand, B. (2012). Experiments in chemically reacting subsonic flames and heated supersonic flows using Laser-Induced Thermal Acoustics (LITA). In *16th Int Symp on Applications of Laser Techniques to Fluid Mechanics, Lisbon, Portugal, 09-12 July, 2012*, pages 1–11.

[96] Hell, A., Förster, F. J., and Weigand, B. (2016). Validation of laser-induced thermal acoustics for chemically reacting H2/air free jets. *Journal of Raman Spectroscopy*, 47(9):1157–1166.

[97] Hemmerling, B. and Kozlov, D. N. (2006). Diagnostics of water-containing gas mixtures using thermal laser-induced gratings. *Journal of Chemical Physics*, 320:103–117.

[98] Hemmerling, B., Kozlov, D. N., and Stampanoni-Panariello, A. (2000). Temperature and flow-velocity measurements by use of laser-induced electrostrictive gratings. *Optics Letters*, 25(18):1340–1342.

[99] Hemmerling, B., Neracher, M., Kozlov, D., Kwan, W., Stark, R., Klimenko, D., Clauss, W., and Oschwald, M. (2002). Rocket nozzle cold-gas flow velocity measurements using laser-induced gratings. *Journal of Raman Spectroscopy*, 33:912–918.

[100] Hemmerling, B. and Stampanoni-Panariello, A. (2001). Investigation of soot by two-colour four-wave mixing. *Chemosphere*, 42:647–653.

[101] Hield, P. A. and Brear, M. J. (2008). Comparison of open and choked premixed combustor exits during thermoacoustic limit cycle. *AIAA Journal*, 46(2):517–526.

[102] Higgins, B. (1802). On the sound produced by a current of hydrogen gas passing through a tube. *Journal of Natural Philosophy, Chemistry, and the Arts*, 1:129.

[103] Hochgreb, S., Dennis, D., Ayranci, I., Bainbridge, W., and Cant, S. (2013). Forced and self-excited instabilities from lean premixed, liquid-fuelled aeroengine injectors at high pressures and temperatures. In *Proceedings of the ASME Turbo Expo, San Antonio, TX, USA*, pages 1–12.

[104] Hollingshead, C. L. (2011). *Discharge coefficient performance of venturi, standard concentric orifice plate, v-cone, and wedge flow meters at small reynolds numbers*. PhD thesis, Utah State University.

[105] Horowitz, A., Meller, R., and Moortgat, G. K. (2001). The UV – VIS absorption cross sections of the alpha-dicarbonyl compounds: pyruvic acid, biacetyl and glyoxal. *Journal of Photochemistry and Photobiology A: Chemistry*, 146:19–27.

[106] Howe, B. M. S. (1979). Attenuation of sound in a low Mach number nozzle flow. *Journal of Fluid Mechanics*, 91:220–229.

[107] Howe, M. S. (2010). Indirect combustion noise. *Journal of Fluid Mechanics*, 659:267–288.

[108] https://www.safran group.com/, S. (2019). Safran.

[109] Hubschmid, W., Hemmerling, B., and Stampanoni-Panariello, A. (1995). Rayleigh and Brillouin modes in electrostrictive gratings. *Journal of the Optical Society of America*, 12(10):1850–1854.

[110] Huet, M. (2016). Nonlinear indirect combustion noise for compact supercritical nozzle flows. *Journal of Sound and Vibration*, 374:211–227.

[111] Huet, M. and Giauque, A. (2013). A nonlinear model for indirect combustion noise through a compact nozzle. *Journal of Fluid Mechanics*, 733:268–301.

[112] Huntley, J. M. (1994). High-speed laser speckle photography. Part 1: repetitively Q-switched ruby laser light source. *Optical Engineering*, 33(5):1692–1699.

[113] Hwang, I. and Kim, Y. (2006). Measurement of thermo-acoustic waves induced by rapid heating of nickel sheet in open and confined spaces. *International Journal of Heat and Mass Transfer*, 49(3-4):575–581.

[114] Ihme, M. (2017). Combustion and engine-core noise. *Annual Review of Fluid Mechanics*, 49:277–310.

[115] Kaminski, C. F., Hult, J., and Alden, M. (1999). High repetition rate planar laser induced fluorescence of OH in a turbulent non-premixed flame. *Applied Physics B*, 760:757–760.

[116] Kiefer, J., Kozlov, D. N., Seeger, T., and Leipertz, A. (2008). Local fuel concentration measurements for mixture formation diagnostics using diffraction by laser-induced gratings in comparison to spontaneous Raman scattering. *Journal of Raman Spectroscopy*, 39:711–721.

[117] Kings, N. (2015). *Indirect combustion noise: experimental investigation of the vortex sound generation in nozzle flows*. PhD thesis, DLR Berlin.

[118] Knobloch, K., Lahiri, C., Enghardt, L., Bake, F., and Peitsch, D. (2011). Hot-Acoustic-Testrig (HAT)- A unique facility for thermoacoustic research. In *Proceedings of ASME Turbo Expo 2011*, pages 1–10, Vancouver, Canada.

[119] Knobloch, K., Neuhaus, L., Bake, F., Gaetani, P., and Persico, G. (2017). Experimental assessment of noise generation and transmission in a high-pressure transonic turbine stage. *Journal of Turbomachinery*, 139(101006):1–12.

[120] Knobloch, K., Werner, T., and Bake, F. (2015). Noise generation in hot nozzle flow. In *Proceedings of the ASME Turbo Expo 2015, Montreal, Canada*, pages 1–14.

[121] Knudsen, J. and Katz, D. (1958). *Fluid Dynamics and Heat Transfer*. McGraw-Hill.

[122] Kovasznay, L. (1953). Turbulence in supersonic flow. *Journal of the Aereonautical Sciences*, 20(10).

[123] Kozlov, D. N. (2005). Simultaneous characterization of flow velocity and temperature fields in a gas jet by use of electrostrictive laser-induced gratings. *Applied Physics B*, 387:377–387.

[124] Lahiri, C. and Bake, F. (2017). A review of bias flow liners for acoustic damping in gas turbine combustors. *Journal of Sound and Vibration*, 400:564–605.

[125] Lamb, D. C., Lin, G. C., and Doukas, A. G. (1977). Picosecond grating spectroscopy for characterizing the acoustic properties of biological material. *Applied Optics*, 36(7):1660–1666.

[126] Latzel, H., Dreizler, A., Dreier, T., Heinze, J., Dillmann, M., Stricker, W., Lloyd, G. M., and Ewart, P. (1998). Thermal grating and broadband degenerate four-wave mixing spectroscopy of OH in high-pressure flames. *Applied Physics B*, 67(5):667–673.

[127] Laumonier, J., Jean, P., and Hardouin, L. (1997). An active anechoic termination for low frequencies with mean flow. *Acta Acustica united with Acustica,*, 83:25–34.

[128] Lemaire, R. and Menanteau, S. (2017). Assessment of radiation correction methods for bare bead thermocouples in a combustion environment. *International Journal of Thermal Sciences*, 122:186–200.

[129] Lempert, W., Wu, P.-F., Miles, R., B., Z., Lowrance, J., Mastrocola, V., and Kosonocky, W. (1996). Pulse-burst laser system for high-speed flow diagnostics. In *34th Aerospace Sciences Meeting and Exhibit. Reno, NV, U.S.A.*

[130] Leyko, M., Moreau, S., Nicoud, F., and Poinsot, T. (2011). Numerical and analytical modelling of entropy noise in a supersonic nozzle with a shock. *Journal of Sound and Vibration*, 330(16):3944–3958.

[131] Leyko, M., Nicoud, F., and Poinsot, T. (2009). Comparison of direct and indirect combustion noise mechanisms in a model combustor. *AIAA Journal*, 47(11):2709–2716.

[132] Lieuwen, T. (2012). *Unsteady Combustion Physics*. Cambridge University Press.

[133] Lieuwen, T. C. and Yang, V., editors (2005). *Combustion Instabilities In Gas Turbine Engines: Operational Experience, Fundamental Mechanisms, and Modeling*. American Institute of Aeronautics and Astronautics.

[134] Lighthill, M. (1952). On sound generated aerodynamically I. General theory. *Proceedings of the Royal Society*, 211(107):564–587.

[135] Lighthill, M. (1954). On sound generated aerodynamically II. Turbulence as a source of sound. *Proceedings of the Royal Society*, 222(1148).

[136] Liu, X., Wang, G., Zheng, J., Liangliang, X., Sirui, W., Li, L., and Qi, F. (2018). Temporally resolved two dimensional temperature field of acoustically excited swirling flames measured by mid-infrared direct absorption spectroscopy. *Optics Express*, 26(24):31983–31994.

[137] Lord Rayleigh, J. (1894). *The Theory of Sound*. Macmillan.

[138] Lourier, J. M., Huber, A., Noll, B., and Aigner, M. (2014). Numerical analysis of indirect combustion noise generation within a subsonic nozzle. *AIAA Journal*, 52(10):2114–2126.

[139] Lowe, S. M. (2018). *Quantitative measurements of temperature using laser-induced thermal grating spectroscopy in reacting and non-reacting flows*. PhD thesis, University of Cambridge.

[140] Lucht, R. P., Roy, S., Meyer, T. R., Gord, J. R., Roy, S., and Meyer, T. R. (2006). Femtosecond coherent anti-Stokes Raman scattering measurement of gas temperatures from frequency-spread dephasing of the Raman coherence. *Applied Physics Letters*, 89(251112):1–3.

[141] Luers, A., Salhlberg, A. L., Hochgreb, S., and Ewart, P. (2018). Flame thermometry using laser-induced-grating spectroscopy of nitric oxide. *Applied Physics B: Lasers and Optics*, 124(3):1–13.

[142] Magnotti, G., Cutler, A., and Danehy, P. (2012a). Development of a dual-pump CARS system for measurements in a supersonic combusting free jet. In *50th AIAA Aerospace Sciences Meeting, Nashville, TN, USA*.

[143] Magnotti, G., Cutler, A. D., and Danehy, P. M. (2012b). Beam shaping for CARS measurements in turbulent environments. *Applied Optics*, 51(20):4730–41.

[144] Magri, L. (2017). On indirect noise in multicomponent nozzle flows. *Journal of Fluid Mechanics*, 828(R2):1–14.

[145] Magri, L., O'Brien, J., and Ihme, M. (2016). Compositional inhomogeneities as a source of indirect combustion noise. *Journal of Fluid Mechanics*, 799(R4):1–12.

[146] Mahmoudi, Y., Giusti, A., Mastorakos, E., and Dowling, A. P. (2018). Low-order modeling of combustion noise in an aero-engine: the effect of entropy dispersion. *Journal of Engineering for Gas Turbines and Power*, 140(011502):1–7.

[147] Marble, F. and Candel, S. (1977). Acoustic disturbance from gas non-uniformities convected through a nozzle. *Journal of Sound and Vibration*, 55(2):225–243.

[148] Maznev, A., McAuliffe, D., Doukas, A., and Nelson, K. (1999). Wide-band acoustic spectroscopy of biological material based on Laser-Induced Grating Technique. *Ultrasound in Medicine & Biology*, 25(4):601–607.

[149] Mazur, M. (2017). *Etude expérimentale du bruit de combustion dans un foyer de type aéronautique*. PhD thesis, Université Paris-Saclay.

[150] Miles, R., Forkey, J. N., and Lempert, W. R. (1992). Filtered Rayleigh scattering measurements in supersonic/hypersonic facilities. In *28th Joint Propulsion Conference and Exhibit, AIAA, Nashville,TN, U.S.A.*

[151] Miller, J. D., Slipchenko, M. S., Mance, J. G., S, R., and Gord, J. (2016). 1-kHz two-dimentsional coherent anti-Stokes Raman scattering (2D-CARS) for gas-phase thermometry. *Optics express*, 24(22):1340–1342.

[152] Moase, W., Brear, M., and Manzie, C. (2007). The forced response of choked nozzles and supersonic diffusers. *Journal of Fluid Mechanics*, 585:281–304.

[153] Morfey, C. L. (1973). Amplification of aerodynamic noise by convected flow inhomogeneities. *Journal of Sound and Vibration*, 31(4):391–397.

[154] Morgans, A. S. and Duran, I. (2016). Entropy noise: a review of theory, progress and challenges. *International Journal of Spray and Combustion dynamics*, 8(4):285–298.

[155] Morgans, A. S., Goh, C. S., and Dahan, J. a. (2013). The dissipation and shear dispersion of entropy waves in combustor thermoacoustics. *Journal of Fluid Mechanics*, 733(R2):1–11.

[156] Motheau, E., Nicoud, F., Mery, Y., and Poinsot, T. (2013). Analysis and modelling of entropy modes in a realistic aeronautical gas turbine. *Journal of Engineering for Gas Turbines and Power*, 135(092602):1–7.

[157] Motheau, E., Nicoud, F., and Poinsot, T. (2014). Mixed acoustic–entropy combustion instabilities in gas turbines. *Journal of Fluid Mechanics*, 749:542–576.

[158] Mühlbauer, B., Noll, B., and Aigner, M. (2009). Numerical investigation of the fundamental mechanism for entropy noise generation in aero-engines. *Acta Acustica united with Acustica*, 95(3):470–478.

[159] Muthukrishnan, M., Strahle, W. C., and Nealej, D. H. (1977). Combustion noise in a gas turbine combustor. *AIAA Journal*, 16(4):320–327.

[160] Neely, W. and Hall, T. (1972). Vapor pressure of biacetyl. *Journal of Chemical and Engineering Data*, 17(3):294–295.

[161] Nelson, K. and Fayer, M. (1980). Laser induced phonons: A probe of intermolecular interactions in molecular solids interactions in molecular solids. *The Journal of Chemical Physics*, 72(9):5202–5218.

[162] Nielsen, T. (1994). Precision microphone for measurements and sound reproduction. In Gayford, M., editor, *Microphone Engineering Handbook*, pages 62–139. Focal Press.

[163] Paschereit, C. O., Gutmark, E., and Weisenstein, W. (1998). Control of thermoacoustic instabilities and emissions in an industrial-type gas-turbine combustion. *Proceedings of the Combustion Institute*, 27(2):1817–1824.

[164] Patton, R. A., Gabet, N., Jiang, N., Lempert, W. R., and Sutton, J. A. (2012). Multi-kHz mixture fraction imaging in turbulent jets using planar Rayleigh scattering. *Applied Physics B*, 106:457–471.

[165] Paul, P. H., Farrow, R. L., and Danehy, P. M. (1995). Gas-phase contributions to four-wave mixing. *Journal of the Optical Society of America*, 12(3):384–392.

[166] Poinsot, T. (2017). Prediction and control of combustion instabilities in real engines. *Proceedings of the Combustion Institute*, 36(1):1–28.

[167] Poinsot, T. and Veynante, D. (2011). *Theoretical and Numerical Combustion*. R.T. Edwards, Inc, third edition.

[168] Polifke, W., Paschereit, C. O., and Doebbeling, K. (2001). Constructive and destructive interference of acoustic and entropy waves in a premixed combustor with a choked exit. *International Journal of Acoustics and Vibration*, 6(3):135–146.

[169] Raffel, M. (2015). Background-oriented schlieren (BOS) techniques. *Experiments in Fluids*, 56(60):1–17.

[170] Rausch, A., Fischer, A., Konle, H., Gaertlein, A., Nitsch, S., Knobloch, K., Bake, F., and Rohle, I. (2011). Measurements of density pulsations in the outlet nozzle of a combustion chamber by Rayleigh-scattering searching entropy waves. *Journal of Engineering for Gas Turbines and Power*, 133(031601):1–9.

[171] Reader-Harris, M. (2015). Orifice Design. In *Orifice Plates and Venturi Tubes*, page 393. Springer.

[172] Rienstra, S. and Hirschberg, A. (2015). *An Introduction to Acoustics*. Eindhoven University of Technology.

[173] Rolland, E., De Domenico, F., and Hochgreb, S. (2018). Direct and indirect noise generated by entropic and compositional inhomogeneities. *Journal of Engineering for Gas Turbines and Power*, 140(082604):1–9.

[174] Rolland, E. O. (2018). *Sound produced by entropic and compositional inhomogeneities*. PhD thesis, University of Cambridge.

[175] Rolland, E. O., De Domenico, F., and Hochgreb, S. (2017). Theory and application of reverberated direct and indirect noise. *Journal of Fluid Mechanics*, 819:435–464.

[176] Rose, T. S., Wilson, W. L., Wackerle, G., and Fayer, M. (1987). Gas phase dynamics and spectroscopy probed with picosecond transient grating experiments. *The Journal of Chemical Physics*, 86(10):5370–5391.

[177] Roy, S., Gord, J. R., and Patnaik, A. K. (2010). Recent advances in coherent anti-Stokes Raman scattering spectroscopy: Fundamental developments and applications in reacting flows. *Progress in Energy and Combustion Science*, 36(2):280–306.

[178] Roy, S., Kulatilaka, W. D., Richardson, D. R., Lucht, R. P., and Gord, J. R. (2009). Gas-phase single shot thermometry at 1-kHz using fd-CARS spectroscopy. *Optics Letters*, 34(24):3857–3859.

[179] Sahlberg, A.-l., Hot, D., Kiefer, J., and Aldén, M. (2017). Mid-infrared laser-induced thermal grating spectroscopy in flames. *Proceedings of the Combustion Institute*, 36(3):4515–4523.

[180] Sahlberg, A. L., Willman, A. L. C., and Ewart, B. A. O. W. P. (2019). Pressure measurement in combusting and non-combusting gases using laser-induced grating spectroscopy. *Applied Physics B*, 125(3):1–12.

[181] Salcedo, J., Siegman, A., Dlott, D., and Fayer, M. (1978). Dynamics of energy transport in molecular crystals: the picosecond transient-grating method. *Physical Review Letters*, 41(2):131–134.

[182] Salcedo, J. R. and Siegman, A. E. (1979). Laser induced photoacoustic grating effects in molecular crystals. *IEEE Journal of Quantum Electronics*, QE-15(4):250–256.

[183] Salikuddin, M. (1990). Acoustic behaviour of orifice plates and perforated plates with reference to low-frequency sound absorption. *Journal of Sound and Vibration*, 139:361–381.

[184] Sander, T., Altenhöfer, P., and Mundt, C. (2014). Development of laser-induced grating spectroscopy for application in shock tunnels. *Journal of Thermophysics and Heat Transfer*, 28(1):27–31.

[185] Sattelmayer, T. (2003). Influence of the combustor aerodynamics on combustion instabilities from equivalence ratio fluctuations. *Journal of Engineering for Gas Turbines and Power*, 125(1):1–19.

[186] Schuermans, B. (2003). *Modeling and control of thermoacoustic instabilities*. PhD thesis, École Politechnique Federale de Lausanne.

[187] Sepman, A. V., Toro, V. V., Mokhov, A. V., and Levinsky, H. B. (2013). Determination of temperature and concentrations of main components in flames by fitting measured Raman spectra. *Applied Physics B*, 112:35–47.

[188] Smith, G. P., Golden, D. M., Frenklach, M., Moriarty, N. W., Eiteneer, B., Goldenberg, M., Bowman, C. T., Hanson, R. K., Song, S., Gardiner, W. C., Lissianski, V. V., and Qin, Z. (2018). GRI MECH 3.0.

[189] Stampanoni-Panariello, A., Hemmerling, B., and Hubschmid, W. (1998). Temperature measurements in gases using laser-induced electrostrictive gratings. *Applied Physics B*, 130:125–130.

[190] Stampanoni-Panariello, A., Kozlov, D. N., Radi, P. P., and Hemmerling, B. (2005a). Gas phase diagnostics by laser-induced gratings I. Theory. *Applied Physics B*, 81:101–111.

[191] Stampanoni-Panariello, A., Kozlov, D. N., Radi, P. P., and Hemmerling, B. (2005b). Gas-phase diagnostics by laser-induced gratings II. Experiments. *Applied Physics B*, 81:113–129.

[192] Stauffer, H. U., Miller, J. D., Roy, S., Gord, J. R., and Meyer, T. R. (2012). Communication: Hybrid femtosecond/picosecond rotational coherent anti-Stokes Raman scattering thermometry using a narrowband time-asymmetric probe pulse. *The Journal of Chemical Physics*, 136(111101):1–5.

[193] Stevens, R. and Ewart, P. (2004). Single-shot measurement of temperature and pressure using laser-induced thermal gratings with a long probe pulse. *Applied Physics B*, 78(1):111–117.

[194] Stow, S. R., Dowling, A. P., and Hynes, T. P. (2002). Reflection of circumferential modes in a choked nozzle. *Journal of Fluid Mechanics*, 467:1–25.

[195] Strahle, W. C. (1971). On combustion generated noise. *Journal of Fluid Mechanics*, 49(2):399–414.

[196] Strahle, W. C. (1972). Some results in combustion generated noise. *Journal of Sound and Vibration*, 23(1):113–125.

[197] Strahle, W. C. (1978). Combustion noise. *Progress in Energy and Combustion Science*, 4:157–176.

[198] Strobio Chen, L., Bomberg, S., and Polifke, W. (2016). Propagation and generation of acoustic and entropy waves across a moving flame front. *Combustion and Flame*, 166:170–180.

[199] Su, J., Rupp, J., Garmory, A., and Carrotte, J. F. (2015). Measurements and computational fluid dynamics predictions of the acoustic impedance of orifices. *Journal of Sound and Vibration*, 352:174–191.

[200] Tam, C. K. W. and Parrish, S. A. (2018). The physical processes of indirect combustion noise generation. *International Journal of Aeroacoustics*, 16(1-2):22–35.

[201] Tao, W., Schuller, T., Huet, M., and Richecoeur, F. (2017). Coherent entropy induced and acoustic noise separation in compact nozzles. *Journal of Sound and Vibration*, 394:237–255.

[202] Thomsen, D. D., Kuligowski, F. F., and Laurendeau, N. M. (1999). Modeling of NO formation in premixed, high-pressure methane flames. *Combustion and Flame*, 119:307–318.

[203] Thurber, M. C., Grisch, F., Kirby, B. J., Votsmeier, M., and Hanson, R. K. (1998). Measurements and modeling of acetone laser-induced fluorescence with implications for temperature-imaging diagnostics. *Applied Optics*, 37(21):4963–4978.

[204] Thurow, B., Jiang, N., and Lempert, W. (2013). Review of ultra-high repetition rate laser diagnostics for fluid dynamic. *Measurement Science and Technology*, 24:1–22.

[205] Thurow, B., Jiang, N., Samimy, M., and Lempert, W. (2004). Narrow-line megaherz laser for high-speed flow diagnostics. *Applied Optics*, 43(26):5064–5073.

[206] Thurow, B. S., Satija, A., and Lynch, K. (2009). Third-generation megahertz-rate pulse burst laser system. *Applied Optics*, 48(11):2086–2093.

[207] Trilling, L. (1955). On thermally induced sound fields. *The Journal of the Acoustic Society of America*, 27(3):425–431.

[208] Turner, J. and Yoos, T. R. (1961). Pressure loss calculation procedures for high speed gas flow in ducts. Technical report, U.S. Navy Bureau of Ships.

[209] Walker, D. J. W., Williams, R. B., and Ewart, P. (1998). Thermal grating velocimetry. *Optics Letters*, 23(16):1316–1318.

[210] Wang, G. H., Clemens, N. T., and Varghese, P. L. (2005). High-repetition rate measurements of temperature and thermal dissipation in a non-premixed turbulent jet flame. *Proceedings of the Combustion Institute*, 30:691–699.

[211] Wassmer, D., Pause, F., Schuermans, B., Paschereit, C. O., and Moeck, J. P. (2017a). An onion peeling reconstruction of the spatial characteristics of entropy waves in a model gas turbine combustor. In *Proceedings of ASME Turbo Expo 2017:*, pages 1–11, Charlotte, NC.

[212] Wassmer, D., Schuermans, B., Paschereit, C. O., and Moeck, J. P. (2017b). Measurement and modeling of the generation and the transport of entropy waves in a model gas turbine combustor. *International Journal of Spray and Combustion dynamics*, 9(4):299–309.

[213] Weilenmann, M., Yuan, X., Bothien, M., and Noiray, N. (2019). Background-oriented schlieren of fuel jet flapping under thermoacoustic oscillations in a sequential combustor. *Journal of Engineering for Gas Turbines and Power*, 141(011030):1–8.

[214] Williams, B. A. O. (2009). *Quantitative Laser Diagnostics for Combustion*. PhD thesis, University of Oxford.

[215] Williams, B. A. O. and Ewart, P. (2012). Photophysical effects on laser induced grating spectroscopy of toluene and acetone. *Chemical Physics Letters*, 546:40–46.

[216] Williams, S., Rahn, L. A., Paul, P. H., Forsmant, J. W., and Zare, R. N. (1994). Laser-induced thermal grating effects in flames. *Optics Letters*, 19(21):1681–1683.

[217] Willman, C. (2016). *Laser diagnostics for spatially resolved thermometry in combustion and flows*. PhD thesis, University of Oxford.

[218] Willman, C. and Ewart, P. (2016). Multipoint temperature measurements in gas flows using 1-D laser-induced grating scattering. *Experiments in Fluids*, 57(191):1–9.

[219] Wu, P. P. and Miles, R. B. (2000). High-energy pulse-burst laser system for megahertz-rate flow visualization. *Optics Letters*, 25(22):1639–1641.

[220] Xia, Y., Duran, I., Morgans, A. S., and Han, X. (2018). Dispersion of entropy perturbations transporting through an industrial gas turbine combustor. *Flow, Turbulence and Combustion*, 100:481–502.

[221] Yang, D. and Morgans, A. S. (2016). A semi-analytical model for the acoustic impedance of finite length circular holes with mean flow. *Journal of Sound and Vibration*, 384:294–311.

[222] Zhao, D. and Li, X. Y. (2015). A review of acoustic dampers applied to combustion chambers in aerospace industry. *Progress in Aerospace Sciences*, 74:114–130.

[223] Zhou, L. and Bodén, H. (2014). Experimental investigation of an in-duct orifice with bias flow under medium and high level acoustic excitation. *International Journal of Spray and Combustion Dynamics*, 6:267–292.

[224] Zuckerwar, A. (1995). Principles of operation of condenser microphones. In Wong, G. S. K. and Embleton, T. F. W., editors, *AIP handbook of condenser microphones*, chapter 2, pages 37–69. AIP press.